Pulsed Field Magnetization of Composite Superconducting Bulks for Magnetic Bearing Applications

UNIVERSITY OF CAMBRIDGE

Anup Patel

Queens' College

Department of Materials Science and Metallurgy

Dissertation submitted for the degree of Doctor of Philosophy

May 2013

Abstract

Permanent magnets are essential components for many devices such as motors, which currently account for 45 % of global electricity consumption, generators and also superconducting magnetic bearings used for applications such as flywheel energy storage. But even the most powerful rare-earth magnets are limited to a remanent field of 1.4 T, whereas superconducting materials such as YBCO in their bulk form have the extraordinary ability to trap magnetic fields an order of magnitude higher, whilst being very compact. This gives them the potential to increase efficiency and allow significant volume and weight reductions for rotating machines despite the need for cooling. A new design of superconducting magnetic bearing has been developed which uses magnetized bulks as the field source, eliminating permanent magnets. Finite element modelling shows that the bulk – bulk design can achieve much higher force densities than existing permanent magnet – bulk designs, giving it potential to be used as a compact magnetic bearing. A system was created to magnetize bulks using a pulsed magnetic field down to 10 K and then measure levitation force. In proving the concept of the proposed design, the highest levitation forces ever reported between two superconducting bulks were measured, including a levitation force of 500 N between a 1.7 T magnetized YBCO bulk and a coaxial MgB_2 bulk tube.

The biggest factor limiting the use of magnetized bulks in applications is magnetizing them in the first place. Using a pulsed magnetic field is most practical but generates excessive heat dissipation leading to a loss of flux in conventional bulk superconductors, which are 100% superconductor. Although multi-pulse techniques help maximise the trapped field, the poor thermal properties of bulk (RE)BCO are a limiting factor. New composite superconducting structures are reported which can overcome these problems by using high thermal conductivity materials, the motivation for which came from finite element modelling of the critical state coupled with heat transfer. In particular, composite structures created by cutting and stacking 12 mm wide (RE)BCO superconducting tape are shown experimentally to have exceptional field trapping ability due to superior thermal and mechanical properties compared to existing bulks. Up to 2 T was trapped in a stack of commercially available tape produced by SuperPower Inc. in the first reported pulsed magnetization of such a stack. Over 7 T was trapped between two stacks using field cooling at 4.2 K, the highest field yet trapped in such a sample.

Declaration

This dissertation is the result of my own work and includes nothing which is the outcome of work done in collaboration except where specifically indicated in the text. It does not exceed the word limit imposed by the Degree Committee of the Faculty of Physics and Chemistry. No part of this dissertation has been or will be submitted for any other degree or qualification.

Anup Patel

Acknowledgements

I would like to thank all those who have helped and supported me whilst conducting the research for this thesis. I would like to express my sincere gratitude to my supervisor, Professor Bartek Glowacki, for the invaluable support and guidance he has given me, as well as his encouragement to always aim for the best. I would like to thank Dr Simon Hopkins for his continuous support, for always being available to discuss ideas and problems, and for constructive criticism of my work. I'm particularly grateful for the key contribution he made to the pulse magnetization and levitation force measurement system. I would like to thank him for writing sophisticated software for it and creating the electronics with me.

I would like to acknowledge the Engineering and Physical Sciences Research Council for funding. I would like to thank Professor Ryszard Palka of the Department of Power Systems and Electrical Drives, West Pomeranian University of Technology, Poland, for co-supervision of levitation force modelling and valuable discussions on magnetic bearings. I'm grateful to Professor David Cardwell and Dr Yunhua Shi of the Bulk Superconductivity Group, Engineering Department University of Cambridge, for producing and providing the (RE)BCO bulks used for levitation force measurements. I would also like to thank Dr Xavier Chaud and Dr Driss Kenfaui of CNRS, Grenoble, France, for producing and providing the YBCO bulk with an array of holes. I'm very grateful to Dr Alessandro Figini-Albisetti and Dr Giovanni Giunchi of Edison Spa, Milan, Italy, for producing and supplying the MgB_2 bulks of custom dimensions used for levitation force measurements. I would also like to thank them for valuable discussions and general support of my work. I'm very grateful to Professor Fritz Herlach of K U Leuven, Belgium, for his advice when designing the pulsed field coil and for conducting force modelling of the coil. I would like to thank Krzysztof Filar and Professor Victor Nizhankovskii of the International Laboratory of High Magnetic Fields and Low Temperatures, Wroclaw, Poland, for hosting my visit to their lab and assisting with field cooling measurements. I would like to thank Algirdas Baskys and Jordan Rush for their excellent work during their fourth year undergraduate research projects on pulsed magnetization of composite bulks using bulk YBCO. I would like to thank Dr Kemal Ozturk of the Karadeniz Technical University, Turkey, for collaborating on levitation force modelling.

I would like to thank all my friends in the Applied Superconductivity and Cryoscience Group for making my time so fun and enjoyable. In particular, Mariusz Wozniak, Simon Hopkins, Katarzyna Juda, Michal Chudy, Mariusz Mosiadz, Rumen Tomov, Vassilka Tsaneva, Xiao Teng and Eric Wang, many of whom are also known as 'fatty'.

Finally, I would like to thank my parents and family for their loving support.

List of abbreviations

ADC	Analogue to digital converter
DAQ	Digital acquisition
FC	Field cooling
FEM	Finite element method
FES	Flywheel energy storage
HTSC	High temperature superconductor
IBAD	Ion beam assisted deposition
IMRA	Iteratively magnetizing pulsed field operation with reducing amplitudes
ISD	Inclined substrate deposition
LN_2	Liquid nitrogen
LHe	Liquid helium
LH_2	Liquid hydrogen
LTS	Low temperature superconductor
MOCVD	Metal organic chemical vapour deposition
MOD	Metal organic deposition
MPSC	Multi-pulse technique with step-wise cooling
PDE	Partial differential equation
PFM	Pulsed field magnetization
PLD	Pulsed laser deposition
PM	Permanent magnet (of the ferromagnetic kind)
SC	Superconductor
SF	Self field
SMB	Superconducting magnetic bearing
SMES	Superconducting magnetic energy storage
ZFC	Zero field cooling

List of symbols

A	Magnetic vector potential
B	Magnetic flux density
B_c	Thermodynamic critical magnetic flux density
B_{c1}	Lower critical magnetic flux density
B_{c2}	Upper critical magnetic flux density
B_{irr}	Irreversibility flux density
B_n	Normal component of flux density vector
B_t	Tangential component of flux density vector
E	Electric field
ξ	Coherence length
f	Lorentz force density (force per unit volume)
f_p	Pinning force density (force per unit volume)
Φ	Magnetic flux
Φ_0	Fluxon (quantum of magnetic flux)
H	Magnetic field
H_c	Thermodynamic critical magnetic field
H_{c1}	Lower critical field
H_{c2}	Upper critical field
H_{irr}	Irreversibility field
H_p	Penetration field
J	Current density
J_c	Critical current density
J_{c0}	Zero field critical current density
k	Magnetic stiffness
κ	Ginzburg –Landau parameter
λ	Penetration depth
m_0	Magnetic moment
M	Magnetization
ΔM	Width of magnetization loop
n_s	Number density of superconducting charge carriers
$\underline{n}$	Unit normal vector for a surface
ν	Poisson ratio
ρ	Electrical resistivity
σ_t	Magnetic tension (force per unit area)
σ_p	Magnetic pressure (force per unit area)
T	Temperature
T_c	Critical temperature

Publication Record

First Author

1. Patel A, Filar K, Nizhankovskii V, Hopkins S C, Glowacki B A, 2013 Trapped fields greater than 7 T in a 12 mm square stack of commercial high-temperature superconducting tape *Applied Physics Letters*, **102** 102601

2. Patel A, Hopkins S C and Glowacki B A, 2013 Trapped fields up to 2 T in a 12 mm square stack of commercial superconducting tape using pulsed field magnetization *Superconductor Science and Technology*, **26** 032001 (IOP Fast Track Communication)

3. Patel A, Hopkins S C, Giunchi G, Figini Albisetti A, Shi Y, Palka R, Cardwell D A, Glowacki B A, 2013 The Use of an MgB_2 Hollow Cylinder and Pulse Magnetized (RE)BCO Bulk for Magnetic Levitation Applications *IEEE Transactions on Applied Superconductivity,* **23** 6800604

4. Patel A, Palka R, Glowacki B A, Giunchi G, Figini Albisetti A, Shi Y, Cardwell D A, and Hopkins S C, 2013 Permanent Magnet Enhancement of Fully Superconducting MgB_2-YBaCuO Bearing *Journal of Novel Superconductivity and Magnetism*, **26** 923-929

5. Patel A and Glowacki B A, 2012 Enhanced trapped field in a superconducting bulk using high thermal conductivity embedded structures after simulated pulsed field magnetization *Superconductor Science and Technology*, **25** 125015

6. Patel A, Giunchi G, Figini Albisetti A, Shi Y, Hopkins S C, Palka R, Cardwell D A, and Glowacki B A, 2012 High force magnetic levitation using magnetized superconducting bulks as a field source for bearing applications *Physics Procedia*, **36** 937-942

7. Patel A, Palka R, and Glowacki B A, 2012 New bulk - bulk superconducting bearing concept using additional permanent magnets *Przegląd Elektrotechniczny (Electrical Review)*, **88** 108-110

8. Patel A, Palka R, and Glowacki B A, 2011 New fully superconducting bearing concept using the difference in irreversibility field of two superconducting components *Superconductor Science and Technology*, **24** 015009

Second Author

1. Ozturk K, Patel A, and Glowacki B A, 2012 A numerical study to investigate magnetization, current density and trapped field properties of the doped-Sm123 bulk superconductor under different magnetic fields *Physica Status Solidi (a)* **209** 2558-2564

2. Mosiadz M, Juda K L, Vandaele K, Patel A, Glowacki B A, Van Driessche I, Soloducho J, Falter M, and Backer M, 2012 Inkjet printing, pyrolysis and crystallisation of $YBa_2Cu_3O_7$ precursor layers for fully chemical solution deposited coated conductors *Physics Procedia*, **36** 1450-1455

3. Vandaele K, Mosiadz M, Hopkins S C, Patel A, Van Driessche I, and Glowacki B A, 2012 The influence of heat treatment parameters on pyrolysed TFA-derived YBCO films deposited by inkjet printing *Materials Research Bulletin*, **47** 2032-2039

Contents

1 Introduction

1.1 Definition of a superconductor

A superconducting material has two essential properties which make its behaviour distinct from all other materials. These properties are both electromagnetic in nature, and a superconductor's unique response to electric and magnetic fields is what determines its use in various applications such as field trapping and magnetic levitation. These properties are:

i. **Zero electrical resistivity** below a critical temperature, magnetic field and DC current density. This property allows a current to flow around a continuous loop of superconductor without decay (a persistent current).

ii. **The Meissner effect**. This is the macroscopic expulsion of magnetic flux within a superconductor when it is cooled below its critical temperature T_c in the presence of an external magnetic field as shown in Figure 1.1. This effect is not the simple flux exclusion that would occur due to perfect diamagnetism alone.

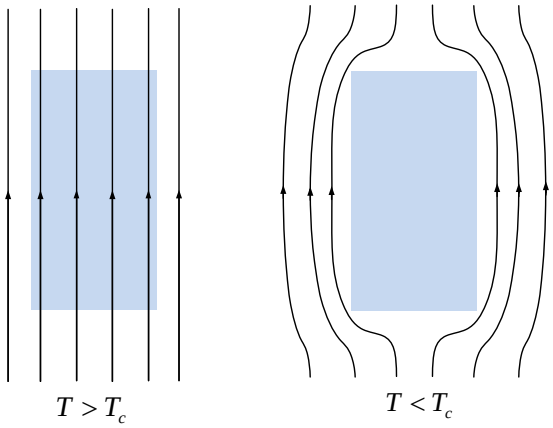

Figure 1.1: The Meissner effect for a solid superconducting cylinder. The cross-section view shows that magnetic flux is expelled from the interior when the temperature is reduced below T_c in the presence of an external magnetic field. Demagnetizing effects have been ignored by assuming infinite cylinder length.

If a metal simply became a perfect conductor as its temperature was lowered, the Meissner effect would not occur as can be demonstrated by the following argument. If resistivity gradually falls to zero in the *E-J* law $E = \rho J$, then the electric field *E* inside the conductor must also fall to zero (non-zero *J* is allowed). It then follows from Faraday's law $\nabla \times E = -\frac{dB}{dt}$ that the magnetic flux density inside the conductor will remain unchanged, $\frac{dB}{dt} = 0$. Therefore zero resistivity alone is not sufficient to explain the Meissner effect.

In addition to the critical temperature T_c there are in theory two other parameters, the critical field H_c and the critical current density J_c which determine whether a superconducting material is in a superconducting or normal state as illustrated by Figure 1.2 .

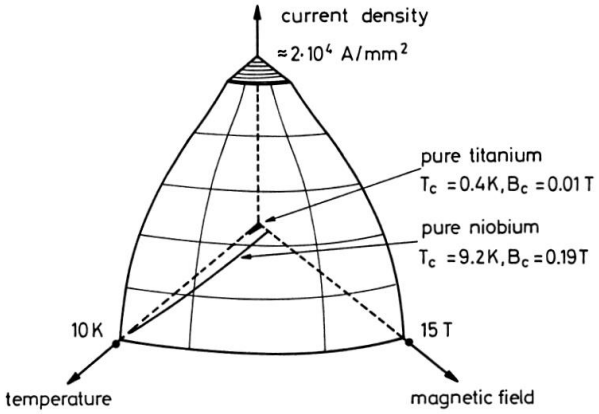

Figure 1.2: Example critical surface of the superconductors NbTi, Nb and Ti as a function of temperature, applied magnetic field and current density. The critical field in this case is the upper critical field rather than thermodynamic critical field. The material is only superconducting for values of the three parameters which lie below the critical surface [1].

1.2 History and applications

Most metallic elements are superconducting at very low temperatures and it was the metallic element mercury in which superconductivity was first discovered by Heike Kamerlingh Onnes in 1911 [2]. Most pure elements have very low critical temperatures: the highest found for any element at ambient pressure is 9.2 K for Nb. Compounds on the other hand have the capacity to exhibit much higher critical temperatures. Figure 1.3 shows the T_c of different materials against year of discovery. The copper oxide family dominates the last 20 years on the graph, with (RE)BaCuO compounds (where RE stands for a rare earth metal) being the most promising for applications. Many compounds in this family of superconductors have critical temperatures above 77 K, the boiling point of liquid nitrogen making them very economical to cool given the low price of LN_2 (as low as a few p/litre). For T_c < 77 K cryocoolers or liquid helium (LHe) usually need to be used, which although more expensive, can often be justified given the significant increase in J_c at low temperatures. Superconductors with T_c > 77 K can broadly be classed as high temperature superconductors (HTS) but it is not only T_c which determines the usefulness of a superconductor. $J_c(B)$, mechanical properties and other factors which will be explored later also determine performance.

A compound more recently discovered to be superconducting is MgB_2 [3] which, although having a low T_c of about 40 K compared to YBCO, has superior mechanical properties [4] and is easier to fabricate in bulk form.

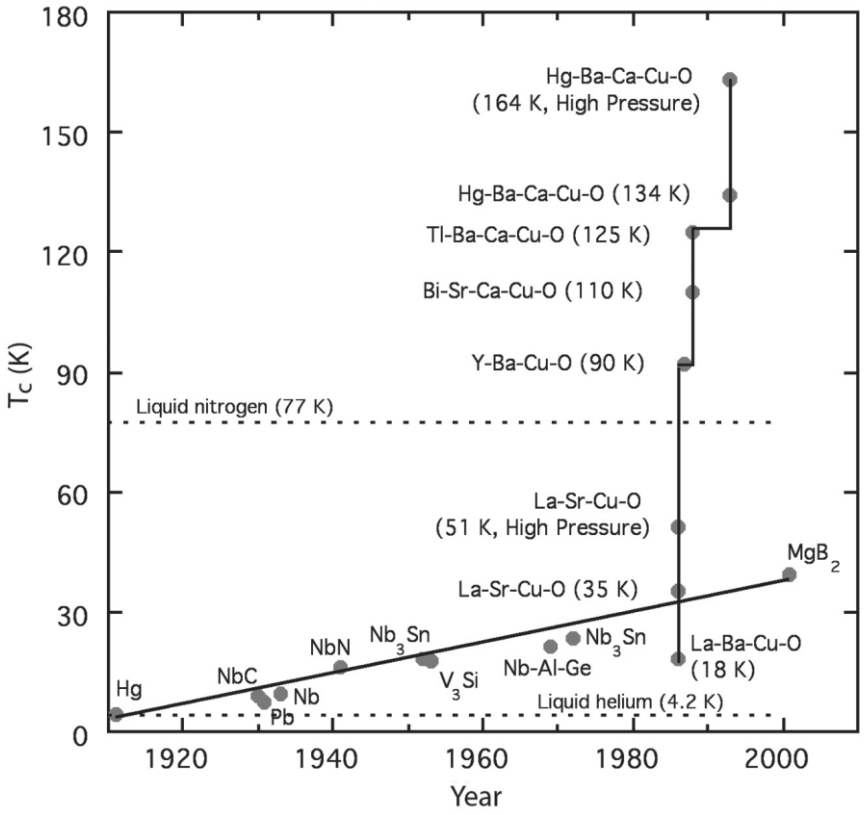

Figure 1.3: Critical temperature for selected superconducting materials against year of discovery. The vertical line represents the cuprates which clearly have on average a significantly higher T_c than the remaining compounds and elements [5].

Superconductors have made an important contribution to applications in a variety of different fields. Figure 1.4 gives an overview of the most common applications to date, with the developments reported in this thesis contributing to magnetic bearings, motors and generators.

Figure 1.4: The most common applications of superconductors. The most dominant commercial applications rely on the generation of high magnetic field densities. Magnetized bulks are becoming increasingly feasible for use in rotary machines.

1.3 Basic theory of superconductivity

1.3.1 London equation

The London equation (1.1) succeeded in explaining the Meissner effect shown in Figure 1.1.

$$\underline{j} = -\frac{n_s e^2}{m}\underline{A} \tag{1.1}$$

The current $\underline{j}$ represents screening current, n_s is a phenomenological constant associated with the number density of superconducting charge carriers, m is the mass of the electron, e the electron charge and $\underline{A}$ is the magnetic vector potential. It is simple to show how the London equation explains the Meissner effect by applying it to an infinite plane boundary between a superconducting

region and a vacuum with a uniform parallel applied magnetic field in the vacuum region. Taking the curl of both sides and using $\nabla \times \underline{A} = \underline{B}$,

$$\nabla \times \underline{j} = -\frac{n_s e^2}{m} \underline{B} \tag{1.2}$$

Applying Maxwell's equations the solution for the chosen geometry emerges:

$$\nabla^2 \underline{B} = \frac{\mu_0 n_s e^2}{m} \underline{B}$$
$$\Rightarrow \lambda^2 \frac{d^2 B}{dx^2} = B$$
$$B(x) = a e^{-x/\lambda} \tag{1.3}$$

Where a is a constant and λ is the London penetration depth:

$$\lambda = \sqrt{\frac{m}{\mu_0 n_s e^2}} \tag{1.4}$$

Equation (1.3) shows that a uniform non-zero internal flux density is not allowed by the London Equations and describes the external magnetic field falling off exponentially into the superconductor with a characteristic length scale of λ. This parameter is very important in determining the properties of a superconductor as will be shown in the next section.

1.3.2 Type I and II superconductors

Superconductors can be divided into two types based on how magnetic flux penetrates the interior of the superconductor as applied magnetic field is increased. As mentioned earlier there exists a critical magnetic field above which a superconductor makes a transition to its normal state. This transition is simple for Type I superconductors but more complex for Type II. As shown by the Meissner effect in Figure 1.1 the exclusion of magnetic flux density B from a superconductor when exposed to an external magnetic field *H* must cause the superconductor to acquire a macroscopic magnetization equal and opposite in value to *H*. This is the only effect that occurs in Type I superconductors until H_c is reached and superconductivity is destroyed as shown in Figure 1.5.

As the applied field for a Type II superconductor passes a lower critical field H_{c1}, magnetic flux begins to partially penetrate the interior of the bulk as shown in Figure 1.6 in the form of a vortex lattice. Total flux penetration occurs at the upper critical field H_{c2} when the superconductor changes to the normal state.

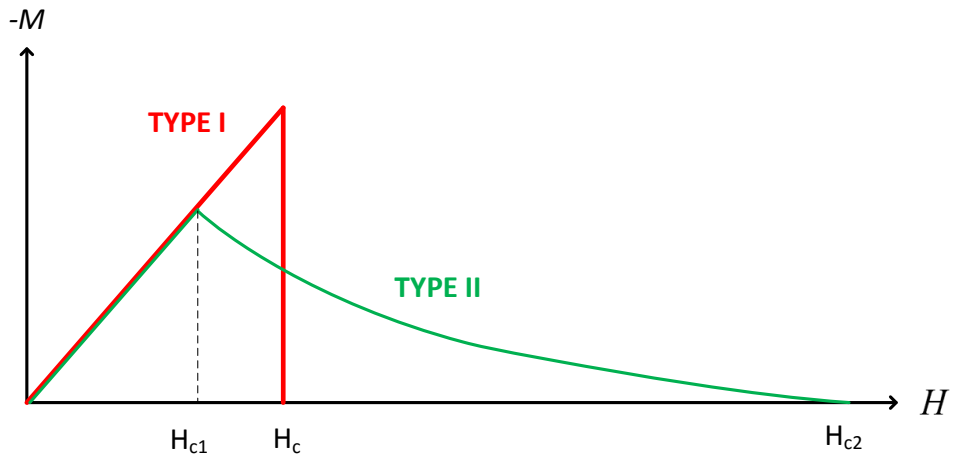

Figure 1.5: The magnetization of a bulk superconductor when exposed to an applied magnetic field H. Type I is perfectly diamagnetic and in the Meissner state up to H_c however type II is not perfectly diamagnetic between H_{c1} and H_{c2} which is the mixed state. Type II only partially screens external field in this region.

As the critical current density of a superconductor depends on the critical field, the current a superconductor can carry is limited by H_{c2} or H_c. Because most applications of superconductors require high current carrying performance and because in practice H_{c2} is often much higher than H_{c1}, and H_c for Type I superconductors (e.g. $B_{c2} \approx 20$ T for YBCO at 77 K), all practical superconducting materials such as NbTi used for wires and YBCO used in bulk form are Type II.

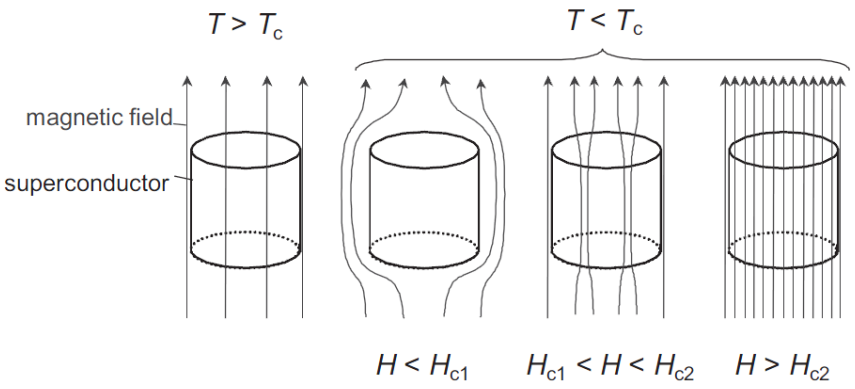

Figure 1.6: Gradual flux penetration occurs in Type II superconductors in the form of flux vortices when below T_c as external magnetic field is increased [6]. Demagnetizing effects have been ignored.

The reason why superconductors come in two different types can be understood by considering the penetration depth given by equation (1.4) and a length scale ξ called the coherence length. The coherence length is a measure of the length scale over which the gradual change from the normal to the superconducting state occurs at the boundary of a superconductor. It can therefore be considered as the scale over which n_s the superconducting charge carrier density from equation (1.1) goes from zero at the boundary to a constant deep inside the superconductor. A comparison of these two lengths as shown in Figure 1.7 explains type I and type II behaviour. If λ is less than ξ, the superconductor is type I, whereas in the opposite case the superconductor is type II. A

thermodynamic consideration of a type I superconductor at the critical field (when the Gibbs free energies of the superconducting and normal state are equal) shows that the ordering of electrons forming the superconducting state lowers the free energy density g_s by $\frac{1}{2}\mu_0 H_c^{\,2}$, a quantity called the condensation energy. The superconductor also has a positive contribution to its free energy (g) resulting from its magnetization. The magnetization energy density in an applied field H_a is $\frac{1}{2}\mu_0 H_a^{\,2}$. By considering the sum of the two energy contributions in the critical case when $H_a = H_c$, Figure 1.7 shows how a surface energy arises. The field H_c no longer has the same significance for the type II superconductor, as shown in Figure 1.7. The negative surface energy favours the existence of normal regions occurring deep within a type II superconductor in the form of flux vortices forming a flux lattice. The surface energy becomes negative at a new critical field H_{c1} at which flux begins to penetrate. The density of the flux vortices increases as H_a is increased due to them becoming more and more energetically favourable until H_{c2} is reached, when the whole superconductor is 'taken over' by these normal regions.

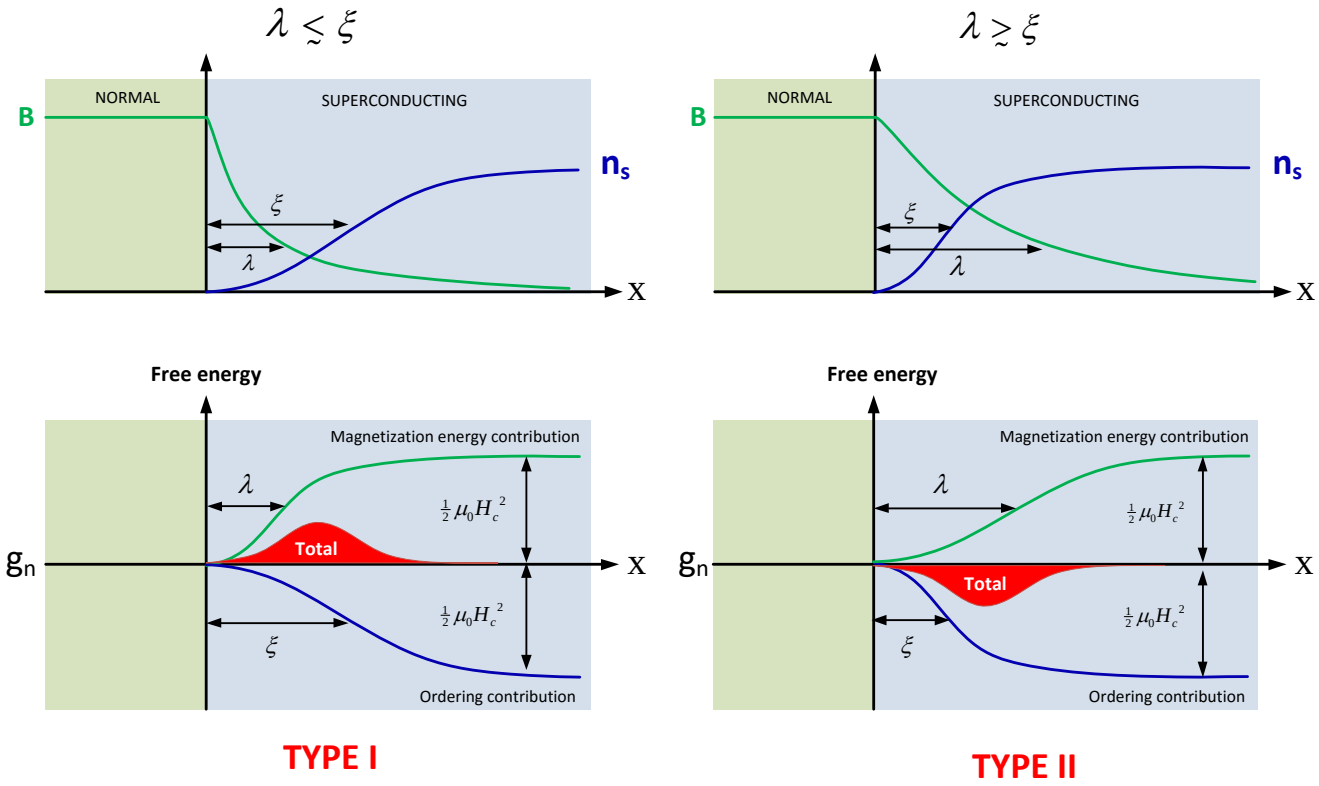

Figure 1.7: A normal/superconducting boundary with an applied field $H_a = H_c$ in the normal region. The change in magnetic flux density B and cooper pair density n_s over the boundary is characterized by the coherence length and penetration depth, which are therefore the length scales over which the magnetization of the superconductor and ordering of the electrons contribute to the free energy inside the superconductor. Deep inside the superconductor the contributions are equal and cancel giving a free energy equal to the normal region. However a significant difference between ξ and λ results in a surface energy shown in red. A negative total surface energy, as in type II superconductors, makes a normal/superconducting boundary favourable.

The Ginzburg-Landau theory of superconductivity used thermodynamic arguments and the introduction of an order parameter to predict the existence of the coherence length ξ and penetration depth λ, and defined the ratio of these two lengths as the Ginzburg-Landau coefficient κ:

$$\kappa = \frac{\lambda}{\xi} \tag{1.5}$$

This is an important parameter that characterizes a superconductor as suggested by Figure 1.7, and it is temperature independent near T_c even though ξ and λ are not. The precise inequalities which determine whether a superconductor is type I or II are found to be:

$$\text{Type I} \quad \kappa < \frac{1}{\sqrt{2}} \tag{1.6}$$

$$\text{Type II} \quad \kappa > \frac{1}{\sqrt{2}} \tag{1.7}$$

The theory also lead to the concept that flux penetration in a type II superconductor occurs in the form of a typically hexagonal lattice of discrete flux quanta $\Phi_0 = \frac{h}{2e}$ known as an Abrikosov flux lattice, as shown in Figure 1.8.

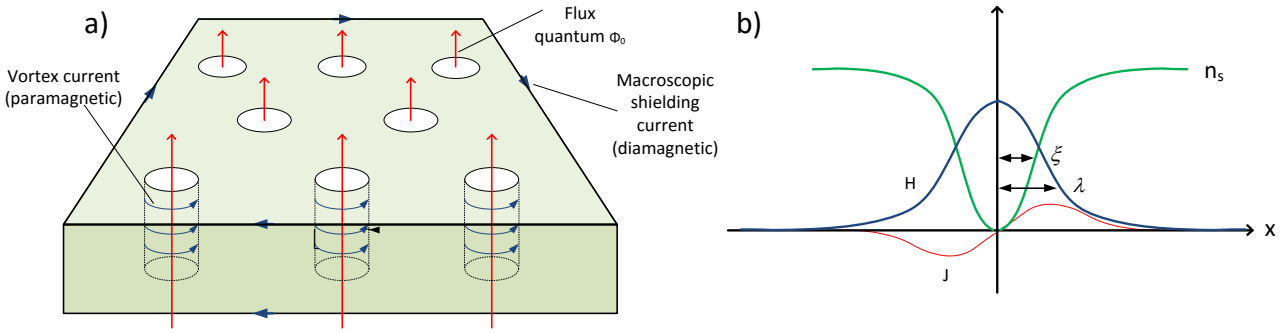

Figure 1.8: a) shows how an external magnetic field penetrates a type II superconductor in the form of a flux lattice with b) showing how the cooper pair density falls to zero in the normal core of a vortex whist the vortex shielding current allows finite magnetic field inside the core.

1.4 The critical state model

As the Meissner effect describes how a type I superconductor responds to an external field by shielding itself using a shielding current confined to a distance $\sim \lambda$ from the surface, the critical state model describes how shielding and trapping of magnetic flux occurs through flux penetration for the mixed state of a type II superconductor. It is therefore essential for understanding the engineering applications of superconducting bulks. The basis of the critical state model is flux pinning.

1.4.1 Flux pinning and critical current density

Consider a current density flowing in a superconducting slab such as the one shown in Figure 1.8. The current will generate its own magnetic field which will thread through the superconductor as a vortex lattice in the same region as the current flow. This must lead to a Lorentz force on each flux vortex, perpendicular to both $\underline{J}$ and $\underline{B}$, $\underline{F} = \underline{J} \times \underline{\Phi}_0$. If $\underline{B} = n\underline{\Phi}_0$ where n is the fluxon number density, the whole lattice is subject to a force density f (units N m^{-3}):

$$\underline{f} = \underline{J} \times \underline{B} \tag{1.8}$$

This force density will try to set in motion the whole flux lattice and if this occurs then the flux will be cutting across the current, leading to a force on the charge carriers parallel to the current direction. Such a force generates an electric field, causing dissipation and a non-zero resistivity. The flux lattice therefore needs to be 'pinned' for any practical use of the superconductor involving current flow. The higher the pinning force, the higher the current density that can be passed through a sample before its self-field causes flux motion, driving the sample normal. It is therefore flux pinning that determines the critical current of type II superconductors rather than H_{c2}, as the maximum fields that can be accommodated by the pinning force density in equation (1.8) are practically much less than H_{c2}. If f_p is the pinning force density the magnitude of equation (1.8) can be used to define J_c, with its field dependence given by the field dependence of f_p:

$$f_p = J_c B \tag{1.9}$$

Pinning is achieved in the form of defects in the crystal structure of a superconductor such as grain boundaries, voids and dislocations on the scale of ξ. So a perfectly pure defect free sample would not be able to carry a supercurrent. The pinning force per fluxon is proportional to the interaction energy between the fluxon and pinning centre, given approximately by $\Delta U = d\pi\xi^2 \tfrac{1}{2}\mu_0 H_c^{\,2}$ where d is the height of the pinning centre. Much research has gone into improving pinning force in order to increase J_c as high as possible.

A summary of the different magnetic states a superconductor can take is shown in Figure 1.9. The flux is pinned only in the vortex lattice state. An irreversibility line $H_{irr}(T)$ marks the boundary between a phase which is irreversible with change in external field and a vortex liquid phase, in which a change in external field is reversible due to the loss of pinning force. For a given temperature it is therefore H_{irr} that marks the magnetic field limit a superconductor can be exposed to before becoming unusable. The actual dependence of irreversibility field on temperature is shown for a few superconductors in Figure 1.10 which shows the rapid increase in H_{irr} for YBCO below its T_c.

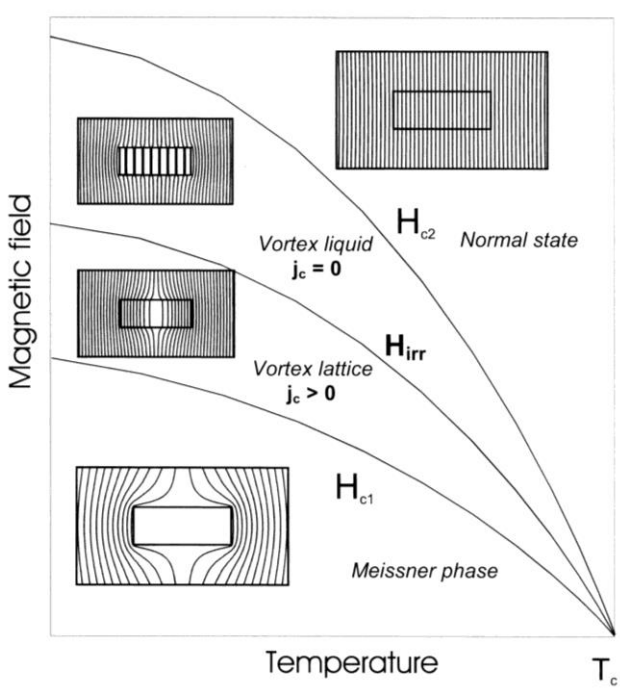

Figure 1.9: Schematic diagram of the magnetic phases in a high temperature superconductor as a function of temperature and magnetic field. The existence of a vortex liquid above the field $H_{irr}(T)$ implies that this is a more important limiting field than H_{c2} for applications. The vortex lattice state is the desired state for most engineering applications. [6]

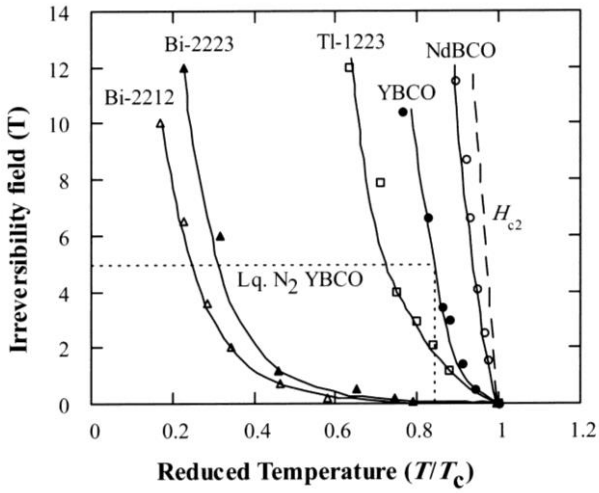

Figure 1.10: Irreversibility field data for a variety of HTS compounds. There is considerable difference in H_{irr} at 77 K for different compounds (chapter B2.3.1 from [7]).

It is important to note that there can be two general contributions to the local magnetic field seen at any point in a superconductor. These are the self field and external field. Consider a single superconducting wire carrying current in a uniform external field. The field experienced on the surface of the superconductor will be the sum of the field generated by the wire current itself (self field) and the external applied field. It is the sum of these fields which determines the critical current density. In the case of currents circulating around a cylindrical bulk throughout most of the cross-section (not just at the surface), the local magnetic field is the contribution from the whole current

density distribution and any external fields, which results in a critical current density that varies spatially over the bulk cross-section.

There are two general forms of current possible in a superconductor. Magnetization current is induced in a superconducting bulk by time-varying external fields whereas transport current in a single wire or superconducting coil is forced. Only magnetization currents are relevant to the applications discussed in this report so the critical state model will be explained in the context of these currents.

1.4.2 The Bean model

When a superconductor is exposed to an external magnetic field, penetration of flux occurs in the form of a vortex lattice leading to a critical state with specific values of current density and field. If there were no currents accompanying the penetration then the case would be simple. However the existence of current density leads to a Lorentz force on the flux and it is important to consider whether this force is greater or less than the flux pinning force. If the distribution of flux density and current gives a Lorentz force density f on flux vortices (Equation (1.8)), equilibrium is only possible if $f \leq f_p$, where f_p is the maximum pinning force density. If the initial distribution gives a Lorentz force that is greater than this pinning force then the Lorentz force will cause a redistribution of magnetic flux until the critical condition is met, $f = f_p$.

This redistribution of flux until a critical state has been achieved is the basis of critical state models such as the Bean model [8], which is the simplest. Consider the superconducting hollow cylinder in Figure 1.11 cooled below T_c in a uniform external field B_0 (field cooling). The zero resistance of the superconductor implies $\frac{d\Phi}{dt} = 0$ inside the hole, so the initial trapped field in the hole is B_0 after the external field is turned off. However flux will immediately start to penetrate the walls ($B_0 > B_{c1}$) and interact with the induced surface shielding current. Ampere's law shows that the initial sudden drop in B at the wall leads to a very high shielding current:

$$\begin{aligned} &\nabla \times \underline{B} = \mu_0 \underline{J} \\ &\Rightarrow J_\theta \propto \frac{dB}{dr} \end{aligned} \tag{1.10}$$

The Lorentz force density is therefore much higher than f_p, causing flux flow until the critical condition $f = f_p$ has been met. The final distribution of flux density is shown in Figure 1.11 for different wall thicknesses.

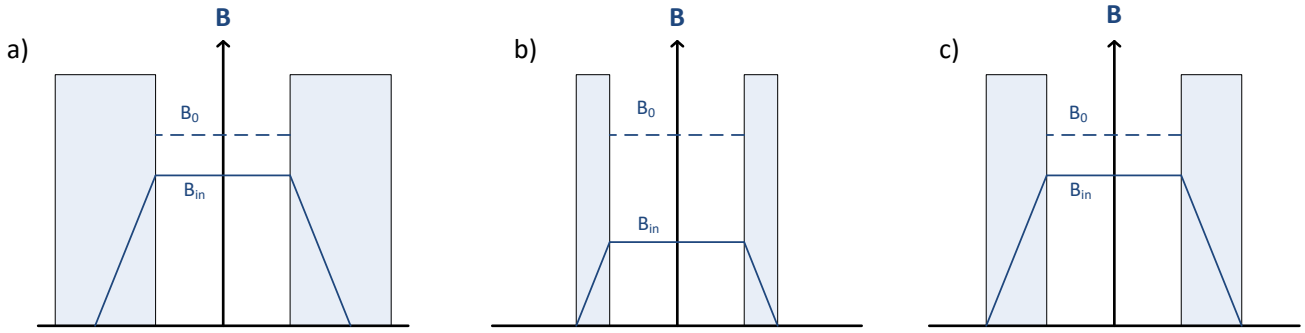

Figure 1.11: The response of hollow superconducting cylinders of different wall thicknesses when field cooled in a uniform external field of flux density B_o. Infinite cylinder length is assumed. Flux trapped in the hole 'leaks' into the superconductor until gradients in B are constant, according to the Bean model, leaving an internal flux density in the hole of B_{in}. a) Cylinder with walls more than thick enough to contain all flux originally in hole. b) Cylinder too thin-walled, causing flux to leak outside. c) Wall thickness just sufficient to contain original trapped flux.

By setting $f = f_p$ in equation (1.8) and combining it with (1.10) to eliminate the magnitude of the current density the resulting equation gives the final field gradients:

$$\frac{f_p}{B} \propto \frac{dB}{dr} \tag{1.11}$$

The Bean model makes the approximation that the pinning force is proportional to the magnetic field, which results in constant current density by equation (1.8) and constant magnetic field gradients for simple infinite geometries by equation (1.11).

$$\text{Assumptions of Bean model: } \begin{matrix} f_p \propto B \\ J = J_c = \text{constant} \end{matrix} \tag{1.12}$$

This approximation predicts that shielding/trapped current can only take the values $\pm J_c$ or 0. Figure 1.12 illustrates this and shows that higher external fields are required to cause significant flux penetration into superconductors with high J_c values.

In reality J_c is not constant but dependent on the magnetic flux density, as it must be zero for $B = B_{c2}$. The Kim model [9] assumes

$$J_c(B) = \frac{J_{c0}}{1 + B/B_0} \tag{1.13}$$

where J_{c0} and B_0 are constants. This equation can successfully be used to predict the form of trapped magnetic fields in bulks and was used for the critical state modelling in this thesis. A more detailed comparison of Bean's, Kim's and an exponential critical state model can be found in [10].

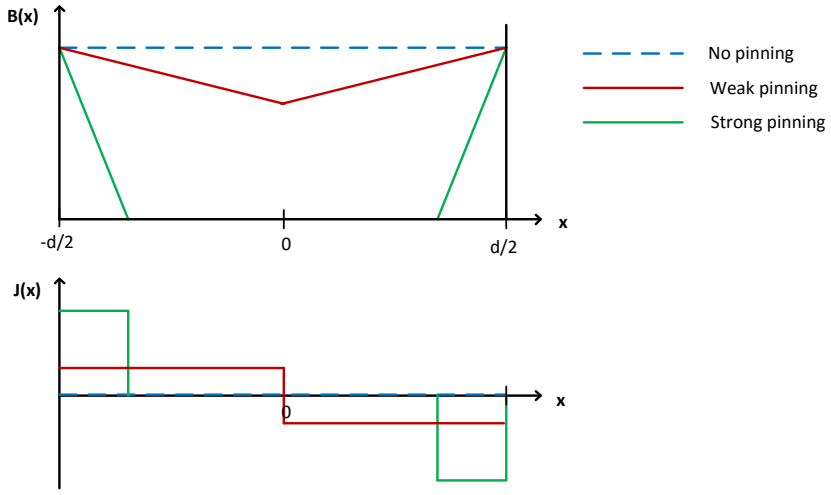

Figure 1.12: The magnetic flux penetration for an infinite superconducting slab of thickness *d* and equivalent current density distributions when exposed to a uniform external field. The magnetic flux density gradients allowed by the Bean model depend on the strength of pinning. The stronger the pinning force, the higher the critical current density and corresponding field gradients.

1.4.3 Magnetization

The magnetization of a superconductor due to macroscopic currents flowing in the interior is fundamentally different from the magnetization of a ferromagnetic material which has a local value at any point throughout the material. Magnetization for a bulk superconductor cannot be defined locally using the standard equation for magnetic materials $\underline{B}(r) = \mu_0(\underline{H}(r) + \underline{M}(r))$ and is instead defined as the total magnetic moment of the whole superconducting sample over its volume:

$$\underline{M} = \frac{\underline{m}_0}{V} = \frac{1}{V}\int(\underline{r}\times\underline{J})\mathrm{d}V \tag{1.14}$$

When applying an external field to a superconductor, the presence of flux pinning causes irreversible magnetization as illustrated by the thick line in Figure 1.13, which also shows the type II reversible magnetization of Figure 1.5.

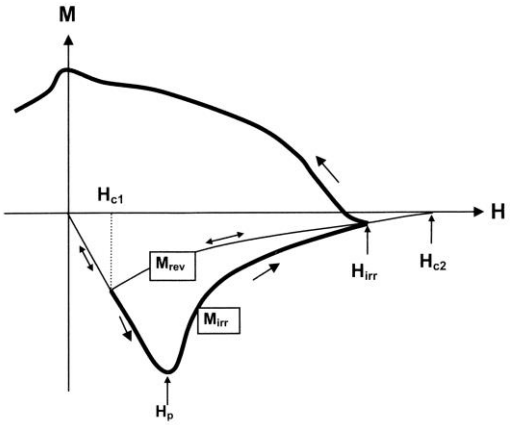

Figure 1.13: Reversible and irreversible magnetization for a superconductor without and with flux pinning respectively [6].

Magnetizing a superconducting bulk, trapping a conical field in it, can be achieved in two ways. i) Field cooling (FC): the sample is cooled below T_c in the presence of an external field, after which the field is turned off. ii) Zero field cooling (ZFC): the sample is exposed to an external field that increases from zero to a peak value before decreasing back to zero. Figure 1.14 shows schematically the evolving field profiles for these methods and demonstrates that, according to the Bean model, an external field twice as high is required for ZFC than FC to trap the maximum possible field. Figure 1.15 shows the magnetization based on Equation (1.14) for the ZFC of a bulk according to the Bean model used in Figure 1.12 and the more realistic Kim model. The decrease in M for the Kim loop as H is first increased past H_p is due to the decrease in current density resulting from Equation (1.13).

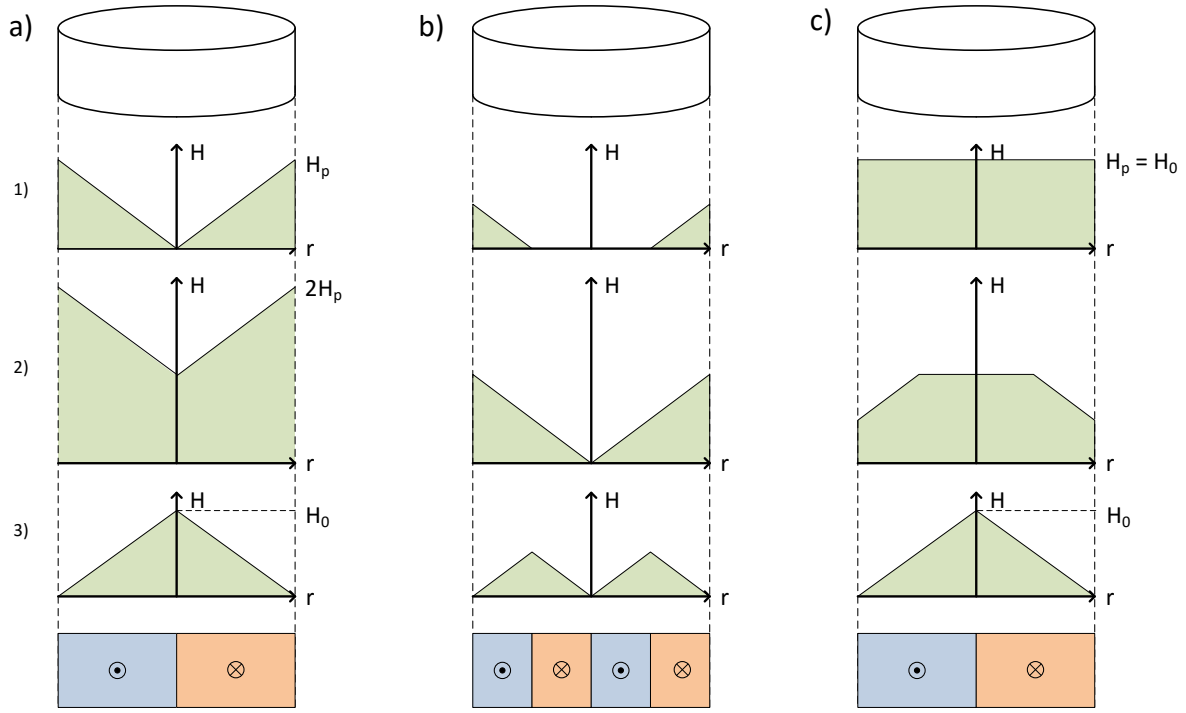

Figure 1.14: The field penetration and trapped magnetic field for a superconducting bulk exposed to a time varying external field. This picture ignores demagnetizing effects by assuming the bulk is a cylinder of semi-infinite length. The final row of graphs shows the final trapped field and the bottom three diagrams, the current density distribution. The penetration field H_p is the external field required for penetration of flux to the centre. a) Zero field cooling: a field of $2H_p$ is required to trap the maximum possible field $H_0 = H_p$. b) Zero field cooling: the field profile trapped when a reduced external field of H_p is used. c) Field cooling: requires an external field equal to the maximum trapped field.

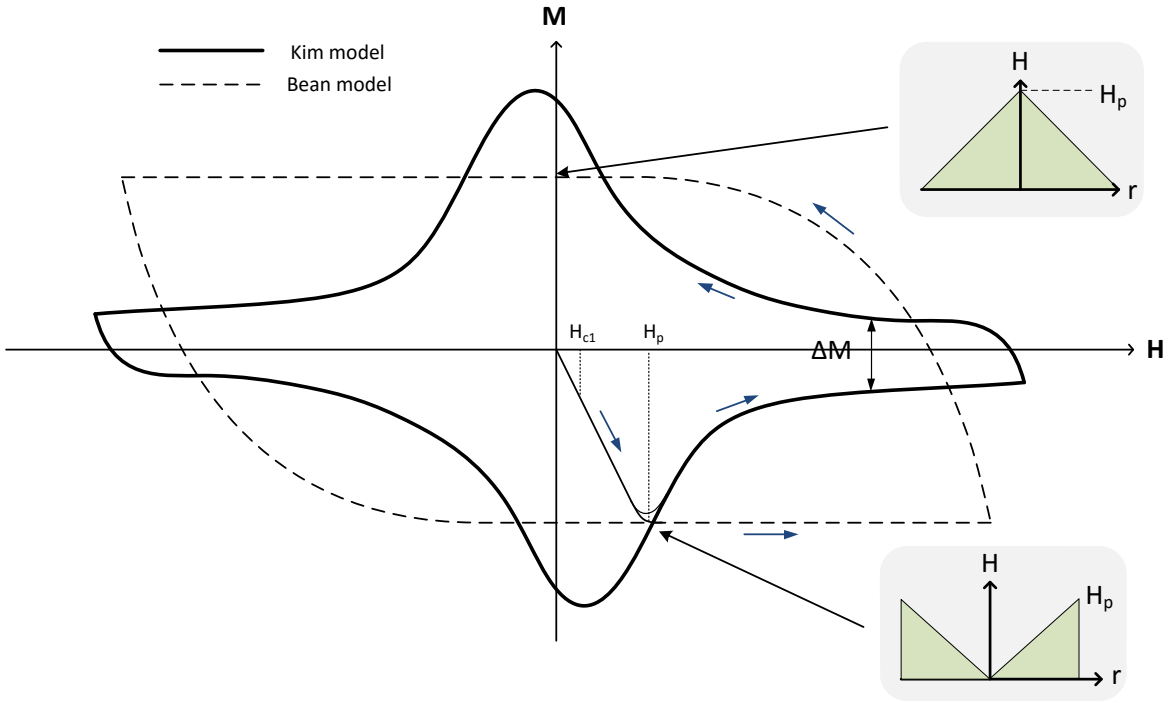

Figure 1.15: The magnetization hysteresis loop predicted by the Bean and Kim models. The difference in loop shape is due to the field dependence of J_c in the Kim model.

Magnetization loops provide a common method for determining $J_c(B)$ for a bulk superconducting sample. $J_c(H)$ can be determined by experimentally measuring ΔM (shown in Figure 1.13) and comparing this to the theoretical value for a particular geometry as a function of J_c using Equation (1.14). The simplest method assumes that for a given H on the M-H loop the variation in trapped H over the bulk is small so that J_c is spatially constant.

1.4.4 Magnetic tensile stress and maximum trapped fields

For the field cooling mode, the magnetic field inside a bulk is never less than the field outside the bulk, so there is expansive stress acting on the bulk. The following equation taken from [6] gives the maximum hoop stress experienced by a bulk during the field cooling process due to magnetic pressure, which may be higher than the stress in the final remanent state depending on the applied field:

$$\sigma = \frac{B_0^{\,2}}{2\mu_0}\left[b_{FC}^{\,2} - b_{ext}^{\,2} - \frac{1-2\nu}{12(1-\nu)}(b_{FC}-b_{ext})^2(b_{ext}^{\,2}+4b_{ext}+2b_{ext}^{\,2}b_{FC}+8b_{FC}-3b_{FC}^{\,2})\right] \qquad (1.15)$$

where $b_{ext} = B_{ext}/B_0$, $b_{FC} = B_{FC}/B_0$ and ν is the Poisson ratio of the sample. B_0 is the maximum possible trapped field for a given sample, B_{FC} is the field cooling field (the maximum external field) and B_{ext} is the external field and the only variable which changes during the field cooling process as the external field is ramped down from B_{FC} to zero. Equation (1.15) shows that if a higher B_{FC} is applied

than necessary i.e. if $b_{FC} > 1$, the maximum stress is greatly increased, which means that when trying to saturate a sample for the first time, one should not simply use the largest possible field cooling field. In the remanent state, the maximum internal stress is given by the following equation, which is also the maximum stress during the field cooling process if $b_{FC} = 1$:

$$\sigma_0 = 0.76\frac{B_0^{\,2}}{2\mu_0} \tag{1.16}$$

This assumes a Poisson ratio of $\nu = 0.3$ for a bulk. This shows that if the maximum tensile stress of a bulk is 30 MPa [6], no more than 10 T can be trapped without extra external reinforcement. Additionally it is worth considering the rotational stress on a bulk given that the bearing designs discussed in Chapter 2 rely on magnetized bulks rotating about their axis on a rotor. The radial and hoop stress are at their maxima in the centre of a rotating solid disk, where they are equal:

$$\sigma_R = \left(\frac{3+\nu}{8}\right)\rho\omega^2 r_0^{\,2} \tag{1.17}$$

where r_0 is the radius of the sample. The maximum stress on a saturated magnetized rotating bulk is therefore the sum of Equation (1.16) and (1.17), and this must not exceed the tensile stress of the bulk material.

1.5 Material properties

1.5.1 (RE)BCO bulk

The rare earth class of superconductors to which YBCO belongs has the chemical formula $(RE)Ba_2Cu_3O_{7-x}$ where RE is a rare earth element, more simply (RE)BCO. YBCO has been the most popular type of bulk produced to date, however GdBCO has gained popularity due to typically having a higher J_c particularly at 77 K. YBCO properties are sensitive to the oxygen content, with superconductivity only present if $0 \leq x \leq 0.65$. (RE)BCO superconductors like YBCO exhibit relatively high H_{irr} as suggested by Figure 1.10, which makes them suitable for high field applications, and a $T_c \approx 90$ K which gives sufficient superconducting properties at 77.4 K to make them usable in LN_2. The ability of a (RE)BCO bulk to sustain a high persistent current makes it suitable to be used as a permanent magnet once magnetized.

The crystal structure of YBCO is highly anisotropic as shown by Figure 1.16a, which leads to anisotropic superconducting and thermal properties.

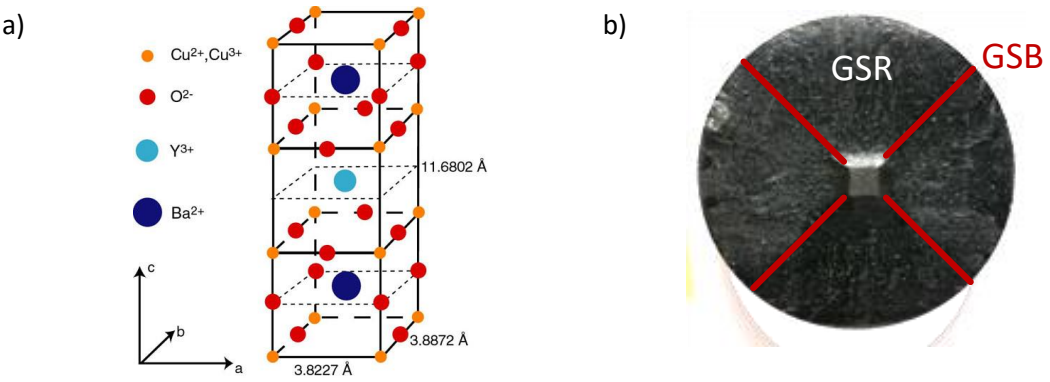

Figure 1.16: a) The crystal structure of $YBa_2Cu_3O_7$. The CuO (ab) planes are responsible for carrying current and give a much higher J_c than for current along the c axis. The thermal conductivity is also anisotropic [11]. b) Top view of an YBCO bulk grown by top seeded melt growth. Although single domain, (RE)BCO bulks exhibit growth sector regions (GSR) and boundaries (GRB) which have different J_c.

Bulk YBCO with the highest J_c performance takes the form of a large single grain, as the presence of misoriented grain boundaries significantly impedes current flow and therefore causes a poor macroscopic J_c. Such a bulk can be produced by top seeded melt growth. This involves placing a small seed crystal with similar lattice parameters to YBCO but a higher melting point (commonly $SmBa_2Cu_3O_{7-x}$ or $NdBa_2Cu_3O_{7-x}$) on top of a pre-sintered YBCO pellet [12]. The temperature is then raised high enough for the YBCO to melt before allowing it to nucleate around the seed to form a single domain during cooling.

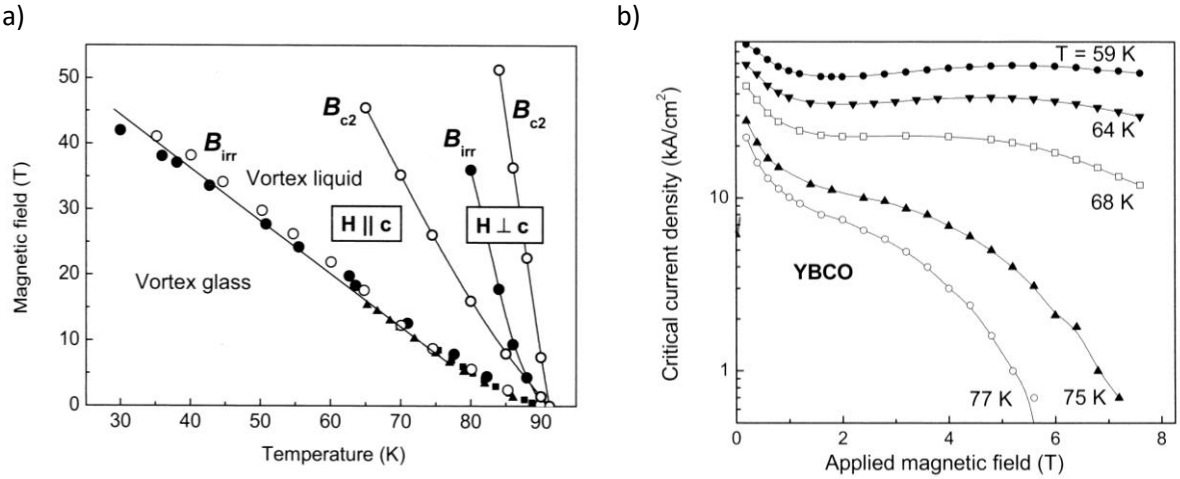

Figure 1.17: a) Typical irreversibility field and upper critical field data for a bulk YBCO sample as a function of temperature. There is a significant difference in properties depending on orientation of applied field. b) Typical data for J_c(B) of YBCO (*H* ll c) at different temperatures. There are large gains in J_c if temperatures lower than LN_2 are used. [6]

Figure 1.17a and b gives the J_c as a function of temperature and applied field for a high quality bulk, with most YBCO bulks having a J_c of the same order of magnitude. It is clear that significant increases in the J_c of YBCO are achieved by reducing temperature. Even a modest drop of 10 K from 77 K more than doubles J_c. As a result, most industrial applications that use bulk (RE)BCO or (RE)BCO

tapes operate below 77 K despite the extra cost of cooling. Even as research pushes the limit of the J_c possible at 77 K, its temperature dependence will remain similar, suggesting that operation of (RE)BCO materials below 77 K will be justified for some time to come or perhaps always for some applications.

The ability of (RE)BCO bulks to trap magnetic field is determined by the magnitude of J_c, its homogeneity and the length scales over which superconducting current can flow. Most research into (RE)BCO bulk production is therefore directed to increasing flux pinning performance and increasing the maximum single domain size that can be grown through top seeded melt growth. More recent research has involved fabricating single domain YBCO bulks with arrays of holes parallel to the c-axis [13, 14]. These holes improve oxygenation and reduce the formation of micro cracks which impede current flow. This new form of bulk has proven successful for trapping fields [13]. Although bulk (RE)BCO is currently the most widely used material for superconducting permanent magnets due to the advantages of high B_{irr}, J_c and T_c, its limitations are a production process that is time-consuming and expensive given the need for a single domain and its brittle mechanical properties as well as low thermal conductivity. The $J_c(B,T)$ values typically vary significantly with radius and axial distance from the seed crystal [15]. For example, the trapped field on the top side of a bulk is typically 1.5 – 2 times greater than the bottom side due to higher J_c near the seed crystal, and research has shown that the top 4 mm of ≈ 26 mm diameter bulks contributes up to 70% of the trapped field at the sample top surface [16]. In addition, the J_c on the growth sector boundary as shown in Figure 1.16b is believed to be approximately 4 times higher than in the growth sector region [17] (although a systematic study of the J_c difference has not yet been reported). This makes the J_c properties of a bulk difficult to characterise and describe. This inhomogeneity causes trapped fields to be higher on the growth sector boundaries, contributing to commonly observed pyramidal trapped fields [18], such as that in Figure 4.3. One way of dealing with the inhomogeneous properties of bulks is to cut rings of varying diameters from a single bulk and then re-assemble them so that the growth sector boundaries are misaligned [19]. This method has been shown to significantly improve symmetry of the trapped field but it is not clear how such an assembly would respond to PFM, and the processing used sandblasting which is only suitable for thin samples.

(RE)BCO bulks are currently produced up to around 60 mm in diameter, and large bulks between 40 – 60 mm, most notably produced by Nippon Steel, have become increasingly popular in research [20-23]. Nippon Steel have also produced a very large 150 mm bulk [24] but its properties and whether it can be easily reproduced are not clear. A summary of the best trapped fields reported in the literature to date is shown in Table 1.1. The record for the highest ever trapped field was achieved for two 26.5 mm diameter YBCO bulks at 29 K, between which 17.2 T was trapped

[25]. When trapping high fields in bulks using field cooling, the maximum field that can be trapped for a given size of bulk depends on temperature and is limited by three different factors: J_c, tensile strength and magneto-thermal instabilities, with the dominance of each factor depending on the temperature range as illustrated by Figure 1.18. For high trapped fields, external reinforcement is needed to overcome the tensile strength limit. The best trapped fields shown in Table 1.1 are often achieved for special samples that cannot be easily reproduced or after magnetizing a number of samples that have mechanically failed. The mechanical and thermal limitations of plain bulks are the basis for research into new composite superconducting bulks which is reported in Chapter 5.

Table 1.1: Best trapped field achieved by field cooling (unless otherwise specified) in (RE)BCO bulks to date. It should be noted that there is some variation in the height above the sample at which the field was measured.

Bulk sample	Diameter/mm x thickness/mm	Trapped field/T	Temp./K	Comment	Reference
GdBCO	50 x 30	2.7	77	Surface of single bulk	Nariki 2002 [26]
GdBCO	24 x 12	1.4	77	Surface of single bulk	Nariki 2002 [26]
GdBCO	65 x 19	3.1	77	Surface of single bulk	Nariki 2005 [27]
[1] YBCO	20 x 8	2.1	77	Surface of single bulk	Weinstein 1998 [28]
[2] YBCO	26 x 10	2.1	77	Surface of single bulk	Fuchs 2003 [29]
YBCO	26.5 x 15	17.2	29	Field between 2 bulks	Tomita 2003 [25]
YBCO	25 x 8	16	24	Field between 2 bulks	Krabbes 2001 [30]
GdBCO	46 x 15	9.1	42	Surface of single bulk	Teshima 2013 [20]
GdBCO	45 x 15	5.2	28-47	Pulsed magnetization Surface of single bulk	Fujishiro 2006 [31]

[1] Uranium doped and neutron irradiated. Not suitable for applications due to cost.
[2] Neutron irradiated. Not suitable for applications due to cost.

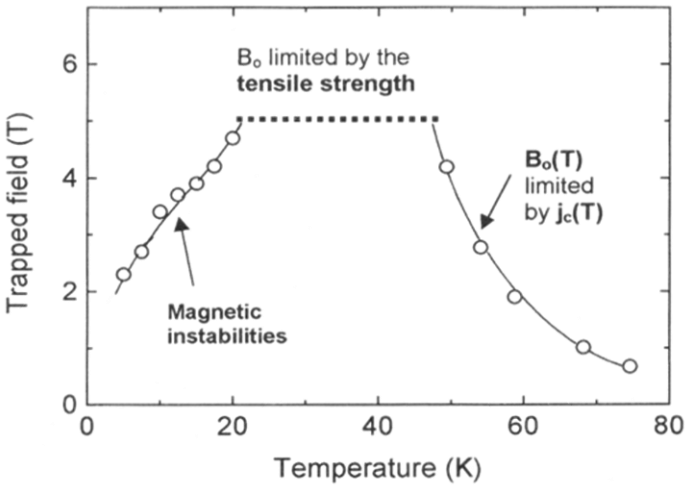

Figure 1.18: Trapped field data and limitations for a single 25 mm YBCO bulk magnetized by field cooling. The dominant factor limiting the trapped field depends on the temperature region [32].

1.5.2 (RE)BCO coated conductor

The second major form in which (RE)BCO superconductor is utilised is as a thin film deposited on a metallic tape substrate, usually referred to as a coated conductor. As in the case of bulks, crystallographic texture is introduced to the growing (RE)BCO material by epitaxial growth from a template. Rather than a localised seed crystal, in a coated conductor the template is either the metallic substrate or a deposited oxide film, with the texture transferred to the (RE)BCO film through intermediate buffer layers. The J_c of the (RE)BCO layer is typically an order of magnitude greater than in bulks, however the layer can only be microns thick. Figure 1.19 shows a schematic of a popular superconducting tape manufactured by SuperPower Inc. These tapes are designed to carry transport current in applications including field coils in motors and generators, transformers, fault current limiters, SMES and power transmission cables. Tapes are based on strong metallic substrates, typically Ni-W or Hastelloy, which provides mechanical stability to the thin and brittle (RE)BCO layer, and typically have a silver overlayer deposited on top of the (RE)BCO for current to flow in case the (RE)BCO turns normal whilst carrying current. For many applications additional stabilization is required and takes the form of copper layers.

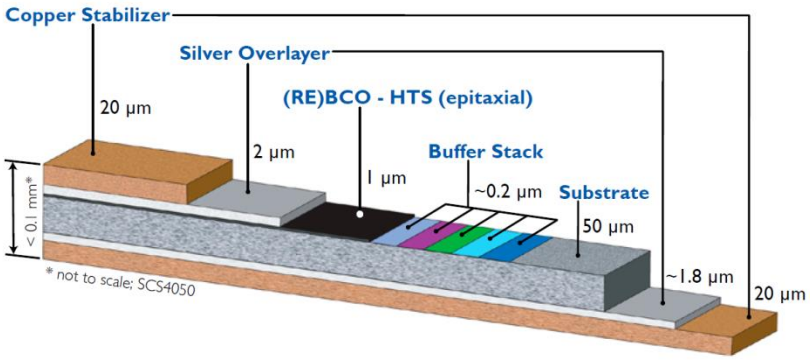

Figure 1.19: Architecture of 12 mm wide commercial (RE)BCO tape with copper stabilisation produced by SuperPower Inc. [33].

It is only in the last three years that another new application of superconducting tapes has been considered. The ability of thin films to sustain persistent current means that tapes can be magnetized to form a permanent magnet like a bulk, as well as being used for transport current applications. The first demonstration of this application is shown in Figure 1.20 which shows a stack of wide (RE)BCO tape pieces that have been cut into square annuli. Field cooling at 77 K achieved a relatively uniform trapped field in the bore of 0.43 T. This is somewhat less than that achieved by a field cooled stack of larger GdBCO bulk rings (up to 2.65 T at 77 K, Tomita et al. [34]). The (RE)BCO tape used was 40 mm wide and produced by AMSC (American Superconductor) who currently

produce such wide tape prior to slitting for commercial use as shown in Figure 1.21. In future they plan to scale the width up to 100 mm.

a) b)

Figure 1.20: a) Prototype NMR device made from 750 YBCO tape annuli [34]. b) Single 80 μm thick layer used the in NMR prototype made from tape produced by American Superconductor [35].

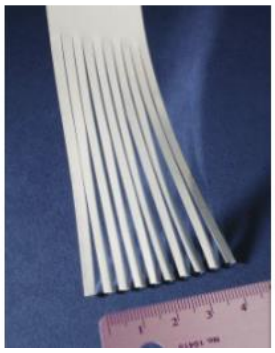

Figure 1.21: 40 mm wide (RE)BCO tape slit into 4 mm wide strips for commercial sale. Produced by AMSC.

Table 1.2. Critical current (in amps per cm width) for existing second generation (RE)BCO tape performance at 77.4 K in self field. Data largely from presentation by C E Bruzek, Nexans, ESAS Summer School 2012, France.

Industrial Supplier	Process	**Best performance** (77 K, SF)		**Commercial performance** (77 K, SF)	
		I_c (A/cm)	Length (m)	I_c (A/cm)	Length (m)
SuperPower (Furukawa)	IBAD/MOCVD	810 300	Few m 1000	200	< 500
AMSC	RABiTS/MOD	457 300	Few m 540	160 – 200	< 500
Brucker	IBAD/PLD	350	100	200	50
Fujikura	IBAD/PLD	600	600	400	< 500
Sumitomo	IBAD/PLD	200	200	No	
Showa	IBAD/MOD	310	500	No	
THEVA	ISD	1018	< 0.1	No	

The best critical current performance values (per tape width) for existing (RE)BCO tapes are shown in Table 1.2 along with performance for commercial grade tape. The stack of commercial (RE)BCO tape for which trapped field results are reported in Chapter 5, was made of 12 mm wide 200 A/cm SuperPower tape. It is important to be able to refer to the performance of currently

available (RE)BCO tape to put the results reported in Chapter 5 in perspective. The best performances include 600 A/cm for long 600 m lengths (Fujikura) [36] and greater than 1000 A/cm for short samples using Inclined substrate deposition (THEVA) [37], all at 77 K and in self-field.

1.5.3 MgB_2 bulk

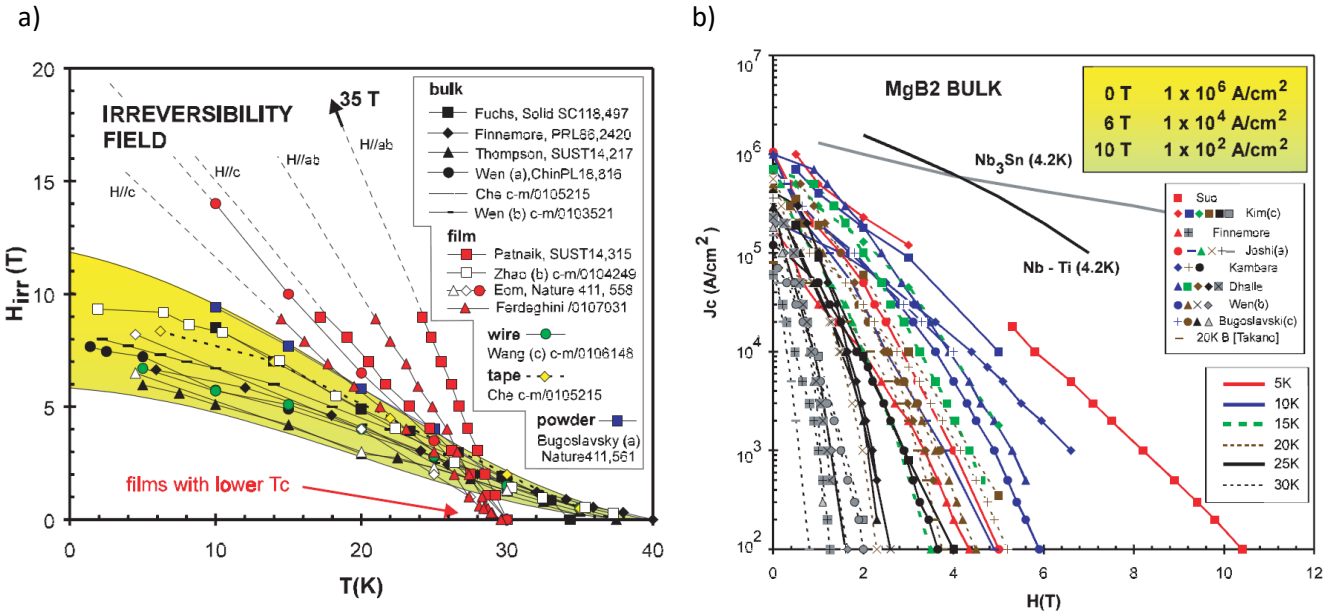

Figure 1.22: a) Irreversibility field data for MgB_2 in various forms from various researchers, with values for bulk MgB_2 shown with black marker points. b) J_c(H) data from various researchers for bulk MgB_2 at different temperatures. H_{irr} is defined here as the effective H_{irr} in polycrystalline form rather than for a single crystal. J_c drops rapidly with field. [38]
The discovery of superconductivity in MgB_2 in 2001 introduced a new material for potential use in large scale engineering applications given its high T_c of 40 K compared to LTS compounds (the highest for a binary compound), high J_c values up to 1 MA cm^{-2} (zero field) and good mechanical strength [38]. Irreversibility field data and $J_c(H,T)$ data can be found in

Figure 1.22. However arguably the most important difference from HTS compounds such as YBCO is the insensitivity of current flow to grain boundaries [39], simplifying fabrication by allowing it to be used in a polycrystalline form [38]. The invention of the reactive liquid Mg infiltration process by Giunchi et al. [40] provides a relatively simple and economical method of producing bulks and is a development from the hot-pressing method [41].

Using this method various geometries of high density MgB_2 bulk can be made, such as cylinders, (Figure 1.23) which are suitable for superconducting magnetic bearings. Complete details of the method and geometries that have been produced with it can be found in [42]. Pulsed field magnetization has been performed on one of these MgB_2 bulk pellets, with 0.47 T achieved at 23 K [43]. The dynamics are significantly different from magnetization of (RE)BCO bulks due to the comparatively high thermal conductivity and low specific heat capacity of MgB_2 [43]. The J_c and the temperature margin to T_c are also lower, which explains why the trapped fields are lower than for

bulk (RE)BCO. The highest fields trapped to date by field cooling are 2 T for an MgB_2 ring at 4 K [44], and 3.1 T between two 25 mm bulk pellets at 17.5 K [45].

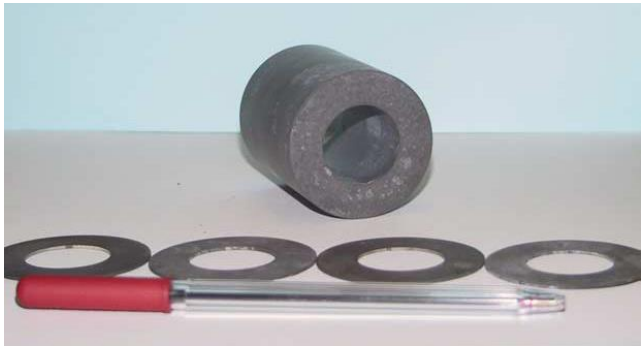

Figure 1.23: Bulk MgB_2 hollow cylinder produced by the reactive liquid infiltration process. The rings have been sliced from the main cylinder. [42]

1.6 Magnetic bearings and superconducting levitation

1.6.1 Magnetic levitation

Magnetic fields offer the ability to levitate mass and can allow an object to rotate around an axis with contactless motion whilst being constrained in other degrees of freedom. Consider a magnetic field $\underline{B}(r)$ which is the sum of the fields from two bodies. The force on each body can be calculated from the total field by using the concept of magnetic tension and pressure (which have the units N m^{-2}). The quantities are given by the equations below, where B_n and B_t are the normal and tangential field components respectively at the body's surface:

$$\text{Magnetic tension} \quad \sigma_t = \frac{B_n^{\,2}}{2\mu_0} \tag{1.18}$$

$$\text{Magnetic pressure} \quad \sigma_p = \frac{B_t^{\,2}}{2\mu_0} \tag{1.19}$$

$$\text{Total magnetic force} \quad \underline{F} = \frac{1}{2\mu_0}\int_{S_1}\left[\left(B_n^{\,2} - B_t^{\,2}\right)\underline{n} + 2B_nB_t\underline{t}\right]dA \tag{1.20}$$

The total magnetic force on one body due to the interaction of its field sources with external field sources is given by the integral of pressure and tension (and also a shear term) over a surface S_1 enclosing the body. The force is repulsive between a PM and a superconductor which is first zero field cooled. Assuming that the field of the PM is low enough and the J_c of the superconductor high enough, there will be very little flux penetration, leading to a Meissner-like flux exclusion effect. Such shielding will cause a large tangential field component around the surface, leading to magnetic pressure. Alternatively if the superconductor is field cooled in the field of the PM, then flux pinning will effectively 'freeze' the PM's field in the superconductor, leading to attractive forces as the PM is

displaced. This is due to dominant normal field components over the surface of the superconductor. Levitation can be achieved by exploiting magnetic tension and pressure.

An important characteristic of a magnetic levitation system is stiffness. In the simplest case when the direction of force and displacement are the same, the translational restoring force on an object for small displacements is given by equation (1.21) which defines the stiffness *k*:

$$F_x(x) = F(0) + \left(\frac{\partial F}{\partial x}\right)_{x=0} \left(x - x_0\right) \tag{1.21}$$

$$\text{Stiffness} \qquad k_x = -\left(\frac{\partial F_x}{\partial x}\right)_{x=0} \tag{1.22}$$

Earnshaw's Theorem states that particles governed by inverse square law forces of attraction and repulsion cannot be in stable equilibrium [46]. This theory can be extended to time independent magnetic field sources, proving that stable levitation in 3D space is not possible with permanent magnets. The theorem can however be avoided in three main ways: fields that oscillate temporally and spatially, active feedback and superconductors. The most widespread technology used in magnetic bearings for applications such as flywheels has been active feedback. This method essentially involves measuring the attractive force between an electromagnet (part of the stator) and a PM (part of the rotor) and adjusting it continuously so that if the rotor starts to accelerate towards or away from the stator, the current in the electromagnet is adjusted to bring the rotor back to its levitation position. Active feedback has been successfully used for commercial flywheel bearings [47] and maglev trains [48] (and also for levitating globe desktop toys). The disadvantages for active feedback bearings are the need for complex electronics and software, and uninterruptable power for the electromagnet.

1.6.2 Superconducting levitation

Bulk superconductors (type II), unlike active bearings, can provide a passive method of magnetic levitation based on two effects:

i. Repulsive levitation based on Meissner-like partial flux exclusion when a superconductor is zero field cooled. Levitation is not generally stable in all spatial degrees of freedom.
ii. Attractive or repulsive levitation when a superconductor is field cooled in the presence of a field source. The flux inside the superconductor is effectively 'frozen' due to flux pinning, allowing stable levitation in all spatial degrees of freedom.

Although the first effect can produce the maximum SC-PM levitation force possible (theoretically a maximum pressure of $\approx$ 25.5 N cm^{-2}), the stability of the second effect and the practicalities of FC compared to ZFC mean it is the preferred technique for superconducting magnetic bearings (SMB). Figure 1.24 shows how a restoring force results from magnetic tension and pressure when a FC superconducting bulk is displaced from its initial position.

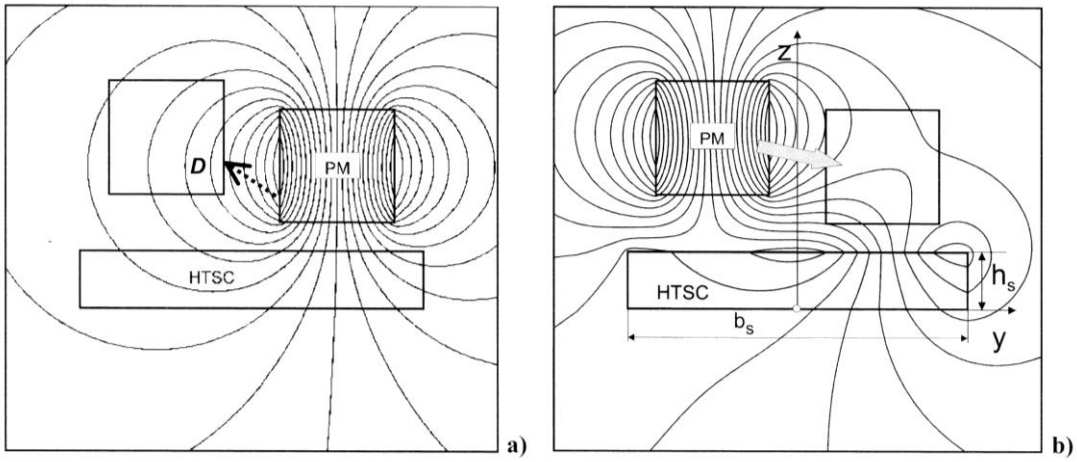

Figure 1.24: The field distributions for a SC-PM system where the superconductor has been field cooled in the field of a PM which is then displaced vertically and horizontally to position D in b). The arrow in b) shows the restoring force. The perfectly trapped flux model has been used as an approximation by forcing the field inside the HTSC to remain unchanged upon displacement from FC position. [6]

The illustration has used the Perfectly Trapped Flux Model to assume that the critical current density is infinite, leading to perfect shielding, and is a good approximation for high quality bulk YBCO at 77 K exposed to low fields. More analytical details about the implementation of this model will be given in Section 2.4.1. Such an approximation is in complete contrast to the total flux penetration that is shown in Figure 1.14 which has to be considered during high field pulse magnetization. The model is not a good approximation when displacements are large such as in Figure 1.25, which shows irreversible levitation force behaviour for the FC and ZFC cases.

The PM in Figure 1.24 experiences a restoring force when displaced due to the presence of magnetic field gradients produced by the PM in its initial position when field cooled. Generally, the higher the field gradients on the boundary between a field cooled PM and bulk superconductor, the larger the magnetic stiffness but the smaller the stability region in space. The basis of modern SMBs is arranging permanent magnets to create high field gradients and there has been modelling research into optimising the levitation force by adjusting configuration parameters [49, 50]. Most configurations rely on arranging PMs with opposing poles facing each other as shown in Figure 1.26.

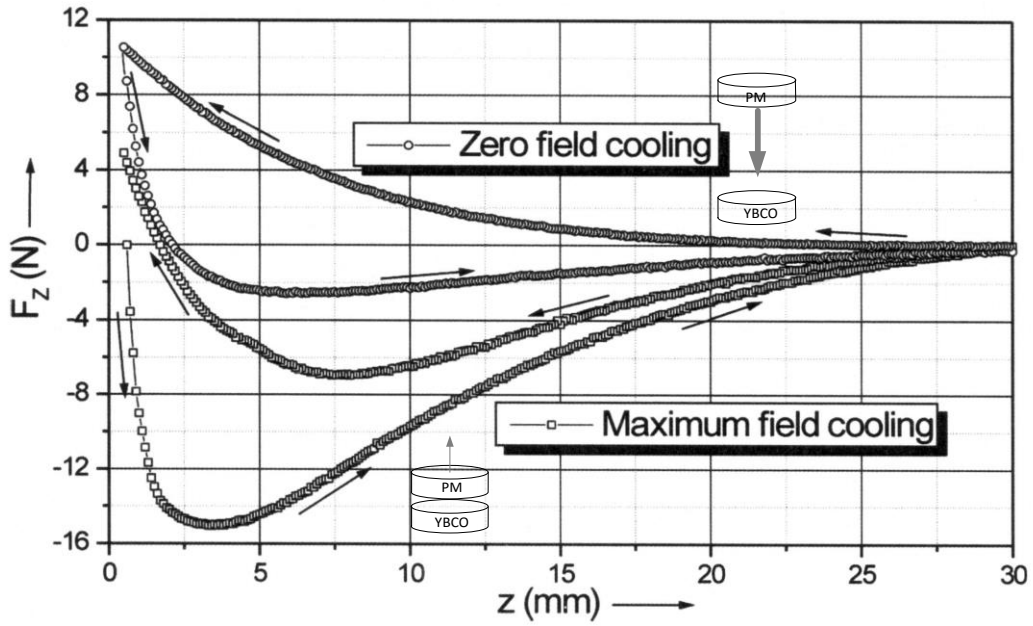

Figure 1.25: Example levitation force hysteresis curves for an YBCO-PM axial configuration after zero field cooling and field cooling. ZFC approach is purely repulsive but withdrawal force can become attractive due to significant flux penetration when the PM is brought very close, exposing YBCO to a high field. Withdrawal force after FC is attractive with high initial stiffness. Approach back to field cooling position is less attractive and may become repulsive due to the bulk retaining some of its initial trapped flux during withdrawal. In both cases stiffness and hysteresis can be reduced, making the behaviour more reversible, if J_c of the bulk is increased. Note: ZFC maximum force is usually higher than FC maximum force but this graph is only intended to give an overview. [51]

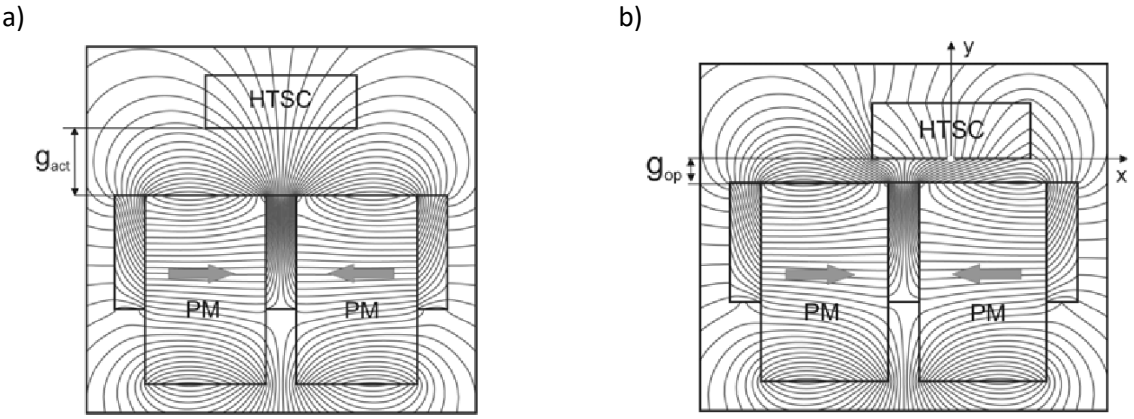

Figure 1.26: Two dimensional HTSC field cooled in the presence of high magnetic field gradients, a) before being displaced, b) after displacement. The HTSC experiences a stable levitation force in *x* and *y*. The PM configuration has used iron shims to guide flux, helping enhance field gradients. [6]

The general factors that have the biggest impact on levitation force in a SC-PM system are J_c, the radius scale R of allowed shielding currents (the size of a single domain for YBCO) and the field gradients on the superconductor surface. Assuming linearity, the equation for force for an axially symmetric system can be given as a first approximation by:

$$F \propto J_c R \frac{dB}{dz} \tag{1.23}$$

Modelling has been done which confirms this equation by varying J_c and the ratio of pole pitch and bulk size for a cylindrical SMB made of a segmented bulk hollow cylinder [52].

1.6.3 Types of superconducting bearings

There are two main types of SMB, both of which rely on PM rings arranged to give high magnetic field gradients on the surface of a superconducting bulk or structure made of a series of bulk pieces (usually YBCO or GdBCO). These two types are cylindrical and planar, as shown in Figure 1.27, with the PM array usually on the rotor and the superconductor usually on the stator for ease of cooling. Much research has been done into modelling and constructing prototype SMBs based on these configurations. Initial research focussed more on planar bearings [53-57] but more recent research has focussed on the cylindrical type [58-60], including the commercial flywheel energy storage system developed by ATZ GmbH [61]. Most systems investigated have used PM-PM bearings with the SMB for stability or to partly support the weight of the rotor. Figure 1.27 shows bearings with a vertical axis, but SMBs can also have horizontal axes. Vertical axis configurations are primarily for flywheel energy storage systems whereas horizontal configurations are used primarily for turbo machinery. In both cases the rotor has to be displaced from its operational position when field cooled in order to use levitation force to counter the weight of the rotor.

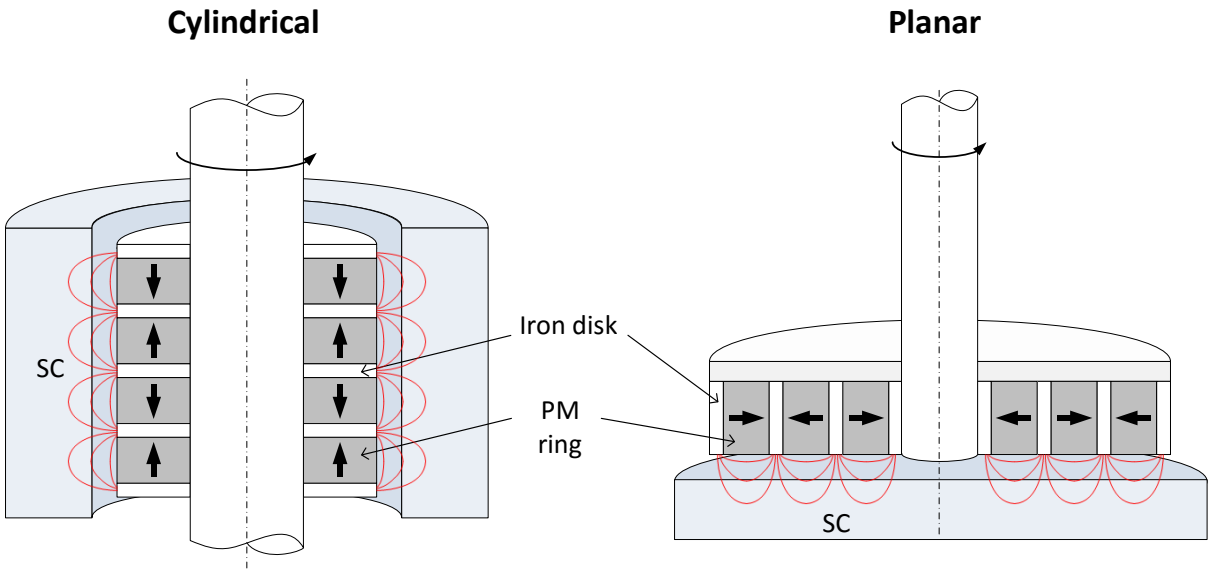

Figure 1.27: The two main SMB configurations, cylindrical and planar. The superconducting hollow cylinder and disk, shown in the figure for cylindrical and planar bearings respectively, are not necessarily a single piece but can be made of separate pieces such as YBCO pellets/tiles.

The confinement of the rotor in all translational degrees of freedom is essential for applications. The illustrated PM rotor configurations achieve this by creating a field with gradients such that the SC sees a large change in the field if the rotor is displaced axially or radially. The rotor is however free to rotate about its axis due to the rotational symmetry of the PM array.

Figure 1.28 shows four examples of SMBs that have been developed over the last decade. The examples show the variety in terms of configuration, size and performance that exists. In almost all complete systems, PM-PM bearings have been used to provide extra stability or to support most of the load and the rotor is usually in a vacuum to minimise losses. One of the most commercially successful bearings, developed by ATZ [61] for use in a flywheel energy storage system, will be explored in section 1.6.5 and can be considered as a benchmark design.

Prototype superconducting magnetic bearing system	Details
Heavy load horizontal axis bearing for industry [62] 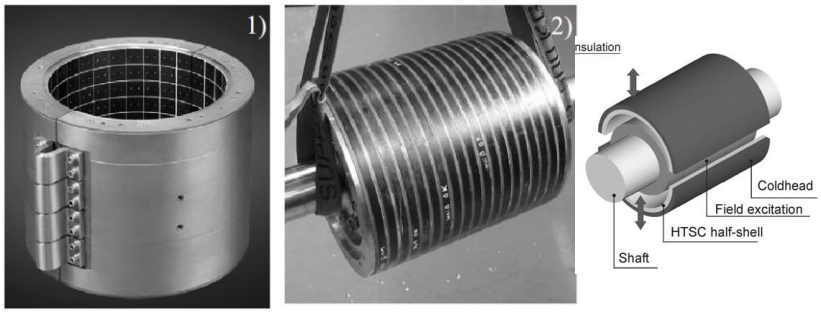	**Type:** Horizontal axis cylindrical SMB. **Application:** Siemens HTS generator **Load:** up to 10 kN **Rotational speed:** 3600 rpm (4400 rpm max) **Superconductor:** stator made of two cylindrical half shells comprising 270 trapezoidal bulk YBCO tiles in total. **Other details:** Superconductor operating temperature approx 30 K. Bore 321 mm. Working gap 3 mm. Radial stiffness 5.1 kN/mm.
Superconducting thrust bearing for flywheel energy storage [53] 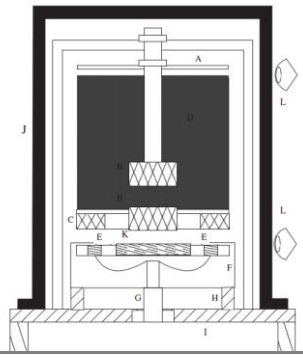	**Type:** Vertical axis planar SMB for stability (bottom) with attractive PM-PM bearing for rotor weight (top). **Application:** Flywheel energy storage for high cycling use. **Load:** 44 kg **Rotational speed:** 720 rpm (limited by drive system) **Superconductor:** stator made of outer ring of bulks and central array of hexagonal bulks.
Superconducting bearing for 5KWh flywheel (Boeing) [56] 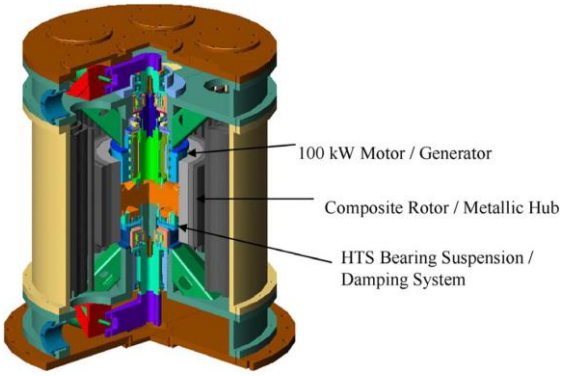 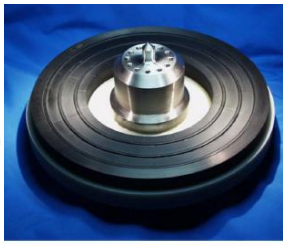 Rotor component of HTS bearing.	**Type:** Vertical axis planar SMB (bottom) used with a PM-PM bearing (top) which carries most of rotor weight. **Application:** 5 kWh/100 kW flywheel energy storage for uninterruptable power protection **Load:** 164 kg **Rotational speed:** 15000 rpm **Superconductor:** stator made of array of hexagonal YBCO bulks **Other details:** Superconductor operating temperature 77 K. Complete energy storage system.
Energy storage flywheel system with SMB and PMB [60, 63] 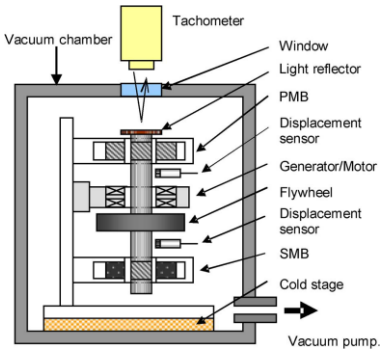	**Type:** Vertical axis cylindrical SMB (bottom) used with a PM-PM bearing (top) which carries most of rotor weight. **Application:** flywheel energy storage for uninterruptable power protection **Load:** 0.32 kg **Rotational speed:** 5000 rpm **Superconductor:** stator made of ring of YBCO bulks **Other details:** Superconductor operating temperature 70 K.

Figure 1.28: Table of four example prototype SMB systems that have been constructed and tested over the last decade. All systems use melt-textured single domain YBCO segments to form large cylindrical or planar superconducting surfaces. Many more than those selected have been built and tested over the last decade.

1.6.4 Rotational loss

Flywheel energy storage requires low rotational energy loss for applications where energy is stored for hours or days. Conventional bearings have high-speed idling energy losses of around 0.1 - 1% per hour whereas the losses for flywheels with SMBs are typically in the range of 0.001 - 0.1% per hour [59, 64]. There are two main sources of loss in an SMB:

i. **Eddy currents:** Radial inhomogeneity of the PM stack on the rotor induces eddy currents in conducting parts of the stator when rotating. Eddy currents are also induced if there is any rotor eccentricity. A more subtle contribution comes from using segmented superconducting stator parts such as YBCO tiles for the hollow cylinder shown in Figure 1.27. When the tiles are field cooled and the rotor allowed to move to its equilibrium position, the bulks do not perfectly preserve the axial symmetry of the PM rotor field (as a super-current circulating completely around the stator is not possible), but modify it slightly. This results in radial inhomogeneity of the trapped stator field which induces eddy currents in the conducting parts of the rotor [65] which can include the PMs themselves. Eddy currents tend to cause exponential speed decay.
ii. **Hysteresis:** Radial inhomogeneity of the PM stack causes the superconducting tiles to be exposed to a time varying field which induces hysteretic losses in the superconductor as a result of the critical state. These losses can be reduced by increasing J_c. These losses tend to cause linear speed decay.

1.6.5 Flywheel energy storage applications

This section will focus on existing applications of SMBs for flywheel energy storage (FES) systems which are an alternative to batteries and capacitors for some applications [66].

The most widely reported use of an SMB has been in the flywheel energy storage system developed by ATZ GmbH in Germany [61, 67-72] for uninterruptable power supply applications. The SMB is central in this system as it is entirely responsible for supporting the rotor weight, with a PM-PM bearing used only for radial stability, as shown in Figure 1.29a.

SMB load capacity is proportional to the area between the superconductor and field excitation PMs. For the same surface area, planar bearings have a larger radius than cylindrical ones, which leads to disadvantages compared to the cylindrical type of bearing shown in Figure 1.27.

a)

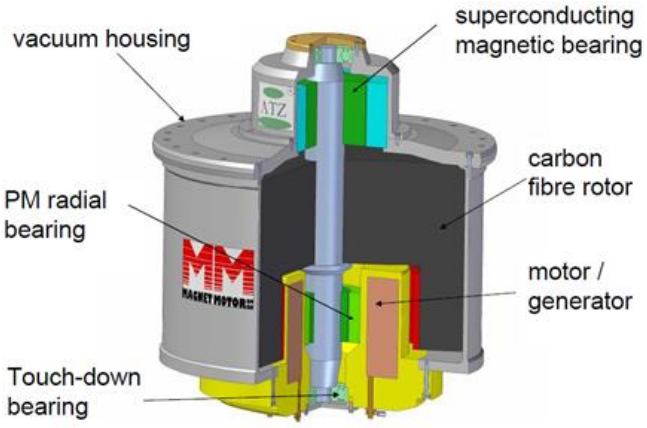

b)

Bearing type	Radial type
Diameter x height	205 x 120
Magnetic area	768 cm²
Superconductor type	YBCO, melt textured
HTS size/number of elements	65 x 35 x 13 / 55 pcs.
Rotor configuration	200 mm PM rings
Bearing housing	Fe / Al / G-10, vacuum
Magnetic gap	2.5 mm
Free rotor movement	2.0 mm
Cooling YBCO	GM cooler, 40 W@77 K 45 – 60 K after 12 hours
HTS bearing weight	55 kg
Maximum load, axial	10800 N / 3 mm displacement
radial	4700 N / 3 mm displacement
Stiffness, axial	4.5 kN/mm
radial	1.8 kN/mm
Speed (test)	3200 rpm
Thermal loss	12-15 W @ 10^{-3} mbar
Rotational friction	-5 x 10^{-4} Nm

Figure 1.29: a) ATZ 5kWh/250kW flywheel energy storage system with a top cylindrical SMB of diameter 205 mm. YBCO structure shown in blue, PM stack shown in dark green [61]. The lower PM-PM bearing is for radial stiffness and has negative axial stiffness which is compensated by the SMB. b) 1 ton HTS bearing parameters for ATZ flywheel [72].

These include higher mechanical stresses for PMs at large radii on planar bearing rotors than on cylindrical bearings, the cooling area for the planar type usually being larger and less efficient, and field inhomogeneity of the PM stack usually being more problematic at the higher radii of planar bearings. Due to these considerations, the new SMB designs considered in Section 1 will focus on the cylindrical type. The large load capacity and stiffnesses for the ATZ bearing are primarily due to the large SC-PM area and small magnetic gap.

The maximum axial pressure (maximum axial load divided by SC-PM area), which can be used to characterise the bearing, is 14 N cm^{-2}. A significant engineering achievement of this design is the cooling and insulation of the HTS stator part at 45-60 K which is separated from the room temperature bore of the rotor by less than 1 mm.

a)

b)

Figure 1.30: Multi seeded melt textured YBCO bulks. a) Tiles used in the ATZ 5kWh/250kW FES cylindrical bearing. Right: hollow cylindrical monolith with radial c-axis orientation that could be used in a bearing, although it should be noted that the domains only transmit a fraction of current so the cylinder is not 'fully connected'. Bulks fabricated by ATZ. [70]

Although one of the most successful SMB configurations used for a commercial application, the ATZ bearing has limitations which are important to identify in order to focus future research. The use of an YBCO-rare earth PM cylindrical configuration with a small magnetic gap pushes the axial pressure as high as is practically possible for an YBCO-PM bearing. For a large axial load of more than 1 tonne, this means that the size of the SMB becomes considerable (>200 mm diameter) and requires significant cost for over 50 high J_c YBCO tiles of consistent quality. However there are suggestions that the market for flywheel energy storage demands higher energy storage and therefore higher bearing load capacity. Another limitation is the need to segment the superconducting stator part to utilise the high J_c and H_{irr} properties of YBCO, which cannot be made economically in pieces greater than ~ 70 mm in size. This segmentation contributes to rotational loss as described in Section 1.6.4. The use of MgB_2 and the new ideas proposed in Chapter 2 will aim to overcome these limitations by using magnetized (RE)BCO bulks as a field source.

1.6.6 Use of MgB_2 for superconducting bearings

The use of the liquid Mg infiltration process described in Section 1.5.3 to create massive hollow cylinders of MgB_2 offers new possibilities for the use of this material in SMBs. Giunchi et al. have demonstrated the effectiveness of replacing a segmented YBCO stator in an SMB with an MgB_2 tube [73]. The benefits of using an MgB_2 tube over YBCO tiles are: fully connected superconducting paths, production is simpler and probably less expensive than YBCO tiles and higher mechanical strength than YBCO [4]. For MgB_2 at 20-30 K, $J_c \sim 10^5$ A cm^{-2} (self field) as shown by

Figure 1.22, which is comparable to YBCO between 50-70 K at zero field. MgB_2 cylinders up to 65 mm in diameter and 100 mm in height have so far been produced by liquid infiltration and their use at 20-30 K is not a huge cryogenic limitation given the 45 K lower temperature the ATZ bearing has been designed to operate at. Such a temperature range would also be suitable for a future hydrogen economy [74], in which hydrogen stored in its liquid form (20 K) could be used to indirectly cool superconductors. The configurations shown in Figure 1.31 were tested between 21 and 38 K. The b) configuration gave the highest stiffness at 22 K of ≈ 100 N mm^{-1}. Configuration a) with its low field gradients gave only ≈ 30 N mm^{-1} and configuration c) ≈ 65 N mm^{-1}.

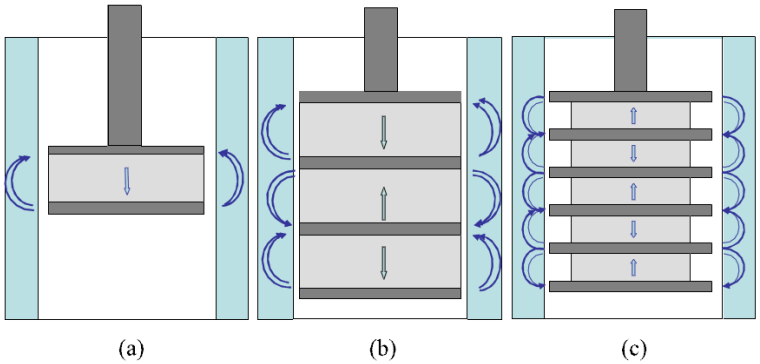

Figure 1.31: Schematic of the MgB_2 cylinder levitation force experiments carried out by Giunchi et al. [73] with different NdFeB PM excitation arrangements. The dimensions of the cylinder used are d_{in} = 25 mm, d_{out} = 39

mm and h = 43 mm. Field cooling was used at different heights, with stiffness as well as levitation force measured during removal of the PM stack.

The stiffness of the 5PM/6 iron stack configuration (a stack of 5 PMs and 6 iron disks as shown in Figure 1.31c) as well as the maximum axial levitation force was reported for a range of temperatures shown in Figure 1.32. The 20-25 K temperature range clearly gives the best performance.

a) b)

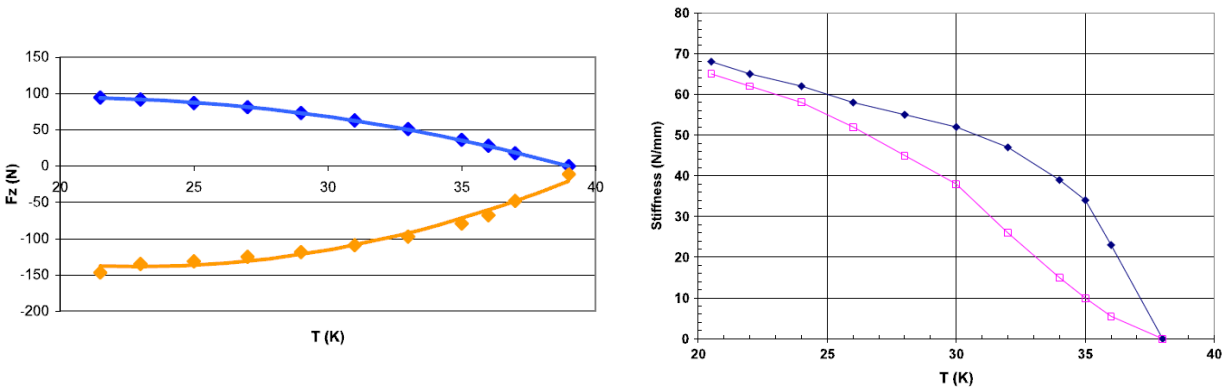

Figure 1.32: a) Temperature dependence of maximum axial levitation force between a 5PM stack and MgB_2 cylinder with first maximum (blue) and minimum (orange) of $F_z(z)$. b) Stiffness of an insertion/extraction cycle. Showing stiffness at start of cycle (blue) and stiffness at end of cycle(pink). [73]

The results for the 3PM configurations at 26 K gave an axial force density of 13 N cm^{-2}, a performance similar to the maximum force density for the ATZ design based on Figure 1.29b (14 N cm^{-2}), demonstrating the feasibility and potential for using bulk MgB_2 in new SMB designs.

1.7 Pulse field magnetization of superconducting bulks

1.7.1 Differences from field cooling

Superconducting bulks exhibit the ability to trap extraordinarily high magnetic fields and therefore have potential to be used as very powerful 'permanent' magnets. However one of the main factors limiting their use in applications is the difficulty of magnetizing them. The two ways to trap a field in bulks are field cooling and zero field cooling. Figure 1.14 displays how these two modes can be used to trap an approximately conical field profile. In practice, field cooling is carried out using large superconducting coils which have to maintain a large static field whilst cooling the sample below T_c to the desired temperature, after which the applied field is ramped down to zero slowly. However because zero field cooling does not require a static field whilst waiting for the sample to reach the desired temperature, ZFC can be achieved by rapid changes in field. Pulsed field magnetization is a special case of zero field cooling in which short pulses of field (typically < 0.1 s) are applied. Due to the short durations, reinforced copper coils (with suitable cooling) can be used

instead of superconducting coils, in conjunction with a capacitor bank to supply pulses of current (typically ~ kA). The technology is therefore relatively simple, inexpensive and compact compared to a superconducting coil and has therefore attracted significant research [13, 14, 25, 75-78]. Pulsed field techniques currently allow for magnetic flux densities of over 3 T to be trapped in bulks around 45 mm in diameter using an applied field of 6 T and a pulse rise time of 12 ms [23]. Figure 1.33 illustrates the trapped field resulting from various maximum applied pulsed fields. At least twice the maximum applied field is needed to saturate the bulk for a given temperature compared to FC.

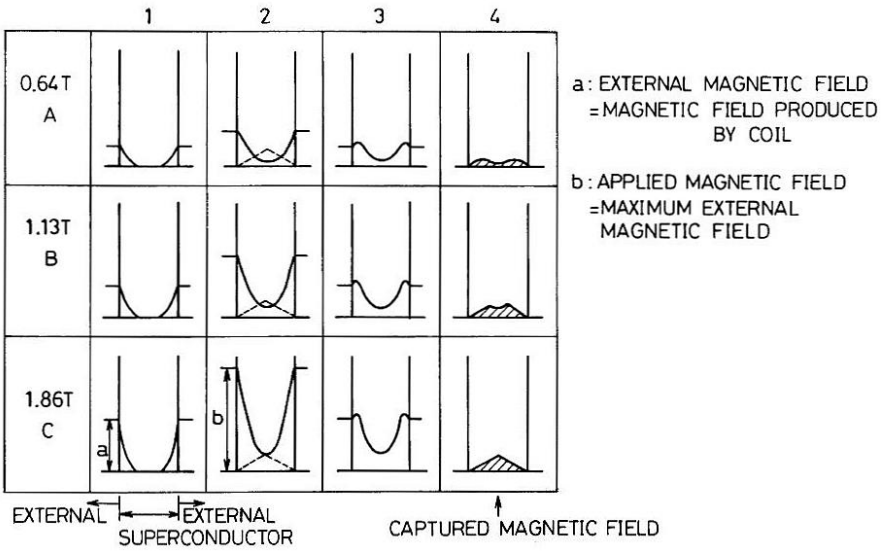

Figure 1.33: The trapped magnetic field profiles for different applied pulsed fields. A conical field profile such as in C is only achieved for a sufficiently high pulsed field. Based on results for a 35 mm x 14 mm YBCO bulk. [79]

The Bean model suggests that the peak in trapped field B_{max} for a superconducting bulk scales linearly with size ($B_{max} \propto RJ_c$) so, unlike a conventional PM, the maximum possible trapped field value of a SC bulk is more limited by its size. The real advantages of magnetized bulks are therefore often only seen in large bulk diameters ($\gtrsim$ 20 mm). Cooling an YBCO bulk below 77 K to say 30 K allows for an order of magnitude increase in B_{max}, however as its value at these low temperatures is typically over 5 T the limiting factor becomes the maximum field that can applied by the pulsed field coil/capacitor bank (and also the limitations illustrated in Figure 1.18). At low temperatures the increase in J_c can instead be exploited by increasing the total trapped flux Φ_T, which is equally important as B_{max}, as will be explained in the next section.

The biggest problem and limitation of PFM is the significant heating of the bulk caused by the penetration of the pulsed field and resulting flux flow. The rapid motion of penetrating flux induces a high electric field parallel to the super-currents in the outer regions of the bulk, resulting in losses. Such losses heat the superconductor, reducing J_c in the outer regions and suppressing the maximum trapped field possible compared to quasi-static ZFC. The shorter the pulse duration and the higher

the applied field, the greater the heating effect due to the more rapid flux motion, so it is important to use as long a pulse duration as is practically possible. Another contribution to the reduced performance of PFM is the viscous force on the penetrating flux discussed by Mizutani et al. [75], which seems to have significant effects for lower applied fields.

Pulse durations of the order of 10 ms give reasonable performance without being too long for pulse current systems to produce. Longer durations would require unfeasibly higher inductance coils and/or larger more costly capacitor banks. The effect of pulse heating and viscous force on total trapped flux is shown by the data in Figure 1.34, which shows that a higher applied field is needed for PFM than if there was no heating (quasi-static ZFC). The curves exhibit a peak because there is an optimum applied field which just achieves the maximum trapped flux, beyond which a higher field increases heating effects, leading to a decrease in performance.

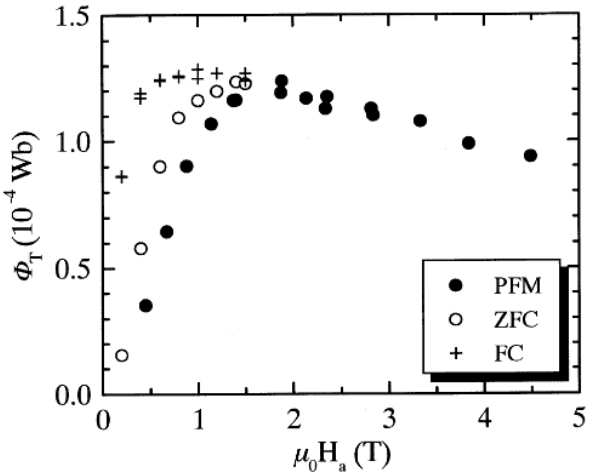

Figure 1.34: Data from Mitzutani et al. [75] for the magnetization of an YBCO bulk 34 mm in diameter and 14 mm thick at 77 K. The graph shows the dependence of total trapped magnetic flux Φ_T on applied field for pulsed field magnetization (PFM), field cooling (FC) and quasi-static zero field cooling (ZFC). PFM gives a lower trapped flux than quasi-static ZFC due to the generation of heat inside the bulk during the pulse, which reduces J_c.

Because the specific heat capacity of materials becomes very small at temperatures approaching absolute zero, the effects of heat generation are particularly limiting for magnetization at temperatures below approximately 30 K.

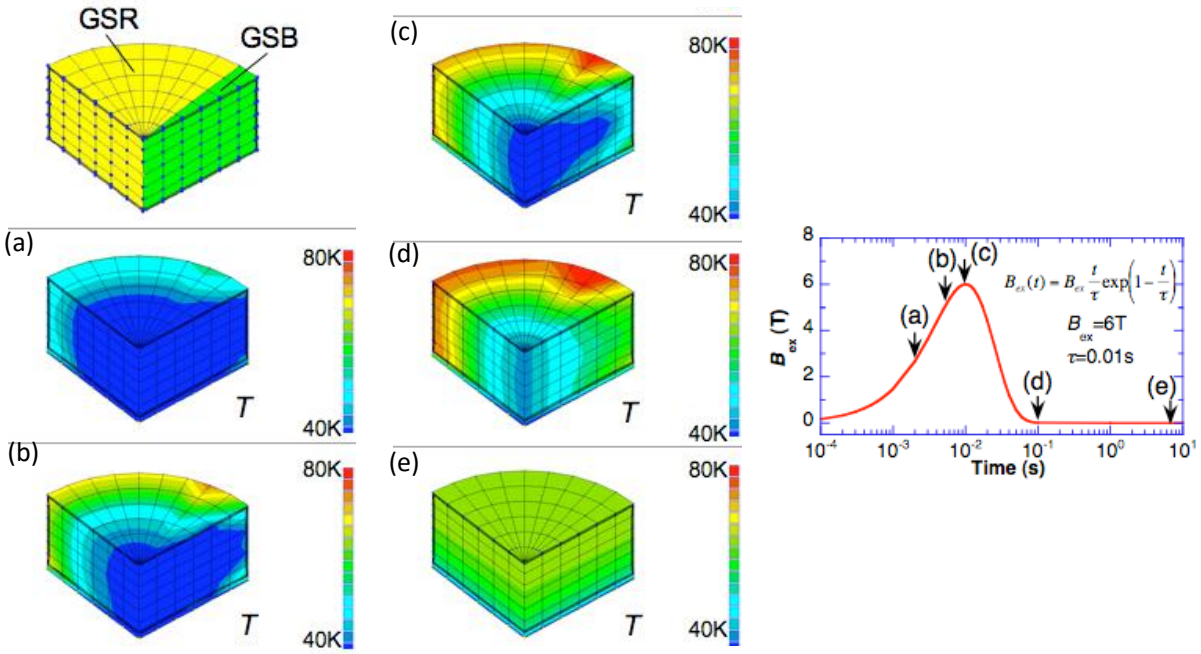

Figure 1.35: Simulation of heating in a bulk during PFM by Fujishiro et al. The growth sector boundary (GSB) has been modelled with 4 times the J_c of the growth sector region (GSR). This inhomogeneity leads to hotspots inside the GSR [17].

Regions of relatively low J_c in a bulk are regions with weak links. These weak links are largely in the growth sector region of a bulk and lead to hotspots during pulsed field magnetization as shown in Figure 1.35, which can cause a collapse in trapped field for low temperatures and high applied fields, and a saturation in the maximum field that can be trapped below a certain temperature, as will be demonstrated in Section 5.3. So whist J_c inhomogeneity is not necessarily a problem for trapping fields using field cooling, it is usually problematic for pulsed magnetization. This means that a bulk characterised as high performance based on a field cooling test is not necessarily suitable for PFM.

Due to excessive heat generation during pulsed magnetization, effective cooling of the bulk is particularly important to bring its temperature back down to equilibrium temperature as quickly as possible, thus minimising flux creep. The two general methods of cooling are direct cooling using a cold head, or indirect cooling using a liquid cryogen or gas. The system constructed for this project, as reported in Chapter 3, used indirect cooling by helium gas. This method allows flexibility in testing samples of different shapes and sizes and is therefore excellent for research. Liquid neon has been used to cool bulks in one motor prototype as part of a closed loop neon-thermosyphon system [80]. Direct cooling has been used in a research system [22] and has the advantage of having lower thermal inertia, however eddy current heating of cold head components may add extra heat during a pulse.

1.7.2 Maximising peak trapped field at fixed temperature

There are various ways to increase the trapped field and/or flux above that which would result simply from one pulse as shown in Figure 1.33. The simplest method is 'Iteratively magnetizing pulsed field operation with reducing amplitudes' (IMRA), which involves repeated pulses at a fixed temperature. This technique enhances the trapped flux by first applying a pulsed field large enough to magnetize the centre of the bulk, before applying pulses with reduced amplitude to top-up the flux in the outer regions of the bulk, which escaped due to heating during the first large pulse [75]. As shown by Figure 1.36, the IMRA technique also offers a way of reducing the limitations of PFM at low temperature due to excessive temperature rise. The technique typically involves applying around 10 pulses to the bulk as shown by Figure 1.36b, with the final pulsed field approximately half the initial pulsed field.

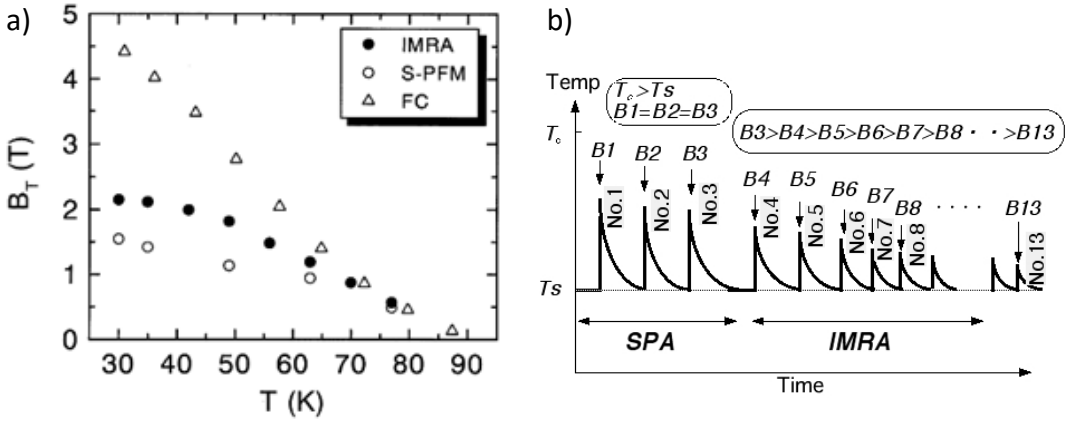

Figure 1.36: a) Data from Mizutani et al. [75] showing the increase in maximum trapped field that can be achieved by using the IMRA technique compared to a single pulse S-PFM. IMRA is particularly advantageous at lower temperatures. b) Schematic illustrating the temperature rise and sequence of pulsed field for IMRA (SPA, which involves pulsing the same field more than once, is a variant of IMRA) [81].

1.7.3 Multi-pulse technique with stepwise cooling (MPSC)

As mentioned before, the total trapped flux in a bulk is as important for applications as maximum trapped field. For example, the induced emf in a conductor is proportional to the rate of change of flux it experiences which is relevant for a generator. The increase in J_c at temperatures lower than 77 K can be exploited to increase trapped flux even though the maximum trapped field for a saturated profile for these low temperatures is too high to achieve due to limitations of maximum applied field and excessive heating. The 'multi-pulse technique with stepwise cooling' (MPSC) exploits the increase in J_c as temperature is lowed by pulsing a bulk at approximately the same applied field repeatedly as the temperature is lowered. It is particularly important for magnetizing larger ≈ 40 mm diameter bulks, for which saturation is very difficult to achieve. A good

example of this is the use of IMRA and MPSC together to trap a broad field of 3 T field profile in a 45 mm bulk using applied field pulses up to 6 T with a 12 ms rise time over the 30 – 70 K temperature range [23]. The MPSC technique builds up flux in the outer regions as illustrated by Figure 1.37.

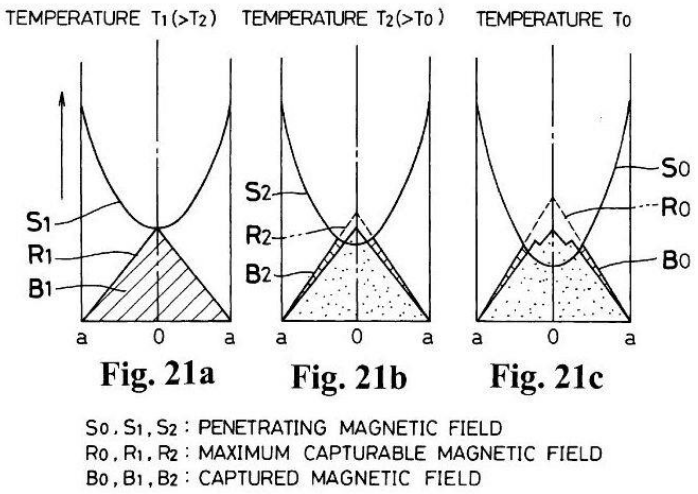

Figure 1.37: Schematic showing the increase of trapped flux in the periphery of a cylindrical bulk when pulsed with a field of the same value at 3 different temperatures decreasing in value. [79]

The details of how flux is built up in the bulk using MPSC can be seen in Figure 1.38, which shows how a field distribution similar to a conventional PM can be achieved. The dynamics of flux penetration for MPSC are complex, involving effects such as sudden redistribution of already trapped flux during new pulses [77]. The final trapped field resulting from an optimised sequence of pulses can be reproducible, however different bulk samples may require difference pulse sequences due to differences in the magnitude and inhomogeneity of J_c.

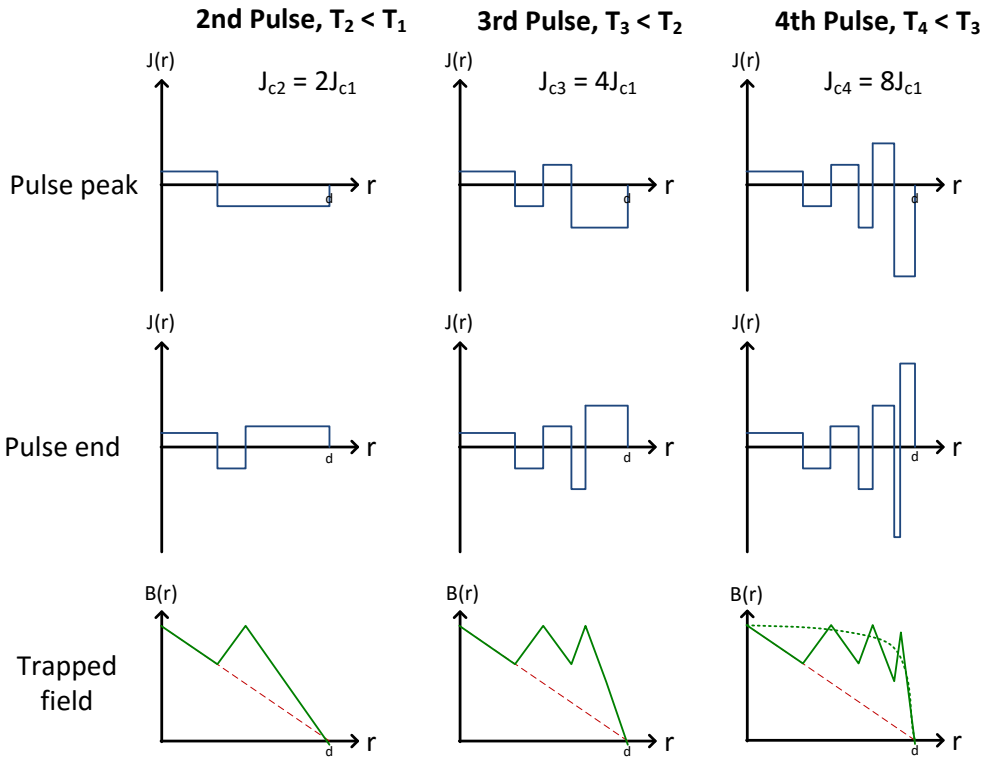

Figure 1.38: The build-up of trapped flux in a cylindrical bulk when pulsed 3 times at decreasing temperature, after an initial pulse at T_1 has trapped B_{max}. The Bean model is assumed and demagnetization effects ignored. The increase in J_c as temperature is lowered allows a spatially alternating current distribution to be built up. The dotted green line shows the approximate trapped field after relaxation, demonstrating a significant potential increase in trapped flux compared to that achieved by the single initial pulse (red dotted line). In practice the best results are achieved by combining the IMRA technique with MPSC at each temperature.

There exists some confusion about trapped fields, applied fields and maximum possible trapped fields and their relation to one another. Table 1.3 attempts to summarise general trapped field and flux ratios for different magnetization methods based on experiments conducted for this thesis and a literature review. It is important to note that B_{trap} is defined as the trapped field on the *surface* of a single bulk and is approximately half the maximum trapped field *inside* a magnetized bulk. Only for a pair of magnetized bulks is the field measured (in between the bulks) ever similar to the maximum field trapped inside the bulks. Also, the values for $B_{trap}/B_{applied}$ are influenced by demagnetizing effects and the fact that J_c decreases for increased applied fields. With these points in mind, the field that you need to apply using field cooling to saturate a bulk is actually twice the field that you trap on the bulk surface due to demagnetizing effects, unlike the simple picture in Section 1.4 which is strictly only true for an infinitely long slab or cylinder. Quasi-static ZFC, in which the field changes slowly enough as to not cause heating, has a higher $B_{trap}/B_{applied}$ ratio than would be expected from the Bean model combined with demagnetizing effects. This is because the applied field needed is higher than for FC, but as $J_c(B)$ decreases for increasing B, you do not need to apply twice the FC field to penetrate the bulk.

The row for IMRA shows that although the trapped field can be maximised, in general only the trapped flux can ever reach the ideal value. The only way to trap fields close to the applied field is to use different temperatures, as shown by the values for MPSC + IMRA.

Table 1.3: Maximum trapped field and flux for various methods of magnetization. B_{trap} is defined as the maximum trapped field possible for the surface of a bulk for a given method. $B_{applied}$ is defined as the applied field needed to achieve B_{trap}. B_{ideal} is defined as the absolute maximum trapped field on the surface of a bulk possible for a sample (using FC, for which there is no heating) for the magnetization temperature considered. Similar definitions apply to Φ. MPSC combined with IMRA is able to trap a maximum surface field closest to the applied field. B_{ideal} and Φ_{ideal} not valid for MPSC + IMRA as this type of magnetization occurs over a temperature range.

Pulsed field type	$B_{trap}/B_{applied}$	B_{trap}/B_{ideal}	Φ_{trap}/Φ_{ideal}
FC	1/2	1	1
Quasi-static ZFC	≈ 1/3	1	1
Single pulse	≈ 1/4	1/2 - 2/3	< 1
IMRA (fixed Temperature)	1/4 – 1/3	≈ 2/3	≈ 1
MPSC + IMRA	1/3 – 3/4	-	-

1.7.4 Flux creep

The permanence of the field trapped in a superconducting bulk is limited by thermally activated flux creep. At currents below J_c the flux lattice is effectively pinned as the fluxons lie in potential energy wells, however at any temperature above 0 K there is still a non-zero probability of fluxons overcoming the pinning energy barriers [82]. This results in gradual jumping of flux bundles from one pinning site to another over time. Therefore thermally activated creep reduces field gradients as flux leaks out of the bulk, resulting in a logarithmic decay in trapped field as described by the equation below [83], where B_0 is the central trapped field on the bulk surface a time t_0 after magnetization.

$$\frac{B(t)}{B_0} = 1 - a\log\left(\frac{t}{t_0}\right) \tag{1.24}$$

The creep rate can also be described in terms of magnetization decay, and is often expressed using a natural logarithm in literature:

$$S \equiv \frac{1}{M}\frac{\mathrm{d}M}{\mathrm{d}\ln t} \tag{1.25}$$

which, for purely logarithmic decay, leads to

$$\frac{M(t)}{M_0} = 1 + S\ln\left(\frac{t}{t_0}\right) = 1 - b\log\left(\frac{t}{t_0}\right) \qquad (b = -2.303S) \tag{1.26}$$

Flux creep is usually highest at or above 77 K. Below this temperature, the dependence of creep rate on temperature is not generally linear or monotonic, but can exhibit a field dependent peak [6, 84]. Typical creep rate values, $|S|$, for magnetized (RE)BCO bulks are between 0.02 and 0.03 ($b \approx 0.05 – 0.07$) for 10 – 60 K and around 0.05 ($b \approx 0.12$) for 77 K [6]. The parameters *a* and *b,* defined as relaxation rates, are not necessarily equal, as flux can initially flow from the periphery of a magnetized sample faster than from the centre.

Figure 1.39 shows some example data for the decay of field trapped in a bulk. It is clear that the quasi-static ZFC case and the FC case fit the logarithmic behaviour very well (constant relaxation rate as defined earlier) but some of the PFM data do not obey simple logarithmic decay, and this is due to the effect of heating, which modifies the decay. The sudden heating that results from penetration of high pulsed fields raises the temperature of the bulk during magnetization. After magnetization the bulk is cooled back to the initial temperature, suppressing flux creep. This is a positive effect which accompanies the unwanted reduction in maximum trapped field when using PFM.

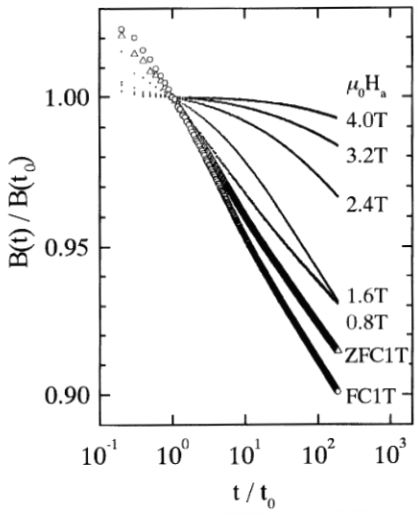

Figure 1.39: Data from Mizutani et al. [75] showing decay in normalized magnetic flux density due to flux creep at a position between the centre and edge on top of a bulk. The decay in trapped field is shown for a number of applied pulsed fields, as well as 1 T quasi-static ZFC and FC. ZFC and FC exhibit logarithmic decay, but the PFM data shows an initial slow decay before accelerating and tending to a logarithmic decay. t_0 was 10 s.

The suppression of flux creep, due to a decrease in temperature from the magnetization temperature, can be used in a more direct way. An exponential decrease in creep rate is achieved by decreasing temperature after magnetization [83] which means that the critical state achieved by flux trapped in a bulk can effectively be frozen if temperature is lowered by ~ 10 K. Proof of this phenomenon can be found in Section 4.1.2.

1.7.5 Application in motors and generators

a) b)

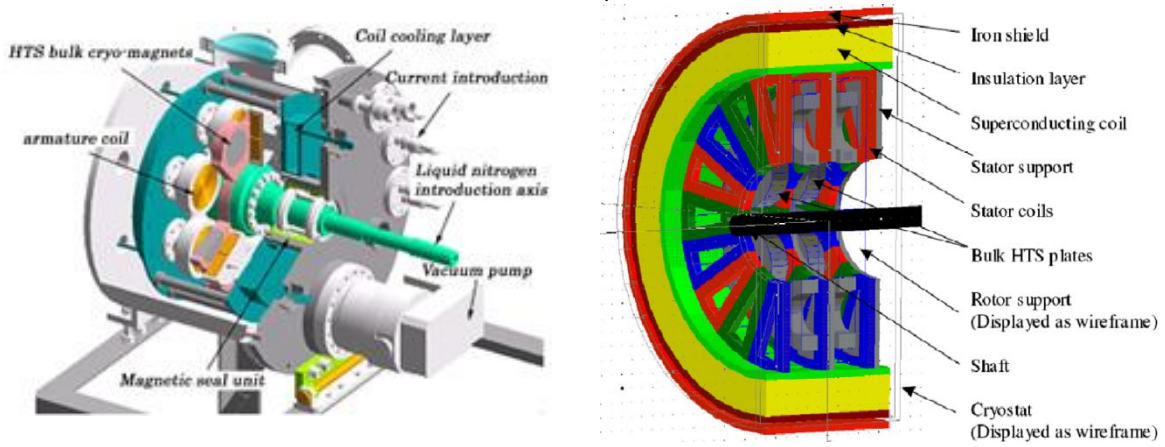

Figure 1.40 Examples of superconducting motors that use magnetized (RE)BCO bulks. a) An axial gap-type synchronous motor with bulks magnetized using pulsed field magnetization [85]. b) Design for an axial flux distribution synchronous motor with bulks magnetized using field cooling by an outer HTS coil [86].

One of the main applications currently being developed for bulk superconductors is superconducting motors and generators. The ability of bulks to act as powerful yet compact permanent magnets makes them attractive to use in motors and generators, as they can trap magnetic fields an order of magnitude higher than the best rare-earth permanent magnets. This higher field results in a higher power or torque density, allowing for powerful yet compact and lightweight designs [87]. In addition, the efficiency can be higher than conventional motors and generators due to lower joule heating resulting from less dependence on copper coils, and also the elimination of eddy current and hysteresis losses in ferromagnetic cores, which are not required [87]. The efficiency gains resulting from these factors can outweigh the power needed for cooling. Although a number of large scale projects exist for motors and generators using (RE)BCO coated conductor coils, magnetized bulks offer a more persistent and compact source of field.

Figure 1.40a shows a motor in which the copper stator coils double as pulse magnetization coils, whereas b) uses a large outer HTS coil to achieve field cooling. The need for HTS excitation coils when using field cooling adds significant cost to the design and so pulsed magnetization is generally cheaper, more compact and probably the most practical method of magnetization if the field that can be trapped in the bulks is maximised. For these reasons the modelling and experimental results on pulsed magnetization reported in this thesis are relevant to motor and generator applications, particularly the results for composite superconducting bulks reported in Chapter 5 which address the lack of thermal stability present in existing bulks when magnetized using PFM. The new structures reported in this chapter have significant potential to be used as trapped field magnets in motors and generators given the high trapped fields achieved experimentally.

2 New superconducting bulk – bulk bearing designs

A new design of magnetic bearing was invented and modelled as described in this chapter. The motivation behind the design was to address the fundamental force density limitation for existing superconducting bearings which use PMs, and represents a significant departure from all designs previously reported in the literature.

2.1 Magnetized superconducting bulks as a field source

As magnetic pressure and tension are proportional to the square of field components, a modest increase in field can give a large increase in levitation force. In applications such as flywheel energy storage, increases in the levitation force and stiffness would result in increased performance. There are four possible sources of field excitation available to provide the field experienced by a passive superconducting bulk which is field cooled in an SMB:

i. Permanent magnets, most commonly of the rare-earth kind.
ii. A solenoid coil made of a normal conductor such as copper.
iii. A solenoid coil made of superconducting wire or tape.
iv. A magnetized superconducting bulk with a trapped field.

The first source is the simplest and the only one to be used in commercial applications, but permanent magnets are limited in field strength. The most powerful rare earth PMs are limited to a remanent flux density of ≈ 1.4 T, which corresponds to a typical maximum surface flux density of ≈ 0.4 T [88]. This sets a minimum limit on the bearing surface area required to levitate a certain load. A coil made of normal wire has the disadvantages of requiring an electrical power supply and of dissipating heat continuously when in operation, the latter of which is unfavourable in proximity to a cooled superconductor. In contrast, a superconducting coil in persistent mode can achieve fields many times higher than those of permanent magnets without requiring continuous electrical power during operation. This new type of bearing is under investigation [89, 90] and may prove promising, however operation at liquid helium temperature for LTS coils is a disadvantage, as well as the wiring required to set up a persistent current in the coil. The fourth field source proposed in the above list, a superconducting magnetized bulk, has not previously been used for bearings and is the basis of the ideas in this section. Although this field source has similar disadvantages to a superconducting coil due to cooling requirements and the need for a magnetizing coil, it provides an alternative more compact source of high magnetic field.

A demand for increased levitation and restoring forces is partly driven by the need for a bearing to support a greater flywheel rotor weight. As the weight of a flywheel rotor is proportional to the energy it can store, and because the mass of a rotor is approximately proportional to the square of its radius, using more massive flywheels can significantly increase the energy stored without significantly increasing the size of the flywheel unit. The levitation force density for a cylindrical type bearing could be significantly increased by using magnetized superconducting bulks, which means that the bearing could remain compact for higher load applications.

Cylindrical field source bulks can be stacked along their common axis and magnetized along that axis but with alternating polarity, such that between two bulks the magnetic field is expelled radially outward in the gap, like the permanent magnet stacks used in existing cylindrical bearings. This configuration is illustrated in Figure 2.1, with high magnetic field gradients on the surface of the stator hollow bulk cylinder (SC1) resulting from a high trapped field in the magnetised bulks of the rotor (SC2). The problem of having to magnetize two bulks with opposing fields in situ, whilst already stacked next to each other, can be solved by using a coil on the stator which produces an opposing field. Such a coil would be split into two parts, each wound with opposite sense. This allows a pair of bulks to be magnetized simultaneously with opposite polarity. Simultaneous magnetization overcomes demagnetizing effects between the bulks that would result if they were magnetized individually, one after the other. These pairs would then be the basic field source unit of the rotor and would each produce the high magnetic field gradients required for high levitation force. A

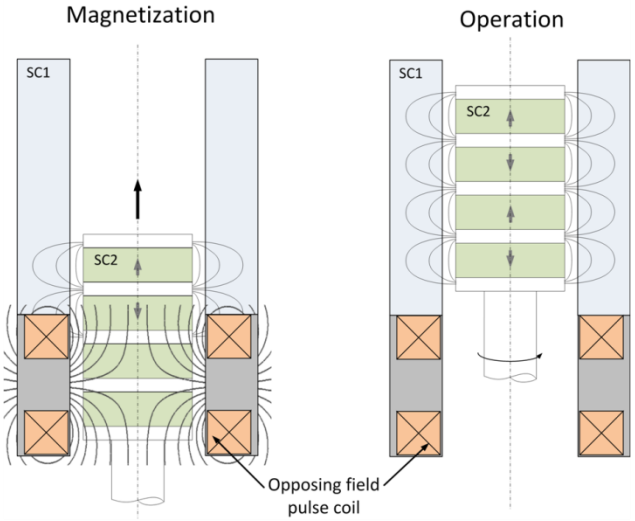

Figure 2.1: Schematic illustrating a possible configuration of a superconducting magnetic bearing in which the field source on the rotor is made of cylindrical magnetized bulks of superconductor (SC2). The stator component is a hollow cylinder of superconductor (SC1). The rotor bulks are magnetized by displacing the whole rotor to allow alignment with a magnetizing coil on the stator. Opposing field magnetization is shown in which a bulk pair is simultaneously magnetized with opposite polarity by a coil split into two parts wound with opposite sense.

material with high permeability such as iron would not be as useful in guiding flux between the bulks at high fields, due to magnetic saturation, although it can still have a significant effect for trapped fields below 2 T as suggested by basic modelling using the COMSOL AC/DC module and the non-linear permeability relation for iron. A more flexible but complex design is shown in Figure 2.2, with pulse magnetization coils being built in to the rotor to allow one or more pairs to be pulsed simultaneously.

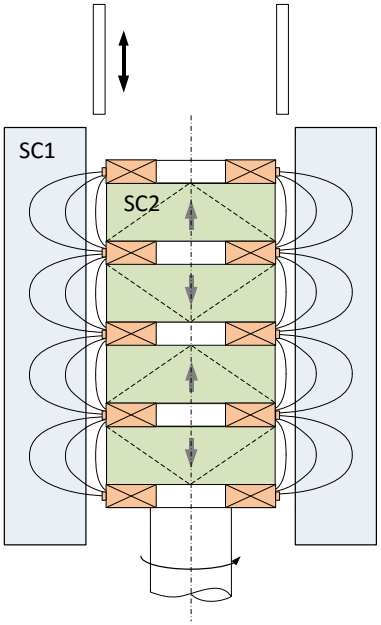

Figure 2.2: Illustration of a SMB design in which field source bulks are magnetized by coils mounted in the rotor. Current would be supplied to one or more coils by means of a retractable contact mounted on the stator. This design allows flexibility in magnetizing the bulks but places size demands on the coils.

2.2 Field cooling using difference in irreversibility field

In order to achieve field cooling of the stator superconductor in the field of magnetized rotor bulks, the T_c of the field source rotor bulks needs to be higher than that of the passive stator bulks if they are kept at the same temperature. However a more general requirement is that the irreversibility field lines need to be significantly different, as illustrated by Figure 2.3. The steep irreversibility line of YBCO, along with its other properties, makes it a suitable choice for the rotor bulks. The advantages of hollow cylindrical bulk MgB_2 for bearings, such as ease of manufacture and complete current paths (as described in Section 1.5.3), make it a good choice for the stator part of the bearing. The critical temperature and irreversibility line of MgB_2 also make it possible to magnetize the YBCO rotor bulks above 40 K with a high trapped field and then cool the whole system down below 40 K in the operating configuration so that field cooling of an MgB_2 hollow cylinder is achieved. A T_c of 40 K is ideal because it allows for the MPSC technique to be used, exploiting the remarkable increase in YBCO J_c below 70 K. Following magnetization at between 40 and 77 K, the bearing could then be cooled to an operating temperature of 20–25 K.

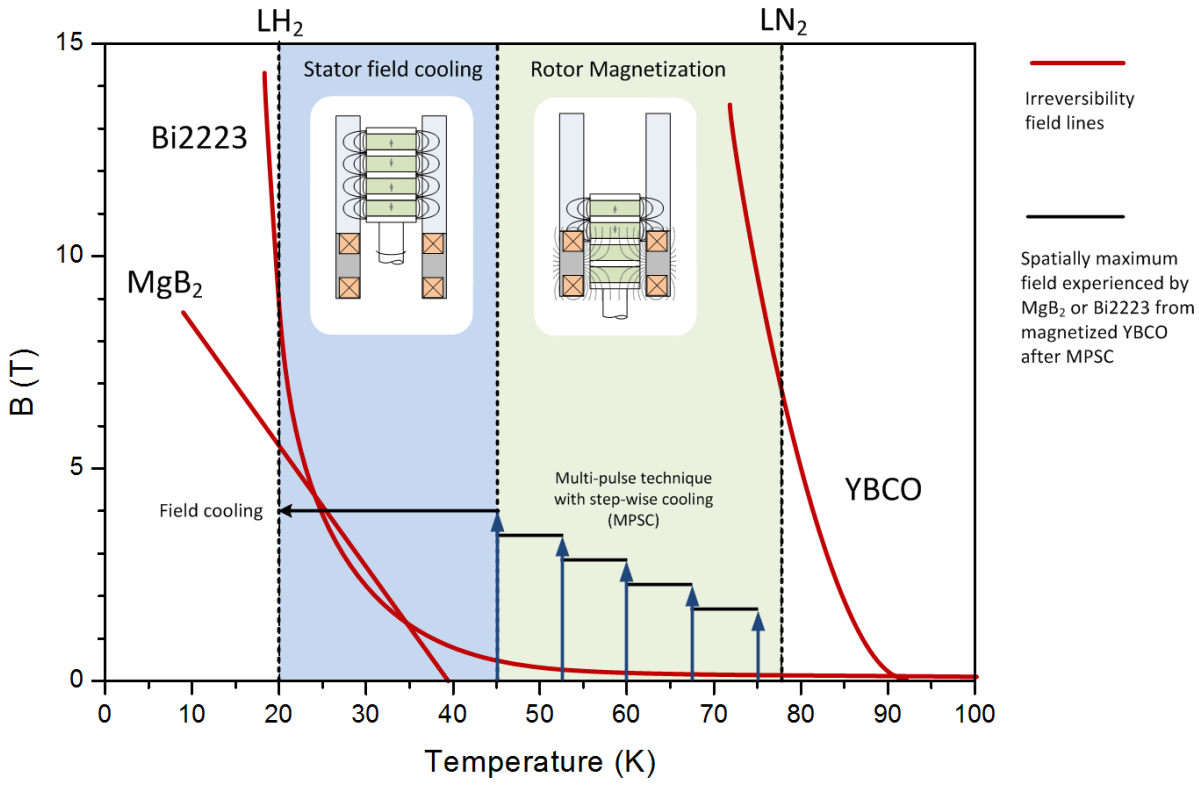

Figure 2.3: Irreversibility field lines shown in red for YBCO, MgB_2 and $Bi_2Sr_2Ca_2Cu_3O_{10+x}$ (Bi-2223) based on data from [91]. B_{irr} for MgB_2 is defined as the field for which there is loss for macroscopic currents in a polycrystalline bulk. The Bi-2223 curve is shown to illustrate that a difference in T_c is not strictly necessary, but rather a large difference in B_{irr} or J_c.

2.3 FEM modelling of pulsed field magnetization

2.3.1 The H formulation for modelling the critical state using COMSOL

The critical state in superconductors can be modelled using FEM. Many different methods have been implemented, mostly in 2D, with the main three formulations being the $A - V$ formulation which solves for the magnetic vector potential [92-94], the $T - \Omega$ formulation based on the current vector potential [95], and the H-formulation which solves directly for the magnetic field components H_x and H_y, which indirectly gives the current density. Boundary conditions such as applied field are generally easier to impose in this formulation [96] and the formulation can also be used for 3D models [97]. All the critical state modelling presented in this thesis used the H-formulation in COMSOL. In this section the formulation was implemented using version 3.5a, as first reported by Z Hong et al. [98], who applied the method to the 2D case of a bulk magnetized in uniform and non-uniform fields and the case of current forced through a superconducting wire. No thermal physics was taken account of in [98] or the results presented in this Chapter, however it is considered in the modelling of pulsed magnetization reported in Chapter 5. A 2D axially-symmetric geometry was modelled, with the general space in which the field components are solved shown in Figure 2.4.

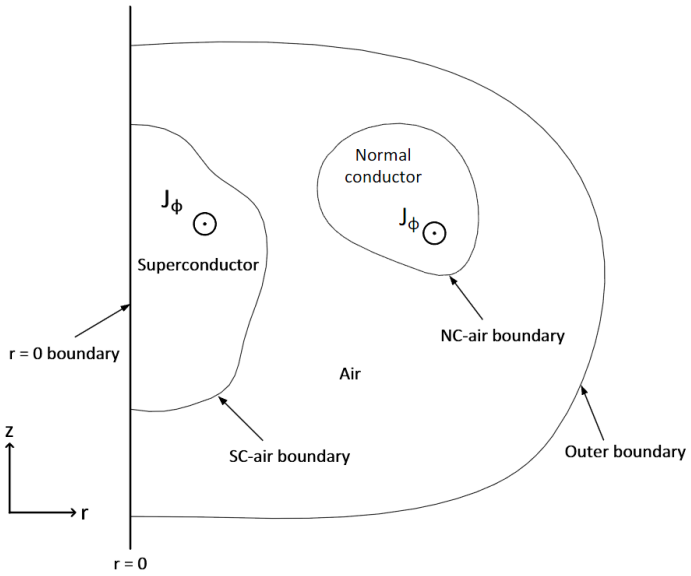

Figure 2.4: The space over which the magnetic field is modelled consisted of superconductor, air and normal conductor domains. The field lies in the plane whilst induced superconducting currents and forced normal conductor currents are perpendicular to the plane, flowing azimuthally.

The numerical scheme involves solving two PDEs using the general form PDE mode in COMSOL for the dependent variables H_r and H_z. Quadratic curl elements were used. The PDEs are derived as follows, starting from Faraday's law:

$$\nabla \times \underline{E} = -\mu_0 \mu_r \frac{\partial \underline{H}}{\partial t} \tag{2.1}$$

which has the following form for our axially symmetric geometry:

$$-\underline{\hat{r}} \frac{\partial E_\phi}{\partial z} + \underline{\hat{z}} \frac{1}{r} \frac{\partial (r E_\phi)}{\partial r} = -\mu_0 \mu_r \left(\underline{\hat{r}} \frac{\partial H_r}{\partial t} + \underline{\hat{z}} \frac{\partial H_z}{\partial t} \right) \tag{2.2}$$

For the superconductor, the electric field is given by an *E-J* power law in which the *E* field is proportional to a high power of the current density. This form is a good practical approximation for the resistance of a bulk superconductor [99]. The transition from the superconducting to the normal resistive state is not sudden, but has a non-zero width. This reflects the existence of thermally activated flux creep below J_c and also the small spatial inhomogeneity in J_c found in real bulks. The non-zero resistance below J_c takes account of flux creep. The *E-J* law used in the model was:

$$E_\phi = E_0 \left(\frac{J_\phi}{J_c(B)} \right)^n \tag{2.3}$$

where the power *n* used was 21, the same as in [98]. Such a high power is used to give physically accurate flux creep rates, but it causes problems for modelling. The highly non-linear PDEs that

result cause instability, and it is very common to have a divergent solution if parameters such as mesh element size and time steps are not carefully controlled. A detailed discussion of these parameters will be given in Chapter 5 when discussing the full magneto-thermal model. It also leads to significant computational time, although developments in computing power and FEM packages allow useful models to be solved in less than an hour. The *E-J* law used for the air and normal conductor domains was simply Ohm's law, $E_\phi = \rho J_\phi$. The most commonly used $J_c(B)$ relation is the Kim model,

$$J_c(B) = \frac{J_{c0}}{1 + {}^{B}\!/_{B_0}} \tag{2.4}$$

where $B = \mu_0 \mu_r \sqrt{H_r{}^2 + H_z{}^2}$. Although this does not take into account the peak effect often present for bulks, it's a good approximation for the general J_c behaviour. The critical current density is related to the field components using Ampere's law,

$$J_\phi = \frac{\partial H_z}{\partial r} - \frac{\partial H_r}{\partial z} \tag{2.5}$$

Combining Equations (2.3)-(2.5) in (2.2) to eliminate J_z and E_z, the final two PDEs expressed in terms of the field components are given by:

$$\begin{bmatrix} \dfrac{\partial\left(rE_0 \left(\dfrac{\frac{\partial H_z}{\partial r} - \frac{\partial H_r}{\partial z}}{J_c(B)} \right)^n \right)}{\partial z} \\ \dfrac{-\partial\left(rE_0 \left(\dfrac{\frac{\partial H_z}{\partial r} - \frac{\partial H_r}{\partial z}}{J_c(B)} \right)^n \right)}{\partial r} \end{bmatrix} = -\mu_0 \mu_r r \begin{bmatrix} \dfrac{\partial H_r}{\partial t} \\ \dfrac{\partial H_z}{\partial t} \end{bmatrix} \tag{2.6}$$

The boundary conditions used for the four boundaries are as follows. A Dirichlet boundary condition was used for the outer boundary and r = 0 boundary. When applying a uniform external field to magnetize the superconducting region, the outer boundary condition was:

$$\begin{aligned} H_r &= 0 \\ H_z &= H_0 \sin \omega t \end{aligned} \tag{2.7}$$

Half a cycle of a sine wave is a reasonable approximation for the pulsed field used in pulsed field magnetization. When magnetizing the superconductor using the field from current flowing in a normal conductor, the outer boundary condition was magnetic insulation,

$$\underline{n}.\begin{pmatrix} H_r \\ H_z \end{pmatrix} = 0 \tag{2.8}$$

The r = 0 boundary condition was simply H_r = 0, as no radial field components are allowed by symmetry. The internal SC-air and NC-air boundary conditions were continuity of the electric and magnetic field components parallel to the boundary surface:

$$\begin{aligned} &\underline{n}\times(\underline{H}_1 - \underline{H}_2) = 0 \\ &\underline{n}\times(\underline{E}_1 - \underline{E}_2) = 0 \Rightarrow E_{\phi 1} - E_{\phi 2} = 0 \end{aligned} \tag{2.9}$$

The PDE mode used in COMSOL requires equations to be entered in the general form:

$$\nabla.\Gamma + d_a \frac{\partial u}{\partial t} = F \tag{2.10}$$

where the various coefficients can be vectors or matrices of vectors. For the present case, the coefficients for both domains shown below give Equation (2.6) when substituted into (2.10).

$$\Gamma = \begin{pmatrix} \begin{pmatrix} 0 \\ rE_\phi \end{pmatrix} \\ \begin{pmatrix} rE_\phi \\ 0 \end{pmatrix} \end{pmatrix}, \qquad d_a = \mu_0 \begin{pmatrix} \begin{pmatrix} r \\ 0 \end{pmatrix} \\ \begin{pmatrix} 0 \\ r \end{pmatrix} \end{pmatrix}, \qquad u = \begin{pmatrix} H_r \\ H_z \end{pmatrix} \tag{2.11}$$

In order to solve the above equations using the FEM method, careful attention had to be paid to the mesh used and maximum time steps allowed to ensure stability. Refining the mesh increases stability but significantly increases the solution time. Smaller time steps increase solution time but lead to a more significant increase in stability. Solving for an axially symmetric 14 mm diameter bulk using the mesh shown in Figure 2.5 below took less than 15 min on a dual core 2.67 GHz PC. A mapped mesh was used for the superconducting domain as opposed to a triangular mesh. Although it gives similar stability to a triangular mesh, a mapped mesh is much better defined (in terms of the number, size and location of elements) and it is very easy to control the number of elements, which is critical in finding the optimum number, which is stable enough to solve but does not take an excessive amount of time.

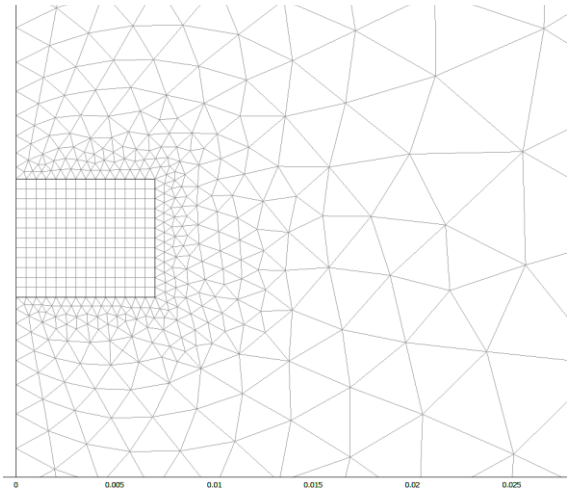

Figure 2.5: The mesh used to model a 14 x 6 mm superconducting bulk in axial symmetry exposed to a uniform external field pulse. The total mesh consisted of 1204 elements.

2.3.2 MPSC magnetization of single 25 mm bulk

The MPSC technique for magnetizing bulks was modelled using the H-formulation in COMSOL Multiphysics 3.5a. The model requires $J_c(B,T)$ data from a field of zero to over 10 T and for a temperature range of 50 – 77 K. The $J_c(B,T)$ relations used for the bulk YBCO were based on data for bulk YBCO shown in Figure 1.17b from [6]. The $J_c(B,T)$ curves were extrapolated from these data for very high fields and temperatures lower than 59 K using a polynomial fit.

No heating or viscous forces were considered in the magnetization model, so the resulting trapped fields indicate an upper limit for the given applied fields; however the technique of IMRA would be used in practice to compensate for some of the flux lost from the periphery of a bulk due to excessive heating during a pulse.

In the simplest model, a 25 mm diameter, 9 mm thick YBCO bulk was magnetized using the MPSC method by applying four uniform field pulses at 75 K, 68 K, 59 K and 50 K. Each 1 ms pulse was half a period of a sinusoidal field with an amplitude of 3.5 T. The $J_c(B)$ data from [6] were used directly for the $J_c(B)$ fits, but the 50 K relation was an extrapolation of the higher temperature curves. The temperatures were chosen such that, for each temperature drop, J_c approximately doubles. As Figure 2.6a shows, this allows each 3.5 T pulse to induce layers of spatially alternating current approaching the bulk edge. The development of the radial current density profile is shown in Figure 2.6b and is linked to the magnetization loops shown in Figure 2.7a, with the magnitude of residual magnetization shown to increase after the second, third and fourth pulse, demonstrating the benefit of MPSC. Magnetization was calculated using the volume integral of $\boldsymbol{r} \times \boldsymbol{J}$. The final magnetization is 77% higher than after the initial pulse, with the significant increase being linked more to a broadening of the trapped field profile as shown in Figure 2.7b, rather than an increase in

peak trapped field. The changes in current density with radius would in reality not be so sharp given heat and flux creep effects after magnetization.

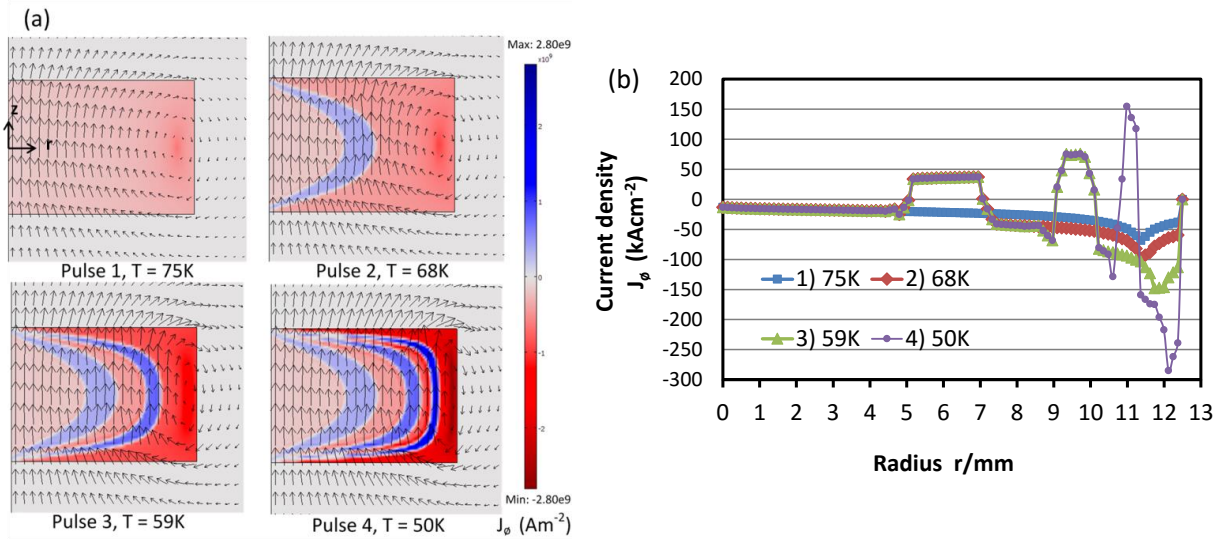

Figure 2.6: a) Current density distributions and magnetic field after each MPSC pulse of amplitude 3.5 T applied to a 25 mm diameter YBCO bulk. b) Current density as a function of radius for a plane cut through the middle of the bulk (z = 0) after each pulse.

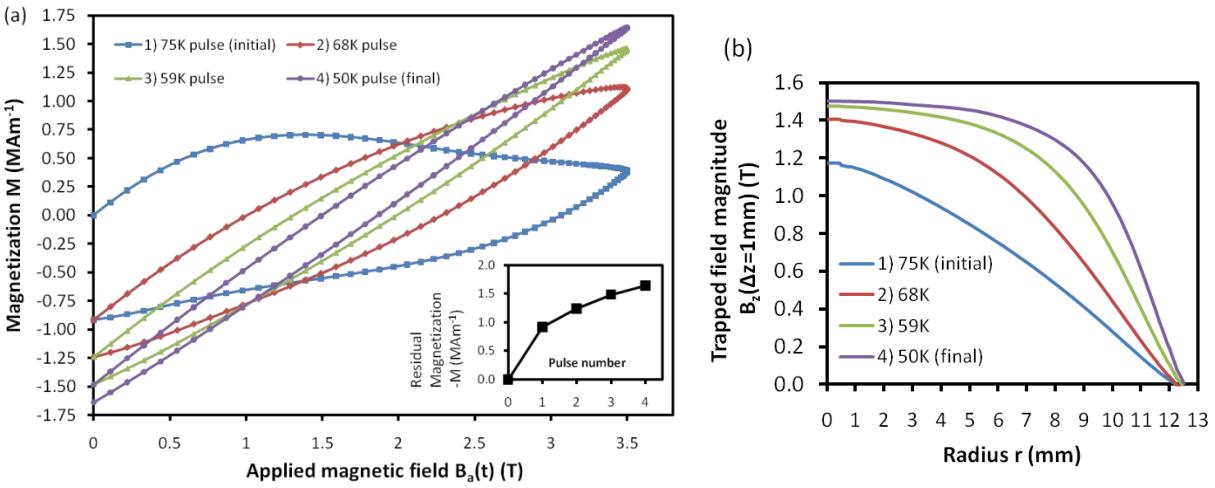

Figure 2.7: a) Magnetization loops for a 25 mm bulk during each MPSC pulse applied with (inset) residual magnetization after each pulse. b) z component of trapped field 1 mm above top bulk surface after each MPSC pulse.

In practice, MPSC would be used at temperatures lower than selected based on simple $J_c(T)$ data, to compensate for the temperature rise, and the resulting decrease in $J_c(B)$, during a pulse. This would mean that the final magnetization in the model would be achieved by the same pulse sequence but with, say, a 10 K temperature shift (65 K, 58 K, 49 K, 40 K), as a 10 K temperature increase is typical for pulse magnetization [100]. This temperature rise resulting from heat production is a problem for PFM, but it has the beneficial effect of suppressing flux creep shortly after a pulse [75].

2.3.3 Opposing field magnetization of 25 mm bulk pair

In order to show the feasibility of magnetizing a pair of YBCO bulks simultaneously to create an opposing field, MPSC magnetization was modelled for a pair of 25 mm diameter bulks exposed to the field of an opposing field coil. Figure 2.8 shows the current distributions in each bulk resulting from each pulse, using the same pulse temperatures as for the single 25 mm bulk in a uniform field. It is not as simple to describe the applied field from an opposing field coil as it is for a conventional coil. The reference point E was chosen on the edge of one of the bulks, as this point experiences the greatest magnitude of applied field from the coil. The peak applied field at this point, B_E, required for significant flux penetration is typically much higher than the uniform applied field needed to saturate a single bulk. In fact it is very difficult to saturate the bulk pair with the initial pulse due to the very low field near the centre of the coil, but this does not significantly limit the trapped fields possible. A pulse sequence of B_E = 7 T, 9.5 T, 15 T, 15 T was used for MPSC. Lower fields were used for the initial pulses to keep the $J_c(B)$ values across the whole bulk non-zero according to the $J_c(B,T)$ data used.

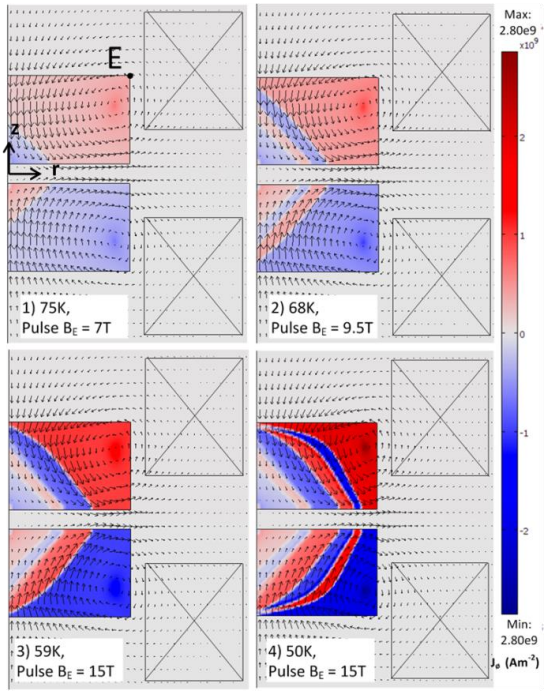

Figure 2.8: Current density distributions and magnetic field after MPSC pulses of various amplitudes applied to a pair of 25 mm diameter YBCO bulks separated by a gap of 2 mm. An opposing field coil has been used.

The magnetization after each pulse is given in Figure 2.9a for one of the bulks. The increase with pulse number is approximately linear. An appropriate measure of surface trapped field for this configuration is $B_r(z)$ at r = 13.5 mm (Δr = 1 mm), the radial field component along a line 1 mm away from the bulk cylindrical surface. The development of this field is shown in Figure 2.9b, with a high final gradient of 2.5 T over 8 mm.

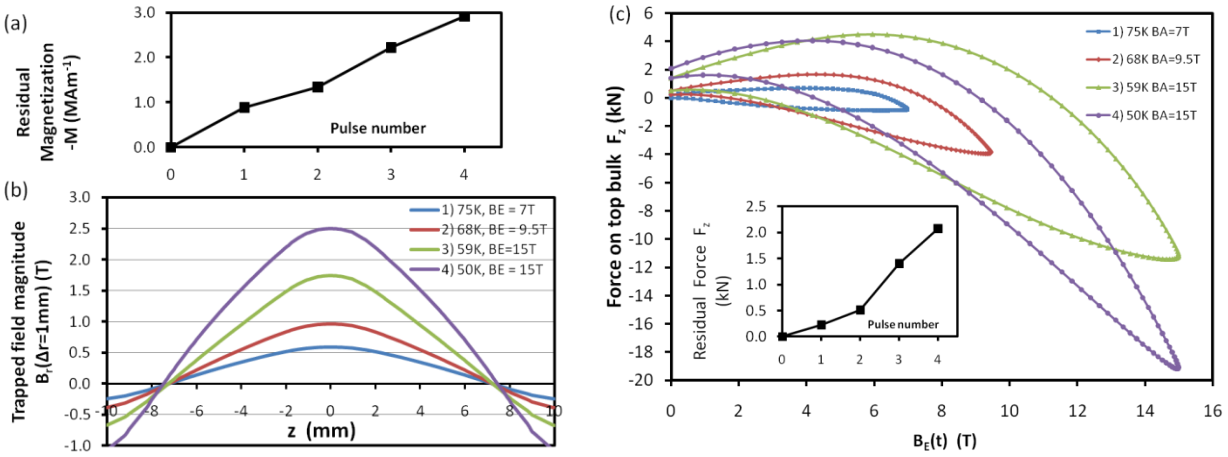

Figure 2.9: a) Residual magnetization for the top bulk after each MPSC pulse applied to a 25 mm bulk pair. b) Variation of radial component of trapped field 1 mm away from the bulk pair radius after each MPSC pulse. c) Axial force on the top bulk during each pulse, with residual force after each pulse also shown (inset).

In order to use a pair of bulks magnetized with opposite polarity, sufficient reinforcement is required to counter the axial repulsive forces present on each bulk after magnetization, in addition to reinforcement against internal radial pressure. The force on the top bulk during magnetization, calculated using the Lorentz force method, is shown in Figure 2.9c, with the residual repulsive force increasing with each pulse to a final value of 2.07 kN. As well as residual repulsive forces, the curves also show that the bulks experience a large transient attractive force due to the non-uniform applied field.

The exact rate of flux creep resulting from the highly non-uniform trapped field of a bulk pair is not clear, but the fact that the final state of trapped field was achievable using the critical state model means that the flux creep should not be fundamentally different from that for a single magnetized bulk. As a result, a pair of bulks magnetized in this way would not simply demagnetize each other (similarly a pair of permanent magnets would not simply demagnetize after being magnetized in the same opposing field).

2.3.4 Opposing field magnetization of 50 mm bulk pair

The size of the rotor part of the bearing is limited by the maximum size of (RE)BCO bulks that can be grown and easily magnetized using a pulsed field coil. However, for a single bulk pair, a large diameter is desired to increase rotor-stator surface area. Therefore the dimensions of the second bulk pair modelled were 50 mm diameter and 15 mm thick separated by a 4 mm gap, which can be considered an ideal size for the bearing design given that such large bulks are produced but not too large to magnetize.

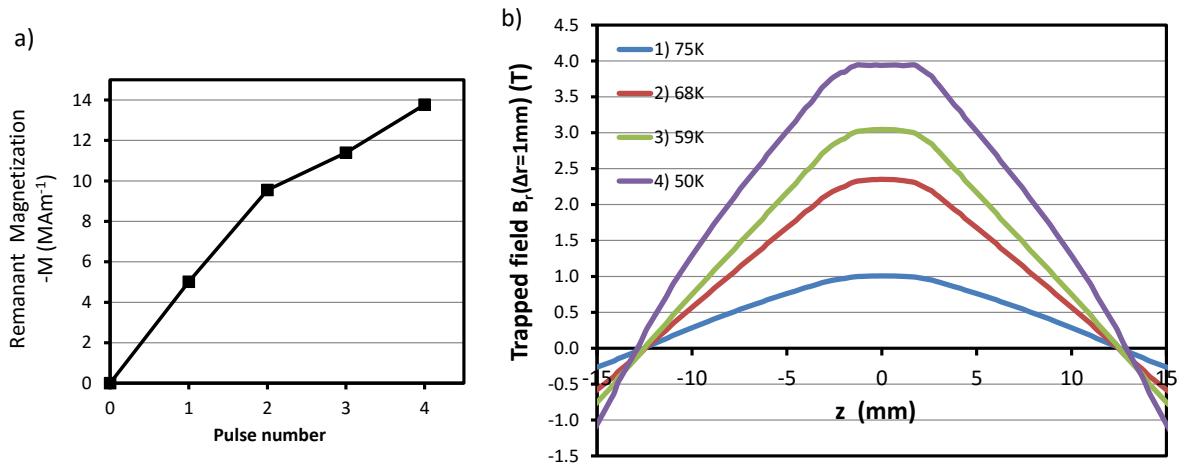

Figure 2.10 a) Residual magnetization for 50 mm bulk pair after 4 pulse MPSC. b) Corresponding radial components of trapped magnetic field 1 mm outside the 50 mm bulk pair surface after each MPSC pulse. All pulse amplitudes B_E = 14.5 T.

An opposing field coil similar to that used for the 25 mm bulk pair was used for magnetization but, unlike the 25 mm case, the same applied field was used for all pulses applied to the 50 mm bulk pair. A peak applied field of B_E = 14.5 T was applied at 75 K, 68 K, 59 K and 50 K. Although a very high value of B_E is required for each pulse, it does not appear so unfeasible when considering that the coil has a significantly lower inductance than if current was flowing the same way in both parts of the coil, as in a conventional coil. The inductance of the opposing field coil in the model is 10.25 mH. Assuming the coil were connected to the same capacitor bank system used for the PFM experiments reported later (see Chapter 3), and was wound with the same wire as the pulse find coil used in the experiments, the maximum pulsed field for B_E would be 10.3 T with a rise time of 14 ms. In order to achieve 14.5 T with the experimental pulse system, the coil could be made with a smaller outer diameter to lower inductance, which would also lead to a smaller rise time, or a higher energy capacitor bank would be needed. LN_2 cooling of the coil should be sufficient for the expected pulsed currents of up to 2 – 3 kA.

The high B_E of 14.5 T leads to fields larger than B_{irr} at the peak of the pulse for the edges of the bulk. Temporarily exceeding B_{irr} at the peak of the pulse leads to a field cooling type effect due to the destruction of current induced during the pulse rise. The increase in magnetization after each pulse is shown in Figure 2.10a, with the corresponding increase in the field gradient shown in Figure 2.10b. The results give a qualitative picture of the MPSC process and also an upper limit for the fields that can be trapped, however they are not meant to be an accurate prediction of experimental trapped fields.

2.4 FEM modelling of bulk – bulk levitation force

The modelling of pulsed magnetization of bulk pairs shows that that they can be magnetized with opposing fields, and the approximate predicted magnetized states can be used in another levitation force model to predict the best forces that could be expected for a bearing based on magnetized 25 and 50 mm diameter bulks.

2.4.1 Perfectly trapped flux model

The perfectly trapped flux model was introduced in Section 1.6.1. As its name suggests, this model preserves the flux density vector field inside a bulk superconductor when it is displaced relative to a field source. In reality, when a superconductor is exposed to changes in external field such as that caused by the movement of a PM, shielding currents are induced a non-zero depth below the surface of the superconductor. In the extreme limit of very small changes in field or J_c increasing to infinity, the currents are induced as surface currents ($\underline{J}_s = \underline{n} \times (\underline{H}_1 - \underline{H}_2)$, where $\underline{n}$ is the normal to the surface and $\underline{H}_1$ and $\underline{H}_2$ are the inner and outer field vectors) for the bulk boundary, without any depth. In this case, perfect shielding of the interior field state is achieved whatever the change in external field. This case is the basis of the perfectly trapped flux model and is an excellent approximation for a PM – SC levitation force system. This approximation is useful in providing a theoretical maximum levitation force, but it cannot reproduce hysteresis and so its high accuracy predictions are limited to small displacements. The results reported in Chapter 3 will show that the approximation breaks down for large field changes as in the case of a magnetized bulk – passive bulk system.

The computational method used to implement the perfectly trapped flux model, as developed by R Palka et al. [6], is shown in Figure 2.11. Unlike the method of images model [101], the PTF model does not assume symmetry planes and can therefore be used for asymmetric geometries. For the results reported in this thesis, the model was adapted to be used in the AC/DC module of COMSOL. Instead of modelling three different vector potential distributions and adding them, the PTF model was achieved by simply using a single boundary condition. The boundary condition for the superconductor boundaries was set to the vector potential of the field cooling state, such as in Figure 2.11a. During subsequent movement of the field source, this boundary condition preserved the internal field and satisfied the required condition that there can be no induced currents in the domains at all. Although simpler, this method is less reliable, and so checks were always made to ensure that the field inside the superconductor really had been unchanged.

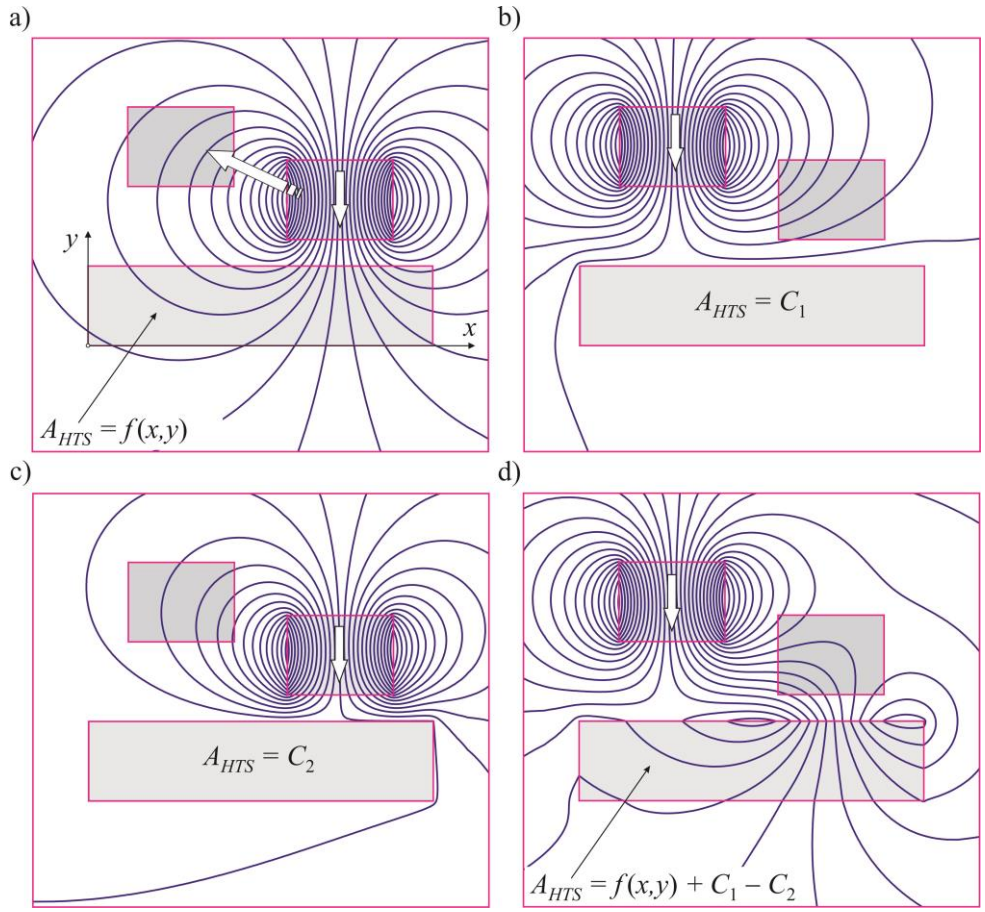

Figure 2.11: Illustration of how the perfectly trapped flux model is implemented by summing vector potential distributions. $f(x,y)$, C_1 and C_2 apply to the whole model space. Drawing created by Ryszard Palka of the Department of Power Systems and Electrical Drives, West Pomeranian University of Technology, Poland.

For the displaced states, such as that shown in Figure 2.11c, the restoring force was calculated using the Maxwell surface stress tensor, which leads to Equation (1.20). The final force vector resulting from integration around the superconductor boundary gives a reliable result for axisymmetric cases, however, in COMSOL, the method is often unreliable for general 2D cases, as errors can be quite large even when using very fine meshes. This does not affect the results here as all cases modelled were axisymmetric.

It should be noted that this behaviour is distinct from a PM exposed to external flux density, which results in an internal field that is the sum of the external field and the PM remanent magnetization.

A fundamental difference between previous modelling using the PTF model and the modelling presented in this thesis is that there are two superconducting bulks moving relative to each other and both require shielding, which is not a case that has previously been reported. This means that the field inside the field source superconducting bulk is also perfectly preserved, unlike in the case of a PM field source. A comparison of the levitation force resulting from this enhanced shielding to the force expected if there were no shielding of the field source is presented in Section 2.4.3.

A full critical state model for levitation force which simulates induced current density inside all superconducting domains has not yet been developed for bulk – bulk levitation, although it is possible to use this for PM – SC bulk systems [51]. This type of model would give more realistic hysteretic force behaviour. Although attempts were made, a full critical state model for two bulks moving relative to each other was very difficult to achieve using the H formulation in COMSOL. Even if it were possible to solve such a model, it is likely to be very computationally demanding. One of the benefits of using the PTF model is the very fast solution times involved.

2.4.2 Four 25 mm diameter magnetized bulks

The perfectly trapped flux model was used to model levitation force for a magnetized YBCO – bulk MgB_2 bearing. After magnetization, the flux inside the YBCO bulks remains perfectly unaltered, in order to approximate the effects of shielding currents. In this way the maximum possible force between the field excitation system and the passive bulk (MgB_2) for a given rotor magnetization can be obtained. Four fully saturated YBCO pellets (25 mm diameter, 9 mm thick) are placed into the MgB_2 cylinder of diameter 27 mm (Figure 2.12a). The bearing has then been cooled to an operating temperature of 20 – 30 K. As an approximation, a uniform current density was used for the bulks (533 A mm^{-2}), which gives the same overall magnetization per bulk as that which resulted from the previous MPSC modelling of a bulk pair. A comparison has been made to the levitation force resulting from permanent magnets of the same dimensions (Figure 2.13). A more conservative estimate for the levitation force possible in the new bearing design is also given using a uniform current density of 300 A mm^{-2}. The movement of the YBCO excitation system leads to the axial forces in the superconducting magnetic bearing. Figure 2.12a shows field plots for the initial position of the YBCO bulks and for four other positions of moving YBCO bulks (the magnetic field within the MgB_2 cylinder remains unaltered). The force dependence on displacement is shown in Figure 2.12b for all three field source configurations. The maximum force arises for a displacement of 6 mm, below which the force stiffness is positive.

It is clear from Figure 2.12b that the high currents in the YBCO resulting from MPSC, as modelled earlier, give a significantly higher force than the permanent magnet equivalent. However, with a lower current density (300 A/mm^2), the force is similar and a larger bulk size is required for an improvement [6].

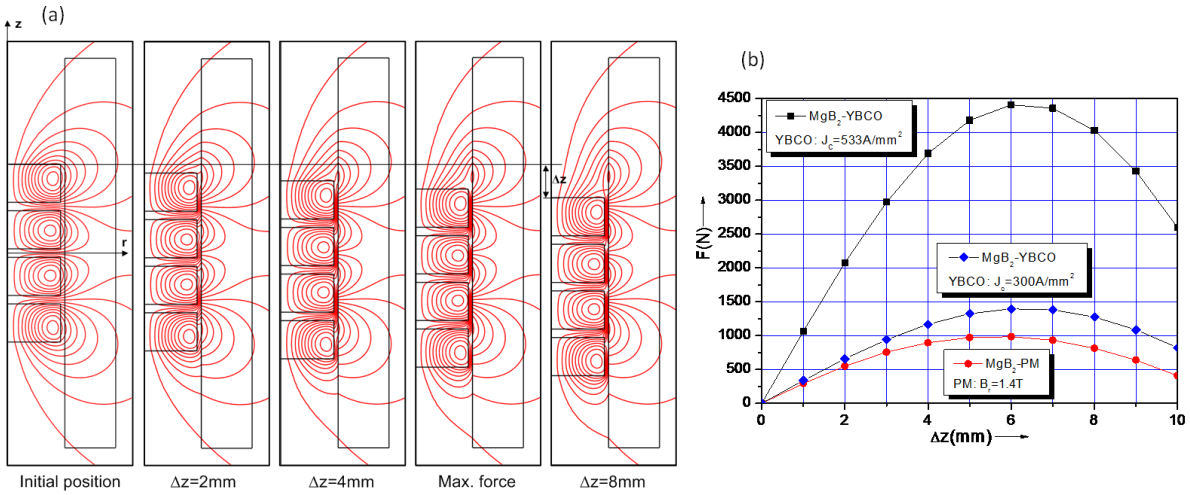

Figure 2.12: a) Field plots for different positions of a moving stack of magnetized YBCO bulks inside a field cooled MgB_2 hollow cylinder. b) Axial force for displacement of the bearing rotor made of magnetized YBCO and PMs of 1.4 T remanence. The gap between rotor and stator is 1 mm.

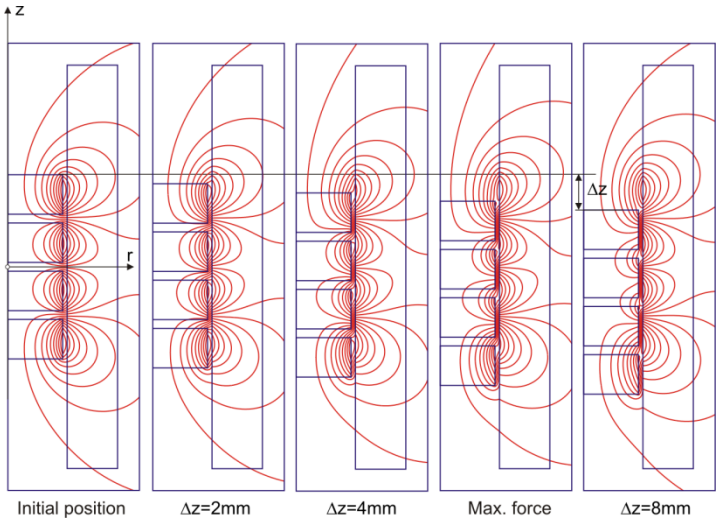

Figure 2.13: Field plots for different positions of a moving stack of permanent magnets inside a field cooled MgB_2 hollow cylinder. The geometry is the same as for the bulk YBCO stack.

2.4.3 Double 50 mm diameter magnetized bulk – 1 tonne bearing

Significantly higher forces can be achieved for 50 mm diameter, 15 mm thick bulk pairs. A uniform current density was used (409 A mm^{-2}), which gives the same magnetization as the state achieved by the MPSC modelling. Before reporting the full results, it is worth considering to what extent the shielding of the magnetized YBCO bulks adds to the levitation force, compared to the case without shielding, for which the bulks behave like coils. This comparison is shown in Figure 2.14. It is clear that the shielding of the YBCO gives rise to much higher distortion and gradients of magnetic field in the gap between them and the MgB_2 bulk hollow cylinder. As expected this enhances the levitation force, by a factor of 2.2 for the peak force occurring at 6 mm displacement. Although the

high flux densities caused on the surface of the MgB_2 bulk when there is YBCO shielding would inevitably cause flux penetration, it is the correct approximation to start from. The preservation of the flux inside the YBCO is an excellent approximation given the large increase in J_c when cooling by ≈ 20 K from ≈ 40 K (the final magnetization temperature).

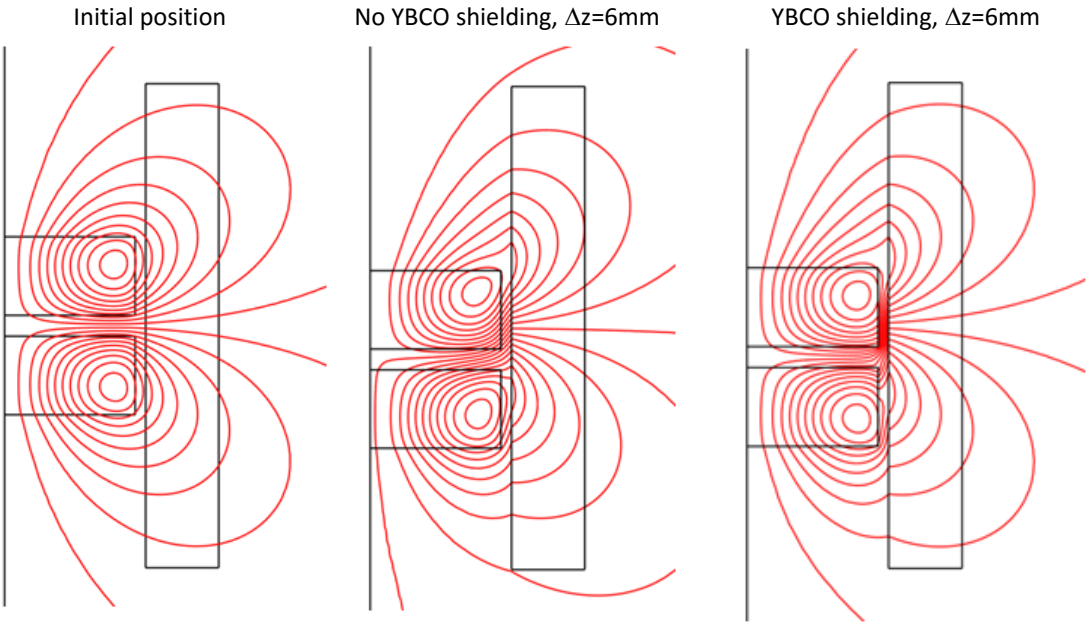

Figure 2.14: Field distortion for an opposingly magnetized bulk pair inside a superconducting tube. Field distortion is much higher when the PTF model is applied to the magnetized bulks as well as the outer tube. The peak levitation force for 6 mm displacement is 4.87 kN without YBCO shielding and 10.80 kN with shielding.

The full force behaviour with YBCO shielding is shown in Figure 2.15. The restoring force reaches a maximum of 16,520 N for the displacement Δz = 13 mm. It is therefore sufficient to use one such YBCO bulk pair to achieve an ideal 1 tonne bearing. If the current density was lower, such as 300 A mm^{-2}, two or three bulk pairs would be needed. The results show that force densities for the new bearing design have the potential to be as high as 168 N cm^{-2} with sufficient stiffness, a density significantly higher than that achievable using permanent magnets. This value assumes a 10,800 N load at 6 mm displacement divided by the outer cylindrical surface area of the field source unit.

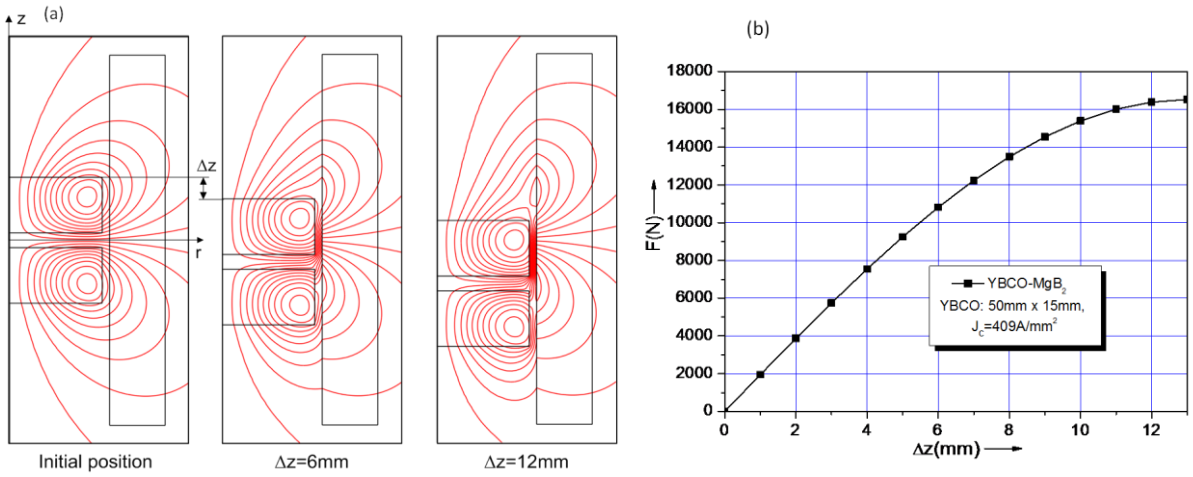

Figure 2.15: a) Field plots for different positions of moving HTS bulks 50 mm in diameter. b) Axial force for displacement of the bearing rotor made of a pair of 50 mm diameter YBCO bulks. Gap between rotor and stator is 2 mm.

In summary, a magnetic bearing design composed of magnetized bulk YBCO and MgB_2 has been proposed. The difference in T_c for YBCO and MgB_2 make field cooling of an MgB_2 hollow cylinder in the field of magnetized YBCO possible. The MPSC process has been modelled for the magnetization of pairs of 25 mm and 50 mm diameter YBCO cylindrical bulks, which form the basic field source units of the new bearing design. A temperature range of 40 – 77 K allows flexibility in choosing the temperatures for the MPSC pulses to suit the $J_c(B,T)$ properties of the bulks. Modelling of a pair of these bulks exposed to an opposing field coil has demonstrated that high magnetic field gradients can be created and optimised using the MPSC process. Using the perfectly trapped flux model to model levitation force shows that a bulk pair has the potential to achieve force densities higher than 100 N cm^{-2}.

2.4.4 Uniform current density for an unsaturated bulk

The previous modelling assumed a uniform current density throughout the bulk for simplicity. This current density was chosen to give the same magnetization as that resulting from the MPSC modelling, which actually led to higher currents induced at the outer edges of the bulk than in the centre. It is interesting to know whether a higher current density near the periphery of a bulk actually gives the same force behaviour as a lower current density throughout the whole bulk. To find out, a model with a uniform current density confined to a region between the outer surface and a depth *d* from the surface, as shown in Figure 2.16a, was created. This is perhaps a better approximation for the trapped fields resulting from MPSC where high current densities in the bulk periphery dominate. The two current densities modelled, which acted over different depths, were chosen to given the same magnetization (for a single bulk), as given by the following equation:

$$M = \frac{2J_{\phi}R}{3}\left(1-\left(\frac{R-d}{R}\right)^{3}\right) \tag{2.12}$$

derived from Equation (1.14), where R is the radius of the bulk and J_{ϕ}, the current density. The resulting levitation force curves, as shown in Figure 2.16b, show that higher current density at the edges of the bulk should in theory lead to a higher levitation force. This result shows that the MPSC procedure using low temperatures (where full field penetration is not possible) is not only suitable for the bulk – bulk bearing design, but it can also enhance the levitation force.

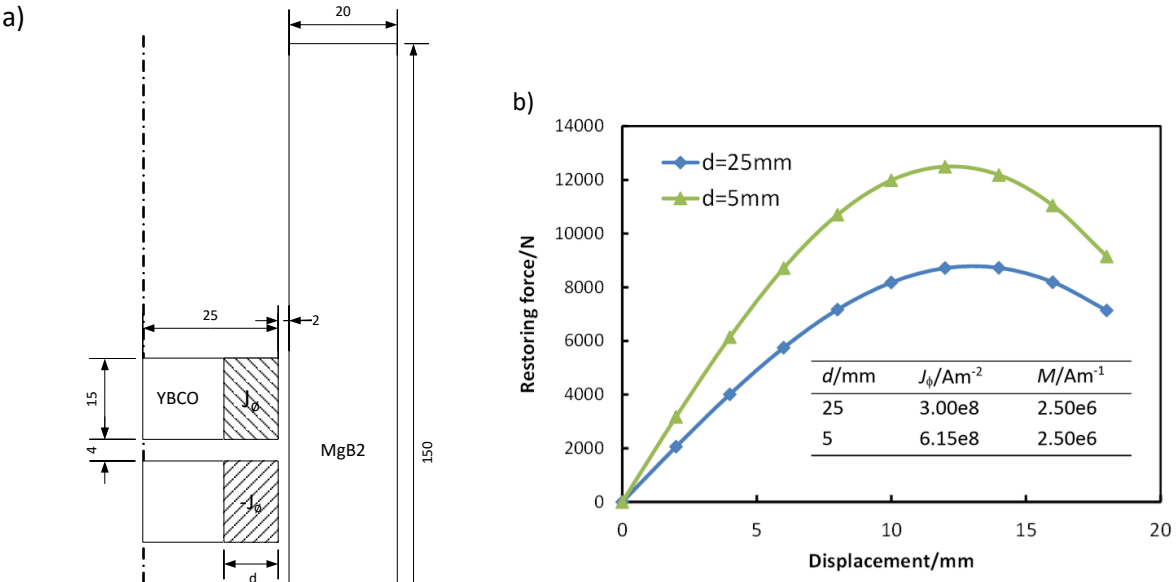

Figure 2.16: a) The geometry of the opposing magnetized bulk pair with variable current density depth. b) Levitation force for the displacement of the bulk pair after field cooling of the MgB_2 tube for two different depths of current density, both of which result in the same magnetization.

2.5 Permanent magnet enhancement of bulk – bulk force

The section considers an extension to the superconducting bulk – bulk bearing designs already proposed. Although the original design concept for a bulk – bulk magnetic bearing was to replace the PMs as they do not provide high enough field, PMs added to a bulk – bulk design can still provide a surprisingly strong enhancement to the levitation force, as well as providing additional safety through repulsive zero field cooled forces which are generally higher than forces resulting from field cooling. The concepts discussed are related to bulk – PM bearing concepts previously reviewed by J Hull [64]. These are repulsive force augmentation [102] and trapped field augmentation [103].

2.5.1 Altering the field trapped in MgB_2

For simplicity, only a single magnetized bulk has been considered for the additional PM arrangements modelled. Figure 2.17 shows the various additional PM ring configurations that have been considered to enhance the levitation force. A uniform current density giving a 2.5 T trapped field was modelled for the YBCO, giving a similar trapped flux to the experimentally magnetized bulk reported later in Chapter 4, and the PMs had a remanent flux density of 1.2 T to match real rare-earth magnets. The interaction of these PMs only with the magnetized YBCO is relatively intuitive, but there is another contribution that the PMs make to the force. The field trapped in the MgB_2 originating from the PM also interacts with the YBCO bulk during its displacement in a more subtle and non-trivial way.

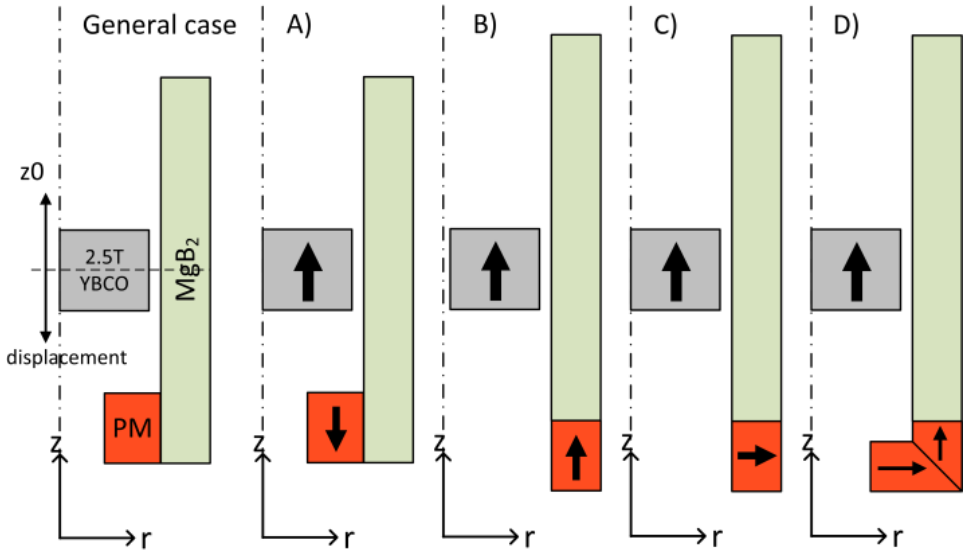

Figure 2.17: Various configurations of additional ring PMs used to enhance levitation force between magnetized YBCO and the MgB_2 tube.

By altering the trapped field pattern inside the MgB_2 as shown in Figure 2.18, the PMs give rise to their own unique force behaviour. The force can be significantly enhanced by increasing the field lower down in the MgB_2 to a similar magnitude to that trapped near the magnetized YBCO, and by rotating its direction towards horizontal. The modelling shows that this is possible even though the surface field of the PM is only ≈ 0.5 T.

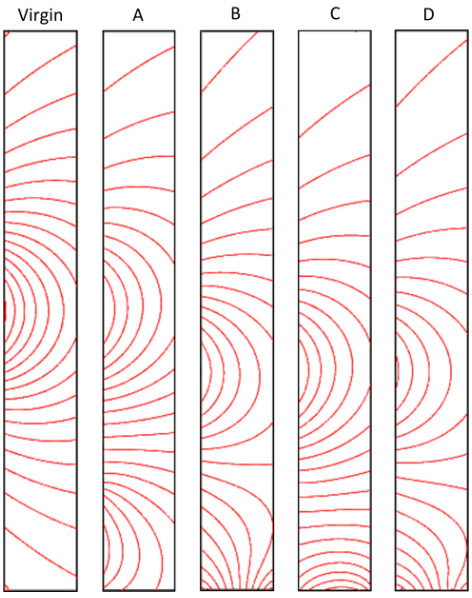

Figure 2.18: Field trapped in MgB_2 cylinder following field cooling for various configurations of additional permanent magnets, showing the distortion of field caused by the PMs.

2.5.2 Repulsive ring permanent magnet

Configuration A is the most obvious way in which an additional PM can boost the levitation force. Figure 2.19a shows the magnetic field lines resulting from displacement. Unlike the PM, the YBCO is a field source which has perfectly preserved internal flux. This is modelled the same way as for the MgB_2 but is a far more accurate approximation for YBCO, as the J_c of YBCO is much higher at 20 K than MgB_2 and the YBCO is therefore insensitive to changes in the surrounding field. The force curve corresponding to configuration A is shown in Figure 2.19b for various field cooling positions *z0*. *z0* = 0 corresponds to field cooling of the YBCO in the centre of the MgB_2 cylinder. In all cases the PM has enhanced the force to a value greater than that existing if there were no PM (shown in black). The enhancement in force is greatest when the YBCO is field cooled nearest to the PM (*z0*=0, green curve), for which the peak force is over 70% improved. This enhancement cannot be explained by the relatively small force existing between the YBCO and PM only (red curve), and must therefore be due to the altered field trapped in the MgB_2 as discussed earlier. It can also be seen that field cooling further away from the PM reduces the peak force and stiffness, but extends the zone of negative stiffness required for axial stability.

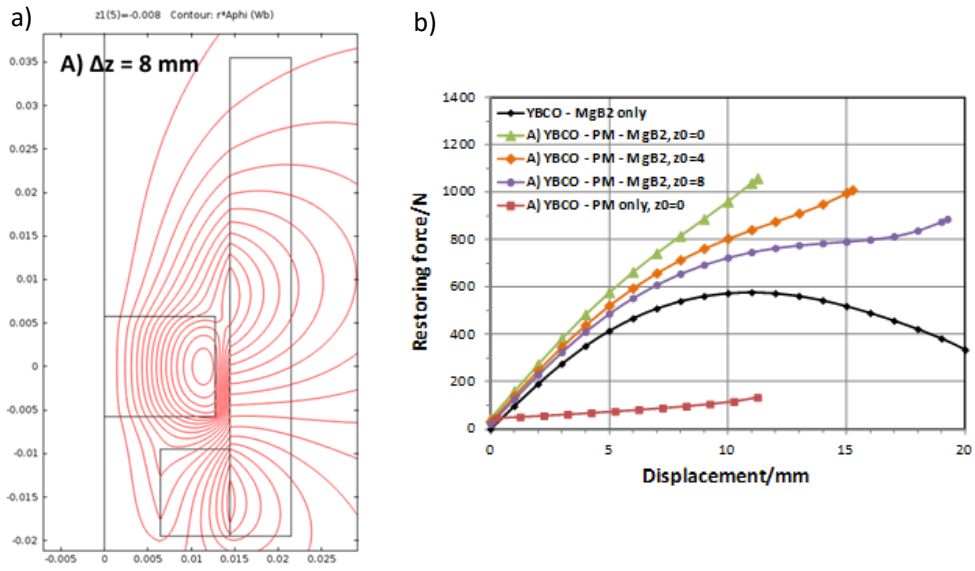

Figure 2.19: a) Magnetic field lines for additional PM configuration A after displacement, showing the distortion of magnetic field responsible for a restoring force acting on the magnetized YBCO. b) Levitation force for additional PM configuration A for different field cooling positions. Also shown is the force curve with no PM and the repulsive force between the magnetized YBCO and PM only for *z0* = 0 mm.

2.5.3 Other permanent magnet configurations

The other PM arrangements were also modelled as shown in Figure 2.20. Configurations B and C have the advantage of not blocking movement of the rotor, which may be more practical in a real bearing design. However these do not give as significant a force enhancement as configuration A, as can be seen from the force curves in Figure 2.21a and b. Configuration C gives greater stiffness for the zone of stability but is more unstable than B for large displacements.

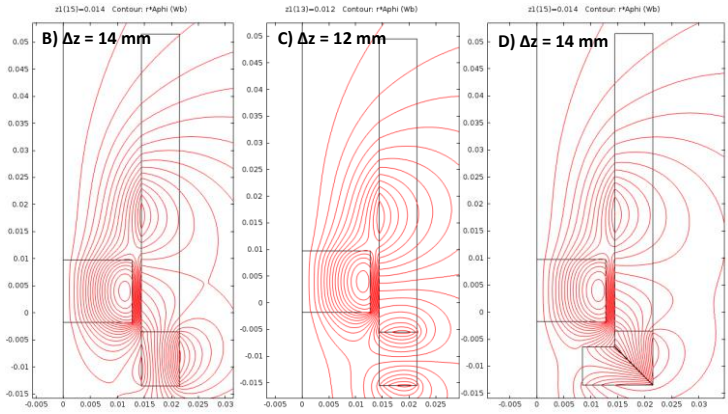

Figure 2.20: Magnetic field lines for additional PM configurations B, C and D after displacement, showing the distortion of magnetic field responsible for a restoring force acting on the magnetized YBCO.

Configuration D is a more complex PM arrangement that aims to provide a 'magnetic cushion'. Figure 2.21c shows that although the force enhancement for smaller displacements is not significant, the configuration gives the highest levitation force of them all when approaching closely to the PM.

The 'magnetic cushion' contributes to increasing the force to 1 kN, 6.25 mm away from the maximum possible displacement. This enhancement in force is largely due to the direct zero field cooled force between the magnetized YBCO and PM. The 'magnetic cushion' can provide safety for a bearing in case the MgB_2 component warms up. In this situation the rotor would displace from its operating position as the YBCO-MgB_2 force gives way, but will be slowed down by the PM repulsion as the displacement exceeds ≈ 12 mm.

The limitations to the proposed designs include a restriction in axial movement for configurations A, B and D, a risk of demagnetizing the PMs if the magnetized YBCO bulks approach too closely, and also the likely reduction in radial stability for configuration D if the YBCO comes to sit on the 'magnetic cushion'. The results should also be interpreted within the limits of the PTF model.

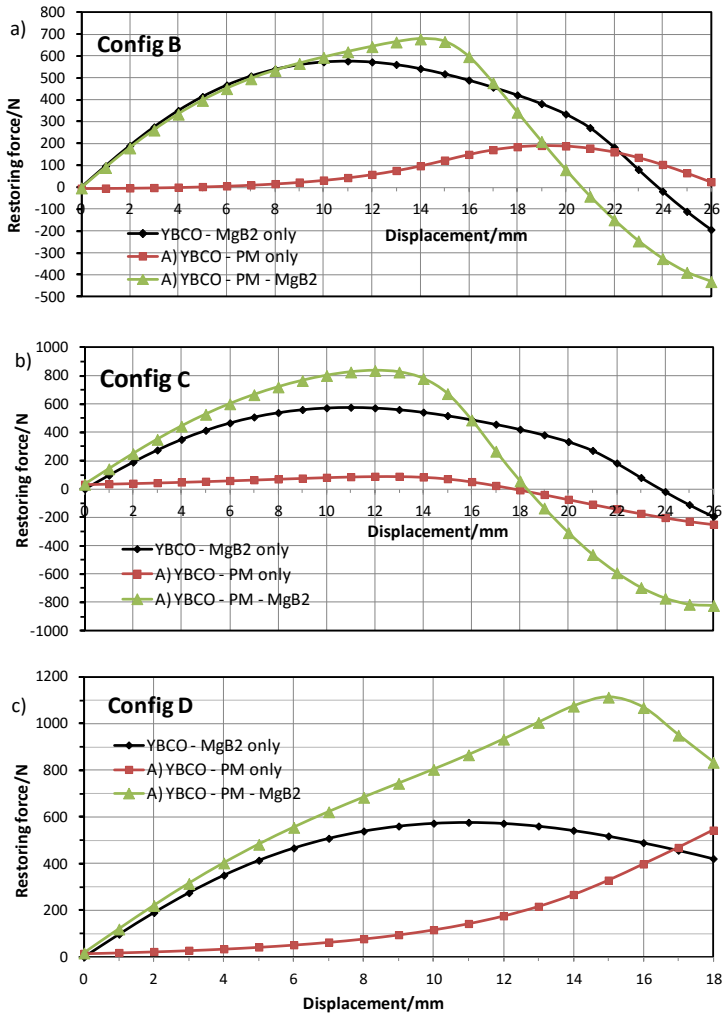

Figure 2.21 Levitation force enhancement curves. a) Configuration B shows only slight improvement at higher displacement. b) Configuration C shows greater improvement than B. c) Configuration D shows significant enhancement in force for large displacement.

2.6 Engineering challenges

There are a number of engineering challenges imposed by an SMB design using magnetized superconducting bulks as a field source for another superconductor in practical applications such as flywheel energy storage. Four main issues are listed below.

i. **Mechanical demands** placed on bulks due to trapped field and centrifugal forces when rotating at high speed. The repulsive forces on a stack of bulks magnetized with alternating polarity would be significant. Also the construction of opposing pulsed field coils remains untested and would need careful design to withstand Lorentz forces in unconventional directions.
ii. **Cooling of the bearing rotor** as well as the stator would be required, but without any contact with the stator.
iii. **Heating effects from the pulse magnetization coil** may cause problems at lower magnetization temperatures (such as 40 – 60 K) due to heat generation around YBCO bulks and inefficient removal of the heat.
iv. **Limits to the radius of the bearing rotor** due to the maximum size of (RE)BCO pellets that can be grown and the maximum bore of coils that can provide high pulsed fields would force the cylindrical bearing to have a large height compared to radius for high loads.

The sum of the maximum tensile stress resulting from rotational and internal magnetic stresses must be less than the tensile stress of the bulk material. Equation (1.17), which gives the rotational stress on a rotating cylinder, shows that a rotational speed of say 10,000 rpm for a 50 mm diameter bulk would lead to 1.7 MPa of tensile stress, which would limit the field that could be trapped. The 50 mm rotor bulks modelled in Section 2.3.4 with opposing magnetizations would experience a static repulsive force up to 1.5 tonnes (up to 2 tonnes transient force) and the (RE)BCO bulks need to be designed to survive these stresses. These forces are most likely to determine the maximum trapped fields used in practice. It is therefore not beyond the capacity of high strength steel (yield strength 690 MPa) or composites (such as the carbon-fibre wrapping used in [25]) to be used as a thin walled cylindrical container for the bulks. The holes in the YBCO grown by X Chaud et al. [14] could also be used for reinforcement against axial forces by allowing rods to run internally through the stack in addition to external reinforcement.

The temperatures used in high performance bearings for flywheel applications have been achieved by cryo-coolers cooling the stator part of the bearing, with thin walled insulation between the rotor and stator, so that the whole rotor and rest of the system operates at room temperature.

A solution to the problem of having to cool the rotor as well as the stator is enclosing both in a single cryostat, so that the bearing stator and whole rotor operate at the same cryogenic temperature.

Figure 2.22 illustrates this possibility for a SMB that uses superconducting coils in an opposing field configuration as a field source. A magnetic clutch can be used to transfer energy to and from the flywheel rotor.

a) b)

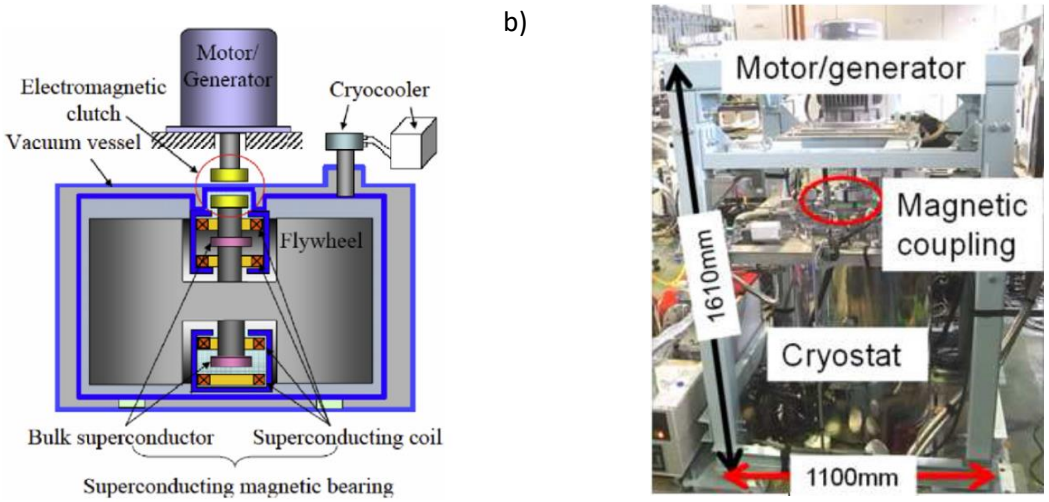

Figure 2.22: a) Schematic illustrating the cooling configuration for a flywheel energy storage system that would utilise a SC coil – SC bulk bearing investigated by K. Nagashima et al. [89]. b) Prototype of the SC coil – SC bulk bearing [90].

One option for cooling the flywheel system to 20 – 25 K is indirectly using a liquid hydrogen storage system as shown in Figure 2.23. A closed helium gas loop can be used for indirect cooling, minimising the explosion hazard.

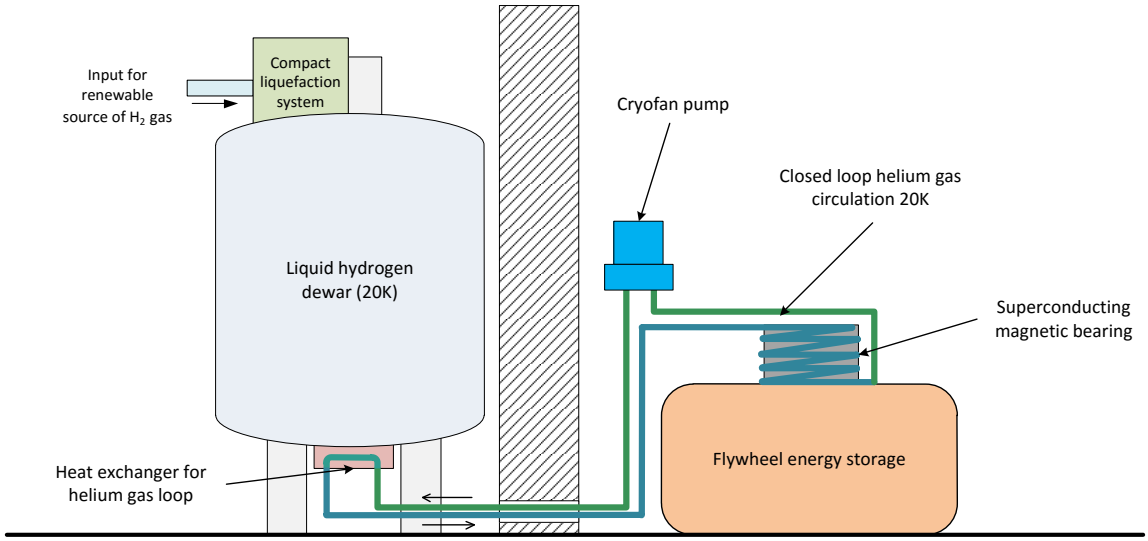

Figure 2.23: Indirect cooling of an SMB using a liquid hydrogen dewar and CryoFan (developed by Cryozone [104]). Helium gas is pumped around a closed loop with one end cooled to 20 K via a heat exchanger connected to a liquid hydrogen dewar.

Whilst heating from the pulse coil may be problematic, designs using magnetized bulks in motors have been constructed with the pulse coils and (RE)BCO bulks enclosed in the same overall cryogenic environment. An example is the axial gap type motor shown in Figure 1.40 which uses vortex coils for PFM and operates at around 30 K. The coils are not in direct contact with (RE)BCO bulks which would also be the case in the bulk – bulk bearing design proposed. Also, it is not important if heat flows directly from the pulse coil to the MgB_2 bulk cylinder, as would be the case in the configuration illustrated in Figure 2.1, because it does not matter if the MgB_2 is in the normal state when magnetizing the (RE)BCO bulks. The only times it has to be superconducting, the pulse coil is not in use. Use of a vacuum wall to separate the pulse coil from the (RE)BCO bulks is also feasible and is actually the case in the experimental system outlined in the next chapter.

The modelling of an ideal one tonne bearing as shown Figure 2.15, used a 50 mm diameter bulk pair. If this is considered as the largest size bulk that can be practically magnetized with high trapped fields using PFM, then more than one bulk pair would be needed for loads of greater than a tonne. The design would not be feasible for levitating many tonnes as it would likely be impractical to magnetize many bulk pairs forming a bearing with a large overall height compared to diameter.

3 Pulsed magnetization and levitation force measurement system

A unique system was designed and constructed capable of magnetising superconducting samples up to 50 mm in diameter at temperatures down to 10 K and with applied fields up to 10 T. This system is also capable of measuring levitation force between two bulks, which was essential for proving the concept of bulk – bulk bearings. Due to the complexity, duration of construction, and versatility of the system, it is worth describing in some detail. For simplicity, the system as a whole can be referred to as the Magnetoforce system.

3.1 Introduction and overview

A summary of the system parameters can be found in Table 3.1 and an overview of the system can be seen in Figure 3.1. The system is based around an Oxford Instruments Variox pulse tube cryostat. The insert, force measurement part, tail and coil were all custom made to work with the cryostat. The system is operated by sealing the sample space inside the cryostat and filling the space with helium gas. The cold head of the cryostat is in the form of a copper ring embedded in the wall of the cryostat bore and is therefore not in direct contact with the insert. Cooling is provided indirectly by conduction of heat by the helium gas, which is a good heat conductor at low temperatures [105]. This indirect cooling by gas gives more flexibility for sample size and shape than a conduction-cooled design, in which samples have to be rigidly mounted directly onto a cold head. Due to the magnetic forces that the system is designed to measure, the insert shown in

Figure 3.1c is designed for axial compressive and tensile forces of 1 kN. The pulsed current supplied to the pulse coil was provided by a commercial capacitor bank system from Metis. The capacitor bank system was originally designed to deliver pulsed current to a separate 30 T small bore coil for critical current measurements on wires.

Table 3.1: Summary of key parameters of the Magnetoforce system

Specifications	
Minimum operating temperature	10 K
Cooling of bulks	Helium gas
Force rating	1 kN
Cryostat bore	50 mm
Pulse coil bore	65 mm
Maximum pulsed field	10 T
Pulse rise time	15 ms

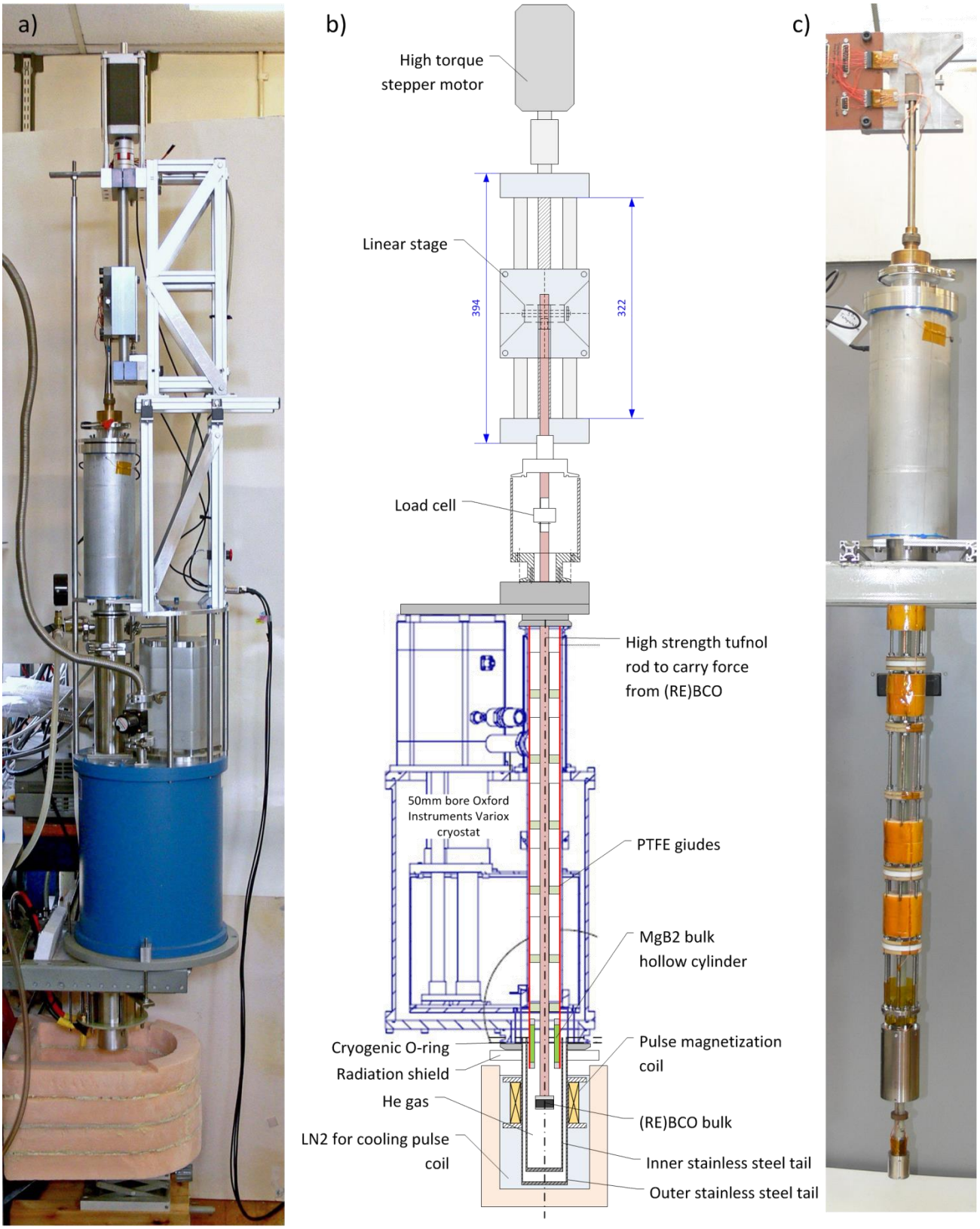

Figure 3.1: a) Photo showing the Magnetoforce system for pulse magnetization of superconducting bulks and magnetic force measurements. The system is built around an Oxford Instruments Variox cryostat. b) A schematic illustrating the various parts of the system: the top part for force measurement and the bottom part for pulse magnetization. c) Photo of the insert for the cryostat which contains all the sample holders and sensors (load cell, hall probes and temperature sensors). All parts except the blue cryostat were constructed specifically for the system.

3.2 System details

3.2.1 Pulse field coil

The most important part of the system is the pulse magnetization section, comprising a pulsed field coil and stainless steel tails as shown in Figure 3.2. The drawing shows the system when used to magnetize a (RE)BCO bulk that is later moved into an MgB_2 tube for field cooling and force measurement. The coil sits around specially made tail extensions added to the bottom of the Variox cryostat.

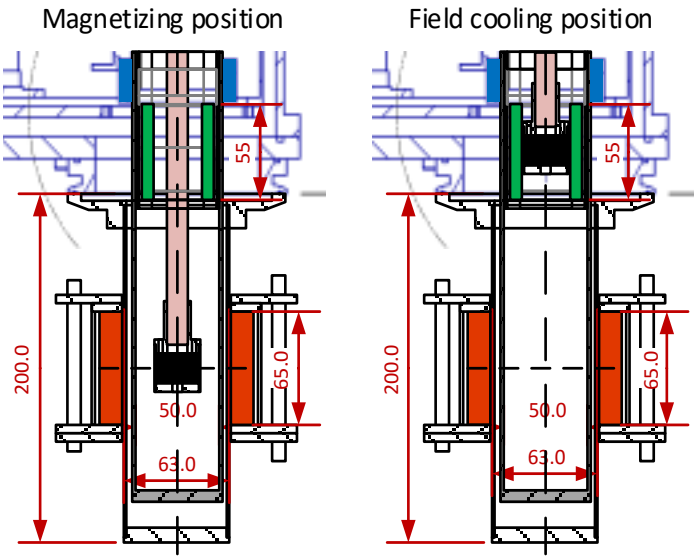

Figure 3.2: Engineering drawing showing the bottom 'tail' part of the system in a position for pulse magnetization of (RE)BCO and also in the field cooling position, after which force measurements would be made. In this configuration, red is the pulse coil, black a (RE)BCO bulk, green an MgB_2 hollow cylinder, and blue the copper cold head ring of the cryostat.

Part of the practicality of pulsed field magnetization is related to only needing a copper coil, rather than a large and expensive superconducting coil. However the copper coil still requires careful design and construction. The number of turns and dimensions of the coil were optimised to give an inductance which allowed a long enough pulse duration but also a large maximum field. Coupled differential equations were solved to give the transient solution to the circuit in the capacitor bank system, combined with the new coil. An inductance of 8.3 mH was chosen, which gave a maximum pulsed field of around 10 T when using the full available discharge voltage of 3 kV (36 kJ). Too small an inductance would lead to a higher maximum pulsed field but too short a pulse duration. Too large an inductance, although giving a longer pulse duration, would limit the maximum field and would require a short coil with relatively inhomogeneous field. The maximum pulse current possible was 1.9 kA, which can only be sustained for ~ 10 ms without melting the wire, even with LN_2 cooling. Heating is not the only problem. The large Lorentz forces on the copper wires resulting from the high

currents and fields mean that significant reinforcement is required, in the form of composites between layers and also outside the coil windings, to prevent the coil distorting or even exploding in the worst case. It is common to use glass fibre for pulsed field coils [106]. Following force modelling conducted for the coil by F Herlach of K U Leuven, the correct thickness of reinforcement layers was determined for a 10 T pulsed field given the type of fibre used and the dimensions of the coil wire, which was square rather than circular in cross-section to help distribute stress. The fibre used was S-2 glass cloth as shown in Figure 3.3b, which has approximately 1.4 times the tensile strength of standard E-glass fibre. After a layer of wire was wound, a layer of Stycast resin was painted on during the winding of the glass fibre cloth strip, to achieve a similar result as more complex vacuum impregnation. After all the coil layers were wound, a thick layer of the glass fibre composite was wound on the outside. After curing, as shown in Figure 3.3a, the outer layer was machined down into a cylinder, ready for hot press fitting of the stainless steel cylinder, also shown in the figure, for added reinforcement and containment. The entire coil winding and reinforcement process was conducted manually in-house, which was a challenging task largely due to the rapid curing of the resin and because mistakes, such as slight misalignment of a turn, could not be tolerated due to stress concentrating at weak points during a pulse. Winding of pulse field coils takes great care to contain forces acting on highly conductive but relatively soft copper wire.

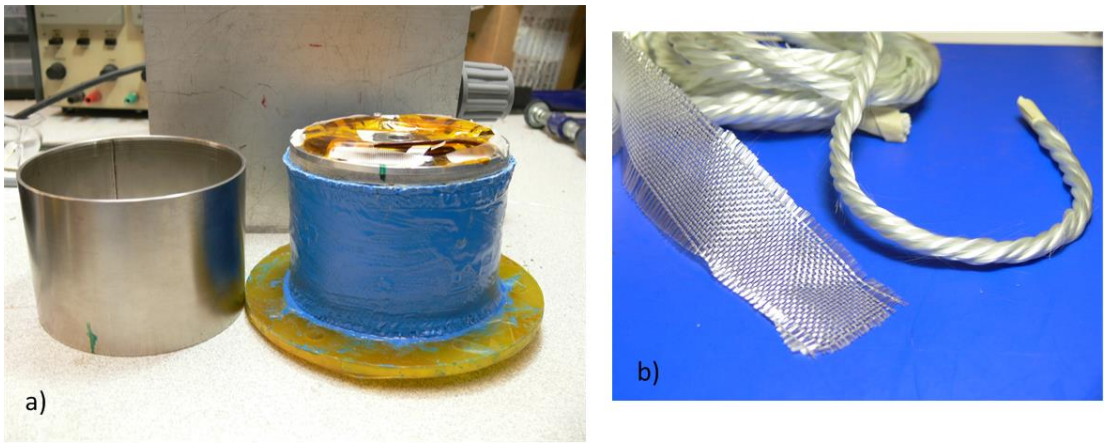

Figure 3.3: a) Final stage of the construction of the 10 T pulse field coil. Blue Stycast resin visible before being machined down to allow hot-pressing of the stainless steel cylinder for extra reinforcement. b) Samples of the S-2 glass fibre cloth and string used with Stycast to internally reinforce the coil.

The tail pieces that came with the Variox cryostat were aluminium, with the outer tail being greater than 65 mm in diameter. This presented three problems: the high conductivity of aluminium would lead to eddy current heating during pulses, the eddy currents would lead to large magnetic pressure, and the larger outer diameter of the tail would force the coil to have a large inductance and therefore limit the maximum applied field to much less than 10 T. Modelling of induction heating using COMSOL was performed, which showed significant heating of the aluminium tails by

eddy currents (a spontaneous temperature rise of up to 70 K) and large compressive forces. This was confirmed by a simple experimental test in which an aluminium tube was inserted into the pulse coil in LN_2 and a 6 T pulse delivered. The heating was evident by the large splash of LN_2 as the liquid was instantly boiled off between the coil and the tube, an effect which in itself would cause unwanted pressure on the outer tail. To solve these problems, a new pair of tails was created from stainless steel with a small outer diameter to fit inside the desired coil, as seen in Figure 3.4. The parts of the tail were glued together using Stycast, which was able to hold high vacuum ($\sim 10^{-6}$ mbar) as well as being mechanically strong. Modelling and experiment confirmed that the comparatively low electrical conductivity of stainless steel did not lead to significant eddy current heating.

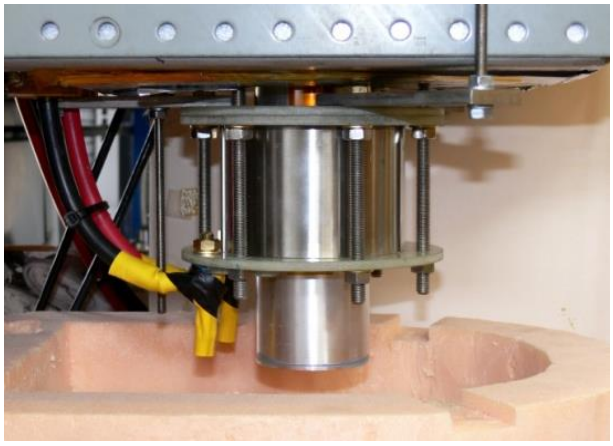

Figure 3.4: Photo of the installed pulse field coil around the stainless steel tail. Polystyrene cryostat visible below, which is used to immerse the coil in LN_2 during operation.

3.2.2 Sample holder insert

There were a number of constraints placed on the design of the bulk sample holders shown in Figure 3.5. They had to accommodate a range of sample sizes in order for the system to be a flexible research tool, yet they also had to be well suited to proving the concept of bulk (RE)BCO – MgB_2 levitation force. Grade 316 stainless steel was chosen for its strength at low temperatures, relatively low electrical conductivity (minimising eddy currents) and non-magnetic properties. In order to maximise the use of the 50 mm cryostat bore, the thin walled sample holders were assembled using grub screws as shown in Figure 3.5. A prototype of the smaller (RE)CBO sample holder, using the same grub screw design, was tested in a tensometer which showed that it could survive more than 2 kN of axial tensile force without damage.

Figure 3.5: Sample holders for (RE)BCO bulk (left) and MgB_2 bulk (right). The larger sample holder can be used to hold superconducting bulks of any kind up to 46 mm in diameter. Both holders have been engineered to survive up to 1 kN of compressive/tensile force.

In order to maximise the levitation force between the magnetized (RE)BCO bulk and the MgB_2 hollow cylinder, the radial gap between the two had to be as small as possible. Figure 3.6a shows the tight tolerance achieved between the (RE)BCO sample holder and the MgB_2 hollow cylinder inside which it moves, visibly exposed on the inside. The sensing plate for the (RE)BCO bulk sample holder, as shown in Figure 3.6a, also presented a number of challenges. In order to get an accurate measure of the central trapped field, a high linearity Arepoc cryogenic hall probe (model LHP-MP) was used. However a number of hall probes were desired to give an accurate measure of the whole trapped field profile. Rather than scanning a sensor over the bulk, which is difficult at temperatures below 77 K and interrupts pulse magnetization sequences, an array of 9 hall probes were used. The four small hall probes on either side of the central probe were simple Toshiba hall probes (model THS118) which each had to be individually calibrated up to 6 T and down to 10 K. All the hall probes were aligned to measure field 0.5 mm away from the sample surface when a thin stainless steel cover is attached to the sensor plate.

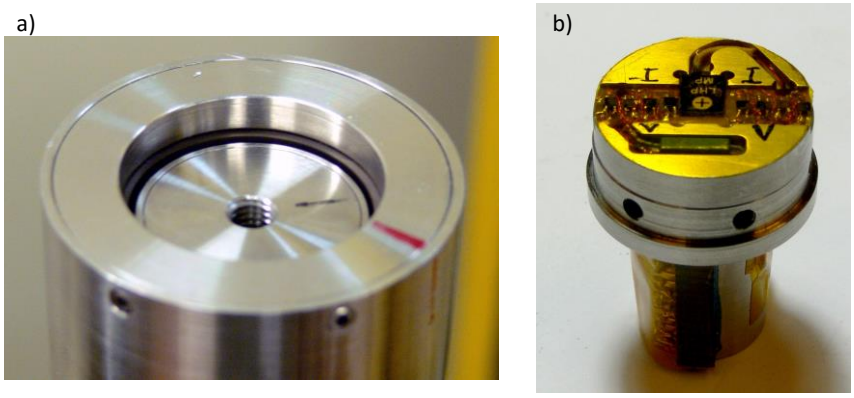

Figure 3.6: a) Photo showing the two sample holders coaxially aligned as they would be during force measurement. The gap between the visible dark grey MgB_2 cylinder and (RE)BCO sample holder is only 1.75 mm, showing the small tolerances in the system. b) Sensor plate of the (RE)BCO sample holder showing a central Arepoc hall probe and a further 8 Toshiba hall probes used to map the trapped field profile along a line. There is also a carbon ceramic temperature sensor (green) to measure (RE)BCO temperature.

3.2.3 Levitation force measurement

As can be seen from Figure 3.1a and b, the upper part of the Magnetoforce system is composed of an aluminium cylinder housing a load cell, a linear stage, and a high torque stepper motor. The load cell is incorporated inside the insert space which is filled with helium gas during operation. This is so that the force on the rod can be measured without any interference from an O-ring seal which is placed above the load cell and lubricated to allow movement. In order to meet the high mechanical demands placed on the central rod as well as minimising heat input into the cryostat, a glass composite rod (Tufnol 10G/40) was used to carry the force from the sample. In order to move the rod against forces up to 1 kN, a linear stage was used, connected to a 1.8° hybrid stepper motor driven with a micro-step driver (20 micro-steps per step). This combination allows for linear movement with a positioning resolution of 1 µm (20 µm for a full step), which is easily sufficient to provide accurate force-displacement curves, for which the typical position increment was 0.25 mm. The motor has sufficient holding torque to prevent movement of the stage against 1 kN of force. In order to measure the force-displacement curves, the motor takes a step and then pauses to allow the load cell to be read, which does not prevent speeds of 1 mm/s, which is typical for levitation force measurements [107].

3.2.4 Data acquisition and software

The measurement, magnetization and positioning hardware was interfaced with a computer via custom electronics and a National Instruments DAQ card (NI-6251). The DAQ provided analogue inputs (multiplexed via a 16-bit ADC), which could be sampled at an aggregate rate of up to 1.25

MHz, and digital I/O lines capable of waveform generation. In addition, several digital multimeters were used to measure temperature.

The intermediate electronics were developed with Dr Simon Hopkins of the Applied Superconductivity and Cryoscience Group, University of Cambridge. These provided excitation currents/voltages for the sensors, signal conditioning (including multiplexing and pre-amplification of Hall probe and load cell signals), a safety circuit for the movement stage, and interfacing for the stepper motor driver.

The final aspect of the system to be developed was complex software to allow flexible measurements using all the available sensors, as well as automated pulse magnetization and force measurement. The software was written by Dr Simon Hopkins. The automation of the pulse sequences to implement IMRA and MPSC is advantageous given the number of pulses required, and an important demonstration of how pulse magnetization could be controlled for real applications.

The pulse field coil was externally calibrated and its resistance monitored to measure heating. This allowed a cool-down time to be calculated, which is the time it takes for the coil to return to around 77 K following heating by the pulsed current. The software is designed so that it is impossible to deliver a pulse within the cool-down time of a previous pulse (for example 140 s for 5 T), which protects the coil from overheating. This places a minimum time for a pulse sequence to be delivered at a particular temperature. For example, if starting from 5 T and going down in steps of 0.2 T to 2.8 T, which is a typical sequence, the total time would be at least 22 minutes. Figure 3.7 shows the interface in the Magnetoforce software used to pre-program the pulses that are desired. These can be amended during the pulse magnetization process if changes need to be made, as would be typical if testing a new sample, and it is also possible to override the automation and pulse manually if desired. Once started, the software waits for the sample temperature to fall below the desired temperature, after which the capacitor bank is automatically charged and discharged to deliver a pulse. During the pulse, the central hall probe is rapidly sampled to show how the field is penetrating the sample (Pulse Data tab in Figure 3.7).

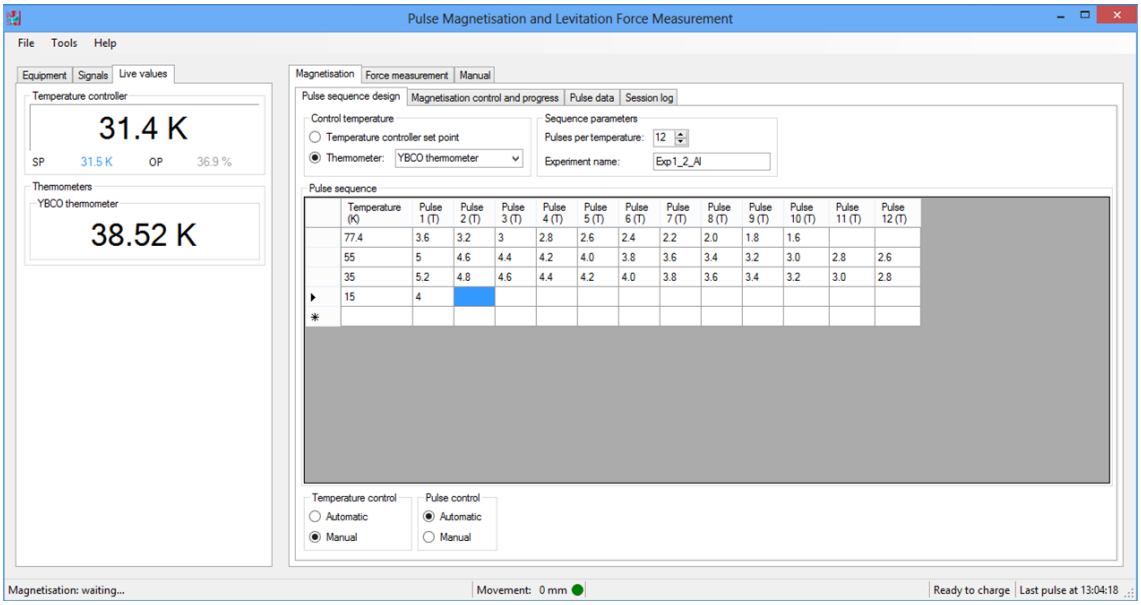

Figure 3.7: Screen-shot of the software capable of automated pulse magnetization. The tab shown allows all field pulses at all temperature stages to be pre-programmed before starting automated magnetization.

The remaining hall probes, which are multiplexed, are read along with the central probe immediately after the pulse and again 30 s after the end of the pulse. The software permits any number of readings of the hall probe array at fixed intervals after a pulse, but 30 s has been chosen as a standard measurement time, as before 30 s there is significant flux creep. Although flux creep for pulsed magnetization continues after 30 s, it is not so significant and choosing a longer measurement time would delay the delivery of the pulse sequence. The measurements of the hall probe arrays are immediately plotted by the software, as seen in Figure 3.8, which shows the profiles 30 s after a number of pulses have been delivered to a 25 mm diameter YBCO bulk as well as the final trapped field profile at the end of the last temperature stage. In Figure 3.8 the software is in the middle of delivering the sequence of pulses and is waiting for the coil to cool down, and also for the bulk to cool down to the desired temperature. Although automatic control of the temperature is possible, the tests presented in this thesis used manual control whereby the temperature of the cold head was set to a value below the desired sample temperature to effectively cool the bulk after a pulse, but the triggering of the pulses was still done by the software. In order to see the trends for the results, the trapped field and flux are plotted during magnetization as can be seen in the right hand plot of Figure 3.8. The flux is calculated using interpolation of the field measured by the hall probes and integration over the 25.5 mm diameter sample holder area. It is not a reliable measure of the real trapped flux for asymmetric profiles or samples significantly smaller than 25.5 mm.

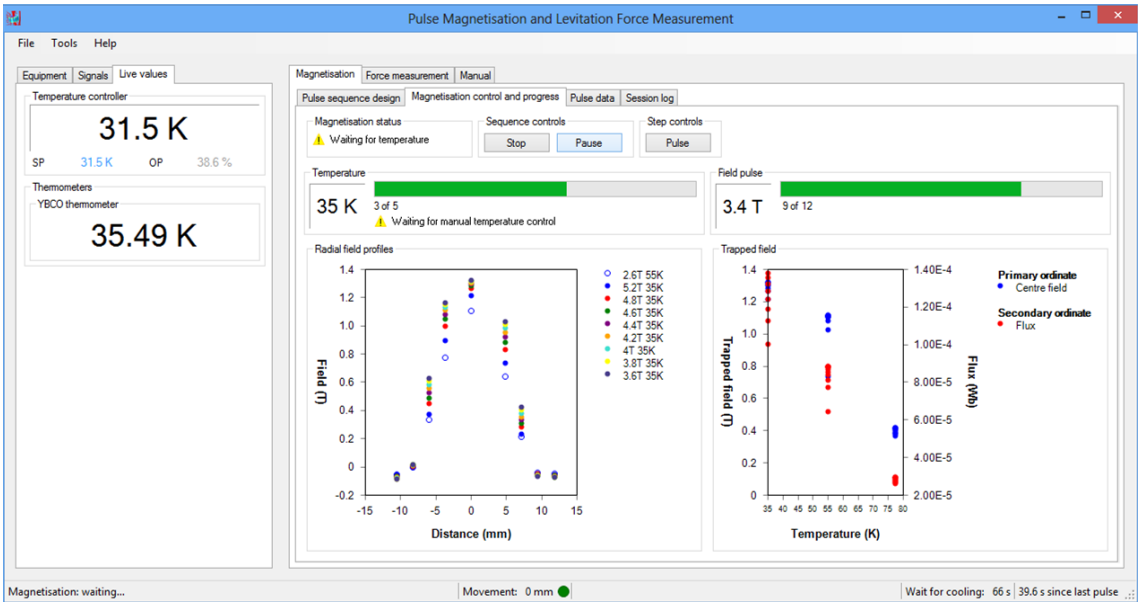

Figure 3.8: Screen-shot showing the progress tab of the automated magnetization. The evolution of trapped field and flux can be monitored during the magnetization process, giving instant feedback on how each pulse is modifying the trapped field.

The automatic plotting and processing of the trapped field data during magnetization makes the system a powerful and easy to use tool for characterising pulsed magnetization performance of bulks, which can be unpredictable and therefore exhibit confusing behaviour if only unprocessed data is available during experiments. The software can also control the force measurements by performing a back and forth displacement of the desired magnitude and measurement step to give a live force displacement curve.

3.2.5 Measurement errors

The largest contribution to the error in the measurement of the central field is a systematic error coming from the uncertainty of the hall probe distance from the bulk sample surface. Although confined by the stainless steel sample holder (Figure 3.6b), it is not permanently mounted in order to allow possible removal for other tests. Therefore there is an uncertainty in separation between the hall sensor and the bulk surface of approximately ± 0.05 mm. Using a simple model in COMSOL for uniform current density circulating in a 25.5 mm x 12 mm bulk, this corresponds to an error in the measured field at 0.5 mm above the sample surface of up to ± 1.5 %. Even at a low field of 0.3 T, the sensitivity of the Arepoc sensor (12.5 mV/T) results in a signal 500 times larger than the ADC resolution; and each reading is averaged over 8000 samples, so random errors are negligible.

The Toshiba hall probes were rigidly and permanently mounted to the sample holder. Unlike the central Arepoc hall probe, they are not highly linear in field or temperature and therefore had to be individually calibrated using the Arepoc hall probe with a third order polynomial fit used for the field

dependence of hall voltage and a second order polynomial used for the temperature scaling. The main source of error was the error in the polynomial fits, which was approximately no more than ± 2 %. The Toshiba probes are measured via a multiplexer. A settling time of 50 ms was allowed on switching, and each reading was averaged over 500 samples. The general alignment and reliability of the hall probe array was confirmed by measuring the field profile of a 25 mm diameter rare-earth PM, which fitted the smooth relatively flat profile expected, as well as being a good match with a separate scanning hall probe measurement of the same PM.

The error in the load cell measurement due to non-linearity and hysteresis is no more than 0.4 %. A small force error is also possible during movement due to 'stick and slip' of the tufnol rod against the guides. This error leads to small oscillations ($\sim \pm 3$ N) in the force displacement curve, the impact of which can be reduced by averaging.

The resistance of the carbon ceramic temperature sensors was found using four point measurement with voltage and current measured by digital multimeters. The main source of error for the temperature readings was the error in the calibration curves. A sixth order polynomial was used for the fit which gives a maximum error in the temperature of ± 0.3 K. Another uncertainty when describing the temperature of a bulk in the system, is the presence of thermal gradients which mean that the bulk could have a non-uniform temperature distribution. The variation is likely to be negligible for the (RE)BCO bulk given its small size and relatively uniform cooling by helium gas, but may be significant for the MgB_2 tube used, which is 55 mm in height and had its top half close to the system cold head (see Figure 3.2). It is difficult to estimate, but the temperature variation throughout the MgB_2 bulk is probably no more than 1 K.

4 Magnetized bulk (RE)BCO – MgB_2 levitation force results

Experimental measurements on PFM and levitation force between a magnetised 25.5 mm diameter YBCO bulk and a coaxial MgB_2 hollow cylinder were performed, proving the concept of a bulk–bulk superconducting bearing. The maximum force achieved after field cooling the MgB_2 bulk cylinder to 20 K in the field of a 1.68 T magnetised YBCO bulk was 501 N, and 560 N was achieved for another bulk at a lower temperature. These are the highest levitation forces known to have been measured to date between two superconducting bulks.

4.1 Pulse magnetization of 25.5 mm (RE)BCO bulks

Before performing any levitation force test, 25.5 mm x 12 mm YBCO bulks were magnetized in the Magnetoforce system using PFM. The diameter of the bulks was ideal when used with an MgB_2 tube that could fit inside the system bore of 50 mm. In order to maximise the trapped field and flux, the IMRA and MPSC techniques were used, which also allowed the trapped field performance of the bulks to be characterised as a function of temperature. The results presented in this section are for two YBCO bulks, referred to as Y1 and Y2, produced using top seeded melt growth by Yunhua Shi of the Bulk Superconductivity Group, Engineering Department, University of Cambridge. All trapped fields were measured 0.5 mm above sample surfaces and along the growth sector boundary of the bulk.

4.1.1 IMRA method and pulse sequence

When magnetizing an untested bulk for the first time, its response to a pulsed field can be quite uncertain, even for bulks which have trapped a highly symmetric conical field profile after field cooling. Therefore all bulks used for this thesis were at some point pulse magnetized at 77 K, which gives a good indication of the applied fields needed for lower temperatures. The thermal stability at 77 K means that the IMRA procedure (as first introduced in Section 1.7.2) can be successfully completed even when starting with applied fields much higher than necessary, but the same is not true for lower temperatures. Applying more than around 5.5 T for bulks Y1 and Y2 results in either complete or partial collapse in the trapped field at temperatures below ~ 40 K, which cannot typically recover to its maximum value during further pulses unless warmed back to a higher temperature.

The applied pulse field sequences chosen for Y1 and Y2 after initial testing are shown in Table 4.1. Fields at higher temperatures may be slightly higher than necessary, but the maximum fields at lower temperatures penetrate the bulks as much as possible without collapsing the field due to thermal instability. For the bulks tested, it is not possible to saturate them at the lower temperature stages. MPSC is therefore needed to add as much flux to the bulk centre as possible at higher temperatures, before the lower temperature stages add flux to the bulk periphery as detailed in Section 1.7.3. Due to these factors, for typical ~ 25 mm diameter (RE)BCO bulks, the maximum applied fields needed are approximately between 4 – 5 T.

Table 4.1: Full PFM sequence used for YBCO bulks Y1 and Y2. Three stage MPSC was used to magnetize the bulks for MgB_2 field cooling and force testing. A separate MPSC test including lower temperatures was also performed on Y2.

Temperature		Applied field/T														
	Pulse #:	*1*	*2*	*3*	*4*	*5*	*6*	*7*	*8*	*9*	*10*	*11*	*12*	*13*	*14*	*15*
Y1 MPSC for force test	54 K	4.3	4.2	4.1	4.0	3.8	3.6	3.4	3.2	3.0	2.6					
	40 K	4.8	4.7	4.6	4.4	4.2	4.0	3.8	3.6	3.4	3.2					
	35 K	4.9	4.85	4.8	4.7	4.6	4.5	4.4	4.2	4.0	3.8	3.6	3.4			
Y2 Full MPSC	77.4 K	3.0	4.0	3.8	3.6	3.4	3.2	3	2.8	2.6	2.4	2.2	2.0	1.6		
	60 K	4.4	4.3	4.2	4.0	3.8	3.6	3.4	3.2	3.0	2.6	2.2				
	45 K	5.0	4.9	4.8	4.6	4.4	4.2	4.0	3.8	3.6	3.4	3.2	3.0	2.8	2.6	
	30 K	5.0	4.9	4.8	4.7	4.6	4.5	4.4	4.2	4.0	3.8	3.6	3.4	3.2	3.0	2.8
	15 K	5.0	4.9	4.8	4.7	4.6	4.5	4.4	4.2	4.0	3.8	3.6	3.4	3.2	3.0	2.8
Y2 MPSC for force test	55 K	4.6	4.4	4.2	4.0	3.8	3.6	3.4	3.2	3.0	2.8	2.6	2.4	2.2		
	45 K	5.0	4.8	4.6	4.4	4.2	4.0	3.8	3.6	3.4	3.2	3.0	2.8			
	37 K	4.9	4.8	4.6	4.4	4.2	4.0	3.8	3.6	3.4	3.2	3.0	2.7	2.5		

It is worth considering the evolution of the trapped field profiles during IMRA in order to understand how PFM works, and also to understand the limitations of PFM when applied to (RE)BCO bulks. Figure 4.1 shows the evolution of trapped field for bulk Y1 during the second 54 K magnetization stage of MPSC. It is very clear for this case how important IMRA is in maximising the trapped field and flux, which would otherwise be significantly lower, and just as importantly, unpredictable and not reproducible, if using a single pulse. The fact that the first pulse of a sequence typically produces an asymmetric unpredictable profile is evidence of J_c inhomogeneity inside the bulk, which leads to hotspots and instability. Whilst IMRA can usually deal with this problem at higher temperatures, the same is not necessarily true for lower temperatures, so inhomogeneity remains undesirable. Figure 4.2 shows examples of the trapped field for bulk Y2 which develops an 'M' shaped trapped field profile most likely due to a low J_c region near where the seed crystal was. In this case, such an inhomogeneity is not believed to contribute to thermal instability due to its axial

symmetry (unlike an off centre region of low J_c). Figure 4.2b shows how using a low temperature, such as 15 K, in an MPSC sequence can increase flux rather than field.

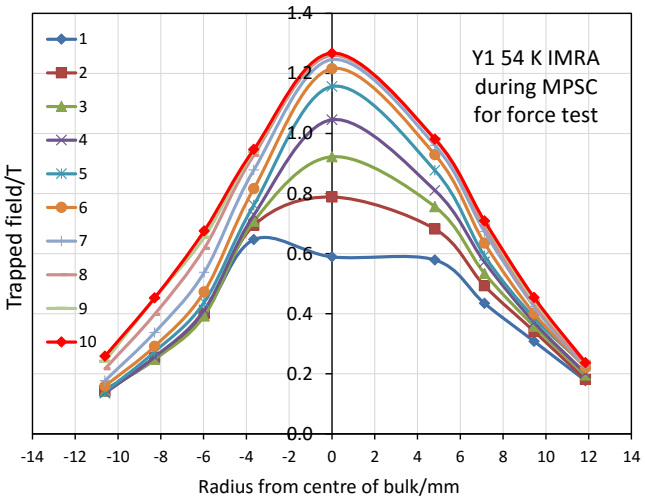

Points illustrated

- Trapped field after first pulse asymmetric due to high thermal instability
- Initial IMRA pulses increase peak trapped field
- Later IMRA pulses mostly increase outer trapped field and therefore flux rather than central trapped field
- Final trapped field state reproducible using IMRA

Figure 4.1: Evolution of trapped field for YBCO Y1 during the IMRA procedure for the 54 K MPSC stage.

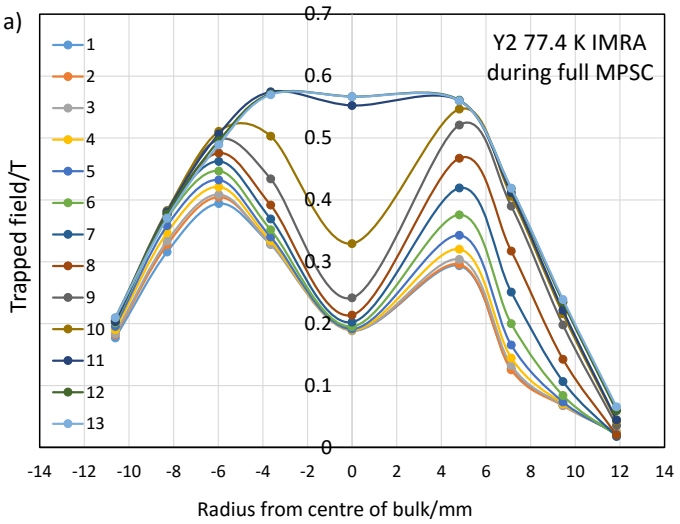

Points illustrated

- J_c inhomogeneity can strongly affect trapped field profile as in the case of Y2, which has a low J_c region in the centre
- Dip in central field is not due to thermal instability as 77 K is relatively stable
- Field can suddenly redistribute during a pulse sequence (pulse #11), an effect that cannot be simulated using a $E - J$ critical state model

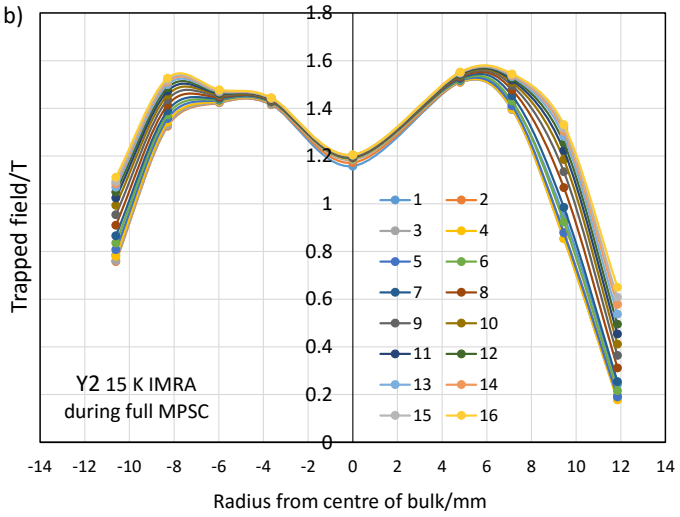

- At low temperatures PFM cannot typically saturate a bulk
- The IMRA pulse sequence in this case is used to build up field in the outer region of the bulk
- Whilst PFM at low temperatures cannot increase the central field by much, it can increase the trapped flux
- At the lowest temperatures, the change in field per pulse can be very small

Figure 4.2: Evolution of the trapped field during the a) highest and b) lowest temperature stages of the full MPSC magnetization of YBCO bulk Y2. The bulk exhibited a low J_c region around the seed crystal point.

4.1.2 Trapped field and flux for MPSC

Having explored the evolution of the trapped field profiles for the bulks during IMRA, it is important to consider the final trapped field and flux possible when using PFM. At higher temperatures, PFM can trap a field around 2/3 of that which can be trapped using field cooling. This is illustrated by Figure 4.3, which shows the trapped field profile for a GdBCO bulk using field cooling and PFM. However, an analysis of the flux using the hall probe scan data shows that PFM can trap almost the same flux as field cooling at 77 K (≈ 95 % in this case). This example contributes to the general comparison of magnetization methods made in Table 1.3. Given the importance of trapped flux in many applications and the relatively high flux to peak field ratio resulting from PFM, care should be taken in interpreting the usefulness of PFM if only peak trapped field values are available.

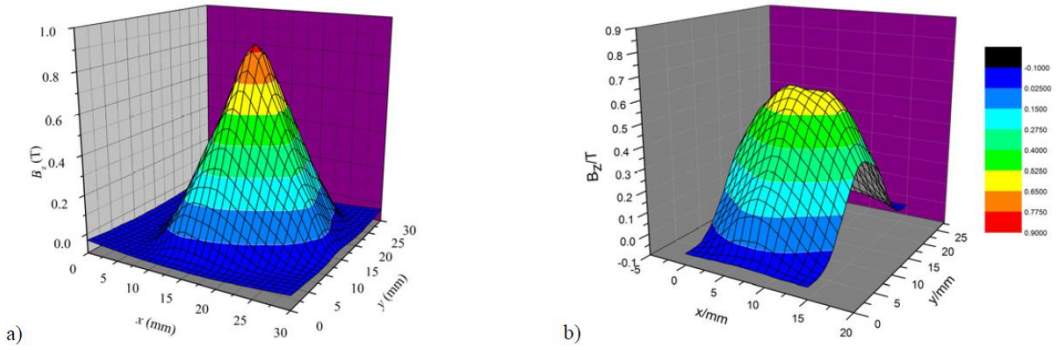

Figure 4.3: Example trapped field profiles for a 26 mm diameter GdBCO bulk magnetized at 77 K using a) field cooling performed by Y Shi (Engineering Department, Cambridge) and b) pulsed magnetization in LN_2. Field cooling traps a higher peak field (0.90 T) than pulsed magnetization (0.63 T), but using IMRA has allowed PFM to trap approximately 95 % of the flux achieved by field cooling.

The trapped field profile achieved for each stage of MPSC applied to bulk Y1 is shown in Figure 4.4. Pre-magnetization at the higher temperature stages was necessary to maximise the trapped field at 35 K, which otherwise would have been limited by thermal instability if starting from zero trapped field. Unlike Y2, Y1 is able to trap a relatively conical trapped field profile at all temperature stages, giving a final trapped field at 35 K which has a high degree of symmetry. This final trapped field profile had a peak of 1.68 T at the bulk centre and was used to field cool the MgB_2 used for levitation force testing. After the last magnetization temperature of 35 K, the bulk was cooled to 20 K. No change in the central trapped field was detected, however there was a very small decrease in the outermost measured field. Following the force measurement detailed in the following section, the system was left overnight, with the YBCO bulk maintained at 20 K, to see if there would be a reduction in trapped field. The central field was measured the next day with no detectable decrease. Due to the measurement error it is only possible to say that there was less than 0.1 % decay in the central field over 12 hours. This confirms the theory that a reduction in temperature following

magnetization can reduce flux creep to a negligible rate. In addition, warming the final 35 K trapped field state to 50 K momentarily, caused a drop in central field of less than 1 %, demonstrating the resilience of fields trapped by PFM to occasional temperature spikes which could occur in applications.

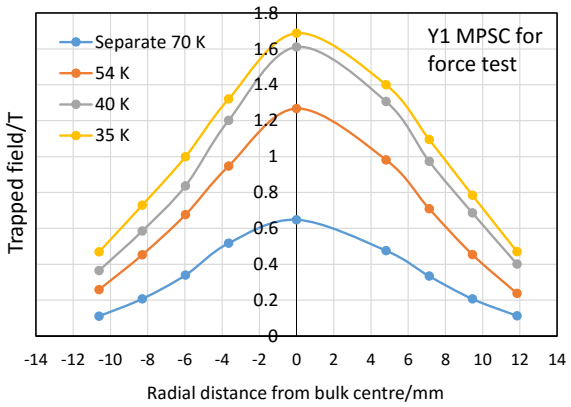

Figure 4.4: Trapped field profiles for YBCO bulk Y1 for the 3-stage MPSC down to 35 K used for the levitation force test. A separate 70 K test is also shown, which is unlikely to have increased the fields for lower temperatures if included in the MPSC procedure. The trapped field exhibits the expected conical shape with high symmetry.

Figure 4.5 shows the final trapped fields for MPSC magnetization applied to bulk Y2. As previously mentioned, the J_c inhomogeneity leads to an 'M' shaped trapped field. It can also be seen that some of the profiles are asymmetric despite using IMRA, which points to further J_c inhomogeneity which is not axially symmetric. The final trapped field after the whole MPSC procedure has reasonably good symmetry for both the full MPSC test and the MPSC for force test. A high degree of axial symmetry would be important for a magnetized bulk being used as a field source in a bulk – bulk bearing in order to allow free rotation. The concept of composite bulks covered in Chapter 5 may make it easier to have a field source with a highly symmetric trapped field.

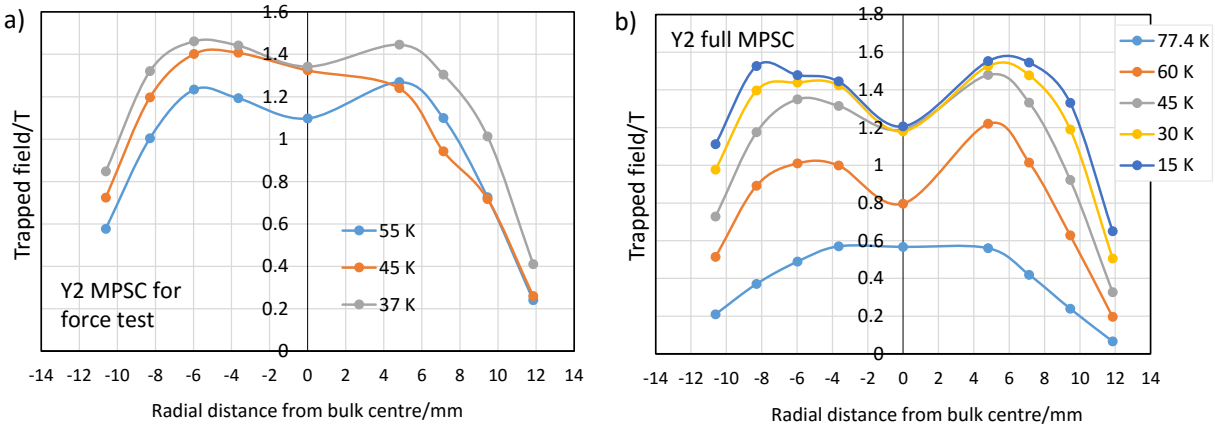

Figure 4.5: Trapped field profiles for YBCO bulk Y2 for a) 3 stage MPSC down to 37 K used for levitation force testing and b) separate full 5 stage MPSC used to determine the maximum trapped field possible (which is off-centre) down to 15 K.

In order to evaluate trapped flux, the field profiles were integrated up to the outer radius of the bulk (*R*), based on the following equation:

$$\Phi = 2\pi \int_0^R B(r)\,\mathrm{r}\,dr \tag{4.1}$$

This method assumes axial symmetry of the trapped field. In order to calculate an approximate solution, the negative radial positions were taken as positive, and the field interpolated linearly between these points. As the trapped field profile is often asymmetric and because the field is only strictly known along a line on the bulk surface, the calculated flux values remain an estimate. For an asymmetric profile such as that for 60 K in Figure 4.5a, the calculated flux corresponds to an effective field profile as a function of radius which is the average of that for the positive and negative radial distances. The calculation method therefore gives at least a rough estimate of the flux for asymmetric trapped fields.

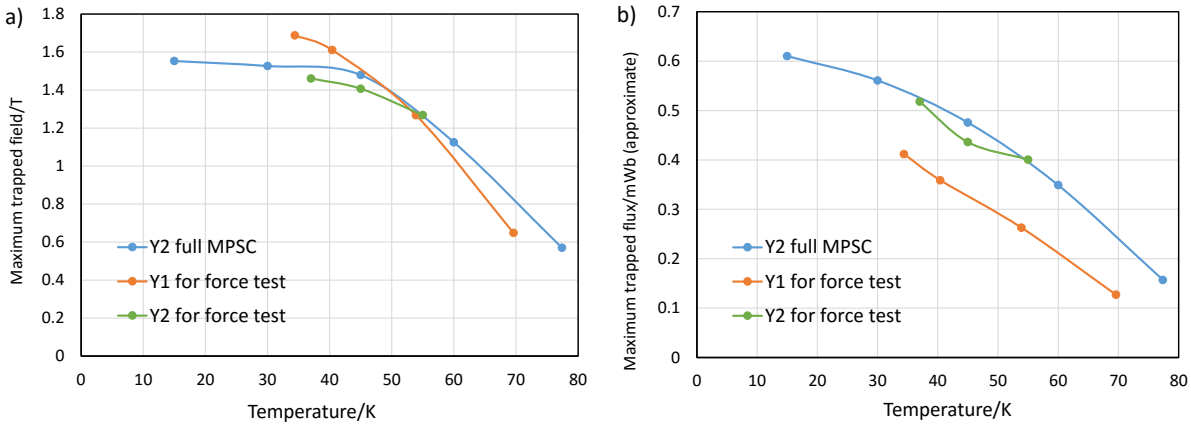

Figure 4.6: a) Maximum trapped field and b) trapped flux for 25.5 mm diameter YBCO bulks used for levitation force testing. Values are for the end of each stage during MPSC. Flux values are only approximate due to possible asymmetries present in the trapped fields.

Figure 4.6a shows the maximum trapped field for the magnetization sequences applied to Y1 and Y2. For Y2, the values are not for the bulk centre, as the peak in field is off centre for this bulk. The general trend is a large increase in the field that can be trapped from 77 K down to around 40 K, after which the trapped field tends to saturate. It also appears that Y1 can trap the highest field (and a much higher centre field). The relatively low trapped field for Y1 at 70 K is probably due to applying a maximum of only 3 T at that temperature, which probably should have been higher. The flux behaviour is different to the field behaviour in two ways. Firstly, the trapped flux does not saturate at lower temperatures in the tested range, but keeps increasing down to 15 K. This behaviour is also present for the trapped field profiles reported in Section 5.2 and 5.3 and appears to be generally true for bulk samples. Secondly, despite trapping a lower peak field for most temperatures, bulk Y2

traps a higher flux at all temperatures, given its 'M' shaped profile, and so both samples have their separate advantages.

This section focussed on bulks Y1 and Y2 (used for most of the levitation force testing), which were YBCO rather than GdBCO. Although GdBCO bulks can typically trap higher fields at 77 K and have become popular for producers of large bulks such as Nippon steel (see Section 1.5.1), the GdBCO bulks tested in the system could not trap a higher field or flux when magnetized using PFM compared to the YBCO bulks. The reason for this is not clear, as field cooling tests performed by the Bulk Superconductivity group, Engineering department, Cambridge (the source of the bulks in question) on typical YBCO and GdBCO bulks they produce, show that GdBCO generally traps a higher field. One likely explanation is that, despite its higher average $J_c(B)$ (at least for the higher temperature MPSC stages), the GdBCO bulks suffer from greater thermal instability which negates the benefit of the higher J_c, making them less suitable for PFM. This could, for example, come from a greater J_c difference between the GSB and GSR parts of the bulk, which would not necessarily be apparent from field cooling data. In future a systematic study is needed to establish if there really is a difference in the relationship between field cooled and PFM trapped field performance for YBCO and GdBCO bulks of the ~ 25 mm diameter size considered in this thesis.

4.2 Levitation force curves

The procedure for conducting the levitation force tests was to move the YBCO bulk into the coaxial MgB_2 tube, which lies above and away from the pulsed field coil, as illustrated by Figure 3.1 in Chapter 3. Both bulks were then cooled below 39 K to achieve field cooling of the MgB_2 tube before the force-displacement curves were produced. The trapped field states of the two YBCO bulks Y1 and Y2 used for the tests are shown by the lowest temperature curves in Figure 4.4 and Figure 4.5 respectively. The MgB_2 bulk tube used for the force tests (see Figure 4.8 for dimensions) was produced by Alessandro Figini-Albisetti and Giovanni Giunchi of Edison Spa, Milan, Italy, using the reactive liquid Mg infiltration process as introduced in Section 1.5.3.

4.2.1 Permanent magnet benchmark

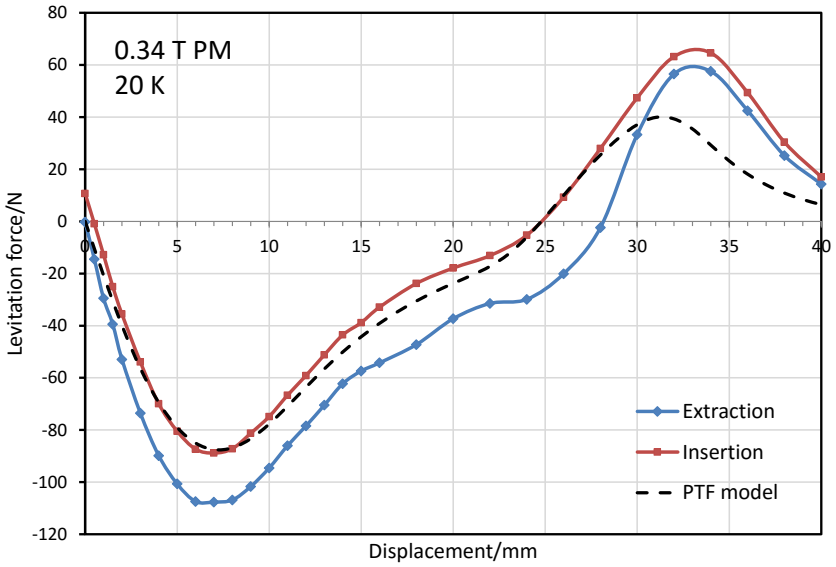

Figure 4.7: Levitation force curve for a 25 mm x 10 mm NdFeB PM with a peak field of 0.34 T inside the MgB_2 tube at 20.2 K. A PTF model prediction is also shown for comparison.

A levitation force test was conducted for a high strength rare-earth PM of a similar size to the YBCO bulks in order to compare to the results for YBCO and also to validate the force measurement system. The force results shown in Figure 4.7 fit the expected behaviour for a PM as confirmed by modelling. The PTF model was used as described in Section 2.4.1 to give the force between a PM of the same remanent field as that determined for the real PM and a coaxial MgB_2 tube of the same dimensions as used experimentally. A comparison of the modelled and experimental curves shows that there is some hysteresis, which is expected for a small amount of flux penetration, but the MgB_2 J_c is sufficiently high at 20 K to largely shield the superconductor from the relatively small field of the PM. Although the shape of the modelled curve is a good fit, it is lower than it should be given that the PTF model is always an upper limit for levitation force. The origin of this error may be that the stainless steel sample holder became slightly magnetized, as it seems to be weakly magnetic at room temperature. Another possibility is that the PM was slightly off-centre when field cooling occurred. Field cooling off-centre (so that the PM and MgB_2 are not coaxial but their axes are still parallel) is likely to give rise to higher axial forces.

4.2.2 YBCO bulk Y1

The exact dimensions of the bulk – bulk levitation force configuration tested are shown in Figure 4.8. A photo of the coaxial configuration and sample holders was shown previously in Figure 3.6a. After the MPSC procedure finished at 35 K, the YBCO bulk was moved into the MgB_2 tube. However, as 35 K is slightly below the T_c of MgB_2, a pulse of heat was delivered to the cold head (which is very

close to the MgB_2 tube) to briefly increase its temperature and destroy any induced currents during insertion. The thermal inertia was high enough for the YBCO bulk not to have experienced a significant temperature rise, although a small temperature fluctuation would likely have had a negligible effect on the trapped field anyway.

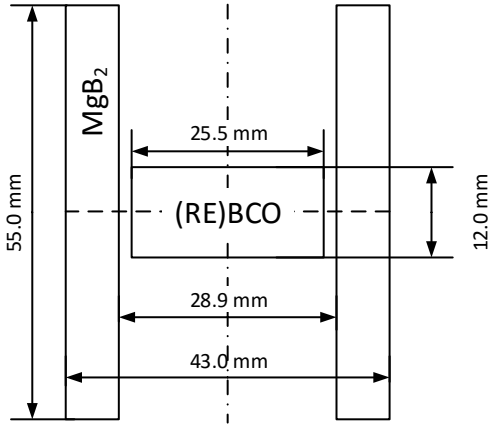

Figure 4.8: Exact dimensions of the experimental bulk – bulk bearing geometry composed of a coaxial YBCO bulk and MgB_2 hollow cylinder.

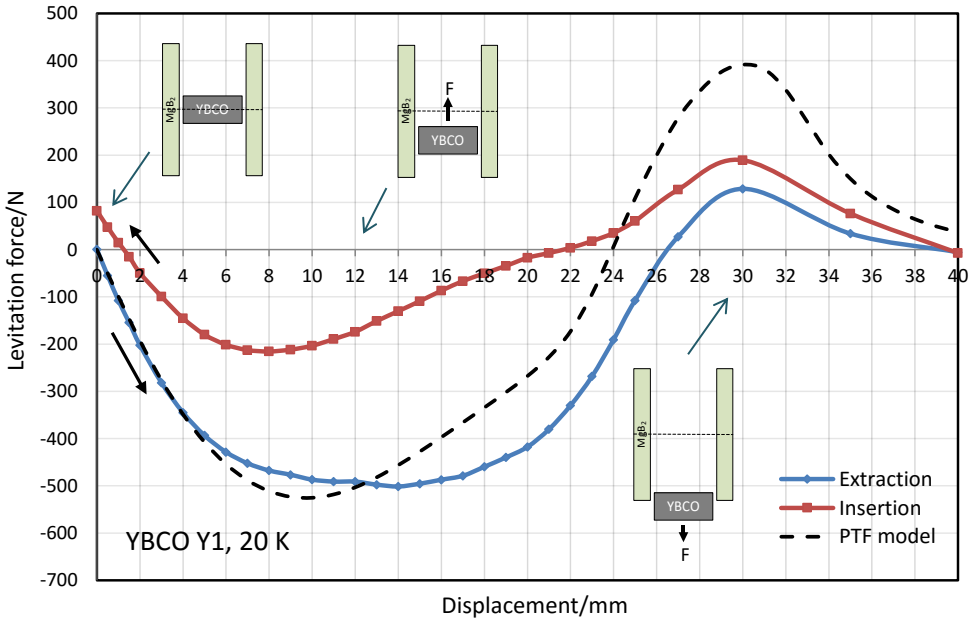

Figure 4.9: Levitation force curve for 1.68 T magnetized YBCO bulk Y1 inside the MgB_2 tube. A peak restoring force of 501 N was measured during extraction. The force resulting from a PTF model for an YBCO bulk with approximately the same trapped flux is also shown.

Figure 4.9 shows the levitation force results for the YBCO bulk Y1. The extraction of the bulks leads to a large stable restoring force, peaking at 501 N at a displacement of 12 mm. When returning after 40 mm of displacement, the insertion force has a similar behaviour but a peak force less than half that of the extraction curve, indicating large hysteresis. The hysteresis indicates that for large

displacements, significant flux penetration has occurred due to the high fields the MgB_2 is exposed to, which would also cause a reduction in the J_c of the MgB_2. A PTF model with YBCO shielding as described in Section 2.4.3 was used to simulate the experiment and gives good agreement for the first 4 mm of displacement, and good qualitative agreement for the rest of the extraction curve. The fact that the peak of the extraction curve is broad is partly due to flux penetration but also due to force creep [64]. The measurement was conducted by manually rotating the motor shaft and recording the force at 0.5 mm intervals as the system was not fully complete at the time of measurement. This led to an average movement speed of around 0.1 mm/s, slow enough for force creep to occur.

For the PTF model, the YBCO bulk was assumed to have the same flux as that estimated for the Y1 trapped field profile, but using a uniform current. This gave a 2.7 T centre trapped field 0.5mm above surface. A model with a uniform current over a limited depth (as in Figure 2.16a) was also created, with the depth chosen to give a ratio between centre field and flux that matched the experiment. However, the force curves for both models were almost identical, so the simpler model with uniform current flowing around the whole bulk was used. The calculated flux following PFM is very useful for relative comparisons but is less reliable as an absolute measure of the trapped flux of a bulk. It is therefore not surprising that the modelled curve should probably have a larger force minimum, suggesting that the real trapped flux has been slightly underestimated. Also, the fact that the modelled bulk (which had similar flux to the real bulk but a much higher peak trapped field) gave a reasonable match to the extraction force curve, suggests that a bulk – bulk bearing is an application for which trapped flux matters more than peak trapped field.

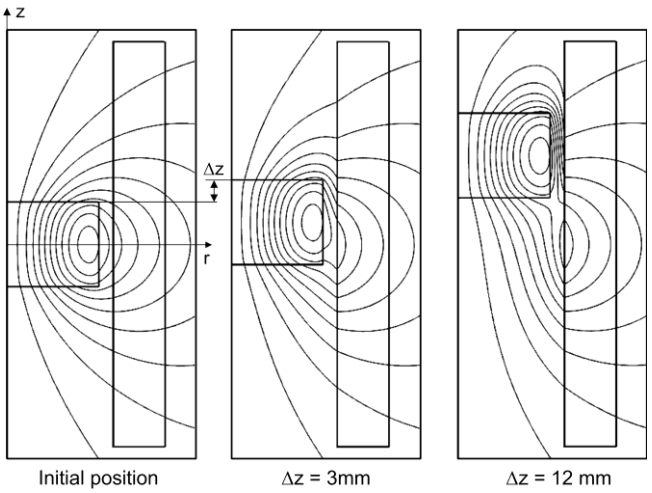

Figure 4.10: Simulation of the PTF model applied to the magnetized YBCO – MgB_2 force experiment, assuming uniform YBCO current density. High levels of flux line distortion occur for larger displacements.

The origin of the large hysteresis occurring for large displacements can be better seen by considering the field distortion predicted by the perfectly trapped flux model, which is illustrated in

Figure 4.10. At 12 mm displacement, when the bulk encounters a part of the MgB_2 with a small perpendicular field, significant flux compression takes place, leading to a high flux density of 2.7 T on the wall of the MgB_2, enough to cause significant penetration and reduction in J_c.

4.2.3 Temperature dependence using YBCO bulk Y2

Bulk Y2 was also used in a levitation force test. 20 K can considered an ideal temperature to operate a bulk YBCO – bulk MgB_2 bearing as the J_c of MgB_2 is sufficiently high, yet 20 K is not unfeasible for cryocoolers to achieve and could even be achieved by using liquid hydrogen. However, it is important to know the force behaviour at higher and lower temperatures. For this reason, levitation force curves were produced at 12, 20 and 30 K as can be seen in Figure 4.11.

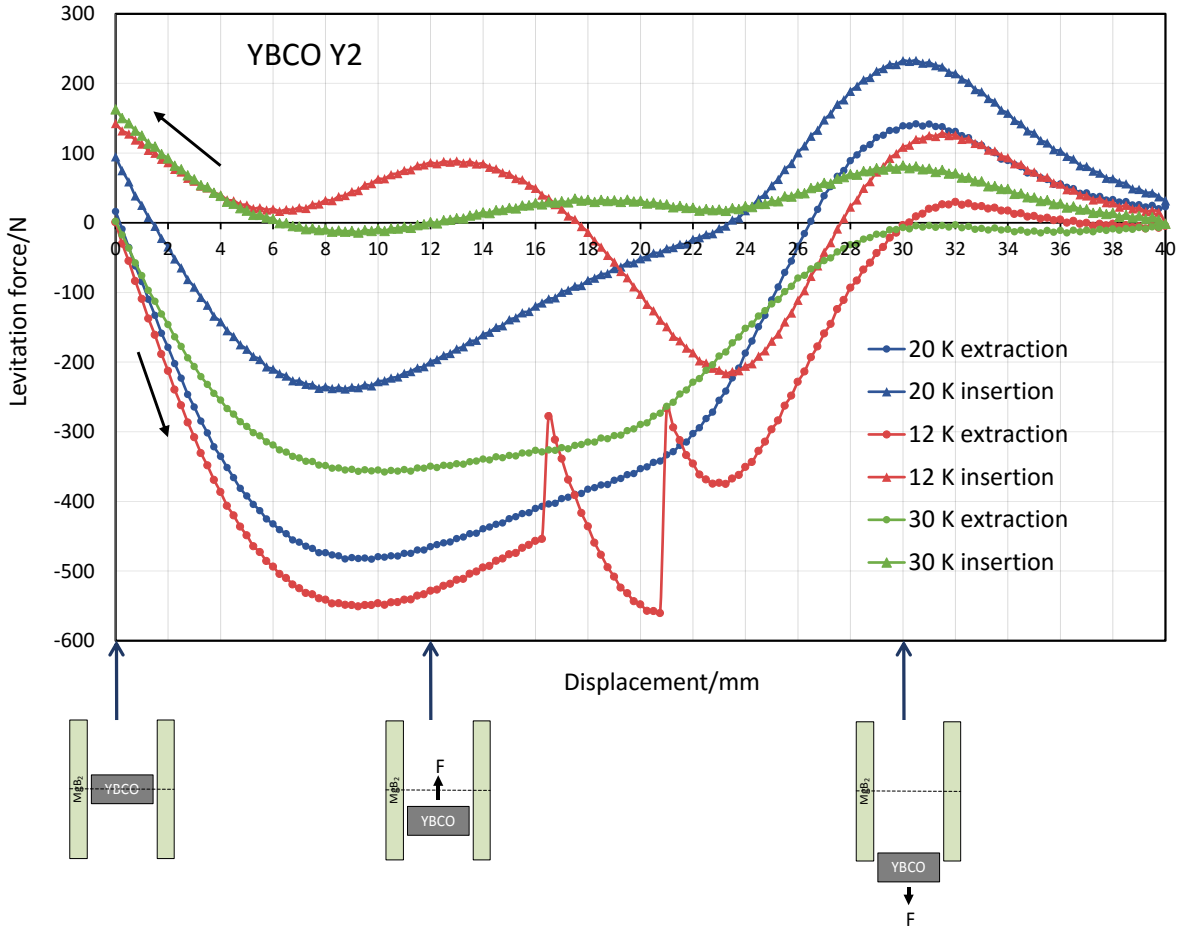

Figure 4.11: Levitation force curves for the YBCO bulk Y2, magnetized with an 'M' shaped trapped field profile, inside the MgB_2 tube. The levitation behaviour was investigated for three different temperatures. The highest temperature of 30 K showed very large hysteresis, whereas the lowest temperature curve for 12 K suffered from force jumps resulting from macroscopic flux jumps.

It is firstly worth focussing on the curve for 20 K and comparing it to the previous result for bulk Y1. The curves are similar but, as expected, the Y2 curve has a less broad force minimum as the force curve was produced by the automated system using a speed of 1 mm/s (0.25 mm measurement

interval), which is typical for levitation force measurements [107]. The most notable comparison, however, is the magnitude of the largest force. According to the trapped flux estimates as shown in Figure 4.6b, bulk Y2 has a 26 % higher trapped flux than Y1 and so should in theory have a much higher levitation force. In fact, the PTF model used for Y2 (which had a uniform current over a depth of 4 mm from the outer cylindrical surface to simulate an 'M' shaped profile) gave a peak force of 888 N, significantly higher than observed. For this reason it is not shown in Figure 4.11.

There are a number of reasons why the force is lower than expected from theory. As the calculated trapped flux for the bulk is only an estimate, it could be out by 10 – 20 %, which would make a larger percentage difference in maximum force. An example of a possible source of overestimation is the fact that the field profile is measured along the growth sector boundaries, which often have a larger field that that growth sector regions. There is also a possibility of flux creep for the flux trapped at the outer edges of the bulk, which contribute significantly to the trapped flux for Y2. This could have occurred during the movement of the bulk up into the MgB_2 tube. Also, for bulks with high trapped field in the outer radius of the bulk, leading to 'M' shaped profiles, it can be seen that the flux density in the gap between the bulk and the MgB_2 tube is larger than for a conical trapped field profile of with the same overall flux. This suggests that the PTF model should give more of an overestimate of the real force for Y2 than for Y1.

The data for 30 K show the force behaviour for a lower J_c in the MgB_2 bulk. Not only is the maximum levitation force less than measured at 20 K, but also the hysteresis is significantly higher. Figure 4.12 illustrates the currents that would be induced in the wall of the MgB_2 due to a moving field source. For the insertion curve at 30 K, the YBCO bulk experiences relatively large fields produced by the currents induced during extraction. These lead to a lack of shielding and the low force values observed.

The lowest temperature curve, 12 K, has the highest maximum force but exhibits very interesting force jump behaviour, which may not have been previously reported between two bulk superconductors. The reason for the sudden drop in force must be a sudden macroscopic flux jump rather than any mechanical damage or slippage in the components (which were carefully examined). The jump is associated with the large flux densities that build up due to flux distortion as shown in Figure 4.10. However, even if the field becomes so high that that it exceeds the irreversibility field for MgB_2 (see

Figure 1.22), the drop in force should be gradual and smooth rather than sudden. The behaviour must also be due to thermal instability occurring at low temperature due to low heat capacity. This instability at low temperatures cannot be modelled even using a full critical state model (which would be able to incorporate irreversibility field), let alone the PTF model. After a jump of flux has

occurred in the bulk, the MgB_2 trapped flux has partially redistributed or relaxed into a lower energy state closer to the field cooled state, which explains why the force curve after a jump is similar to a section of the curve at a lower displacement. The existence of the force jumps shows that there is no benefit in operating at temperatures much lower than 20 K due to thermal instability. It does not necessarily imply that force jumps would occur at 20 K if using a (RE)BCO bulk with a much higher trapped field than Y1 or Y2 had.

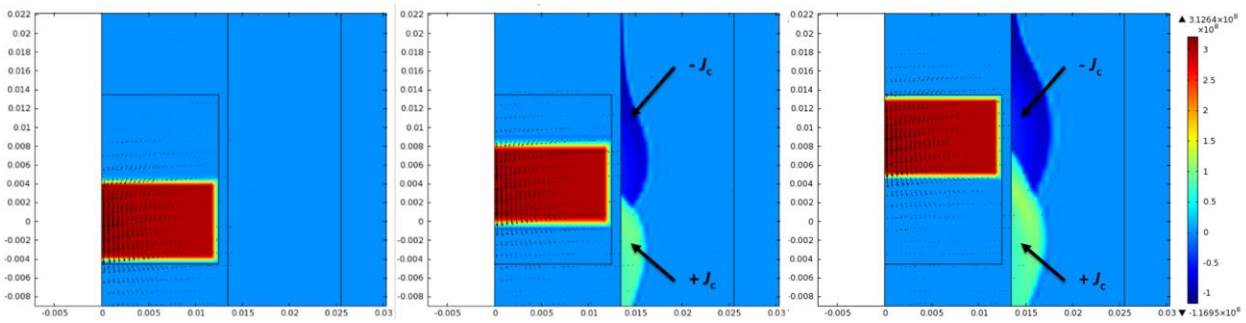

Figure 4.12: Illustrative critical state model for a moving field source inside a field cooled superconducting tube. The levitation force results from shielding currents induced in the wall of the tube. The field source is modelled as a cylinder with a uniform current circulating, giving a 1.2 T surface field but no superconductivity or shielding. The critical current density for the tube is modelled as $J_c = 0.01\ J_c(B, 20K)$ for MgB_2, i.e. a hundredth of what it should be, to exaggerate the depth of induced currents.

4.2.4 Hysteresis force cycling

For a real superconducting magnetic bearing, such as the ones developed for flywheel energy storage, the two essential criteria for the levitation force are negative stiffness for stability, and low hysteretic losses. This means that on the force displacement curve, a load cannot be applied close to the peak restoring force otherwise the stiffness will be too low. To investigate the stiffness and hysteresis for bulk – bulk levitation, a load of approximately 135 N was applied to a magnetized GdBCO bulk, giving 3 mm of displacement. Figure 4.13b shows the full force behaviour for the bulk (conducted separately to the stiffness test) as well as the trapped field profile. A 3 mm displacement should be a very safe place on the force-displacement curve in which to levitate a load given the negative stiffness. The bulk was cycled ± 1 mm, 10 times as shown in Figure 4.13a to simulate the perturbations that might be experienced by a load supported by a magnetic bearing. The hysteresis is not very significant, proving that although the force loop for large displacements gives large hysteresis, the loop that would realistically be experienced by a load in applications does not lead to high losses. The hysteresis settles into the same loop after less than 10 cycles.

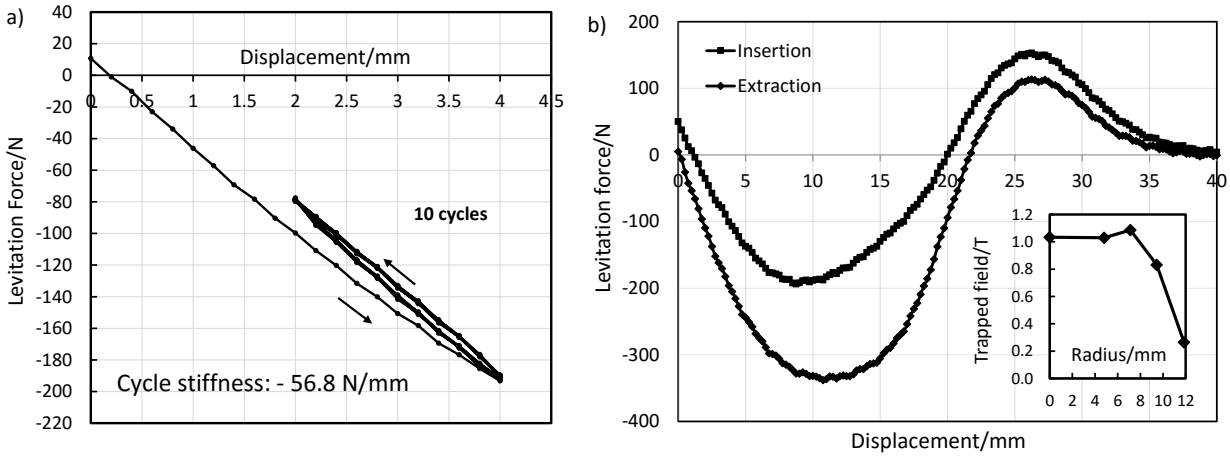

Figure 4.13: a) Levitation force cycling curve for a 25 mm x 12 mm GdBCO bulk magnetized with a 1 T flat-topped field profile. Hysteresis is shown for 10 cycles. b) Full levitation force curve and trapped field profile (inset) for the same bulk.

5 Composite superconducting structures for thermally stable high field permanent magnets

Pulsed field magnetization of bulks is a technology that is under development and far from optimised. As outlined in Section 1.7, significant progress has been made in using pulse sequences to maximise the field and flux that can be trapped, however a fundamental redesign of the bulk itself has not yet been made to optimise its thermal and mechanical properties for trapping high fields. Creating a composite bulk with materials other than (RE)BCO allows these other materials to improve the poor thermal and mechanical properties of bulk (RE)BCO without changing the overall bulk size. By having improved trapped field performance, the structures reported make the use of magnetized bulks more attractive in practical applications such as motors, generators [108, 109] and superconducting bearings [110]. The most significant progress in realising a composite superconducting bulk with high thermal stability, was made by creating stacks of coated conductor as detailed in Sections 5.4 and 5.5. The unique properties of these stacks allowed them to trap higher fields than any other samples magnetized for this thesis.

5.1 Modelling bulks with embedded high thermal conductivity structures

Rapid heat generation is one of the biggest problems facing pulsed field magnetization of (RE)BCO superconducting bulks compared to other methods of magnetization. The effect of various thermal conductivities in the *ab*-plane (k_{ab}) and *c*-axis (k_c) of a bulk on its trapped field performance following pulsed field magnetization was modelled [111]. Highly thermally conducting copper structures embedded in the bulk material were investigated as a practical way to locally increase k_{ab} and k_c, giving greater thermal stability and reducing flux creep following a pulse. The structures investigated increased the trapped field and flux by a maximum of around 30% without increasing the size of the bulk. The results of the modelling provided the motivation behind creating and testing composite structures made from bulk YBCO as reported in Sections 5.2 and 5.3.

5.1.1 Modelling formulation and parameters

The maximum trapped field resulting from pulsed magnetization is always less than that from field cooling due to the heat generated by rapid flux motion. This heat is mostly generated in the bulk periphery and usually causes a temperature rise greater than 10 K, leading to a large decrease

in J_c. The modelling reported follows on from pulsed field modelling focussing on a bulk with real thermal parameters [112] by conducting a full parametric sweep of thermal conductivity and its effect on heat flow, as well as modelling the concept of embedded metallic structures. Predicting the effect of a large range of theoretical thermal conductivities on the performance of a magnetized bulk is useful in probing best case limits and also for helping design the embedded structures.

The modelling of pulsed field magnetization was carried out using the H-formulation in COMSOL Multiphysics 4.2a as outlined in Section 2.3, but this time coupled with the heat transfer module to simulate thermal effects. The framework is similar to that used by Fujishiro et al. [112]. The following *E-J* law, where $E_0 = 1 \times 10^{-4}$ V m^{-1} was used:

$$E_\phi = E_0 \left(\frac{J_\phi}{J_c(B)} \right)^n \tag{5.1}$$

The heat generated in the bulk (power dissipated per unit volume) was given by the following equation:

$$Q = E_\phi J_\phi \tag{5.2}$$

The Kim model was used to describe the dependence of the critical current density on field:

$$J_c = \frac{J_{c0}(T)}{1 + B/B_0} \tag{5.3}$$

with the temperature dependence of J_c given by:

$$J_{c0}(T) = a \left[1 - \left(\frac{T}{T_c} \right)^2 \right]^{3/2} \tag{5.4}$$

The applied field pulse was described by half a cycle of a sinusoidal waveform:

$$B_{ext} = B_a \sin\left(\frac{\pi t}{2t_0} \right) \quad 0 < t < 2t_0, \qquad B_{ext} = 0 \quad t \geq 2t_0 \tag{5.5}$$

The total cooling power applied to the cold head (see Figure 5.1) used in the simulation is described by the following function.

$$\begin{aligned} P_0 &= 0 && T < T_0 \\ P_0 &= Q_c(T - T_0) && T_0 \leq T \leq (T_0 + 15) \\ P_0 &= 15 Q_c && T > (T_0 + 15) \end{aligned} \tag{5.6}$$

This gives realistic cooling above a certain equilibrium temperature T_0, with total cooling power saturating to a maximum of 30 W for a temperature rise greater than 15 K. These parameters together with Q_c approximately reflect the real cooling power of the Variox cryostat used in the Magnetoforce system for pulse magnetization.

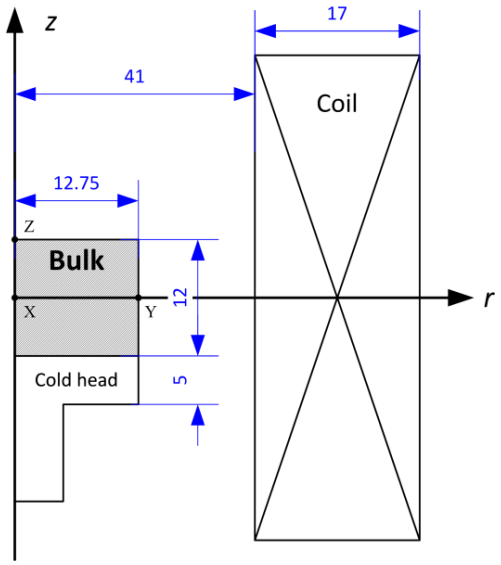

Figure 5.1: Geometry and dimensions (mm) of 25.5 mm diameter bulk modelled for a bulk cooled by a copper cold head. The isolated bulk model had the same dimensions, but without the cold head. The dimensions of the coil match the experimental system as described in Section 3.2.1.

Table 5.1 shows the values of the parameters used in the modelling. An important feature of these simulations is the splitting of the models into two time domains, $0 < t < 0.1$ s (which includes the 28 ms pulsed field) and $0.1 \leq t < 10$ s. For the first time period, in which the pulsed field is applied, $n = 9$ was used in the *E-J* law; and for the second time period, modelled to observe decay, $n = 21$ was used. Typical n values for bulk YBCO are around 20. However for the current study, it was found that $n = 9$ gave a very similar solution to $n = 21$ during the pulse and for $t < 0.1$ s. It was therefore decided to use the lower value, which is more stable to solve and avoids the very high E fields that can be generated during a pulse for high n values. After 0.1 s, $n = 9$ gives excessive flux creep so it is necessary to use $n = 21$ to achieve a physically accurate flux creep rate, as confirmed by comparison to experimental data on flux creep in magnetized bulks [113]. The discontinuity in n, although not ideal, leads to a more reliable trapped field value 10 s after the pulse.

Table 5.1: Descriptions and values of parameters used in modelling.

Parameter	Description	Value
k_{ab0}	Thermal conductivity of real bulk (RE)BCO in the *ab*-plane	20 W $m^{-1} K^{-1}$ [114]
k_{c0}	Thermal conductivity of real bulk (RE)BCO along *c*-axis	4 W $m^{-1} K^{-1}$ [114]
k_{ab}	Theoretical modelled thermal conductivity of bulk in the *ab*-plane	See Table 5.2
k_c	Theoretical modelled thermal conductivity of bulk along *c*-axis	See Table 5.2
C	Heat capacity of bulk	1.32×10^2 J $kg^{-1} K^{-1}$ [114]
n	*n*-value in equation (5.1)	9 for $0 \leq t < 0.1$ s, 21 for $t \geq 0.1$ s
ρ	Density of bulk	5.9×10^3 kg m^{-3}
E_0	Electric field constant in equation (5.1)	1×10^{-4} V m^{-1}
B_0	Flux density constant in equation (5.3)	1.3 T
a	Constant in equation (5.4)	1×10^9 A m^{-2}
T_c	Critical temperature of bulk	92 K
T_0	Equilibrium temperature of bulk	40 K
Q_c	Cooling power increase per degree temperature rise	2 W K^{-1}
t_0	Pulsed field rise time	14 ms
B_a	Applied pulsed field amplitude (bulk diameter)	8 T (25.5mm), 9.5 T (46mm)
$k_{cu}(T)$	Thermal conductivity as a function of temperature for copper, RRR=100	See [115] (1494 W $m^{-1} K^{-1}$ at 40 K)
$C_{cu}(T)$	Heat capacity as a function of temperature for copper, RRR=100	See [115] (57 J $kg^{-1} K^{-1}$ at 40 K)

The equilibrium temperature T_0 was chosen as 40 K in the study as this is a typical temperature at which pulsed magnetization experiments are performed. The properties of copper depend strongly on temperature in the cryogenic region. To model the copper structures and cold head, temperature dependent forms for the thermal conductivity and heat capacity were used for copper with RRR = 100, as this purity of copper is widely available. Modelling not presented here has shown that higher purity copper, although having a higher thermal conductivity at 40 K, does not perform significantly better at conducting heat away for the magnetized bulk. This is because the temperature rises involved bring the copper up to a temperature where the variation of thermal parameters with purity is small. The thermal conductivity of (RE)BCO bulks such as YBCO is anisotropic, with 5 times higher thermal conductivity in the *ab*-plane than along the *c*-axis. The aim of the first section of modelling reported is to show how varying the anisotropy affects the final trapped field by altering the dynamics of heat flow. Table 5.2 shows the values of the two thermal conductivities chosen for the parametric sweep. The sweep mostly consists of keeping one thermal conductivity value constant whilst varying the other, as well as four extreme cases, modelled for a bulk cooled by a cold head.

The mesh used for the superconducting domain was a mapped mesh as shown in Figure 5.2. This allowed precise control over the fineness of the mesh and the number of elements for that domain, which was important for minimising solution time without leading to instability or unreliable results. A detailed list of the modelling settings can be found in Table 5.3, which also shows the typical time taken to solve the models.

Table 5.2. Parametric sweep map for the thermal conductivity (W m^{-1} K^{-1}) combinations modelled. R represents the approximate thermal conductivity of real (RE)BCO bulks.

k_c \ k_{ab}	1	5	10	20	50	100	1000
1							
4				R			
10							
20							
50							
100							
1000							

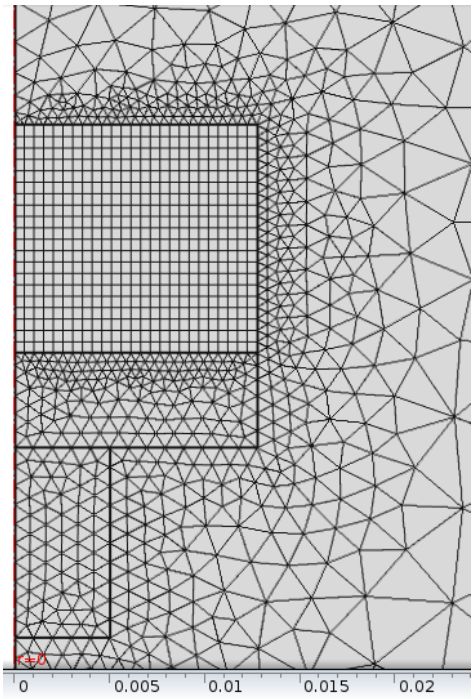

Figure 5.2: Mesh used for the 25.5 mm diameter bulk with cold head model.

Table 5.3: Modelling settings and solution details for the bulk magnetization models with cold heads.

Parameter	Value
Number of mesh elements	≈ 3100 (both 25.5 and 46 mm bulk models)
ρ_{air}/Ω m	1×10^{6} (n=9), 1 (n=21)
Computer specifications	Intel i7 processor, quad core, 12 GB memory
Maximum time step/s	$3 - 8\times10^{-6}$ (up to 0.1 s) 1×10^{-3} (0.1-10 s)
Typical solution times	34 min up to 0.1 s, 15 min 0.1-10 s (25.5 mm bulk) 53 min up to 0.1 s, 4 min 0.1-10 s (46 mm bulk structure A)
COMSOL solver	BDF

5.1.2 Thermal conductivity parametric sweep: isolated bulk

The geometry for the case considered in this section is the same as that shown in Figure 5.1 except without a cold head. By studying the effect of thermal conductivity on a thermally isolated bulk, it is possible to see how altering only the internal flow of heat affects the final trapped field. To model this case, the bulk considered was not attached to a cold head or heat sink, but was cooled only by minimal conduction of heat by helium gas from all sides of the bulk (convection was ignored). The semi-infinite gas domain around the bulk had a thermal conductivity of 5 W m^{-1} K^{-1} and a volumetric heat capacity of 1200 J K^{-1} m^{-1}, with heat energy simply diffusing from the bulk into this domain rather than being removed (Q_c is not relevant in this case).

Figure 5.3a and b shows the results of the parametric sweep in k_{ab} from 0.1 s and 10 s respectively from the beginning of the pulse. The 10 s curves can be considered as the final state of the trapped field, as flux creep is not as significant after this time as it evidently is after 0.1 s. It is clear that, in general, a high thermal conductivity in the *ab*-plane decreases the trapped field but increases the trapped flux. However, reducing k_{ab} below k_{ab0} can actually increase the trapped field. These results can be understood by considering the induced current front during a pulse as flux penetrates the sample. It is at the current front that the heat is actually being generated. The heat energy generated as the flux penetrates has two options. If k_{ab} is low, it will mostly stay where it has been generated on the timescale of the pulse. This can partly be seen in Figure 5.3c for the temperature in a bulk with k_{ab0} = 20 W m^{-1} K^{-1}. For this case most of the heat energy has not had time to flow to the centre of the bulk during a pulse, keeping the region into which the flux is penetrating at a low temperature and therefore high J_c state. This leads to higher induced currents in the inner region than for the periphery of the bulk, hence a higher centre field, but lower overall flux. Conversely, for a high k_{ab} such as k_{ab} = 1000 considered in Figure 5.3c, the heat energy quickly flows to the inner region of the bulk, overtaking the front of induced current and increasing the temperature of the inner region before the penetrating flux has induced current there. The periphery of the bulk does not reach such a high temperature as a result of this inward heat flow, leading to a higher current density in the outer region of the bulk than in the inner. The result is a lower centre trapped field but a higher trapped flux.

The previous discussion highlights how the flow of heat in the direction of the penetrating flux front, or induced current front, can influence the final current distribution and therefore trapped field and flux. It can also be seen from Figure 5.3 that there are large local temperature increases inside a bulk during pulsed field magnetization, especially in the bulk periphery, but the maximum rise can be reduced by a higher k_{ab}. For a thermally isolated bulk, the results show that a high k_{ab} gives a slight improvement in the trapped flux without really affecting the final trapped field.

The results for the k_c parametric sweep are not shown, as k_c had only a negligible effect on the trapped field and flux (a maximum change in field of < 1%, and < 2% in flux). This is not surprising, as the flux penetrates mostly along the *ab*-plane from the outside of the bulk rather than coming in from the top and bottom surfaces of the bulk.

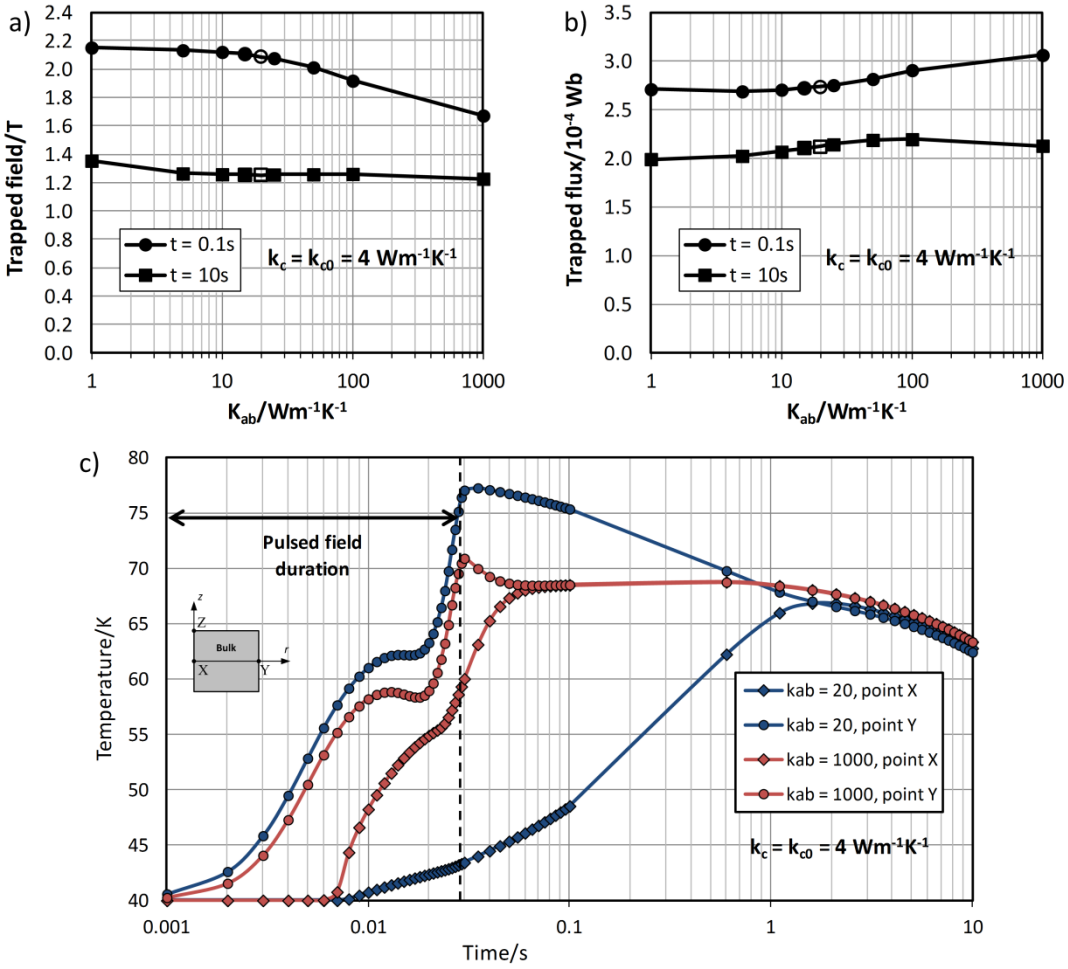

Figure 5.3: a) Trapped field results calculated at point Z for a parametric sweep in k_{ab} after 0.1 s and 10 s with $k_c = k_{c0}$. Open markers show results for k_{ab0}. b) Results for the trapped flux calculated by integrating the field over the top surface of the bulk. Open markers show results for k_{ab0}. c) Temperatures at points X and Y for $k_{ab} = k_{ab0}$ compared to a high theoretical k_{ab} = 1000 W m^{-1} K^{-1}, during and after pulsed magnetization which has a duration of $2t_0$.

5.1.3 Thermal conductivity parametric sweep: bulk with cold head

The most popular method of cooling a magnetized bulk is by attachment to a cold head [22]. A bulk of the same dimensions considered previously was modelled in thermal contact with a cold head of the cooling power specified by equation (5.6) and Figure 5.1. The thermal properties of the copper were described by $k_{cu}(T)$ and $C_{cu}(T)$ in Table 5.1. In all cases, eddy current heating is ignored in the copper cold head, which can be practically achieved by introducing slits or having a laminated structure as used in Sections 5.2 and 5.3 to minimise induced currents.

The key difference compared to the results for an isolated bulk is that k_c now plays an important role in heat flow because cooling is provided from the bottom surface. The results for the trapped field and flux shown in Figure 5.4 are all higher than the corresponding values in Figure 5.3 for the

isolated bulk, showing the significant enhancement that effective cooling can bring (17 % for field and 20 % for flux for k_{ab0} and k_{c0}, with higher increases if $k_c > k_{c0}$).

For this cooling method, the most significant results are for the k_c parametric sweep. A high k_c leads to effective heat removal to the cold head, increasing both the trapped field and flux. For k_c = 1000, the trapped field is over 1.8 T, compared to the value of 1.46 T for the real bulk thermal conductivities. The trapped flux for this value also shows reduced decay. Also shown in Figure 5.4c and d as coloured markers are the results for the four extreme combinations of k_c and k_{ab}. All other points show results where one thermal conductivity is always kept to a real value. The changes due to a low k_{ab} value can now be seen as negligible. Although k_{ab} = 1000 gives a significant enhancement in the trapped flux for t = 0.1 s (and a significant decrease in maximum trapped field), this difference disappears for t = 10 s, with the results showing no change in the final trapped field or flux (t = 10 s) when having a very high thermal conductivity in both directions. This result can be understood by considering how the cold head allows effective heat flow in the *ab*-plane. For a high k_c, heat anywhere in the bulk can quickly travel down the *c*-axis, along the cold head and back up the *c*-axis at a different radius in the bulk. It is therefore not necessary to have high thermal conductivity in both directions. These results can guide efforts to increase thermal conductivity in the direction which matters most, depending on the cooling configuration for the application.

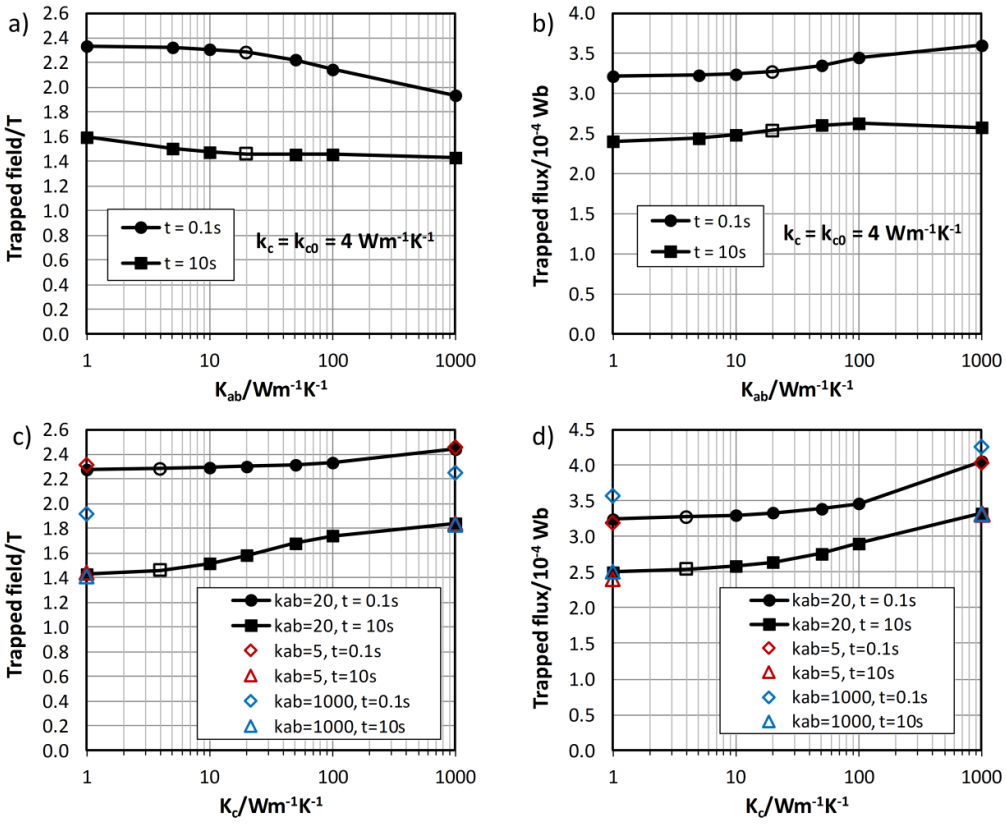

Figure 5.4: Trapped field results for parametric sweeps in k_{ab} and k_c for a bulk cooled by a cold head. Extreme combinations of thermal conductivity parameters are shown by the blue and red coloured markers; open black markers show results for k_{ab0} and k_{c0}. High k_c gives the most significant improvement in trapped field and flux.

5.1.4 Planar and ring structure designs

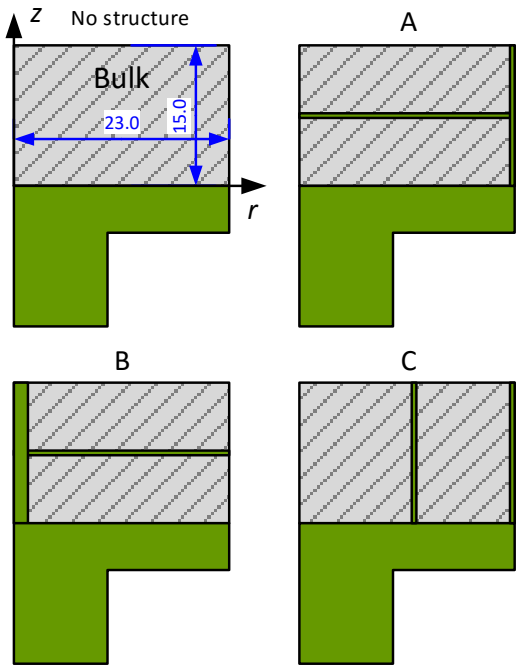

Figure 5.5: Drawing showing the various structures (in green) modelled for a 46 mm diameter bulk cooled by a cold head. The cold head and structures were both modelled as copper, with zero contact resistance assumed between the copper and bulk. The bulk had thermal conductivities k_{ab0} and k_{c0}. The thickness of the disks and rings is 0.5 mm, and the central rod for configuration B is 3 mm in diameter. Drawing to scale.

The results in this section are for a larger 46 mm diameter bulk and cold head. The results of the previous section for a smaller bulk show how increasing the thermal conductivities in a bulk can lead to significant enhancements in trapped field and/or flux after pulsed field magnetization. The greatest enhancements occur for thermal conductivities too high to be realized with existing superconducting materials, but the results are still useful. It is possible to increase the effective thermal conductivity in the *ab*-plane or *c*-axis by creating a composite structure with metal (or other high thermal conductivity materials like sapphire) planes or disks embedded into the bulk structure. These structures have the purpose of channelling heat away as quickly as possible in a particular direction to a cooling surface, in this study the base of the bulk where a cold head is attached. Experimental tests on a (RE)BCO bulk with an aluminium wire inserted in the centre for thermal stability has already been performed [116]. This configuration is related to structure B. The dimensions of the bulk considered and the three conducting structures modelled are shown in Figure 5.5. Only the real values of thermal conductivity, $k_{ab} = k_{ab0} = 20$ W m^{-1} K^{-1} and $k_c = k_{c0} = 4$ W m^{-1} K^{-1}, were used for the (RE)BCO bulk components. The diameter of the bulk was 46 mm, larger than the 25.5 mm bulk used in the parametric sweeps, as a larger bulk would in practice be more suited to cutting and assembling into a composite structure, and 46 mm diameter bulks are now commonly

used. It is very important to note that none of the structures considered change the dimensions of the overall composite bulk. The volume of superconductor is actually reduced. This is a constraint expected for any engineering application. The cold head and metallic structures were modelled as copper with eddy current heating ignored.

5.1.5 Trapped field results

The trapped field profiles for the structures considered are shown in Figure 5.6. The inset shows that there is very little variation in the profiles at t = 0.1 s. However the crucial flow of heat out of the bulk via the copper structures has a significant effect on the temperature distribution, and therefore flux creep, after 0.1 s. As a result, significant differences appear in the profiles at t = 10 s.

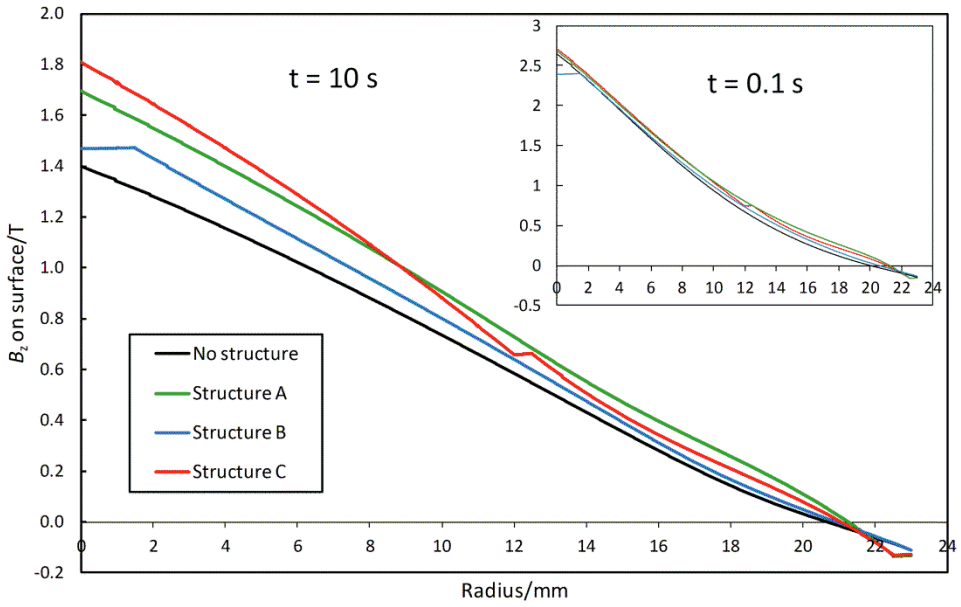

Figure 5.6: Trapped field on the surface of a 46 mm diameter bulk for various embedded copper structures. No real enhancement is seen at t = 0.1s, but after 10 s flux creep causes significant differences to appear in the profiles.

Structures A and B enhance the trapped flux by increasing the effective k_{ab} of the bulk composite, as expected from Figure 5.4b, but also increase the trapped field. This is because k_c has also been increased at the centre or edge of the bulk, by introducing a rod or ring respectively, to channel heat to the cold head. An interesting comparison can be made to the experimental results presented in [116] for a 25 mm diameter GdBCO bulk with a 1 mm aluminium wire inserted into a central hole followed by molten impregnation of a BiSnCd alloy. Trapped field results for this bulk with and without the embedded aluminium show that the aluminium wire and metal impregnation increased the trapped field by up to 25 % for a single applied pulse of field. This increase in the trapped field is in qualitative agreement with the modelled results for structure B. Structure C

achieves the greatest enhancement in trapped field, as confirmed by Table 5.4, whilst structure A achieves the greatest enhancement in trapped flux. An enhancement of around 30% in the trapped field or flux is probably high enough to justify the extra complexity of creating a composite bulk from more than one bulk piece.

Table 5.4: The enhancement in trapped field and flux calculated at t = 10 s for various embedded copper structures compared to the bulk with no added copper structure.

Structure	Enhancement (%)	
	Trapped field	Trapped flux
A	21.3	33.2
B	4.0	11.8
C	29.4	25.4

A greater insight into the dynamics of heat flow after a pulse, and how it affects the final trapped field, can be gained by considering the temperature and current distribution inside the composite bulk. Figure 5.7a) shows the behaviour without any added copper structures. J_ϕ represents the current density circulating around the central axis in the ϕ direction. The strong heating in the bulk periphery after a pulse can be seen at t = 0.1 s, leading to a current density ≈ 3 times higher in the centre of the bulk that the outer regions. However, as the heat flows to the centre and out of the bulk through the cold head, the flux creep is reduced in the outer regions but increased in the central region. At t = 10 s the resulting current density distribution does not vary so dramatically over radius but does exhibit a high value region next to the cold head. The plots show that the current distributions resulting from rapid heat generation and flow are not trivial and can be quite inhomogeneous.

Figure 5.7b shows the temperature and current density plots for structure C, the most successful structure for enhancing trapped field. At t = 0.1 s, the effect of the copper rings can already be seen by reducing the temperature of the outer region of the bulk, leading to an enhanced current density in this region compared to the results for no added copper structure. At t = 10 s the temperature of the composite bulk is already uniform, and lower on average than in the case without an added copper structure, due to more effective heat removal, reducing the rate of flux creep throughout the bulk. This leads to enhanced current density in the top half of the bulk and explains the enhancement in both the trapped field and flux.

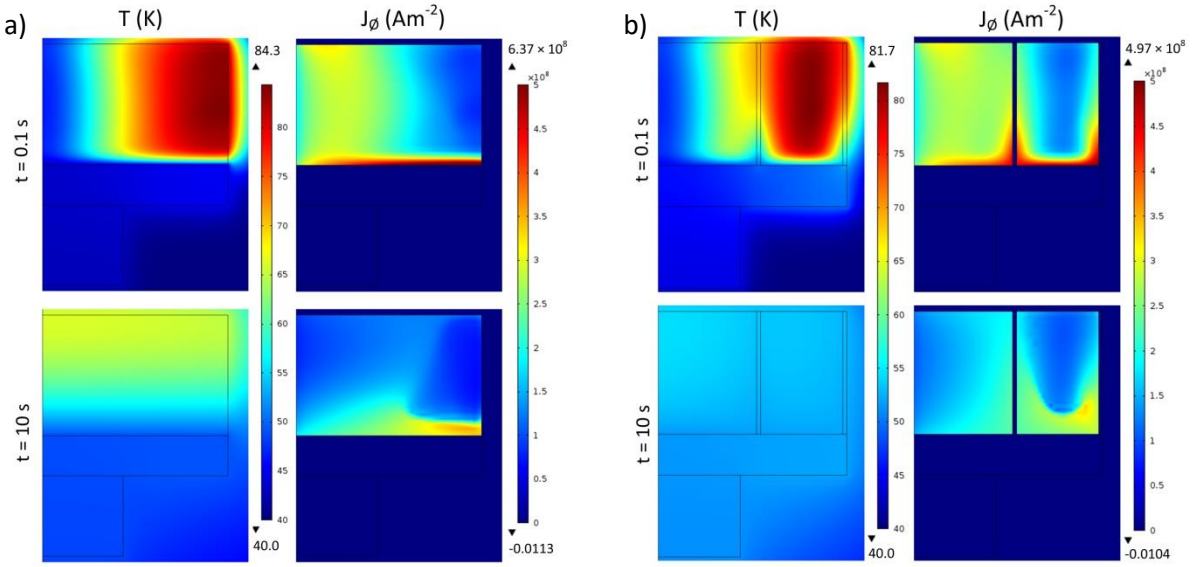

Figure 5.7: a) Temperature and current density distribution for a bulk cooled by a cold head with real thermal conductivities after pulsed magnetization. Cold head composed of two copper blocks. b) Temperature and current density distributions for bulk with copper structure C, the most effective in improving trapped field at *t* = 10 s.

A possible alternative to using rings to increase k_c will be reported in Section 5.3 and involves an array of rods which can be embedded into existing so-called 'thin walled' YBCO bulks produced with an array of vertical holes [13]. Composite structures could also be made for bulk MgB_2, which can more easily be made in a variety of shapes than (RE)BCO bulks [42]. Although bulk MgB_2 can be made with a higher thermal conductivity than bulk (RE)BCO [117], it has to be magnetized below 40 K and is therefore more susceptible to thermal instability, a problem embedded metallic structures could solve. The key conclusions and scope of the thermal simulation results are listed below.

1. During pulsed field magnetization, the speed at which heat energy generated at the bulk periphery flows into the bulk centre or out through external conduction is determined by k_{ab} and k_c. The faster the temperature of a bulk can be brought back down to equilibrium, the greater the suppression of flux creep following a pulse.
2. For an isolated bulk, a high k_{ab} increases trapped flux but decreases trapped field. k_c has negligible effect for magnetization with a solenoid coil. However for a bulk cooled from its base with a cold head, increasing k_c can significantly increase the trapped field and flux at t = 10 s. It is not necessary to have a high k_{ab} in this case.
3. The technique of IMRA (iteratively magnetizing pulsed field operation with reducing amplitudes), which involves multiple pulses, has not been considered, but enhanced thermal conductivity is likely to decrease the number of pulses needed to reach a certain trapped field.

4. A high k_{ab} and k_c could be effectively realised by using highly conductive structures embedded in a bulk without increasing the bulk radius or thickness. Copper disks and planes modelled for a 46 mm diameter bulk increased both the trapped field and flux, with enhancements of around 30% depending on design.

5.2 Pulse magnetization of a bulk YBCO, copper and sapphire assembly

In order to verify the predictions of the modelling conducted in the previous section, assemblies of bulk YBCO with embedded copper and sapphire were experimentally tested. Pulse magnetization was performed on the samples, which were based on a 25.5 mm diameter YBCO bulk produced by the Bulk Superconductivity group, Engineering department, University of Cambridge. The modelling and experiments presented in this section were performed as part of a fourth year undergraduate research project by Jordan Rush under my supervision and guidance.

5.2.1 Cold head and experimental thermal mass

The structures that were chosen to test experimentally were an outer ring and an inner disk plane, such as structure A shown in Figure 5.5, as these were simplest to implement. The thermal model used in the previous section is based on cooling the bulk via a copper cold head at the base of the bulk. However the Magnetoforce system uses indirect cooling via helium gas. Therefore, in order to realise a similar condition and increase the heat flux out of the bulk following a pulse in the real system, a higher thermal conductivity cylinder was mounted to the base of the bulk to act as a thermal mass, which will from now on simply be referred to as a cold head. In order to minimise eddy current heating, a copper cold head was created by gluing 1 mm thick sheets of copper (RRR = 30) with Stycast and machining into a 25.4 mm diameter cylinder. This way, eddy currents are confined to loops no more than 1 mm in diameter, which significantly reduces heating as confirmed by induction heating modelling in COMSOL. As an alternative, single crystal sapphire was also used. Sapphire has exceptional thermal conductivity at low temperatures as shown in Table 5.5 but low electrical conductivity, so avoids eddy current heating. It does however have a significantly lower heat capacity compared to copper. A 25 mm x 12 mm sapphire cylinder was purchased from Pi-Kem Ltd, which was also the source of the sapphire disk ‘embedded’ inside the bulk.

Table 5.5: Thermal conductivity and volumetric heat capacity for copper [115] and sapphire [118] at 40 K.

Material	Thermal conductivity (W m^{-1} K^{-1})	Volumetric heat capacity (J K^{-1} m^{-3})
Copper (RRR = 30)	930	51×10^4
Sapphire	12000	2.7×10^4

5.2.2 Optimisation of geometry through modelling

To begin with, modelling was used to optimise the geometry by determining the thickness of the outer copper ring or sleeve. The effect of thickness on the trapped field is shown in Figure 5.8. The sleeve conforms to the previously stated engineering requirement of not increasing the overall size of the composite bulk, therefore the thermal enhancement effect of the copper on the trapped field and flux is competing with the loss of superconducting material. This leads to peaks in the trapped field and flux, occurring at different optimal sleeve thicknesses for each parameter. Based on these results, 0.6 mm was chosen as the sleeve thickness, as this was predicted to give the optimum flux and also kept minimised the amount of material to that had to be removed manually by grinding down the outer diameter of the bulk, which is a lengthy and difficult process.

The modelling was conducted for two different purities of copper, with the results showing that there is little benefit in using purer copper than that with a residual resistivity ratio of 30 (RRR = 30). This is because, although higher purity copper has significantly higher thermal conductivity at low temperatures, the heating caused by pulsed magnetization leads to a higher temperature at which the difference in thermal conductivities is small. As a result, copper with RRR = 30 was used, as it is widely available and relatively inexpensive.

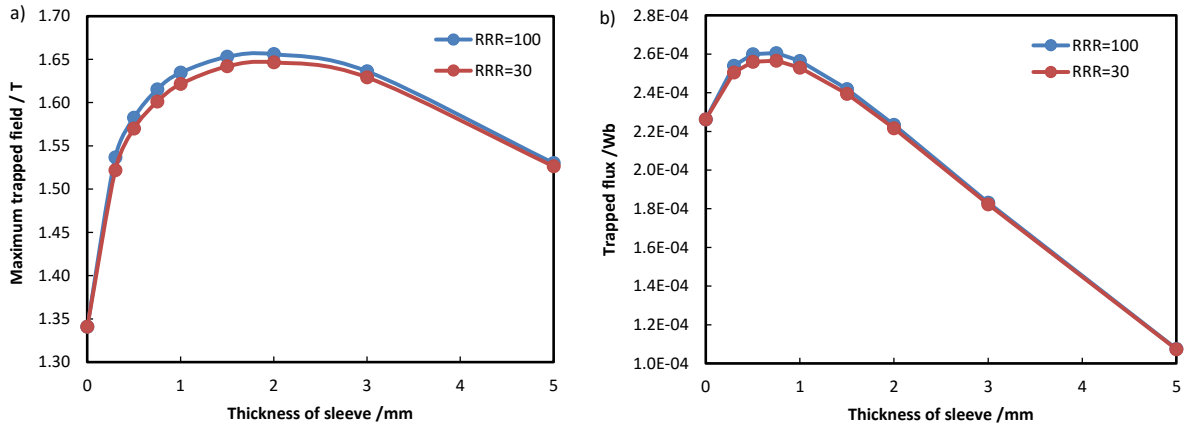

Figure 5.8: Simulated effect on a) the maximum trapped field and b) the flux on the surface of a 25.5 x 12 mm YBCO bulk when embedded with an outer copper ring or sleeve of two different purities. Results are for pulsed magnetization at 40 K and a 9.5 T applied field. The thickness of the sleeve is equal to the reduction in radius of the YBCO cylinder.

With the sleeve thickness determined, the next step was to model the inclusion of high thermal conductivity planes inside the bulk. Sapphire disks of 0.5 mm were chosen, as sapphire has the required thermal conductivity whilst avoiding eddy currents which would be particularly difficult to overcome in a thin copper disk without affecting radial heat flow. A thickness of 0.5 mm only was modelled as this was available to purchase (Pi-Kem Ltd) and any thinner would risk cracking the disk when handling. The thermal contact resistance between all parts of the composite bulk assembly were taken to be zero in the model. Figure 5.9 shows the effect of the embedded disks when used with the copper sleeve.

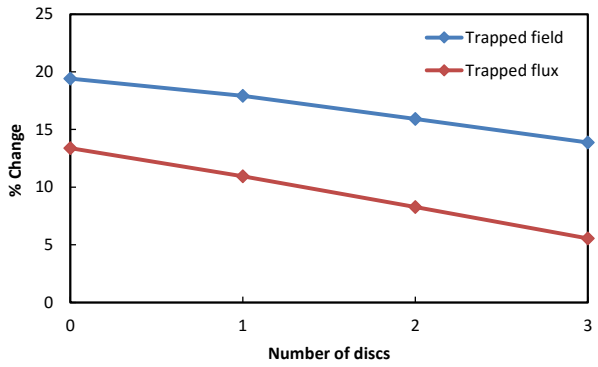

Figure 5.9: The simulated percentage increase in the trapped field and flux on the surface of the composite bulk with an added copper sleeve and 0–3 internal 0.5 mm thick sapphire disks, compared to the standard bulk with no additions.

The purpose of the disks is to channel internal heat to the copper sleeve, which can guide it to the cold head. The figure shows that for the size and aspect ratio of bulk modelled, 0.5 mm disks cannot give any increase in the trapped field, which means that in this case the loss of superconducting material is the dominant factor. However, one embedded disk was still experimentally tested, as the model does not take into account the generation of hot spots at growth sector boundaries and the higher J_c in the top half of the bulk, which should lead to more concentrated heat generation there.

5.2.3 Experimental trapped field and flux

Table 5.6: Temperature stages and applied field pulses used in the MPSC + IMRA procedure

Temperature/K		Applied field/T														
	Pulse #:	*1*	*2*	*3*	*4*	*5*	*6*	*7*	*8*	*9*	*10*	*11*	*12*	*13*	*14*	*15*
MPSC	77.4	4.0	3.6	3.4	3.2	3.0	2.8	2.5	2.2	2.0	1.5					
	55, 35, 15	5.4	5.2	5.0	4.8	4.6	4.4	4.2	4.0	3.8	3.6	3.2	3.0	2.5	2.2	2.0

The MPSC and IMRA pulse magnetization procedure was applied, as specified in Table 5.6. Figure 5.10 shows the various structures tested, and the trapped field and flux results. It is worth

noting that the trapped flux values are calculated by interpolation of the trapped field profile measured along a line using the method described in Section 4.1.2. As the method is not so reliable for trapped field profiles which may be axially asymmetric, the trapped flux values should be taken as approximate. In order to realise the copper sleeve, a number of copper foil strips were layered together with a gap at one point in the diameter to prevent eddy currents. All the parts were temporarily bonded together using Apiezon N grease, which is used to improve thermal contact between cryogenic components and has previously been used by Fujishiro et al. to set a stainless steel ring around a GdBCO bulk [31].

It is clear from the results that the composite structures tested in general do not increase the trapped field and flux, contrary to the modelling predictions.

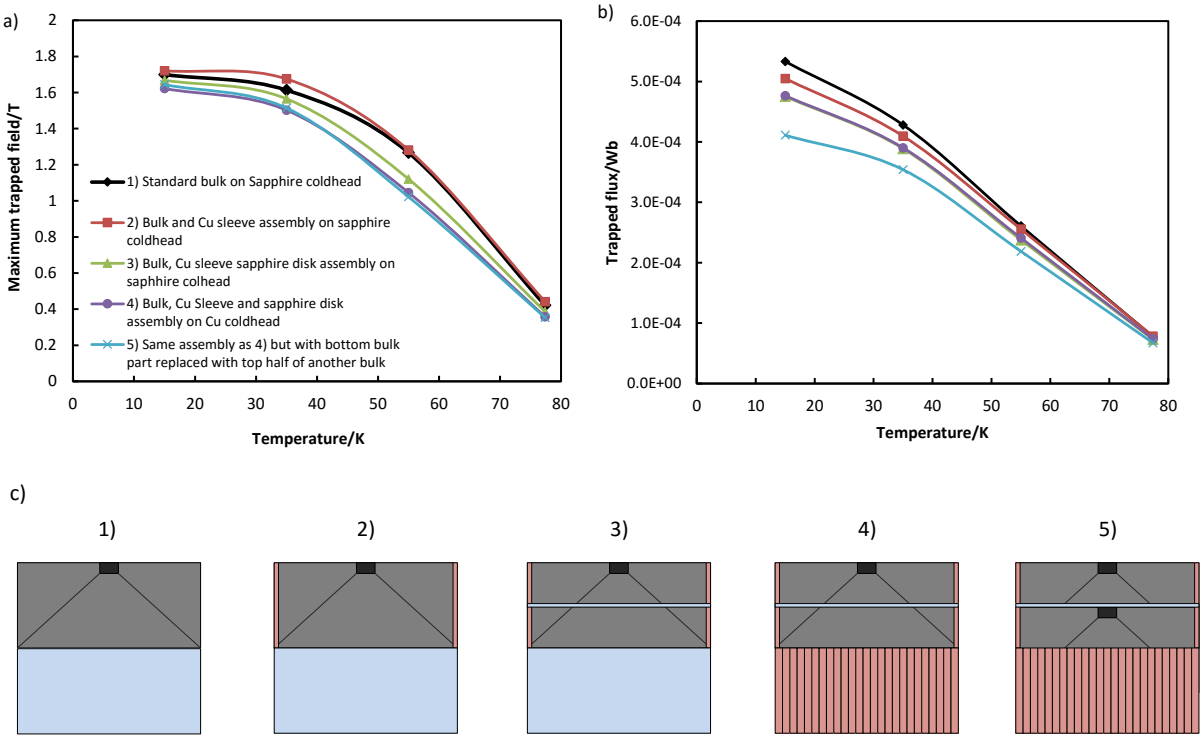

Figure 5.10: Trapped field a) and flux b) measured 0.5 mm above the sample, resulting from pulsed field magnetization of various composite bulk structures c), all 25.5 mm in diameter and 12 mm high, composed of YBCO, sapphire (pale blue) and copper (brown). 1) to 4) used the same YBCO bulk which was also used for the top half of 5).

Comparing the results for structure 2) with those for the standard bulk (black curve), the maximum increase in field was 4%, compared to the predicted increase in peak field of 19%, and the estimated flux is actually decreased. Although there is a large difference between these values, the experiment does confirm the theory that the increase in trapped field brought by high thermal conductivity material can be enough to compensate for the loss of superconducting material. For the remaining structures, the YBCO bulk was cut in the middle using a circular diamond cutting blade, which removed approximately 0.4 mm of material. The introduction of the sapphire disk made little

difference to the results, and neither did the replacement of the sapphire cold head with the copper one. The final test, structure 5), aimed to confirm the belief that the top half of most superconducting (RE)BCO bulks has significantly higher J_c than the bottom half. The bottom half of the YBCO bulk used in the previous experiments was replaced by a piece cut from the top of another YBCO bulk known to have similar properties. Compared to structure 4), structure 5) should have achieved at least the same performance, but the trapped flux results suggest a significantly lower performance, especially at lower temperatures. This final experiment suggests that other unwanted factors limited the performance of the structures which should have higher trapped field and flux.

Figure 5.11 shows the trapped field and flux after the first pulse of each MPSC stage. The results are probably more closely related to the modelling, given that only a single pulse was considered in the model rather than an IMRA sequence. However, as the figure shows, the structures did not lead to an increase in trapped field or flux and in some cases a larger percentage decrease that in Figure 5.10.

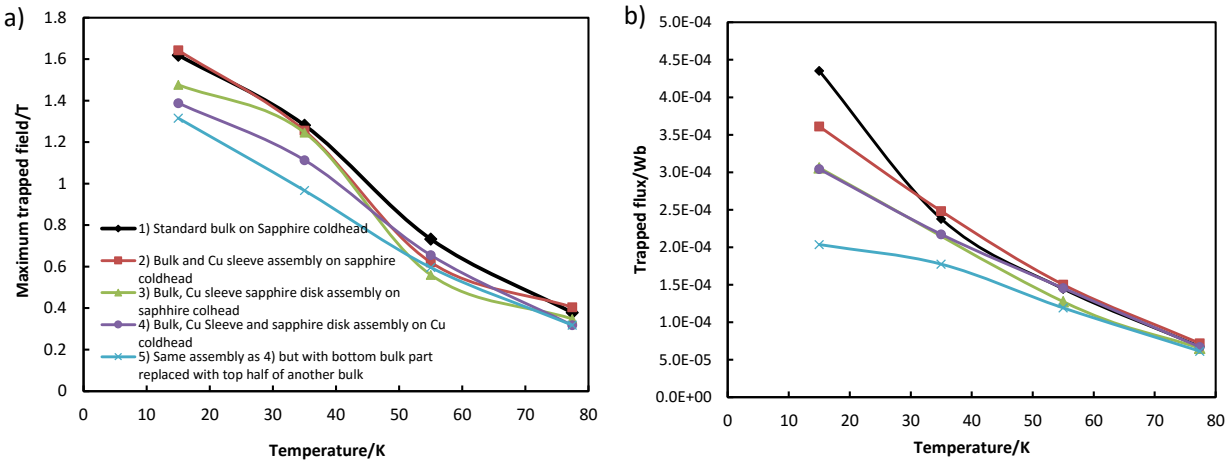

Figure 5.11: Trapped field a) and flux b) after the first pulse for each temperature stage of the MPSC magnetization. The structures tested do not enhance the field or flux after the first pulse.

5.2.4 Comparison between experiment and modelling

There are a number of possible explanations for why the composite structures tested did not have the significantly enhanced trapped field and flux performance that was predicted by modelling. The main two factors are believed to be a lack of good thermal contact between components and damage to superconducting surfaces after the grinding procedure.

The modelling assumes no thermal contact resistance. In practice, thermal contact was maximised by using Apiezon N grease, but this grease has lower thermal conductivity than bulk YBCO at the temperatures used. The outer curved surface of the bulk after grinding for structure 2 was not ideal, leading to numerous bumps and also a conical taper, where one end of the bulk had a larger diameter than the other. Due to the difficulty of obtaining a copper ring of the required

thickness and diameter, thin sheets of copper (0.1 mm thick) were instead cut, stacked and curved around to the bulk to build up the sleeve, which of course leads to gaps and a lower effective density. These realities may significantly reduce the efficacy of the copper sleeve in removing heat, which would partly explain the lack of real enhancement seen in all the subsequent structures tested. Also for structures 3), 4) and 5) it becomes important for the copper sleeves to be exactly the right height to be in contact with the sapphire disk and cold head, without being so large as to protrude over the top and bottom bulk surfaces.

Due to the lack of enhancement in trapped field and flux seen in experiment 5, it is believed that the cutting process may have damaged the bulk surface. Prior to cutting, the top seed side of the bulk is bonded to a mount using hot wax at over 300 ^{o}C. The sudden change in temperature may have caused cracking on the top surface of the bulk, which has the highest J_c and contributes most to the trapped field. Small cracks were visible on the top surface of the bulk, which were not present before the cutting. From examining the cut surfaces of the bulks, it also appeared that some of the cracks did not match up with each other, indicating the formation of new cracks during the cutting procedure. Another uncertainty for experiments 3-5 is the alignment of the growth sector boundaries of the top and bottom bulk parts. In the experiment they were rotated by 45˚ (maximally misaligned), in the belief that spreading hotspots for the central sapphire disk would be better, but it is not theoretically trivial whether this asymmetry would have a positive or negative effect on the ability to trap flux. 3D modelling is needed to determine this.

In future, further tests are required to prove the effectiveness of the high thermal conductivity structures in enhancing trapped field and flux. The geometrical tolerances of all the components need to be significantly improved so that they all fit together in close contact. The outer diameter of the bulk needs to be ground down using a precise method and the parts need to be permanently bonded together using a silver-loaded epoxy, which should have higher thermal conductivity than Apiezon N grease. Tests also need to be carried out to determine how significant the cutting process is in reducing the J_c of the bulk surfaces.

5.3 Pulse magnetization of bulk YBCO with an array of holes

The existence of (RE)BCO bulks with axial holes in them allows for another geometry of composite bulks to be investigated. Some YBCO bulks are produced with an array of holes, which exist in the preform before melt growth occurs [13, 119, 120]. These bulks can be referred to as thin walled. The presence of the holes during melt growth reduces porosity, which occurs away from the seed due to gas bubble formation, and also the extent of cracking due to stress during oxygenation. The holes also reduce the time and temperature needed for oxygenation, due to the high surface

area to volume ratio and reduced diffusion distances. Surprisingly the holes do not affect the single domain growth [119] and can actually enhance J_c enough to outweigh the loss of superconducting material, leading to higher trapped fields than typical YBCO bulks of the same size [120]. Significant work has already been carried out by G P Lousberg et al. on magnetizing bulks with holes, including filling the holes with ferromagnetic powder for field cooling [121], optimising the arrangement of the holes [122] and also embedding small coils in the holes to investigate internal flux dynamics during PFM [14]. However no reported study has looked at the effect of filling the holes with metallic material with the aim of enhancing thermal properties for pulsed magnetization.

The modelling and experiments presented in this section were performed as part of a fourth year undergraduate research project by Algirdas Baskys under my supervision and guidance.

5.3.1 Sample details

The thin walled sample used for the experiments reported in this section was obtained as part of collaboration with CNRS, Grenoble, France. The details of the bulk and its geometry can be found in Figure 5.12 and Table 5.7. The presence of vertical holes in the sample provides the ideal geometry to test the composite bulk concept based on the modelling results shown in Figure 5.4c and d). These results show that, by increasing the bulk thermal conductivity along the *c*-axis when the bulk is attached at its base to a cold head (or thermal mass), the trapped field and flux measured on the top surface can be increased. Filling the holes with a high thermal conductivity material should allow this prediction to be tested experimentally, as an increase in the effective k_c would be realised. Unlike the structures presented in the previous section, no superconducting material needs to be sacrificed in this case. As a simple approximation, the presence of copper increases the average k_c by a factor of 10 to approximately 40 W m^{-1} K^{-1}, which according to Figure 5.4c and d should give a measurable increase in trapped field and flux.

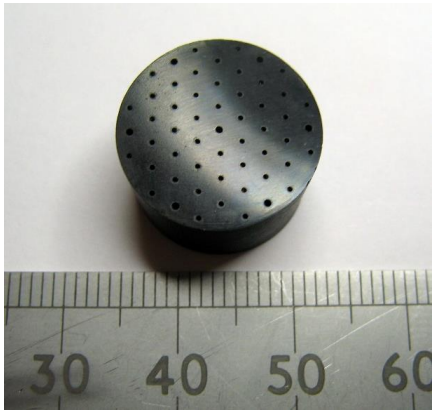

Figure 5.12: Photo of the 16 mm YBCO bulk with holes created by Xavier Chaud and Driss Kenfaui of CNRS, Grenoble, France.

Table 5.7: Details of the geometric properties of the bulk with holes used to create a composite sample for pulse magnetization.

Property	Value
Composition	YBCO
Diameter/mm	16.0
Height/mm	9.75
Number of holes	55
Large hole diameter/mm (#)	0.58 (7)
Small hole diameter/mm (#)	0.42 (48)
Hole volume fraction	4.2 %

5.3.2 3D magneto-thermal model

The 3D critical state magneto-thermal model reported was developed by Algirdas Baskys starting from a 3D critical state model (no thermal effects) developed by M Zhang [97]. The key results of the model will be summarized. Full details will be given in a future publication.

Interestingly, both the modelling and the experimental results show that the holes, which present a very inhomogeneous J_c distribution inside the bulk, do not in themselves fundamentally prevent high fields from being trapped inside the sample when pulse magnetized. This shows that the general idea of all types of J_c inhomogeneity being problematic, as used to help explain the negative effect of growth sector boundaries on pulsed field magnetization, is not strictly true. It appears that some specific forms of J_c inhomogeneity are compatible with pulsed magnetization.

The combination of three dimensions, thermal effects and the complex geometry created by the holes makes modelling the pulse magnetization of the bulk with holes a very challenging task. To solve the model, symmetries had to be exploited to minimise element count, which meant that the xy plane through the centre of the bulk was a symmetry plane. Even then, the full solution time was 50 hours. As a result, the presence of the asymmetric cold head was not modelled. It was also not possible to apply high enough fields to fully penetrate the bulk due to computational instability. As a result, the main purpose of the model developed is to give an insight into flux dynamics for a bulk with 3D anisotropy, and only a qualitative link to the experiments. The same cooling power as defined in Equation (5.6) was used for the bulk, but cooling from all sides of the sample which had an equilibrium temperature of 40 K.

The dynamics of pulse magnetization of the bulk with holes (filled with copper) is illustrated by Figure 5.13, which shows the field, current density and temperature during and after a pulse in the plane cutting through the centre of the bulk. The main difference, compared to the dynamics expected for a normal bulk, is that the current is forced to meander around the holes as it is induced by the penetrating flux front. It does this quite easily, but not without leaving small ‘hotspots’ next to the holes where the current density is highest. This might explain why regions immediately surrounding the copper rods are not visibly cooler. The final trapped field inside the bulk is quite uniform.

Not much difference in the trapped field was seen when modelling the bulk with and without copper filling the holes, but this may be due to the cold head geometry not matching the preferred case and also may be due to some unreliability in the model. The copper filled model had to use a coarser mesh, is relatively untested and could hide a modest increase in trapped field.

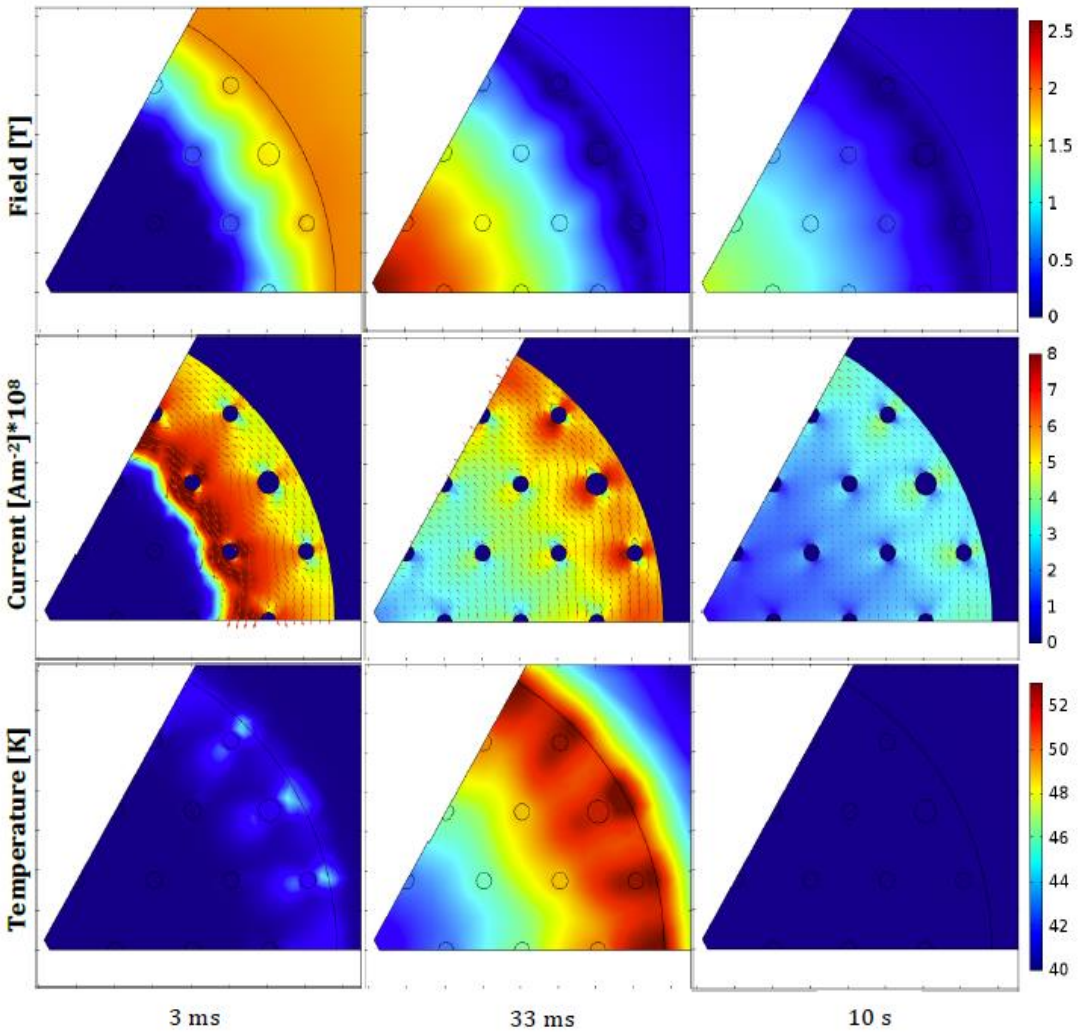

Figure 5.13: 3D critical state model with thermal effects in COMSOL applied to a 16 mm diameter thin walled YBCO bulk with the holes filled with copper. The bulk geometry matches that of the bulk used in the experiment. One twelfth of the geometry with symmetry conditions applied was modelled to give a manageable computational time. The equilibrium temperature was 40 K and applied field 5 T. Model developed by A Baskys under supervision.

5.3.3 Experimental trapped field and flux

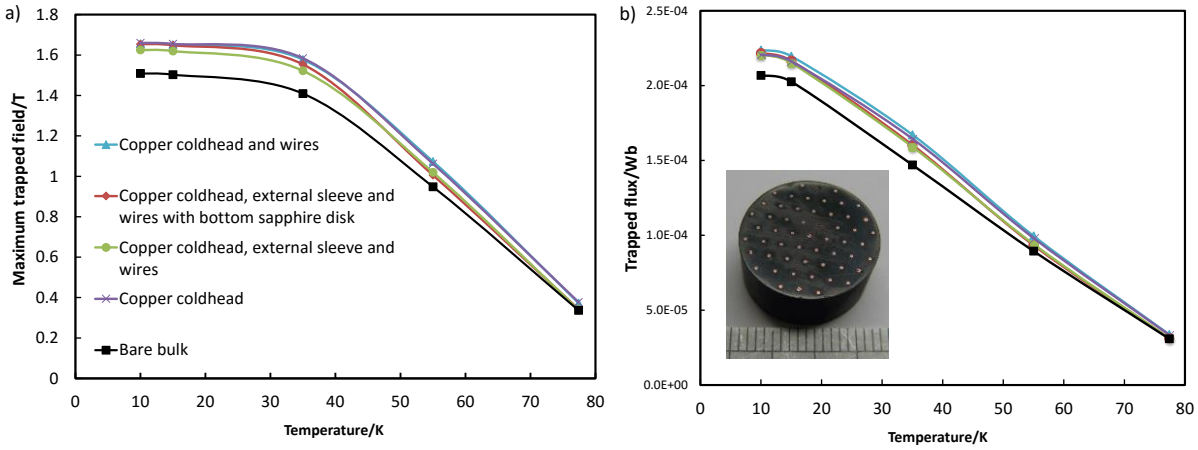

Figure 5.14: a) Trapped field and b) flux (0.5 mm above surface) for the 16 mm YBCO bulk with holes pulse magnetized using MPSC. Various states are reported, including the composite structure where the holes are filled with copper wire as shown inset in b).

Figure 5.14 shows the experimental results for the trapped field and flux following MPSC magnetization of the YBCO bulk with holes. At each temperature stage, approximately 10 pulses were applied, starting from 3.6 T (77 K), 5 T (55 K), 5.8 T (35 K) and 4.8 T (15 K). The first observation is that the maximum field the bulk can trap at lower temperatures is good for a bulk of this size, even when considering the 'bare bulk'. This proves that this type of bulk is suited to pulsed magnetization down to low temperatures. The presence of the holes does not seem to give rise to significant thermal instability in addition to that believed to be already present due to the growth sector boundaries.

The simplest comparison to make is between the 'bare bulk', and the bulk with the copper cold head (the same 25.5 mm cold head used in Section 5.2) and copper wire (RRR = 30) inserted in the holes. The composite bulk was created by inserting wires of 0.4 mm and 0.5 mm diameter into the small and large holes respectively. Any gaps between the wires and the bulk were filled with Apiezon N grease by warming and vacuum de-airing, with the same grease also being used for thermal contact between the bulk and the cold head. The graph shows a significant improvement in the trapped field and flux, however the data show that the wires contributed little to this improvement, as can be seen by considering the curve for the bulk and copper cold head only, which achieved similar performance. Additional changes, such as adding a small external sleeve to the outside of the bulk and adding a thin sapphire disk between the bulk and the cold head to spread heat across the copper plates, did not lead to much change. The increase in the trapped field and flux when using a copper cold head is significant in this case, particularly as the cold head was larger in diameter than the bulk itself. The copper cold head was used instead of the sapphire one as it gave up to 6% better

trapped field compared to a preliminary test carried out using the sapphire cold head, largely because of copper's significantly higher volumetric heat capacity.

The modelling shown in Section 5.1 determined the enhancement in trapped field and flux made by embedded metallic structures after a single pulse rather than at the end of a full MPSC sequence. Therefore it is worth showing the improvements in trapped field and flux after the first pulse of each MPSC temperature stage which are shown in Figure 5.15 for three cases. The changes are similar to that resulting at the end of the IMRA sequence with the cold head giving most of the improvements. However there is a visible improvement in the central trapped field for the intermediate temperatures which appears to be due to the wires.

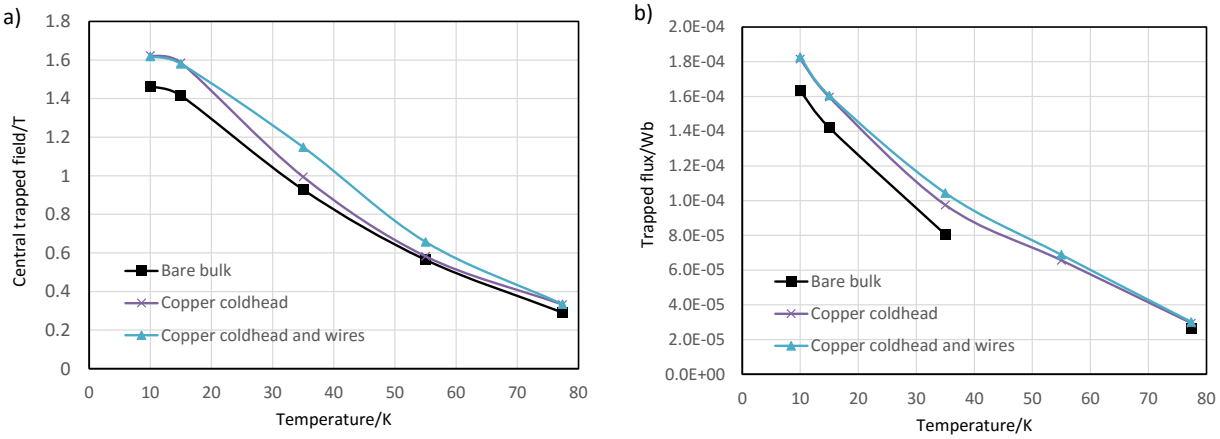

Figure 5.15: Trapped field a) and flux b) after the first pulse for each temperature stage of the MPSC magnetization. Most improvements are due to the copper cold head rather than the wires, although the wires appear to enhance the central trapped field by up to 15 % at 35 K. Calculated flux at 55 K omitted due to anomaly arising from large asymmetry in field profile.

It is important to explain why the copper wires did not give a clear increase in trapped field and flux in all cases. It is largely believed that poor thermal contact was to blame, both between the wires and the bulk and also between the wires and the cold head. It may be that Apiezon N grease simply doesn't have a high enough thermal conductivity to not significantly interfere with heat flow on the time scale of seconds, which is when the heat needs to be removed to see an enhancement as suggested by the modelling in Section 5.1 (which assumed zero thermal contact resistance). Deposition of silver on the bottom surface of a bulk, before attaching to a cold head with thermal grease, is believed to significantly increase heat transfer by filling cracks and voids in the bulk surface with silver [123], so this could be tried in future. Efforts were made to try alternatives for filling the holes but without much success. Before using the grease, silver paint was used to set the wires, with a small increase in trapped field seen (11% better than grease for 77 K, 2.5% for 55K and no difference more than 1% detected for lower temperatures). The performance is limited by the fact that the solvent makes up a large percentage of the paint and therefore is not suited to filling gaps and voids. Metal impregnation using pure indium solder was also tried, by heating the bulk and

metal on a hotplate and applying a vacuum to one side of the bulk to suck the metal into the holes. Unfortunately due to poor wettability between the metals and the bulk, it was not possible to fill all the holes and it is doubtful whether there was good thermal contact for the holes that were filled. Metal impregnation has been used successfully in previous experiments [25, 116] where a 25 % increase in the trapped field was seen at 44 K for a single aluminium wire inserted in a central hole with BiSnCd impregnation (single pulse). Therefore a more dedicated attempt for a bulk with an array of holes may succeed in future. Alternatively a more suitable medium could be used to set the copper wires in the holes, such as silver loaded epoxy.

Another issue which should be looked at with the present experimental setup is the use of a thermal mass acting as a cold head. After multiple pulses, the thermal mass will warm up as it takes heat from the bulk, however in the system, the real cold head (which is a ring embedded in the cryostat wall) is higher than the bulk, meaning that the cooling of the bulk-thermal mass unit is actually more from the bulk side. This means that the thermal mass may not be effectively cooled after multiple pulses. A new design may be proposed which links the thermal mass to the real cryostat cold head for direct cooling.

5.4 Field cooling a stack of coated conductors

Superconducting tape is produced commercially to carry a very high current without energy loss, for use in high field electromagnets or cables. The current is carried in a very thin film of YBCO superconductor which lies on a thick metallic substrate (with intermediate oxide buffer layers) and is covered by silver as outlined in Section 1.5.2. Although not designed to carry a circulating persistent current (as in the case of a bulk), results presented here prove that they are an ideal material from which to construct a composite bulk capable of trapping high fields [124]. The trapped fields reported in this section are between two stacks of commercial (RE)BCO tape each with 120 layers, magnetized by the field cooling method. 7.34 T was trapped at approximately 4.2 K, the highest field ever achieved for such a sample.

The composite sample composed of a stack of superconducting tape pieces did not suffer from the same thermal instability present in bulks, and can therefore be used at or below 20 K. Additionally, for very high trapped fields, existing superconducting bulks require external mechanical reinforcement due to the poor mechanical strength of bulk (RE)BCO, which is a ceramic. A stack of (RE)BCO tapes is fundamentally mechanically strong due to the metallic substrate supporting the superconducting layer, and therefore seems a natural choice for trapping very high fields. Although field cooling is not necessarily the most practical method of magnetization, it is essential for

determining the maximum possible field that a superconductor can trap, which is the purpose of the results reported in this section.

The potential of a stack of (RE)BCO tapes to be used as trapped field magnets in applications is very positive. Such samples have relatively uniform J_c compared to bulks, resulting in predictable performance. There is no fundamental restriction in preventing larger sized samples, and some manufacturers currently produce 40 mm wide tape with no degradation in J_c when scaling width. Tape this wide has already been used to create annuli that have been field cooled at 77 K for NMR applications [34] as detailed in Section 1.5.2. Finally, the cost of superconducting tapes is steadily and predictably falling [125] making the technology attractive for engineering applications.

5.4.1 Sample properties

Figure 5.16a shows the geometry of the stack of tapes sample. The layers were compressed as shown in Figure 5.16b with good mating between each layer. The superconducting tape used to create the stack was produced by SuperPower Inc to specification SP12050 AP ($(Y,Gd)_{1+x}Ba_2Cu_3O_{7-\delta}$ with 7.5% Zr added) and a rated I_c of 240 A (at 77 K and in self-field). Figure 5.16c schematically shows the cross-section of the 12 mm wide (RE)BCO tape that was cut into 12 mm lengths to give square pieces. The cutting does not cause any significant damage to the superconducting properties of the (RE)BCO layer [126]. The volume fractions of the compressed tape stack can be seen in Table 5.8. Remarkably the superconducting (RE)BCO contributes less than 2% of the overall volume, whereas the substrate made of Hastelloy® C-276 (Hastelloy) accounts for 87% of the volume.

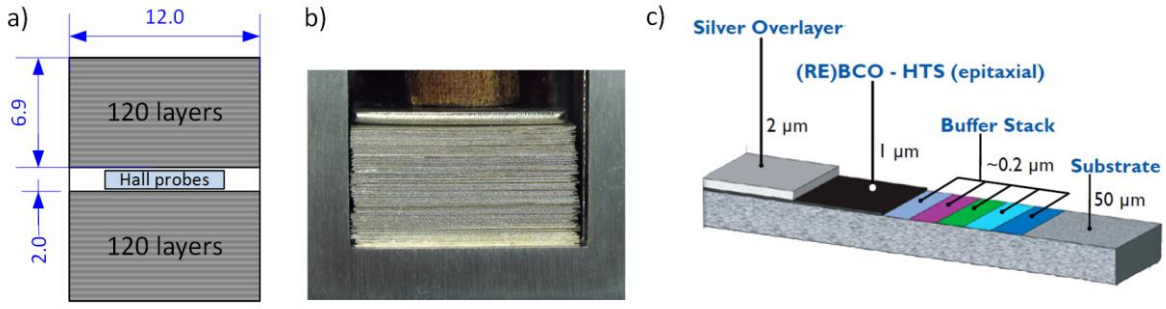

Figure 5.16: a) Schematic of double (RE)BCO tape stack used for the field cooling experiment. b) 120 of the square tape layers compressed to form a tape stack. c) Schematic showing the components and dimensions of the 12 mm wide SuperPower superconducting tape from which layers were cut.

Table 5.8: Parameters and volume fraction for each compressed 120 layer stack of tapes used in the experiment.

Parameter	120 layer (RE)BCO tape stack
Sample height (mm)	6.9
Density (kg m^{-3})	8380
(RE)BCO volume fraction	1.7%
Hastelloy volume fraction	87.0%
Silver volume fraction	5.2%
Stacking space fraction	6.1%

In order to understand the difference in thermal behaviour of the (RE)BCO tape stack compared to a (RE)BCO bulk, the thermal properties of the constituent materials have been listed in Table 5.9.

While the heat capacity of silver, Hastelloy and YBCO all have a similar range of values, the thermal conductivity of the silver over-layer stands out, being over an order of magnitude higher than Hastelloy and (RE)BCO. When considering tensile strength it is clear that Hastelloy is considerably stronger than bulk YBCO, and it is part of the specification of SuperPower tape that 550 MPa of in plane tensile stress can be applied with less than 5% reduction in I_c. This high strength should be able to support extraordinarily high magnetic pressure in the (RE)BCO superconducting layer, given the magnetic pressure inside a saturated bulk in units of MPa is given by [6]:

$$\sigma \approx 0.30 B_0^{\,2} \tag{5.7}$$

where B_0 is the maximum field in the sample, approximately the same as the field trapped between two samples magnetized together like in this study. If higher fields are applied than strictly needed to saturate the sample (as is often the case) then the magnetic stresses can be significantly higher than given by equation (5.7). The 550 MPa limit for the Hastelloy substrate corresponds to a maximum trapped field of 42.8 T, which strongly suggests that there is no real mechanical limit to trapping high fields in a stack of tapes, as other factors would prevent ever reaching such a high value. A similar conclusion is reached when considering other metallic substrates used for superconducting tape. Stainless steel and Ni-5at%W (a nickel tungsten alloy) would in theory allow up to 26.1 T and 29.3 T to be trapped respectively.

Table 5.9: Properties of Hastelloy C-276 and bulk YBCO at cryogenic temperatures. A range of values is given for 10 – 77.4 K where there is temperature dependence. Also shown are some properties for Ni-5at%W used by AMSC for their MOD tape (see Section 1.5.2), and the stainless steel used for IBAD/PLD tape produced by Bruker and others.

Parameter	Hastelloy	Silver over-layer	Bulk YBCO	Stainless steel (304)	Ni5at%W
Density (kg m^{-3})	8890 [127]	10,490	5900 [6]		-
Thermal conductivity (W m^{-1} K^{-1})	3 – 7.5 [127]	≈ 500 – 1500 [128-130]	6 – 20 *ab*-plane, 1 – 4 *c*-axis [114]	1 – 8	-
Heat capacity (J kg^{-1} K^{-1})	2 – 200 [127]	2 – 155 [128]	≈ 1 – 200 [114]	5 – 200	-
Tensile strength (MPa)	670 – 760 (yield) [131]	≈ 60 (yield) [128]	≈ 30 (fracture) [6]	205 (yield)	257 (yield) [131]

The typical tensile stress listed for bulk YBCO is limited by the presence of micro cracks and the weakest part of a bulk often leads to a fracture strength less than that obtained for small test samples (~ 3 mm). Although reinforced YBCO samples can survive the magnetic pressures of high trapped field, they require external reinforcement in the form of a steel ring or composite, which adds complexity and increases the sample diameter. Even then, they can fracture during magnetization or during demagnetization [30]. Stacks of YBCO tape are expected not to fracture like this due to the metallic substrate and its volume fraction.

The magnet used for field cooling the samples was a 15 T Oxford Instruments superconducting magnet at the Laboratory of High Magnetic Fields and Low Temperatures, Wrocław, Poland, where the experiment was conducted. The field cooling procedure involved ramping the field of the magnet up to the desired applied field whist holding the sample at 100 K to ensure it is non-superconducting ((RE)BCO T_c ≈ 92 K), cooling the sample down to the desired field cooling temperature whilst holding the applied field constant, and finally ramping the applied field down slowly to zero leaving a trapped field in the sample. The sample was in a sealed insert filled with helium gas. The insert was cooled directly by immersion in liquid helium, so that the sample was cooled via the helium gas. The temperature of the sample was controlled using a heater mounted close to the sample. A central cryogenic Hall probe (type Arepoc LHP-MP) was used to measure the trapped field, with another Toshiba hall probe used to determine whether the sample was saturated or not by measuring off-centre trapped field.

5.4.2 Trapped field results

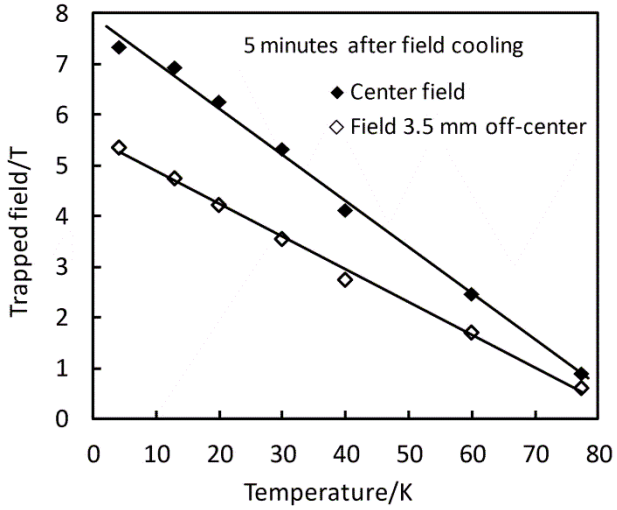

Figure 5.17: Trapped field between two 120 layer tape stacks using the field cooling method at various temperatures. The increase in field as the temperature decreases is approximately linear, reaching a maximum at the centre of 7.34 T at 4.2 K.

The results for the field trapped in the double stack of tapes for different field cooling temperatures are shown in Figure 5.17. The graph shows clearly the significant increase in field that can be trapped if field cooling below 77.4 K. The lower off-centre field shows that the sample was saturated. No damage was observed in any of the tape layers after the tests. The ramp rates used for the applied field were higher for higher temperatures (0.5 T min^{-1} for 77.4 K and 0.34 T min^{-1} for 60 K) and lower when approaching 4.2 K (0.15 T min^{-1} for 20 K and 13 K, with the rate reduced to 0.07 T min^{-1} for the last 1 T of the 13 K ramp). The lower ramp rates required for the 20 K and 13 K temperature stages meant that the field cooling took approximately 1 hour, given that the applied field was 8.5 T in both cases.

The trapped field for 4.2 K was not strictly achieved using field cooling. To begin with, a zero field cooling test was performed with a high ramp rate (0.25 T min^{-1}) to separately test how flux penetrated the sample. Interestingly, the high ramp rate caused flux to penetrate in a series of sudden global flux jumps. As a result of this instability, at the maximum 14 T applied, the central field in the sample was 10.7 T and therefore the stack was saturated. This behaviour shows that even though a stack of tapes may be more thermally stable at low temperatures, even this type of sample will suffer from global flux jumps near 4.2 K if the applied field changes too quickly. Given the saturated state of the sample at the end of the increasing field ramp, the field could be ramped back down to zero to effectively achieve field cooling, and indeed the state achieved at the end should be the same as if field cooling was performed with the same decreasing applied field. During the ramp down in field, a ramp rate of 0.12 T min^{-1} was used from 8 T. On several occasions an increase in temperature was observed and the ramp was temporarily halted until the temperature recovered, and on the final occasion the liquid helium level (which was very low) was increased. This suggests that even a stack of tapes can suffer some instability if cooling power is insufficient, as was the case when the liquid helium level was very low. After the re-fill, full stability was restored and the ramp continued without interruption. The maximum measured temperature rise was 2.5 K but, as the thermometer was not in close contact with the samples (but thermally connected by a brass mount), the warming would be higher inside the sample itself. The field cooling temperature should therefore only be considered as approximately 4.2 K.

When individual flux jumps occur in a superconductor they generate a small amount of heat which leads to a local temperature rise. If the heat cannot be conducted away quickly enough and/or the heat capacity is too low, then the temperature rise can be big enough to lead to a global flux jump (large scale de-pinning and flow of flux). This occurs as the local temperature spike leads to a decrease in J_c and hence de-pinning of neighbouring flux lines and an avalanche effect. A global flux jump corresponds to a sudden measurable drop in the trapped field, including complete collapse,

which is often observed in bulk superconductors for high fields and low temperatures. Therefore flux jumps have a significantly limiting effect for bulks below 20 – 30 K, resulting in a decrease in trapped field when field cooling below these temperatures, as illustrated by Figure 1.18 in Section 1.5.1.

A unique feature of the results for a stack of tapes is a continuous increase in trapped field as temperature decreases all the way down to 4.2 K. The trapped field of 7.34 T is the highest field known to have been trapped in stack of superconducting tapes or thin films. Although the value is not as high as many bulk samples [25, 30, 76] (see also Table 1.1), it is remarkable given the small size of the stack (12 mm square) and the fact that the tapes are commercial with only an 'average' I_c value.

A detailed description of flux jumping in bulk superconductors which have high fields trapped in them has already been developed [132]. However, the description of trapped field stability in a stack of tapes is more complex, and the so-called adiabatic approach – in which locally generated heat from a flux jump is assumed to take a very long time to diffuse through the sample – cannot be used. The fundamental differences between the two cases can be highlighted by considering the simple case of a stack of tapes forming a composite bulk and a plain bulk, both with the same overall engineering J_c. This means that the actual J_c in the thin films of the tape stack is much higher than that of the plain bulk (the J_c of the tapes tested is ~ 2 MA cm^{-2} compared to ~ 30 kA cm^{-2} for a typical bulk at 77 K [6]), and the thin films should therefore have a correspondingly higher instantaneous temperature increase due to a flux jump if both samples have the same overall trapped field. Based on the values presented in Table 5.9, one can also simplify by assuming the heat capacity of all parts of the stack of tapes is the same as the plain bulk. The key differences are then clearer: the total heat generated per unit volume should be the same in both cases, but for the stack of tapes, all the heat is being generated in very thin superconducting layers, which therefore have a very high power density. However, unlike the plain bulk, this heat is almost all conducted away by the upper silver layer with its high thermal conductivity and the lower Hastelloy layer with its large thickness. The high thermal conductivity of the silver layer allows efficient internal cooling of the sample via conduction of heat to the outer sample surfaces. It appears that, despite the heat energy density being much higher for the superconductor in the stack of tapes, the fast removal of heat into a non-superconducting metallic layer suppresses flux instability in the superconductor better than if the heat generation was spread out over a larger superconducting region of low thermal conductivity. The stability provided by the silver layer is analogous to low temperature multi-filamentary wires, in which the non-superconducting metallic matrix prevents a quench by the fast removal of local heat from the superconducting filaments [133].

5.4.3 Flux creep

Flux creep was measured for the trapped fields up to 5 minutes after field cooling, as shown in Figure 5.18. The decay in the trapped field was expected to be logarithmic, as is typically the case for bulks (see Section 1.7.4 and [6]). However, for the time window observed, the creep rate seems to be slightly faster than logarithmic as the curves in Figure 5.18 are not linear. It is difficult to say why the decay is not completely logarithmic as flux creep measurements can be complicated by a number of factors [84]. These include possible residual magnetization in the superconducting coil, which may take minutes to disappear, and also possible heating of the sample. Comparing the results to Figure 1.39 (Section 1.7.4), the initial non-logarithmic decay is similar to that observed for pulsed magnetization of bulks (which also exhibits lower creep rates than field cooling). This suggests there may have been constant heating during the field cooling that would not have been detected by the thermometer, which was not in intimate contact with the sample. Given how short the time window is, it is clear that measurements for an hour or more are needed to get a better picture of the exact form of the decay.

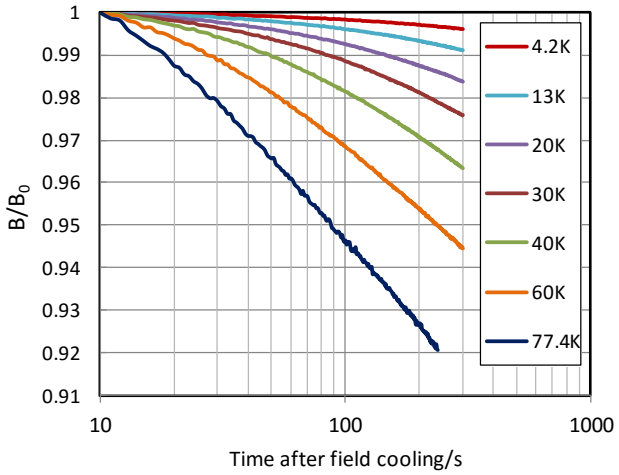

Figure 5.18: Flux creep measurements for trapped field at different temperatures in the first 5 minutes after magnetization. B_0 is the trapped field 10 s after magnetization. The creep rate appears strongly dependent on temperature.

Another interesting feature is the strong decrease in the flux creep rate as temperature decreases. The temperature dependence of creep rate is not generally linear or monotonic but can exhibit a field dependent peak [6, 84]. It is difficult to make a clear comparison of the creep rates to values for (RE)BCO bulks, as the few studies that exist in the literature measure decay in magnetization rather than central field, however it appears that for the time period measured, the flux creep rates are lower than for a typical bulk, particularly at lower temperatures. The temperature dependence of the flux creep rates for the stack of tapes is shown in Figure 5.19, with the definition of α and S being given previously in Section 1.7.4. The advantages of using such a

sample as a permanent magnet at low temperatures are obvious given the more acceptable rates of flux creep. Given the lack of data for high trapped fields in stacks of superconducting tapes, it is clear that a more detailed, longer-duration study of flux creep is needed in future.

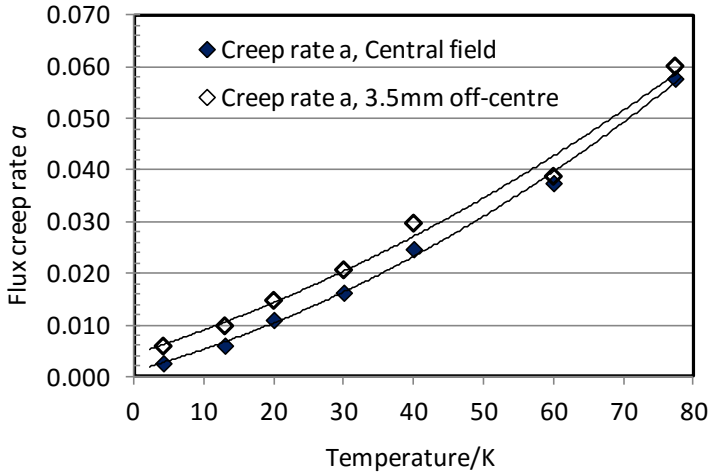

Figure 5.19: Temperature dependence of approximate flux creep rates for the field trapped in a stack of tapes during a 300 s period after field cooling. Assuming that the creep rate for the central field is the same as for the magnetization, typical *a* values for a bulk (Section 1.7.4) are ≈ 0.05 for 77 K and 0.02 for 10 K.

5.4.4 Transport I_c, persistent current and trapped field for a single layer

Measuring the trapped field profile using a Hall probe scan for a single field cooled layer is an important method for characterising the quality of a layer and detecting cracks. This was done for a number of layers chosen at random to determine whether cutting by scissors damages the (RE)BCO layer. An example of the trapped field profile for one of the square tape layers is shown in Figure 5.20a and was produced by an x-y Hall probe surface scan. The symmetrical square profile shows that no detectable damage was caused to the superconducting layer by cutting with scissors. Occasionally some tape pieces that were scanned showed some asymmetry, as illustrated by Figure 5.20b, the most asymmetric profile measured. This striated profile indicates a scratch or weak J_c line along the transport axis, which of course would have little effect on transport current for which the tape is designed but does affect the trapped field profile. This characteristic is believed to be an artefact from the manufacturing process. Although the peak trapped field for b) is similar to the typical symmetric tape piece, it indicates a J_c non-uniformity undesirable for PFM. More extensive testing is required to determine exactly what percentage of tape has such a striation, the existence of which shows that even a stack of tapes has some degree of in-plane J_c non-uniformity. However it is clear from the results that will be presented in Section 5.5 that it does not significantly limit the trapped field using PFM.

It is desirable to extract the I_c of the tape layer from the Hall probe scan data, but this is not easily achieved. The analytical equation for the field produced by a 2D persistent current I_s (A/m) disk circulating in a thin film is given below.

$$I_p = \frac{2fB_0}{\mu_0 A(x,a)} \tag{5.8}$$

B_0 is the peak field peak field, x the height of field measurement above the sample surface, a the radius of current circulation disk and f a correction factor to take account of the increase in field in the case of a magnetic substrate such as Ni-W. $A(x,a)$ is given by,

$$A(x,a) = \ln\left(\sqrt{1+\left(\frac{a}{x}\right)^2}+\left(\frac{a}{x}\right)\right)-\left(1+\left(\frac{a}{x}\right)^2\right)^{-1} \approx \ln\left(\frac{2a}{x}\right)-1 \tag{5.9}$$

with the approximation valid when the scan height is small, leading to $(a/x)^2 >> 1$. Applying the equation to the 39 mT trapped field in Figure 5.20a gives a persistent current per metre equivalent to ≈ 163 A across the 12 mm length of the tape. This is significantly lower than the rated 240 A for the tape. It is believed that the difference between these two values is because persistent current in a single layer generates a very different self field pattern to transport current. Basic modelling shows that the self field experienced by a tape carrying persistent current is on average higher in magnitude, which can significantly reduce the apparent I_c given the steep dependence on field at low field values [134]. The field lines are also in general more perpendicular to the tape surface for a persistent current, which can also have a significant effect on J_c [134]. Flux creep also adds uncertainty to the definition of persistent current. Finally, the difference is not due to there being a lower J_c perpendicular to the tape transport axis, as the I_c of the sample shown in Figure 5.20a was measured to be 275±10 A using a high current goniometer system [135], and in general perpendicular J_c is not expected to be less for MOCVD Superpower tape [134]. The above discussion shows that care must be taken when relating the persistent current that can be induced in (RE)BCO tape pieces to their transport critical current.

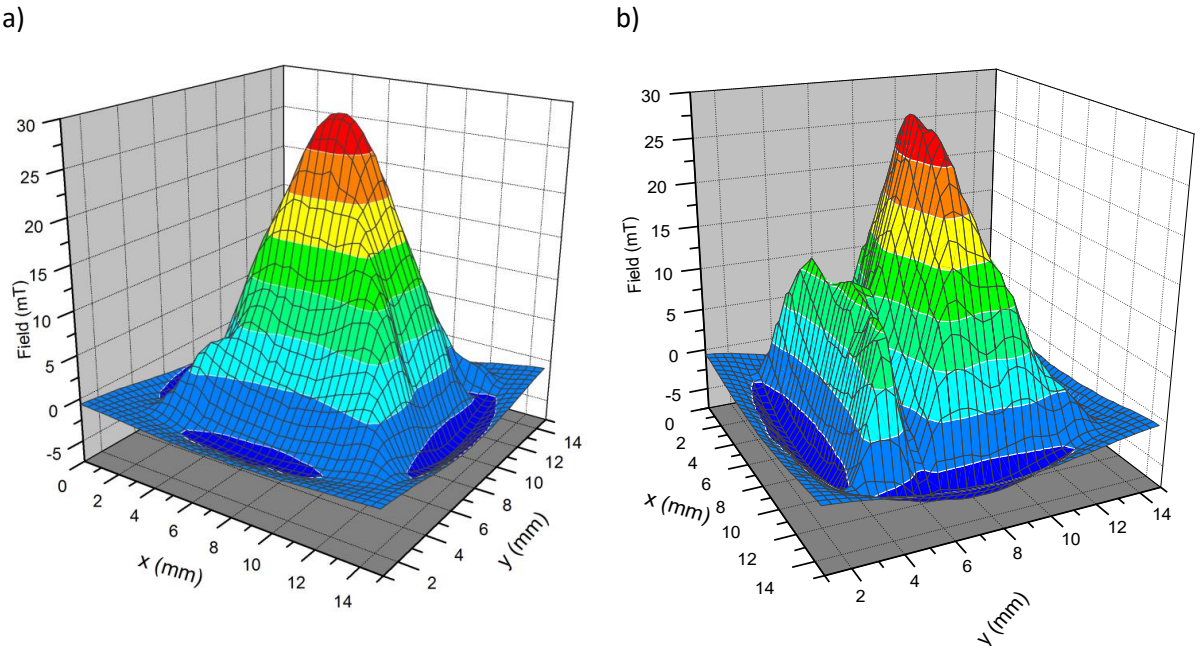

Figure 5.20: a) Typical trapped field profile using field cooling in liquid nitrogen for a single 12 mm by 12 mm layer of (RE)BCO tape cut along the y-axis, perpendicular to the transport axis. b) Striated trapped field profile occasionally seen for a tape piece showing some asymmetry.

5.4.5 Predictions

Trapped fields over 7 T were achieved using the field cooling method of magnetization in a 12 mm square stack of superconducting (RE)BCO tape, and higher thermal stability was observed below ≈ 30 K compared to bulk (RE)BCO. 6.3 T was achieved at 20 K, which is noteworthy given the popular choice of using 20 K as a balance between cooling cost and J_c performance. The SuperPower tape used had an I_c of 240 A (77 K and self-field) corresponding to 200 A cm^{-1}. Assuming approximately linear scaling of trapped field with critical current, much higher trapped fields should be possible using higher performance tape. 12 mm wide, 460 A tape is currently available from SuperPower and should therefore be able to trap approximately 14 T, with even higher fields expected for the research samples reported in Section 1.5.2. These include 600 A/cm for long 600 m lengths (Fujikura) [36] and greater than 1000 A/cm for shorter samples (THEVA) [37], at 77 K. The picture looks even more positive when considering the opportunity to scale up. 12 mm is a relatively small size for a bulk when trapping field, but stacks of tapes should be able to compete with bulks on size given that some manufacturers like AMSC and Bruker produce 40 mm wide tape prior to slitting [34], with future plans to produce 100 mm widths by AMSC. Assuming simple geometric scaling, a 40 mm square stack with the same I_c per cm width as the tape used in this study should in theory trap approximately 24 T. Although this value seems optimistic and may be limited by flux jumps, it can be predicted with some confidence that currently available tape should be able to trap higher fields than the current record of 17.2 T for bulk superconductors [25]. The samples predicted to trap

these high fields should require no external reinforcement. Stacks of superconducting tape therefore have significant potential to be used as trapped field magnets, given the high performance possible and the falling cost of commercial tape. A magnetized stack of tapes would also be able to cope with the additional rotational stress placed on the sample (see Section 2.6) if used in the bulk – bulk bearing design introduced in this thesis.

5.5 Pulsed magnetization of a stack of coated conductors

This section reports the first experimental demonstration of using a stack of superconducting tape pieces as a quasi-permanent magnet activated by a pulsed magnetic field. The stack of tapes used came from the same length of tape used to create the field cooling sample, with many layers actually being the same, but unlike the field cooling case a single stack was magnetized rather than a pair. Sequences of pulses were delivered between 10 and 77.4 K. The results are compared to a commercial 14 mm diameter YBCO bulk showing that the stack of tapes outperformed the bulk at temperatures below approximately 60 K. Particularly high trapped fields were achieved below 50 K, with a maximum of 2.0 T at 10 K measured 0.8 mm from the stack surface. The maximum trapped field possible for a stack of tapes increases significantly with decreasing temperature down to 10 K, rather than saturating at a higher temperature as in the case of the bulk, due to superior thermal stability. The J_c, thermal and mechanical properties of commercial (RE)BCO tapes makes them well suited to pulse magnetization as well as field cooling. It is for the problems facing pulse magnetization of bulks however that a stack of tapes are of particular interest.

When experiencing a pulsed field, bulks suffer from thermal instability below 77 K largely due to inhomogeneous critical current density (resulting from growth sector boundaries as detailed in Section 1.7.1 and Figure 1.35) and poor thermal conductivity. A stack of coated conductors has relatively uniform J_c both radially and axially and so does not seem to suffer from this type of thermal instability when pulse magnetized. Finally the growth of thin films to form superconducting tapes is not as limited in size as bulks given that a buffered metal substrate provides the texture for the (RE)BCO rather than a localised seed crystal. This is particularly true for tapes in which the texture is introduced by thermo-mechanical processing of the metal substrate (e.g. RABiTS), and where non-vacuum deposition techniques are used, e.g. chemical solution deposition (CSD) and ink-jet printing [136]. Large (RE)BCO bulks can be manufactured with high quality [100] but it is a challenge to maintain high J_c far away from the seed crystal which lies at the centre compared to wide (RE)BCO tapes with uniform J_c [35].

It is the intention of this section to make a comparison between standard commercial (RE)BCO tape, and a standard commercial bulk of similar diameter to the tape width which, it should be noted, is smaller than most bulks reported in the literature.

5.5.1 Sample properties

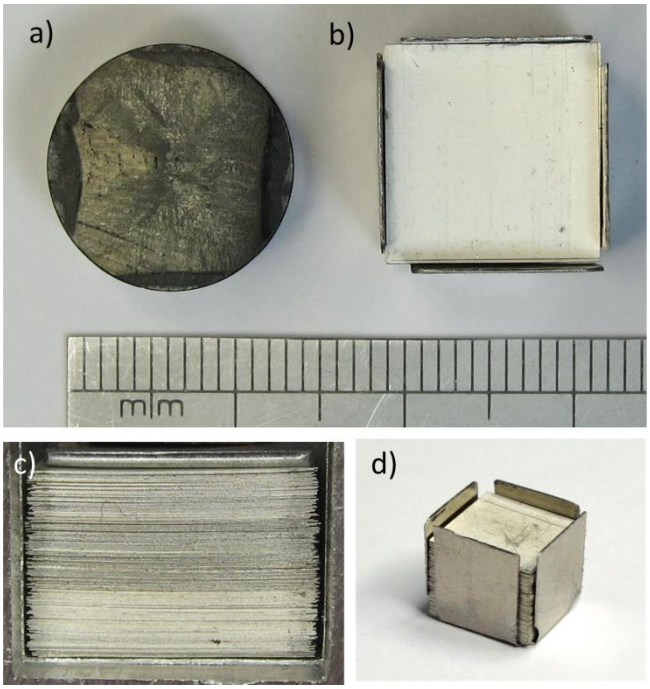

Figure 5.21: a) Top view of 14 mm diameter, 6 mm thick YBCO bulk sample and b) 12 mm square (RE)BCO tape stack in sample holder. c) Side view of compressed stack of 145 (RE)BCO tape layers ≈ 8.1 mm thick, d) Uncompressed tape stack in sample holder.

Table 5.10: Parameters and volume fractions for whole stack of tapes sample and YBCO bulk.

Parameter	145 layer (RE)BCO tape stack	90 layer (RE)BCO tape stack	14 mm bulk sample
Sample height (mm)	8.1	5.1	6.0
Density (kg m^{-3})	8670	8670	5900
(RE)BCO volume fraction	1.8%	1.8%	100%
Hastelloy volume fraction	89.5%	89.5%	-
Silver volume fraction	5.4%	5.4%	-
Stacking space fraction	3.3%	3.3%	-

The stack of tapes used for the PFM tests contained the same tape squares as that used for the field cooling tests in Section 5.4. The individual layers were cut using scissors with no degradation to the J_c detected as discussed in Section 5.4.4. The layers were then stacked into a stainless steel sample holder shown in Figure 5.21b with good mating between the layers, as shown in Figure 5.21c. The 14 mm diameter bulk YBCO sample used, shown in Figure 5.21a, was purchased from Can Superconductors s.r.o.

A comparison of the volume composition of the 145 layer tape stack sample and the bulk is given in Table 5.10. It is clear from Table 5.9 that differences in the thermal properties of the Hastelloy and bulk YBCO are not significant. In addition to the stack of only tapes, sandwich structures were also tested with ferromagnetic NiFe and copper layers, details of which are given in Section 5.5.4.

5.5.2 Trapped field results

The Magnetoforce system (detailed in Chapter 3) was used to pulse magnetise the samples. For all the trapped field results presented, the IMRA method was used to maximise trapped flux by replacing flux lost from the periphery of the samples due to heating. To illustrate the use of this procedure for the reported experiments, the fields applied and trapped in the 90 layer stack at 30 K are shown in Figure 5.22 as an example.

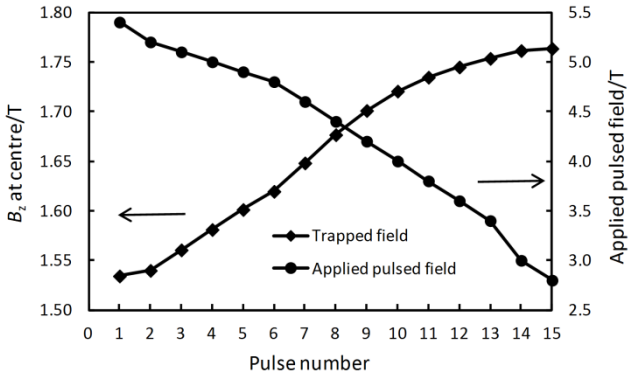

Figure 5.22: Example of an IMRA pulse sequence used for the 30 K stage of magnetizing the 90 layer tape stack.

The maximum possible fields that could be trapped in the stacks of (RE)BCO tapes and YBCO bulk are shown in Figure 5.23. The best documented trapped field performance for bulks is at 77 K, and the 14 mm diameter sample trapped a 0.44 T field at this temperature, higher than the tape stack and a good value for a commercial bulk of this size. The trapped fields in high performance bulks summarised in the introduction are higher than this, by up to a factor of 2 if scaled linearly by diameter down to 14 mm. However, the critical current per tape width of the tested coated conductor is also considerably lower than the best values on metallic substrates (a factor of 3-5 for the quoted examples).

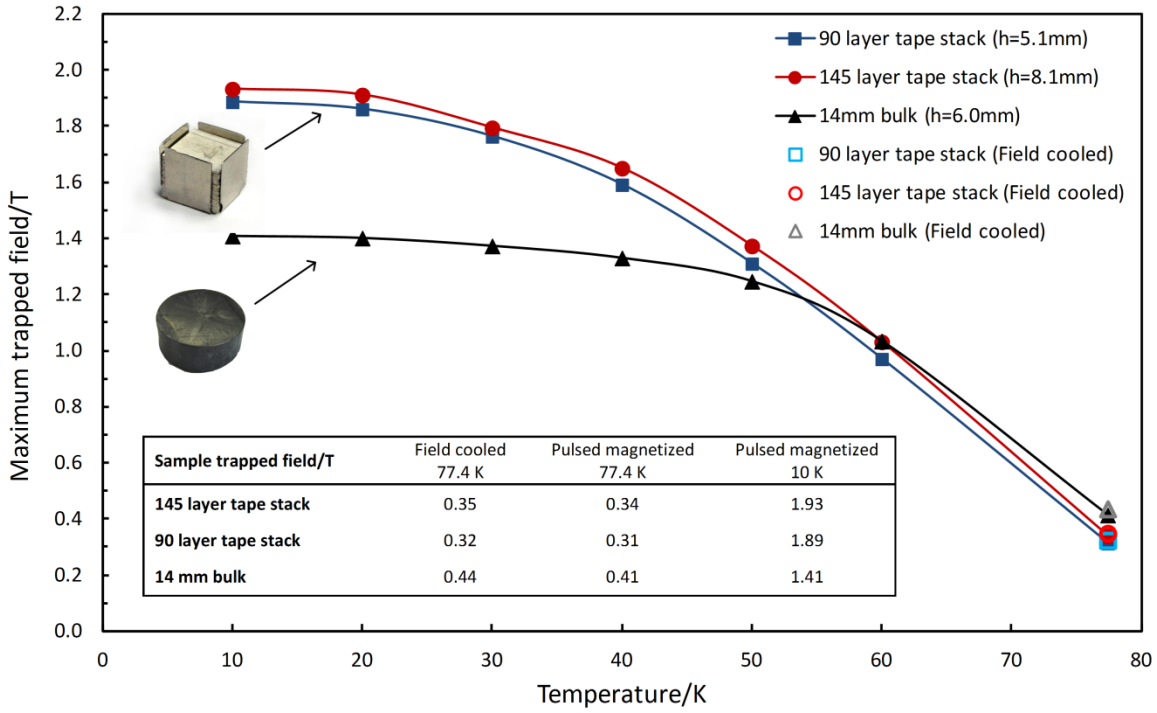

Sample trapped field/T	Field cooled 77.4 K	Pulsed magnetized 77.4 K	Pulsed magnetized 10 K
145 layer tape stack	0.35	0.34	1.93
90 layer tape stack	0.32	0.31	1.89
14 mm bulk	0.44	0.41	1.41

Figure 5.23: Peak trapped field measured 0.8 mm above the tape stack and bulk samples after pulse field magnetization with decreasing temperature. Magnetization was performed using multiple pulses at each temperature, starting at 77.4 K and decreasing. Results for field cooling in an electromagnet are also shown for 77.4 K (open markers).

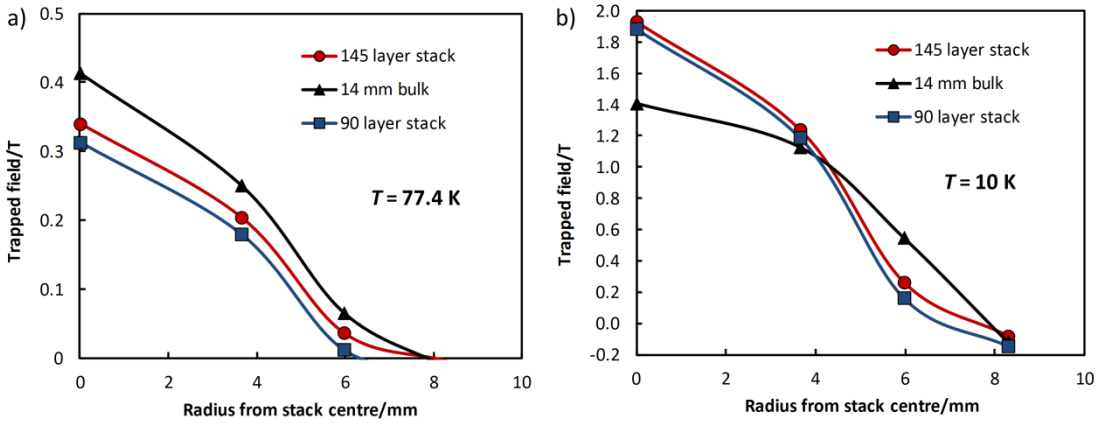

Figure 5.24: Trapped field profiles measured 0.8 mm above the bulk and tape stack samples, a) following magnetization at 77.4 K and b) the final field at 10 K, following magnetization at higher temperatures starting from the trapped fields shown in a).

The increase in J_c of the bulk as temperature decreases does not fully manifest itself in the trapped field results. Although the field increases, it saturates at a temperature around 50 K, reaching a maximum of 1.41 T at 10 K. This strong saturation behaviour is due to thermal instability in the bulk at lower temperatures around 20 K. Because the J_c is so high at these low temperatures, any attempt to penetrate flux a significant depth into the sample will result in larger heat dissipation than at higher temperatures. The inhomogeneous J_c of a bulk leads to hot spots [17] during this

excessive heat generation, linked to asymmetric flux penetration, which causes a large rise in temperature, even enough to cause a sudden loss of all trapped flux if too high a field is applied. This is why the field profiles in Figure 5.24 for the tape stacks are saturated with a conical profile, but the bulk trapped field is broad and has a flatter peak. It was not possible to saturate the bulk at this temperature, as attempting to do so resulted in a collapse of the trapped field to almost zero.

The behaviour of the trapped field for the stack of tapes is significantly different. Although starting lower at 77 K, the trapped field increases rapidly as temperature decreases, showing that the increase in J_c of the (RE)BCO in the tapes can be better exploited. The tape stack must experience a similar amount of total heating at lower temperatures when a high applied field such as 5 T is applied. However, due to the more homogeneous J_c, the generation and dissipation of the heat energy is more cylindrically symmetric, avoiding large local temperature spikes. The silver cap layer deposited on the (RE)BCO is also likely to contribute to thermal stability and faster heat dissipation due to its high thermal conductivity, as predicted by the modelling of composite bulks in Section 5.1 and summarised in [111], however this may be counter-acted in pulsed field applications as some eddy current heating must also be introduced by having such a high electrical conductivity layer. In some applications, the silver layers are ideally suited for cooling directly from the sides of the sample, which is the case for machines using vortex coils for magnetization [137]. The Hastelloy substrate is not believed to contribute as much to the thermal stability of the samples, based on the thermal properties listed in Table 5.9.

The data for a 90 layer stack, is shown in Figure 5.23. Despite having a smaller radius for current to circulate and a smaller height compared to the bulk, stack of tape outperformed the bulk below 60 K. There is no large difference in the trapped fields compared to the 145 layer stack for any of the temperature points, but this might be expected based on the non-linear scaling of field with height for a field cooled bulk [138]. This simple model of the field above a cylinder with circulating current density cannot explain the insensitivity to height present in the results for low temperature. Based on similar numerical calculations as in [138] for the field produced by uniform current density, the field of the 145 layer stack should be 9% higher than the 90 layer stack. This ratio fits the data for 77.4 K however the ratio decreases as temperature decreases, reaching approximately 2.4 % at 10 K. The decrease in the ratio of trapped fields can be understood by the increasing influence of cooling behaviour at lower temperatures. The cooling of the samples in this experiment is largely from the outer surfaces, but heat is generated in the (RE)BCO regions distributed throughout the whole volume of the stack during a pulse. The larger the stack, the smaller the surface area to volume ratio, and as a result the cooling is less efficient for a sample of greater height. This is not so important at 77.4 K due to the relatively small temperature increases, but it becomes a significant limitation at

lower temperatures where thermal instability is present. This is why the 145 layer stack gives only a marginal increase in trapped field at 10 K compared to 90 layers, which means that for low operation temperatures, such as liquid hydrogen temperature, fewer layers can be used without sacrificing trapped field.

Given the trapped field profile data shown in Figure 5.24. It is worth discussing the total trapped flux. For the larger bulks in the previous chapters, the trapped flux was estimated by interpolation and integration (see Section 4.1.2). In this case, the smaller size of the samples considered, makes the reliability of the flux calculation worse given the fewer number of hall probes covering the sample area. In addition, the fact that the stack of tapes most probably has a square trapped field profile (with the profiles in Figure 5.24 measured along the diagonal) introduces further error. Therefore a qualitative comparison of the trapped flux is more appropriate. The trapped fields for 10 K exhibit the largest differences in peak trapped field between the bulk and tape stack, however due to the broader profile of the bulk, the difference in flux is likely to be much smaller and could even be zero. This means that for the bulk, the saturation in trapped flux with decreasing temperature is less significant than for the trapped field. In any case it should be remembered that the bulk has a 7 % larger top surface area than the tape stack, and a circular geometry which is more optimum for generating higher trapped field and flux.

Another factor which needs to be considered when comparing the performance of the bulk and the tape stack is the cooling of the samples by helium gas in the system used. Although compressed, the tape stack has approximately 3% empty space in which the helium can circulate, and the exposed surface area of the periphery of the sample is greater (probably by at least three times) than an equivalent smooth-sided bulk sample, as can be seen in Figure 5.21. These factors must increase the thermal stability of the sample due to more efficient convective cooling. However, if this additional cooling effect was very significant, the field should scale with height even at lower temperatures, as the sample side area and internal empty volume vary linearly with sample height. As discussed previously, this is not the case, with the trapped field being relatively insensitive to the height of the stack below 77 K. For this reason it is believed that the uniformity of J_c and the metallic layers contribute most to the thermal stability. It is nevertheless still important in future to establish the performance of an unsupported stack with layers glued and the sides machined flat, and also to verify that similar results would be obtained with direct conductive cooling.

5.5.3 Comparison to field cooling

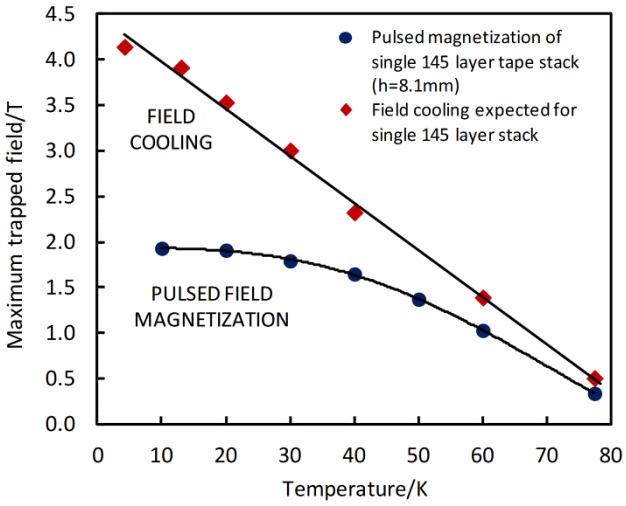

Figure 5.25: Comparison of pulsed magnetization results for a single stack of 145 tapes and prediction for field cooling of the same size stack. The prediction is based on geometric scaling of trapped field for the 120 layer double stack reported in Section 5.4 and assumes the current density would be the same for both stacks.

The field cooling results for the stack of tapes can be compared to a previous study on pulsed field magnetization of a single stack containing 145 layers [126] as shown in Figure 5.25. In order to compare the trapped fields directly, the field cooling trapped fields obtained for the double 120 layer stack have been scaled to give the expected field for a single 145 layer stack measured at the same distance from the stack surface (0.8 mm) as used in the pulsed magnetization study. This scaling, which assumes uniform current density and was achieved using a finite element model, is a good approximation. Such scaling cannot be used for the case of pulsed field magnetization, which gives rise to complex current density distributions due to large heating effects during a pulse. The tape layers used for both samples came from the same tape length, with most of the layers used in the pulsed magnetization study re-used for the sample in the present study. The comparison of the trapped fields gives an important insight into the limitations of the pulsed field method. Although the increase in trapped field with decreasing temperature using PFM saturates less than for a bulk, the difference between the trapped fields achieved by PFM and field cooling for the stack still increases with decreasing temperature. As for field cooling there may be an enhanced cooling effect due to the volume fraction of ‘empty space’ in the stacks (which would be filled with helium gas) and also due to the uneven sample sides (see Figure 5.21c).

The discrepancy between field cooling and pulse magnetization results (Figure 5.25) exceeds a factor of two at the lowest temperatures due to unavoidable heat generation in pulsed magnetization. There should also exist a discrepancy for total trapped flux, but this is expected to be smaller given the broader field profiles which tend to be trapped using pulsed magnetization

compared to field cooling. Although the fields trapped by field cooling represent a limit which can never be reached at low temperatures by pulsed magnetization, for many applications it is worth sacrificing this full potential given the practicality and lower cost of pulsed field magnetization [87].

5.5.4 Sandwich stacks

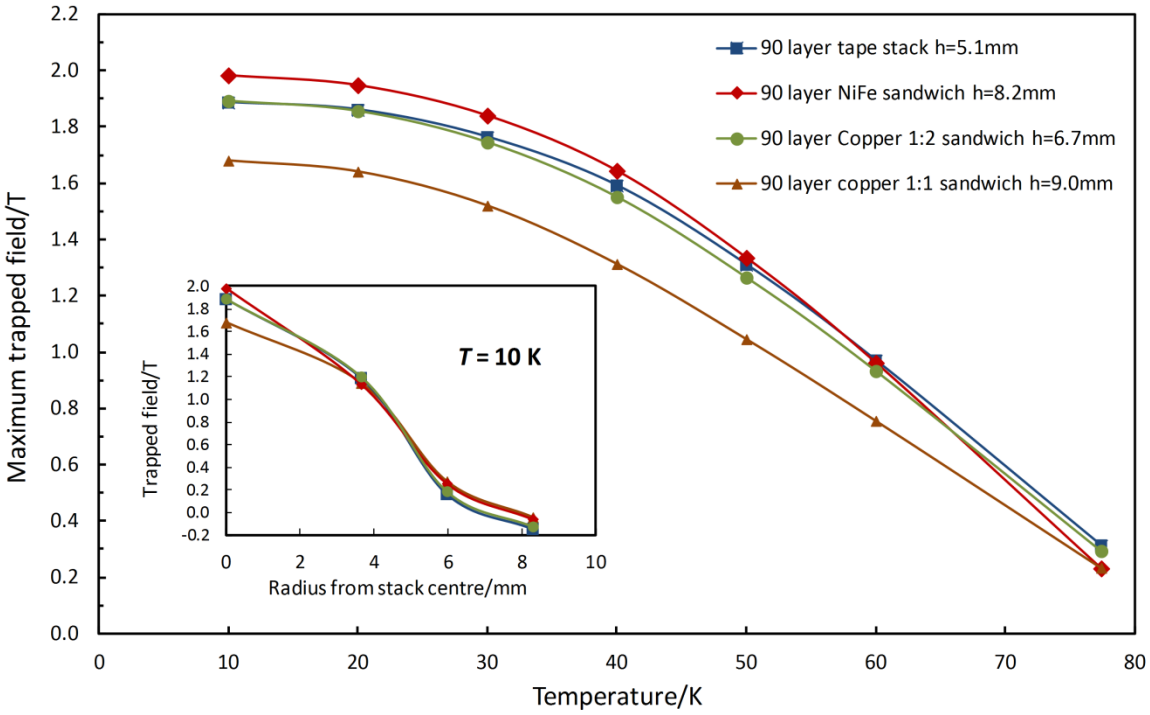

Figure 5.26: Peak trapped field measured 0.8 mm above tape sandwiches after pulse field magnetization with decreasing temperature. The NiFe sandwich had ferromagnetic NiFe layers between each tape layer, whereas the copper sandwiches had a copper layer for every tape layer ('1:1') or every 2 tape layers ('1:2'). The result for 90 layers of tape only is also shown for comparison.

The assembly of a composite bulk from separate tape pieces opens up the new possibility of sandwiching a thin layer of any chosen material between the (RE)BCO tapes in an attempt to enhance certain properties. As a first step towards exploring this possibility, sandwiches were created using ferromagnetic NiFe layers and copper foil. The NiFe layers were cut from 10 mm wide, 35 μm thick "50/50" alloy tape [139] produced by Carpenter Technology Corporation and similar to Carpenter high permeability "49" alloy. The copper layers were 40 μm thick and were made from 12 mm wide 3M adhesive copper tape with the adhesive backing removed. Two copper sandwiches were created, labelled 1:1 for a copper layer between every (RE)BCO tape layer and 1:2 for 1 copper layer inserted for every two layers, with all sandwiches prepared using the same 90 layers of (RE)BCO tape.

The trapped field results for the sandwiches are shown in Figure 5.26. When material is inserted between the layers of tape, the effective J_c of the whole stack is reduced, leading to a decrease in

the trapped field above the stack. Although the height of the sample increases, this is never enough to counter the larger linear decrease in field with effective J_c. Therefore the concept behind creating a sandwich is that the material introduced will somehow enhance the trapped field by a factor greater than the reduction in the effective J_c factor. The aim of using copper foil was to enhance thermal stability and help conduct heat away to the edges of the sample, in a similar way to the expected behaviour of the silver cap layer in the tapes. Any thermal enhancement provided by the copper in the 1:1 sandwich was not enough to counter the decrease in the effective J_c of the stack and any additional heating that might arise due to eddy currents, leading to a lower field than 90 layers of (RE)BCO tape alone, as shown in Figure 5.26. However, when using one layer of copper for every two tape layers, it appears that an enhancement in thermal stability at low temperature has balanced the decrease in the effective J_c of the stack. Although the copper sandwiches reported here did not exceed the trapped field of 90 layers of tape alone, the 1:2 stack indicates that the thermal properties can be enhanced. By choosing copper of the optimum thickness and by slitting the copper layers to minimise eddy current heating during a pulse, it is likely that the thermal stability contribution at low temperatures can exceed the decrease in the effective J_c of the stack, leading to an enhanced trapped field using the same number of tape layers. This prospect is attractive for minimising cost.

The performance of the NiFe sandwich exceeded both the 90 layer stack and also the 145 layer stack presented earlier for low temperatures (2.0 T at 10 K). This enhancement shows that the NiFe had a significant effect on the field, but it is not possible to determine from the present experiments whether thermal or ferromagnetic effects are responsible for this behaviour: literature values of the thermal properties are not very different from Hastelloy. Also, measurement of the field from room temperature down to 10 K, above a stack of the NiFe layers behind which was placed a PM, suggest that the permeability of the NiFe tape is almost independent of temperature. Modelling and further experiments are required to explain the electrodynamics and heating behaviour in this superconducting-ferromagnetic structure.

6 Conclusions and outlook

A new type of superconducting bearing has been designed and modelled, which achieves a significantly higher force density than existing PM – bulk superconductor bearings by using magnetized superconducting bulks instead of PMs as the field source. The concept of the bulk – bulk bearing was proven by levitation force measurements between a bulk MgB_2 hollow tube and single 25.5 mm diameter magnetized YBCO bulks. Pulsed field magnetization was investigated and performed on the YBCO bulks, using the techniques of IMRA and MPSC to maximise the trapped field and flux. The maximum trapped field and flux recorded in the bulks were 1.68 T and 0.61 mWb respectively, measured above the sample surface, showing that (RE)BCO bulks can be an order of magnitude more powerful than rare-earth PMs. Levitation force versus displacement curves were produced for the bulk – bulk configuration following field cooling of the MgB_2 bulk in the field of the magnetized YBCO. The high trapped fields in the YBCO gave rise to peak levitation forces up to 560 N, demonstrating the great potential of the design to levitate large loads. The experiment also showed that 20 K is a suitable temperature for the bearing, as smaller forces and large hysteresis were observed at temperatures above 20 K, and flux jumps due to thermal instability were observed at 12 K. For smaller displacements that would typically be used for a real bearing, the hysteresis was found to be small compared to the full force-displacement curves. Modelling of the force interaction using the perfectly trapped flux model, which assumed perfect shielding for both the MgB_2 and YBCO, is an important tool for understanding the shapes of the force displacement curves and predicting the maximum possible forces.

The pulsed magnetization and levitation force measurements were conducted using a newly constructed experimental facility based on a pulse tube cryocooler, named MagnetoForce, capable of delivering automated sequences of pulsed fields up to 10 T and allowing trapped field performance to be monitored during the magnetization process. Such an automated system is a step towards magnetizing bulks for industrial applications including motors and generators as well as the bulk – bulk bearing design proposed.

The future outlook for the bulk – bulk bearing design is positive given its potential to be suitable for applications such as flywheel energy storage, where a higher load capacity can significantly increase the energy stored, as well as low loss bearings that need to resist high g-forces. However, engineering challenges remain, such as the need to cool both stator and rotor components to cryogenic temperatures. The potential of the design is further increased if the challenge of effectively magnetizing superconducting bulks can be solved, which was addressed in the second half of this thesis.

The most practical method of magnetizing superconducting bulks is using a pulsed field, but as shown by magneto-thermal FEM modelling, the heating and thermal instability caused by a pulsed field lead to a significant reduction in J_c, and loss of flux, giving a final trapped field and flux less than that resulting from field cooling. The J_c inhomogeneity of existing (RE)BCO bulks also significantly limits their potential to consistently trap high fields when pulse magnetized at temperatures below 77 K. To address these problems, the concept of a composite bulk was considered. Magneto-thermal modelling of pulsed magnetization explored the dynamics of heat flow and current density inside a bulk. High thermal conductivity embedded structures were shown to improve trapped field and flux by channelling heat away to a cold head or thermal mass, resulting in enhanced current density. Experimental tests of assemblies of bulk YBCO pieces, copper and sapphire, as well as YBCO bulks with arrays of holes filled with copper wire, showed no significant enhancement in trapped field performance. However, this is largely believed to be due to poor thermal contact between the YBCO and high thermal conductivity components. Future experiments with tighter geometric tolerances and improved thermal contact are needed to establish the full potential of these structures.

A radically new approach to trapped field magnets using coated conductors was shown to be the most successful composite bulk design tested. Starting from commercially available 12 mm wide tape produced by SuperPower Inc. (approximate thickness 55 µm), square stacks were created and magnetized, trapping exceptionally high fields given the specified tape I_c of 240 A (77 K and self-field) which is typical for commercial coated conductors.

Trapped fields over 7 T were achieved between two 120 layer stacks using field cooling, and higher thermal stability was observed below ≈ 30 K compared to that typical for bulk (RE)BCO. Much higher trapped fields should be possible using higher performance tape, potentially up to 14 T for the highest I_c commercial 12 mm wide tape and even more for research samples. The opportunity to scale up to wider widths, such as 40 mm, gives a stack of tapes potential to trap very high flux as well as field compared to the relatively small 12 mm square stacks, an important property for many applications. Based on a review of the properties of commercial and research superconducting tape, it can be predicted with some confidence that currently available tape should be able to trap higher fields than the current record of 17.2 T for bulk superconductors [25]. The samples predicted to trap these high fields should require no external reinforcement due to the strong metallic substrates present. A magnetized stack of tapes would also be able to cope with the additional rotational stress placed on the sample if used in a bulk – bulk bearing design.

The trapped field for a single stack of tape magnetized using pulsed fields was up to 2.0 T, significantly higher than for a commercially available 14 mm diameter bulk for temperatures below 60 K, and higher than the maximum field trapped in any of the larger (RE)BCO bulks tested for

levitation force measurements. This is despite the sample having less than 2 % superconductor by volume. The main reason for the high performance at low temperature is the superior thermal stability of the tape stack resulting from a relatively homogeneous J_c, which reduces hotspots, as well as the silver cap layer. Sandwich structures are possible, as shown, by inserting copper and NiFe layers between (RE)BCO tape layers, but this approach needs to be explored in more detail. The choice of materials, thermal, magnetic and geometric parameters all need to be optimised due to the many competing factors that determine the overall trapped field in these sandwich structures. Future research also includes gluing tape layers together with epoxy resin and machining the stack into a cylinder, to create a self-supporting structure suitable for applications. More experiments are also needed to make a quantitative comparison of the maximum trapped flux possible for a stack of tapes compared to a bulk.

The outlook for using a stack of superconducting tape for real applications, such as in motors and generators, is very positive for a number of reasons. Some prototype rotating machines already use magnetized bulks cooled to 30 or 40 K to exploit the increase in J_c [87], and a stack of tapes is ideally suited to this temperature range. The known, or at least easily measurable, I_c of the commercial (RE)BCO tape used can give a tape stack predictable trapped field behaviour, which is attractive for engineering applications. The concept has scalability: although commercially-available tapes are rarely wider than 12 mm at present, some manufacturers produce tape as wide as 40 mm prior to slitting for long length coated conductors, and there is a growing trend towards increased widths to allow higher production throughput. Finally, the price of (RE)BCO tape is steadily falling, giving stacks of magnetized tapes great potential to be used as cost effective high field permanent magnets.

7 References

[1] Schmuser P, "Superconductivity in high energy particle accelerators," in *Progress in Particle and Nuclear Physics, Vol 49, No 1*. vol. 49, ed Amsterdam: Elsevier Science Bv, 2002, pp. 155-244.

[2] Onnes H K, 1911 The resistance of pure mercury at helium temperatures *Commun. Phys. Lab. Univ. Leiden,* **12** 120

[3] Nagamatsu J, Nakagawa N, Muranaka T, Zenitani Y, and Akimitsu J, 2001 Superconductivity at 39K in magnesium diboride *Nature,* **410** 63-64

[4] Giunchi G, Cavallire T, Bassani P, and Guicciardi S, 2008 The mechanical properties of the MgB_2 bulk materials obtained by reactive liquid Mg infiltration *AIP Conf. Proc.,* **986** 396-404

[5] Abd-Syukor R, 2009 High Temperature Superconductors: Materials, Mechanisms and Applications *Academy of Sciences Malaysia,* ASM Inaugural Lecture 2009

[6] Krabbes G, Fuchs G, Canders W R, May H, and Palka R, *High Temperature Superconductor Bulk Materials*: Wiley-VCH, 2006.

[7] Cardwell D A and Ginley D S, *Handbook of Superconducting Materials*: Institute of Physics, 2003.

[8] Bean C P, 1962 Magnetization of Hard Superconductors *Phys. Rev. Lett.,* **8** 250

[9] Kim Y B, Hempstead C F, and Strnad A R, 1963 Magnetization and Critical Supercurrents *Phys. Rev.,* **129** 528

[10] Chen D X, Sanchez A, Nogues J, and Munoz J S, 1990 Bean Kim and Exponential Critical-State Models for High-Tc Superconductors *Phys. Rev. B,* **41** 9510-9512

[11] *Helsinki Univeristy of Technology Advanced Energy Systems group,* www.tkk.fi/Units/AES/projects/prlaser/supercond.htm (2010)

[12] Cardwell D A, 1998 Processing and properties of large grain (RE)BCO *Mater. Sci. Eng. B,* **53** 1-10

[13] Chaud X, Noudem J, Prikhna T, Savchuk Y, Haanappel E, Diko P, and Zhang C P, 2009 Flux mapping at 77 K and local measurement at lower temperature of thin-wall YBaCuO single-domain samples oxygenated under high pressure *Physica C,* **469** 1200-1206

[14] Lousberg G P, Fagnard J F, Haanappel E, Chaud X, Ausloos M, Vanderheyden B, and Vanderbemden P, 2009 Pulsed-field magnetization of drilled bulk high-temperature superconductors: flux front propagation in the volume and on the surface *Supercond. Sci. Technol.,* **22** 125026

[15] Jiao Y L, Xiao L, Ren H T, Zheng M H, and Chen Y X, 2003 J(c)-B characteristics for bulk single domain YBCO superconductors *Physica C,* **386** 266-270

[16] Gonzalez-Arrabal R, Eisterer M, and Weber H W, 2003 Study of inhomogeneities in the flux density distribution of big monolithic (RE)$Ba_2Cu_3O_{7-d}$ melt-textured superconductors *J. Appl. Phys.,* **93** 4734-4738

[17] Fujishiro H, Naito T, and Oyama M, 2012 Three-dimensional Simulation of Magnetic Flux Dynamics and Temperature Rise in HTSC Bulk during Pulsed Field Magnetization *Phys. Procedia,* **36** 687-692

[18] Surzhenko A B, Schauroth S, Litzkendorf D, Zeisberger M, Habisreuther T, and Gawalek W, 2001 Growth-related profiles of remanent flux in bulk melt-textured YBaCuO crystal magnetized by pulsed fields *Supercond. Sci. Technol.,* **14** 770-774

[19] Sekino M, Yasuda H, Miyazoe A, and Ohsaki H, 2011 Concentric Slitting of a Ring-Shaped Bulk Superconductor for a Reduction in Circumferential Inhomogeneity of the Trapped Magnetic Field *IEEE Trans. Appl. Supercond.,* **21** 1588-1591

[20] Teshima H, Morita M, Arayashiki T, Naito T, and Fujishiro H, 2013 10T class trapped field properties of a large Gd-Ba-Cu-O bulk superconductor *Phys. Procedia ISS2012,* (in press)

[21] Yokoyama K, Oka T, and Noto K, 2011 Evaluation of Pulsed-Field Magnetization on a Superconducting Bulk Magnet System Using a 13 K Refrigerator *IEEE Trans. Appl. Supercond.,* **21** 1657-1660

[22] Oka T, Seki H, Ogawa J, Fukui S, Sato T, and Yokoyama K, 2011 Performance of Trapped Magnetic Field in Superconducting Bulk Magnets Activated by Pulsed Field Magnetization *IEEE Trans. Appl. Supercond.,* **21** 3356-3359

[23] Fujishiro H, Hiyama T, Naito T, Yanagi Y, and Itoh Y, 2009 Enhancement of trapped field and total trapped flux on GdBaCuO bulk by the MMPSC plus IMRA method *Supercond. Sci. Technol.,* **22** 095006

[24] Teshima H and Morita M, 2012 Recent Progress in HTS Bulk Technology and Performance at NSC *Phys. Procedia,* **36** 572-575

[25] Tomita M and Murakami M, 2003 High-temperature superconductor bulk magnets that can trap magnetic fields of over 17 tesla at 29 K *Nature,* **421** 517-520

[26] Nariki S, Sakai N, and Murakami M, 2002 Development of Gd-Ba-Cu-O bulk magnets with very high trapped magnetic field *Physica C,* **378** 631-635

[27] Nariki S and et al., 2005 Melt-processed Gd–Ba–Cu–O superconductor with trapped field of 3 T at 77 K *Supercond. Sci. Technol.,* **18** S126

[28] Weinstein R, Sawh R, Ren Y, and Parks D, 1998 The role of uranium, with and without irradiation, in the achievement of Jc ≈ 300000 A cm^{-2} at 77 K in large grain melt-textured Y123 *Mater. Sci. Eng.: B,* **53** 38-44

[29] Fuchs G, Krabbes G, Müller K H, Verges P, Schultz L, Gonzalez-Arrabal R, Eisterer M, and Weber H W, 2003 High Magnetic Fields in Superconducting Permanent Magnets *J. Low. Temp. Phys.,* **133** 159-179

[30] Krabbes G, Fuchs G, Verges P, Diko P, Stover G, and Gruss S, 2002 16 T trapped fields in modified YBaCuO: materials aspects *Physica C,* **378** 636-640

[31] Fujishiro H, Tateiwa T, Fujiwara A, Oka T, and Hayashi H, 2006 Higher trapped field over 5 T on HTSC bulk by modified pulse field magnetizing *Physica C,* **445** 334-338

[32] Fuchs G, Wenger C, Gladun A, Gruss S, Krabbes G, Schatzle P, and Muller K H, 1999 Different limitations of trapped fields in melt-textured YBCO *Inst. Phys. Conf. Ser,* **1** 111-114

[33] www.superpower-inc.com (2013)

[34] Hahn S, Voccio J, Bermond S, Park D K, Bascunan J, Kim S B, Masaru T, and Iwasa Y, 2011 Field Performance of an Optimized Stack of YBCO Square "Annuli" for a Compact NMR Magnet *IEEE Trans. Appl. Supercond.,* **21** 1632-1635

[35] Hahn S, Kim S B, Ahn M C, Voccio J, Bascunan J, and Iwasa Y, 2010 Trapped Field Characteristics of Stacked YBCO Thin Plates for Compact NMR Magnets: Spatial Field Distribution and Temporal Stability *IEEE Trans. Appl. Supercond.,* **20** 1037-1040

[36] Kakimoto K, Igarashi M, Hanyu S, Sutoh Y, Takemoto T, Hayashida T, Hanada Y, Nakamura N, Kikutake R, Kutami H, Iijima Y, and Saitoh T, 2011 Long RE123 coated conductors with high critical current over 500 A/cm by IBAD/PLD technique *Physica C,* **471** 929-931

[37] Dürrschnabel M, Aabdin Z, Bauer M, Semerad R, Prusseit W, and Eibl O, 2012 $DyBa_2Cu_3O_{7-x}$ superconducting coated conductors with critical currents exceeding 1000 A cm^{-1} *Supercond. Sci. Technol.,* **25** 105007

[38] Buzea C and Yamashita T, 2001 Review of the superconducting properties of MgB2 *Supercond. Sci. Technol.,* **14** 115-R146

[39] Kawano K, Abell J S, Kambara M, Babu N H, and Cardwell D A, 2001 Evidence for high intergranular current flow in a single-phase polycrystalline MgB_2 superconductor *Appl. Phys. Lett.,* **79** 2216-2218

[40] Giunchi G, 2003 High density MgB_2 obtained by reactive liquid Mg infiltration *Int. J. Mod. Phys. B,* **17** 453-460

[41] Sprio S, Tampieri A, Celotti G, and Rinaldi D, "Densification behaviour of MgB_2 superconductor by hot-pressing," in *Euro Ceramics Viii, Pts 1-3*. vol. 264-268, Mandal H. and Ovecoglu L., Eds., ed Zurich-Uetikon: Trans Tech Publications Ltd, 2004, pp. 1201-1204.

[42] Giunchi G, Ripamonti G, Cavallin T, and Bassani E, 2006 The reactive liquid Mg infiltration process to produce large superconducting bulk MgB_2 manufacts *Cryogenics,* **46** 237-242

[43] Fujishiro H, Tamura T, Arayashiki T, Oyama M, Sasaki T, Naito T, Giunchi G, and Albisetti A F, 2012 Pulsed Field Magnetization of Large MgB_2 Bulk Fabricated by Reactive Liquid Mg Infiltration *Jpn. J. Appl. Phys.,* **51**

[44] Giunchi G, Perini E, Cavallin T, Bassani E, Quarantiello R, Cavaliere V, and Matrone A, 2008 Superconducting permanent magnet made by a bulk MgB_2 ring *IEEE Trans. Appl. Supercond.,* **18** 1216-1219

[45] Durrell J H, Dancer C E J, Dennis A, Shi Y, Xu Z, Campbell A M, Babu N H, Todd R I, Grovenor C R M, and Cardwell D A, 2012 A trapped field of > 3 T in bulk MgB_2 fabricated by uniaxial hot pressing *Supercond. Sci. Technol.,* **25**

[46] Earnshaw S, 1842 On the nature of the molecular forces which regulate the constitution of the luminiferous ether *Trans. Camb. Phil. Soc.,* **7** 97-112

[47] *Beacon Power Corporation*, www.beaconpower.com (2010)

[48] Mao B, Huang R, and Jia S, 2008 Potential Applications of Maglev Railway Technology in China *J. Transp. Syst. Eng. Inf. Technol.,* **8** 29-39

[49] Di Barba P, May H, Mognaschi M E, Palka R, and Savini A, 2009 Multiobjective design optimization of an excitation arrangement used in superconducting magnetic bearings *Inter. J. Appl. Electromagn. Mech.,* **30** 127-134

[50] Di Barba P and Palka R, 2007 A multiobjective approach to the shape design of HTSC magnetic bearings *Prz. Elektrotech.,* **83** 228-230

[51] May H, Palka R, Portabella E, and Canders W R, 2004 Evaluation of the magnetic field - high temperature superconductor interactions *COMPEL,* **23** 286-304

[52] Hofmann C and Ries G, 2001 Modelling the interactions between magnets and granular high-T-c superconductor material with a finite-element method *Supercond. Sci. Technol.,* **14** 34-40

[53] Coombs T A, Cansiz A, and Campbell A M, 2002 A superconducting thrust-bearing system for an energy storage flywheel *Supercond. Sci. Technol.,* **15** 831-835

[54] Day A C, Hull J R, Strasik M, Johnson P E, McCrary K E, Edwards J, Mittleider J A, Schindler J R, Hawkins R A, and Yoder M L, 2003 Temperature and frequency effects in a high-performance superconducting bearing *IEEE Trans. Appl. Supercond.,* **13** 2179-2184

[55] Rastogi A, Alonso D R, Coombs T A, and Campbell A M, 2003 Axial and journal bearings for superconducting flywheel systems *IEEE Trans. Appl. Supercond.,* **13** 2267-2270

[56] Strasik M, Johnson P E, Day A C, Mittleider J, Higgins M D, Edwards J, Schindler J R, McCrary K E, McIver C R, Carlson D, Gonder J F, and Hull J R, 2007 Design, fabrication, and test of a 5-kWh/100-kW flywheel energy storage utilizing a high-temperature superconducting bearing *IEEE Trans. Appl. Supercond.,* **17** 2133-2137

[57] Deng Z, Lin Q, Wang J, Zheng J, Ma G, Zhang Y, and Wang S, 2009 Basic design and characteristics study of a double-axial superconducting magnetic bearing system *Cryogenics,* **49** 259-262

[58] Rastogi A, Coombs T A, Campbell A M, and Hall R, 2005 Axial stiffness of journal bearings in zero-field and field-cooled modes *IEEE Trans. Appl. Supercond.,* **15** 2242-2244

[59] Viznichenko R, Velichko A V, Hong Z, and Coombs T A, 2008 Advantage of superconducting bearing in a commercial flywheel system *J. Phys.: Conf. Ser.,* **97** 012120

[60] Mitsuda H, Inoue A, Nakaya B, and Komori M, 2009 Improvement of Energy Storage Flywheel System With SMB and PMB and Its Performances *IEEE Trans. Appl. Supercond.,* **19** 2091-2094

[61] Werfel F N, Floegel-Delor U, Riedel T, Rothfeld R, Wippich D, Goebel B, Reiner G, and Wehlau N, 2007 A compact HTS 5 kWh/250 kW flywheel energy storage system *IEEE Trans. Appl. Supercond.,* **17** 2138-2141

[62] Walter H, Bock J, Frohne C, Schippl K, May H, Canders W R, Kummeth P, Nick W, and Neumueller H W, 2006 First heavy load bearing for industrial application with shaft loads up to 10 kN *J. Phys.: Conf. Ser.,* **43** 995-8

[63] Murakami K, Komori M, Mitsuda H, and Inoue A, 2007 Design of an energy storage flywheel system using permanent magnet bearing (PMB) and superconducting magnetic bearing (SMB) *Cryogenics,* **47** 272-277

[64] Hull J R, 2000 Superconducting bearings *Supercond. Sci. Technol.,* **13** R1-R15

[65] Kita M, Ichihara T, Masaie I, Demachi K, Sakai N, and Hirabayashi I, 2005 Rotation loss reduction of superconducting magnetic bearings by stacking and rearranging the shape of the bulks *Physica C,* **426** 821-825

[66] Dell R M and Rand D A J, 2001 Energy storage -- a key technology for global energy sustainability *J. Power Sources,* **100** 2-17

[67] *Aldewitz Technologiezentrum GmbH (ATZ), Rittergut Aldelwitz, O4886 Arzberg, Germany*, www.atz-gmbh.com (2010)

[68] Werfel F N, Floegel-Delor U, Riedel T, Rothfeld R, Wippich D, and Goebel B, 2004 Operation and design selection of high temperature superconducting magnetic bearings *Supercond. Sci. Technol.,* **17** 1192-1195

[69] Werfel F N, Floegel-Delor U, Riedel I, Rothfeld R, Wippich D, and Goebel B, 2005 Encapsulated HTS bearings: Technical and cost considerations *IEEE Trans. Appl. Supercond.,* **15** 2306-2311

[70] Werfel F N, Floegel-Delor U, Rothfeld R, Goebel B, Wippich D, and Riedel T, 2005 Modelling and construction of a compact 500 kg HTS magnetic bearing *Supercond. Sci. Technol.,* **18** S19-S23

[71] Werfel F N, Floegel-Delor U, Riedel T, Rothfeld R, Wippich D, and Goebel B, 2006 Flywheel challenge: HTS magnetic bearing *J. Phys.: Conf. Ser.,* **43** 1007-1010

[72] Werfel F N, Floegel-Delor U, Riedel T, Rothfeld R, Wippich D, Goebel B, Reiner G, and Wehlau N, 2008 250 kW Flywheel with HTS Magnetic Bearing for Industrial Use *J.Phys.: Conf. Ser.,* **97** 012206

[73] Perini E and Giunchi G, 2009 Field cooling of a MgB_2 cylinder around a permanent magnet stack: prototype for superconductive magnetic bearing *Supercond. Sci. Technol.,* **22** 045021

[74] Marbán G and Valdés-Solís T, 2007 Towards the hydrogen economy? *Int. J. Hydrog. Energy,* **32** 1625-1637

[75] Mizutani U, Oka T, Itoh Y, Yanagi Y, Yoshikawa M, and Ikuta H, 1998 Pulsed-field magnetization applied to high-T-c superconductors *Appl. Supercond.,* **6** 235-246

[76] Fuchs G, Schatzle P, Krabbes G, Gruss S, Verges P, Muller K H, Fink J, and Schultz L, 2000 Trapped magnetic fields larger than 14 T in bulk $YBa_2Cu_3O_{7-x}$ *Appl. Phys. Lett.,* **76** 2107-2109

[77] Sander M, Sutter U, Koch R, and Klaser M, 2000 Pulsed magnetization of HTS bulk parts at T < 77 K *Supercond. Sci. Technol.,* **13** 841-845

[78] Chaud X, Haanappel E, Noudem J G, and Horvath D, 2008 Trapped field of YBCO single-domain samples using pulse magnetization from 77K to 20K *8th European Conference on Applied Superconductivity (Eucas'07), Supercond. Sci. Technol.* **97** 4855

[79] Yanagi Y C, Oka T O, Itoh Y C, and Yoshikawa M K, "Superconducting magnet apparatus and method for magnetizing superconductor," US Patent US 7026901, 2006.

[80] Felder B, Miki M, Tsuzuki K, Izumi M, and Hayakawa H, 2010 Optimization of a condensed-neon cooling system for a HTS synchronous motor with Gd-bulk HTS field-pole magnets *J. Phys. Conf. Ser.,* **234**

[81] Fujishiro H, Naito T, Kakehata K, Yanagi Y, and Itoh Y, 2010 Estimation of temperature rise from trapped field gradient on superconducting bulk magnetized by multi-pulse technique *Supercond. Sci. Technol.,* **23**

[82] Anderson P W, 1962 Theory of Flux Creep in Hard Superconductors *Phys. Rev. Lett.,* **9** 309

[83] Beasley M R, Labusch R, and Webb W W, 1969 Flux Creep in Type-2 Superconductors *Phys. Rev.,* **181** 682

[84] Yeshurun Y, Malozemoff A P, and Shaulov A, 1996 Magnetic relaxation in high-temperature superconductors *Rev. Mod. Phys.,* **68** 911-949

[85] Matsuzaki H, Kimura Y, I O, Izumi M, Ida T, Akita Y, Sugimoto H, Miki M, and Kitano M, 2005 An axial gap-type HTS bulk synchronous motor excited by pulsed-field magnetization with vortex-type armature copper windings *IEEE Trans. Appl. Supercond.,* **15** 2222-2225

[86] Masson P J, Breschi M, Tixador P, and Luongo C A, 2007 Design of HTS axial flux motor for aircraft propulsion *IEEE Trans. Appl. Supercond.,* **17** 1533-1536

[87] Zhou D, Izumi M, Miki M, Felder B, Ida T, and Kitano M, 2012 An overview of rotating machine systems with high-temperature bulk superconductors *Supercond. Sci. Technol.,* **25** 103001

[88] Association M M P, "MMPA Standard OlOO-Standard Specifications for Permanent Magnet Materials."

[89] Nagashima K, Seino H, Sakai N, and Murakami M, 2009 Superconducting magnetic bearing for a flywheel energy storage system using superconducting coils and bulk superconductors *Physica C,* **469** 1244-1249

[90] Arai Y, Seino H, Yoshizawa K, and Nagashima K, Development of Superconducting Magnetic Bearing with Superconducting Coil and Bulk Superconductor for Flywheel Energy Storage System *Physica C,* **97** 4855

[91] Larbalestier D, Gurevich A, Feldmann D M, and Polyanskii A, 2001 High-T-c superconducting materials for electric power applications *Nature,* **414** 368-377

[92] Barnes G, McCulloch M, and Dew-Hughes D, 1999 Computer modelling of type II superconductors in applications *Supercond. Sci. Technol.,* **12** 518-522

[93] Coombs T A, Campbell A M, Murphy A, and Emmens M, 2001 A fast algorithm for calculating the critical state in superconductors *COMPEL,* **20** 240-252

[94] Lousberg G P, Ausloos M, Geuzaine C, Dular P, Vanderbemden P, and Vanderheyden B, 2009 Numerical simulation of the magnetization of high-temperature superconductors: a 3D finite element method using a single time-step iteration *Supercond. Sci. Technol.,* **22** 055005

[95] Amemiya N, Murasawa S, Banno N, and Miyamoto K, 1998 Numerical modelings of superconducting wires for AC loss calculations *Physica C,* **310** 16-29

[96] Ainslie M D, Yuan W J, Hong Z Y, Pei R L, Flack T J, and Coombs T A, 2011 Modeling and Electrical Measurement of Transport AC Loss in HTS-Based Superconducting Coils for Electric Machines *IEEE Trans. Appl. Supercond.,* **21** 3265-3268

[97] Zhang M and Coombs T A, 2012 3D modeling of high-T-c superconductors by finite element software *Supercond. Sci. Technol.,* **25**

[98] Hong Z, Campbell A M, and Coombs T A, 2006 Numerical solution of critical state in superconductivity by finite element software *Supercond. Sci. Technol.,* **19** 1246-1252

[99] Rhyner J, 1993 Magnetic-Properties and Ac-Losses of Superconductors with Power-Law Current-Voltage Characteristics *Physica C,* **212** 292-300

[100] Fujishiro H, Tateiwa T, Kakehata K, Hiyama T, Naito T, and Yanagi Y, 2008 Trapped field characteristics on phi 65 mm GdBaCuO bulk by modified multi-pulse technique with stepwise cooling (MMPSC) *Physica C,* **468** 1477-1480

[101] Kordyuk A A, 1998 Magnetic levitation for hard superconductors *J Appl. Phys.,* **83** 610-612

[102] Xia Z, Chen Q Y, Ma K B, Mcmichael C K, Lamb M, Cooley R S, Fowler P C, and Chu W K, 1995 Design of Superconducting Magnetic Bearings with High Levitating Force for Flywheel Energy-Storage Systems *IEEE Trans. Appl. Supercond.,* **5** 622-625

[103] Hennig W, Parks D, Weinstein R, and Sawh R P, 1998 Enhanced levitation forces with field cooled $YBa_2Cu_3O_{7-\delta}$ *Appl. Phys. Lett.,* **72** 3059-3061

[104] *Cryozone BV, Ekkersrijt 4611, 5692 DR Son, Netherlands,* www.cryozone.nl

[105] Sychev V V, Vasserman A A, Kozlov A D, Spiridonov G A, and Tsymarnyi V A, *Thermodynamic properties of helium*, 1987.

[106] Fritz H, 1999 Pulsed magnets *Rep. Prog. Phys.,* **62** 859

[107] Hull J R and Cansiz A, 1999 Vertical and lateral forces between a permanent magnet and a high-temperature superconductor *J. Appl. Phys.,* **86** 6396-6404

[108] Itoh Y, Yanagi Y, Yoshikawa M, Oka T, Harada S, Sakakibara T, Yamada Y, and Mizutani U, 1995 High-Temperature Superconducting Motor Using Y-Ba-Cu-O Bulk Magnets *Jpn. J. Appl. Phys. 1,* **34** 5574-5578

[109] Hull J R and Strasik M, 2010 Concepts for using trapped-flux bulk high-temperature superconductor in motors and generators *Supercond. Sci. Technol.,* **23** 124005

[110] Patel A, Palka R, and Glowacki B A, 2011 New fully superconducting bearing concept using the difference in irreversibility field of two superconducting components *Supercond. Sci. Technol.,* **24** 015009

[111] Patel A and Glowacki B A, 2012 Enhanced trapped field achieved in a superconducting bulk using high thermal conductivity structures following simulated pulsed field magnetization *Supercond. Sci. Technol.,* **25** 125015

[112] Fujishiro H and Naito T, 2010 Simulation of temperature and magnetic field distribution in superconducting bulk during pulsed field magnetization *Supercond. Sci. Technol.,* **23** 105021

[113] Itoh Y, Yanagi Y, and Mizutani U, 1997 Flux motion during pulsed field magnetization in Y-Ba-Cu-O superconducting bulk magnet *J. Appl. Phys.,* **82** 5600-5611

[114] Fujishiro H, Ikebe M, Naito T, Noto K, Kohayashi S, and Yoshizawa S, 1994 Anisotropic Thermal-Diffusivity and Conductivity of YBCO(123) and YBCO(211) Mixed-Crystals .1. *Jpn. J. Appl. Phys. 1,* **33** 4965-4970

[115] Marquardt E D, Le J P, and Radebaugh R, 2001 Cryogenic material properties database *Cryocoolers 11,* 681-687

[116] Kimura Y, Matsumoto H, Fukai H, Sakai N, Hirabayashi I, Izumi M, and Murakami M, 2006 Pulsed field magnetization properties for Gd–Ba–Cu–O superconductors impregnated with Bi–Sn–Cd alloy *Physica C,* **445–448** 408-411

[117] Cavallin T, Young E A, Beduz C, Yang Y, and Giunchi G, 2007 Thermal conductivity of bulk MgB_2 produced by infiltration of different boron powders *IEEE Trans. Appl. Supercond.,* **17** 2770-2773

[118] Berman R, Foster E L, and Ziman J M, 1955 Thermal Conduction in Artificial Sapphire Crystals at Low Temperatures. I. Nearly Perfect Crystals *Proc. R. Soc. Lond. Ser. A.: Math. Phys. Sci.,* **231** 130-144

[119] Diko P, Kracunovska S, Ceniga L, Bierlich J, Zeisberger M, and Gawalek W, 2005 Microstructure of top seeded melt-grown YBCO bulks with holes *Supercond. Sci. Technol.,* **18** 1400-1404

[120] Noudem J G, Meslin S, Horvath D, Harnois C, Chateigner D, Eve S, Gomina M, Chaud X, and Murakami M, 2007 Fabrication of textured YBCO bulks with artificial holes *Physica C,* **463** 301-307

[121] Lousberg G P, Fagnard J F, Chaud X, Ausloos M, Vanderbemden P and Vanderheyden B, 2011 Magnetic properties of drilled bulk high-temperature superconductors filled with a ferromagnetic powder *Supercond. Sci. Technol.,* **24** 035008

[122] Lousberg G P, Ausloos M, Vanderbemden P, and Vanderheyden B, 2008 Bulk high-T(c) superconductors with drilled holes: how to arrange the holes to maximize the trapped magnetic flux? *Supercond. Sci. Technol.,* **21** 025010

[123] Taekyung K, Sangkwon J, Young Hee H, and Byung Jun P, 2013 Thermal Packaging of High Temperature Superconductor Bulk for Superconducting Flywheel Energy Storage *IEEE Trans. Appl. Supercond.,* **23** 5701104-5701104

[124] Patel A, Filar K, Nizhankovskii V I, Hopkins S C, and Glowacki B A, 2013 Trapped fields greater than 7 T in a 12 mm square stack of commercial high-temperature superconducting tape *Appl. Phys. Lett.,* **102** 102601-5

[125] Selvamanickam V, 2011 Second-generation HTS Wire for Wind Energy Applications *Symposium on Superconducting Devices for Wind Energy February 25, 2011 – Barcelona, Spain,* www.superpower-inc.com/content/technical-documents

[126] Patel A, Hopkins S C, and Glowacki B A, 2013 Trapped fields up to 2 T in a 12 mm square stack of commercial superconducting tape using pulsed field magnetization *Supercond. Sci. Technol.,* **26** 032001

[127] Lu J, Choi E S, and Zhou H D, 2008 Physical properties of Hastelloy (R) C-276 (TM) at cryogenic temperatures *J. Appl. Phys.,* **103** 064908

[128] Smith D R and Fickett F R, 1995 Low-Temperature Properties of Silver *J. Res. Natl. Inst. Stan.,* **100** 119-171

[129] Naito T, Fujishiro H, Yamamura Y, Saito K, Okamoto H, Hayashi H, Fujiwara N, Gosho Y, and Shiohara Y, 2011 Thermal Conductivity of YBCO Coated Conductors Reinforced by Metal Tape *IEEE Trans. Appl. Supercond.,* **21** 3037-3040

[130] Schwarz M, Schacherer C, Ehrlich A, and Weiss K P, 2010 Thermal Conductivity of High Temperature Superconductor Coated Conductors *Adv. Cryog. Eng. (Mater.), Vol 56: Trans. Int. Cryog. Mater. Conf. - ICMC,* **1219** 388-393

[131] Clickner C C, Ekin J W, Cheggour N, Thieme C L H, Qiao Y, Xie Y Y, and Goyal A, 2006 Mechanical properties of pure Ni and Ni-alloy substrate materials for Y–Ba–Cu–O coated superconductors *Cryogenics,* **46** 432-438

[132] Mints R G and Rakhmanov A L, 1981 Critical State Stability in Type-II Superconductors and Superconducting-Normal-Metal Composites *Rev. Mod. Phys.,* **53** 551-592

[133] Critchlow P R, Gregory E, and Zeitlin B, 1971 Multifilamentary superconducting composites *Cryogenics,* **11** 3-10

[134] Weigand M, Rutter N A, Sahonta S L, and Durrell J H, 2011 Critical Current Densities of MOCVD Tapes for Different Current Directions *IEEE Trans. Appl. Supercond.,* **21** 3347-3351

[135] Chudy M, Hopkins S C, Wozniak M, Glowacki B A, Eisterer M, and Weber H W, 2011 Full angular critical current characteristics of coated conductors studied using a two-axis high current goniometer *Supercond. Sci. Technol.,* **24** 075018

[136] Van Driessche I, Feys J, Hopkins S C, Lommens P, Granados X, Glowacki B A, Ricart S, Holzapfel B, Vilardell M, Kirchner A, and Backer M, 2012 Chemical solution deposition using ink-jet printing for YBCO coated conductors *Supercond. Sci. Technol.,* **25** 065017

[137] Miki M, Tokura S, Hayakawa H, Inami H, Kitano M, Matsuzaki H, Kimura Y, Ohtani I, Morita E, Ogata H, Izumi M, Sugimoto H, and Ida T, 2006 Development of a synchronous motor with

Gd–Ba–Cu–O bulk superconductors as pole-field magnets for propulsion system *Supercond. Sci. Technol.,* **19** S494

[138] Eisterer M, Haindl S, Zehetmayer M, Gonzalez-Arrabal R, Weber H W, Litzkendorf D, Zeisberger M, Habisreuther T, Gawalek W, Shlyk L, and Krabbes G, 2006 Limitations for the trapped field in large grain YBCO superconductors *Supercond. Sci. Technol.,* **19** S530-S536

[139] Glowacki B A, Vickers M E, Rutter N A, Maher E, Pasotti F, Baldini A, and Major R, 2002 Texture development in long lengths of NiFe tapes for superconducting coated conductor *J. Mater. Sci.,* **37** 157-168